MODEL REFINEMENT OF UNSTEADY RANS AND ITS PRACTICAL APPLICATIONS IN THE FIELD OF HYDRAULIC ENGINEERING

MD. SHAHJAHAN ALI

June, 2008

MODEL REFINEMENT OF UNSTEADY RANS AND ITS PRACTICAL APPLICATIONS IN THE FIELD OF HYDRAULIC ENGINEERING

MD. SHAHJAHAN ALI

June, 2008

Abstract

Turbulent flow is of central importance to many engineering applications in the field of hydraulic engineering, aerospace industry, process engineering, internal combustion engines, environmental engineering, etc. Turbulence, intermittently, is a three-dimensional, time dependent phenomenon. The major approaches to study such flows numerically are Reynolds Averaged Navier-Stokes (RANS), Large Eddy Simulation (LES) and Direct Numerical Simulation (DNS). Considerable effort has been made to develop these methods in the recent decades and an important advancement has been achieved. Since LES and DNS are more memory and CPU intensive than RANS, the methods are not suitable for practical applications. That is why the RANS type turbulence models, such as two equation model or Reynolds stress model, are still the popular tool used for practical engineering applications. Therefore, the clarification of the possibility, the limitations and areas of improvement of RANS models still deserve attention.

Among the turbulence models, k–ε eddy viscosity model is the simplest 'complete' model that can be used on modern personal computers. Although standard k–ε model has been applied in many turbulent flows with high degree of success, the prediction is not satisfactory for some fundamental flows containing strong streamline curvature, vortices and rotations. This deficiency is due to the isotropic assumption of eddy viscosity. Thus, the non-linear k–ε model is thought to be a superior tool for predicting such complex flows. Considering the draw backs in the existing models, some refinements are proposed in the second order non-linear model incorporating new functions for the coefficient of eddy viscosity and for that of non-linear quadratic term. The model constants in the functional forms are estimated considering the realizability conditions and anisotropy of turbulence in some baseline flows, such as, plane shear layer, plane strain, axisymmetric contraction and axisymmetric expansion. Thereafter the model is applied to following engineering applications to study the model applicability as well as to gain in-depth knowledge about these turbulent flows: (i) Turbulent jets with and without swirl (ii) An idealized vortex street (iii) Compound channel with single and double flood plains (iv) Rankine vortices with and without axial flow and (v) Open channel flows with rectangular side cavity.

Approximate solutions for the fundamental properties of swirl and non-swirl jets are derived based on the non-linear k–ε model. Tuning the model constants, the approximate solutions are compared with the previous experimental results.

Since coherent vortices are important element that governs many turbulent flows, the spatial distribution and topological change of turbulent structures with singular points are studied. It is observed that the turbulent kinetic energy and normal stresses show elliptical structure at vortex center, which changes to hyperbolic profile at saddle point at a stream-wise periodic distance of π. However, the shear stresses show hyperbolic structures at vortex center and the structure changes to elliptical at saddle point. The turbulent structures of the vortex street are found sensitive to the functional form of the coefficient of eddy viscosity.

Due to shear layer, coherent vortices are generated in a compound channel at the interface of main channel and flood plain. The flow field in a compound channel is reproduced using standard as well as non-linear k–ε models. The flow equations are discretized with finite volume method based on a staggered grid system.The result shows that the velocity and shear stress values are under-predicted near the interface region, if the momentum transfer due to horizontal vortex is not considered. The pattern and magnitude of secondary currents are found in good agreement with previous experimental results. The horizontal vortices and secondary current both are found to play significant role to increase the compound roughness of the channel.

The unsteady numerical simulations are performed for an isolated axial vortex (trailing vortex) with different swirl numbers using standard and non-linear *k–ε* models. Although a rapid decay of tangential and axial velocity is seen in standard model, the non-linear model shows good agreement with previous DNS results. Five different time periods are observed in the growth/decay profile of turbulence kinetic energy. It is found that the rate of temporal decay in tangential velocity increases with the decrease of swirl number (q). 3D numerical simulation is carried out for an ideal Rankine vortex using both RANS and LES. The prediction of vortex decay by RANS model shows good agreement with LES. The profile of water surface is found to be depressed near the central area of the vortex with a minimum water depth at the center.

A numerical simulator based on the full staggered boundary fitted coordinate method incorporated with 2nd order non-linear *k–ε* model is used for the analysis of complex turbulent flows in an open channel with rectangular side-cavity. Simulation shows that the flow in a dead zone is characterized by three types of flow phenomena: circulation inside the dead-zone, periodic coherent vortices at the interface, and water surface oscillation inside the dead zone. The temporal variation of water surface shows a depressed water depth at the center of coherent vortices. This depression of the free surface moves downward with time along the interface, as seen in the movement of coherent vortices in flow vectors. It is observed that the period of dead-zone oscillation is same as that of instability vortex. Each cycle of velocity variation consists two components of oscillations. The long period oscillation is due to seiche, and the short oscillation is caused by shear instability.

Acknowledgements

The research work presented in this manuscript is conducted in River System Engineering Laboratory, Department of Urban Management, Kyoto University, Japan. First of all, I wish to acknowledge gratefully the financial support from the Japanese Government's "Monbukagusho" scholarship, which enabled me to undertake my Ph. D. studies in Japan.

I wish to express my deepest gratitude and sincere thanks to Professor **Dr. Takashi Hosoda,** my supervisor, for introducing the CFD research field to me. His inspiration and guidance, constant and kind advices show me the way of research. His ideas, handouts, teaching and tireless efforts pushed me to finish up my work in time.

I am very grateful to Professor **Dr. Gotoh Hitoshi** and Associate Professor **Dr. Satoru Ushijima**, the examiners of my thesis, for their comments and suggestions to improve my thesis.

I would like to express my thanks to Associate Professor **Dr. Ichiro Kimura** (Hokkaido University) for his useful advices. I also wish to thank Assistant Professor **Dr. Shinichiro Onda** for his help and valuable suggestions over the time.

Thanks to all the members in the River Engineering Laboratory, especially **Mr. Eddie Puay** and **Mr. Bidur Ghimire,** for their assistance and fruitful discussions over many issues.

Finally, I have dedicated this dissertation to my parents whose care and endurance during my prolonged life of studies deserve my most sincere and warmest gratitude.

Preface

This manuscript of *Ph.D. Thesis* includes the contents of the following published and/or accepted journal and conference papers:

1. Ali, M. S., Hosoda, T., Kimura, I. and Onda, S., Approximate solution of an axisymmetric swirling jet using non-linear k–ε model with consideration of realizability, *Journal of Applied Mechanics*, *JSCE*, vol. 9, pp. 821-832, 2006.
2. Ali, M. S., Hosoda, T. and Kimura, I., Effect of empirical functions of non-linear k–ε model on the prediction of flow resistance in a compound channel, *Proceedings of International Conference on Water and Flood Management*, Dhaka, Bangladesh, vol. 2, pp. 735-743, 2007.
3. Ali, M. S., Hosoda, T. and Kimura, I., Unsteady RANS computations of compound channel flows with large scale vortices and secondary currents, *5th International Symposium on Environmental Hydraulics*, ASU, Tempe, Arizona, 2007 (CD-ROM Proceedings).
4. Ali, M. S., Hosoda, T. and Kimura, I., A non-linear k–ε model to predict the spatial change of turbulent structures in large scale vortices, *Journal of Applied Mechanics*, *JSCE*, Vol. 10, pp. 723-732, 2007.
5. Ali, M. S., Hosoda, T. and Kimura, I., Resistance coefficient of open channel flows in a compound channel with horizontal vortices and secondary currents, *Proceedings of 2007 Annual Meeting, Japan Society of Fluid Mechanics*, Tokyo, Japan, 2007 (CD-ROM Proceedings).
6. Ali, M. S., Hosoda, T. and Kimura, I., Unsteady simulation of turbulent axial vortex by means of a non-linear k–ε model, Accepted for *Journal of Applied Mechanics*, *JSCE*, Vol. 11, 2008.

7. Ali, M. S., Hosoda, T. and Kimura, I., Study on spatial distribution and topological change of turbulent structures in coherent vortex with a non-linear k–ε model, Accepted for *8th International Conference on Hydro-Science and Engineering*, Nagoya, Japan, 2008.
8. Ali, M. S., Hosoda, T. and Kimura, I., Unsteady RANS computation of turbulent trailing vortex, Accepted for *2nd International Symposium of Shallow Flows*, HKUST, Hong Kong, 2008.

Table of contents

Title Page i

Abstract iii

Acknowledgment vi

Preface vii

Table of Contents ix

List of Figures xiv

List of Tables xxiv

Chapter 1. INTRODUCTION **1**

- 1.1 Preliminaries 1
- 1.2 Numerical Methods 2
  - 1.2.1 RANS Model 3
  - 1.2.2 Large Eddy Simulation 4
  - 1.2.3 Direct Numerical Simulation 5
- 1.3 Objectives and Justification of the Study 5
- 1.4 Scope of the Research 7
- 1.5 References 9

Chapter 2. NON-LINEAR k–ε MODEL **10**

- 2.1 Introduction 10
- 2.2 Mathematical Formulation in 3D Cartesian Coordinate 12

2.2.1 Basic equations 12

2.2.2 Turbulence models 12

2.3 Tuning of Model Constants 16

2.3.1 Tuning of coefficients in c_β 16

2.3.2 Consideration of realizability for plane shear layer 18

2.3.3 Distribution of c_μ in S-Ω plane 20

2.3.4 Model performance in homogeneous strain 21

2.4 Mathematical Formulation in 3D Curvilinear Coordinate 25

2.4.1 Basic equations 25

2.4.2 Constitutive equations 26

2.5 Summary 27

2.6 References 27

Chapter 3. TURBULENT ROUND JET WITH AND WITHOUT SWIRL **29**

3.1 Introduction 29

3.2 Governing Equations 30

3.3 Procedure for the Solution 32

3.4 Approximate Solution of Turbulent Swirling Jet 33

3.4.1 Assumed profiles 33

3.4.2 Swirl parameter 34

3.4.3 Derived solutions 35

3.5 Results and Discussions 37

3.5.1 Round jet without swirl 37

3.5.2 Swirl jet 42

3.6 Summary 46

3.7 References 49

Chapter 4. SPATIAL DISTRIBUTION AND TOPOLOGICAL CHANGE OF TURBULENT STRUCTURES IN AN IDEALIZED VORTEX STREET **51**

4.1 Introduction 51

4.2 Governing Equations 53

4.3 Methods of Investigations 54

 4.3.1 Stuart vortices 54

 4.3.2 Approximate solution 55

 4.3.3 Numerical simulation 56

4.4 Turbulent Structures at Vortex Center (Focus) 57

 4.4.1 Approximate solution 57

 4.4.2 Numerical simulation 64

4.5 Turbulent Structures at Saddle Point 68

4.6 Summary 73

4.7 References 75

Chapter 5. UNSTEADY 3D COMPUTATION OF COMPOUND OPEN CHANNEL FLOWS **76**

5.1 Introduction 76

5.2 Governing Equations 78

5.3 Numerical Procedure and Flow Configurations 80

 5.3.1 Numerical schemes and boundary conditions 80

 5.3.2 Flow configurations and test models 82

5.4 Results and Discussions 86

 5.4.1 Plan view of flow pattern 86

 5.4.2 Characteristics of secondary currents 88

5.4.3 Prediction of discharge 92

5.4.4 Prediction of flow resistance 94

5.4.5 Velocity and shear stress profiles 98

5.4.6 Compound channel with two flood plains 99

5.4.7 Turbulent properties of coherent vortices in compound channel 102

5.5 Summary 109

5.6 References 111

Chapter 6. THE STRUCTURE AND DECAY OF TURBULENT RANKINE VORTEX WITH AND WITHOUT AXIAL FLOW **113**

6.1 Introduction 113

6.2 Non-Linear k-ε Model 117

6.3 Large Eddy Simulation 118

6.4 Simulation Details and Flow Configurations of Test Cases 120

6.4.1 Initial conditions 120

6.4.2 Flow domain and computational schemes 122

6.5 Simulation of Turbulent Trailing Vortex with Swirl Number q =1.0 123

6.5.1 Decay of trailing vortex 125

6.5.2 Self-similarity of profiles 131

6.5.3 Instability vortices 132

6.5.4 Temporal growth/decay of turbulence 133

6.5.5 Comparison with Qin's DNS data 136

6.6 Simulation of Turbulent Trailing Vortex with Swirl Number q =0.5 139

6.7 Simulation of Turbulent Trailing Vortex with no Axial Velocity 143

6.8 3D Simulation of Rankin Vortex using LES and RANS 144

6.9 Summary 149

6.10 References 151

Chapter 7. 3D UNSTEADY SIMULATION OF OPEN CHANNEL FLOWS WITH A RECTANGULAR SIDE-CAVITY **153**

7.1 Introduction 153

7.2 Non-Linear k-ε Model in 3D Curvilinear Coordinate 155

7.3 Computational Scheme and Flow Domain 156

7.4 Numerical Results and Discussions 159

  7.4.1 Time averaged flow properties 159

  7.4.2 Temporal variations of flows 159

  7.4.3 Secondary currents 168

7.5 Summary 171

7.6 References 172

Chapter 8. CONCLUSIONS **173**

8.1 Summary of the Findings 173

8.2 Recommendation for Further Studies 178

8.3 References 179

List of Figures

Chapter 1

Figure 1.1 Time averaging of velocity in RANS method (a) Steady RANS (b) Unsteady RANS………………………………………………………….. 3

Figure 1.2 Plan view of flow vector in a compound channel showing the coherent vortices at the interface of main channel and flood plain (simulated flow field in the present study)………………………………………………… 6

Chapter 2

Figure 2.1 Comparison of anisotropy of turbulence in plane shear layer using Eq.(2.22) and (2.23) for the coefficient c_β……………………………….. 16

Figure 2.2 Relation between c_μ and M in a simple shear layer………………………. 17

Figure 2.3 Profile of c_μ (S, Ω) on an S – Ω plane [Eq. (2.16a)]……………………… 17

Figure 2.4 Profile of c_μ (S, Ω) on S – Ω plane for the function in (a) Eq. 2.14a (by Kimura & Hosoda, 2003), (b) Eq. 2.16a (proposed function)………….. 20

Figure 2.5 Model performance in homogeneous strain considering the anisotropy of turbulence and realizability limit………………………………………... 23

Figure 2.6 The anisotropy of turbulence for the baseline flows in homogeneous strain predicted by (i) Non-linear k-ε model with c_β=constant and (ii) Standard k–ε model…………………………………………………. 24

Chapter 3

Figure 3.1 Definition sketch of swirl jet (Pratte and Keffer, 1972)…………………. 33

Figure 3.2 Distribution of turbulent intensity of the axial velocity in a round jet without swirl………………………………………………………………... 38

Figure 3.3 Distribution of turbulent intensity of the radial velocity in a round jet without swirl………………………………………………………………... 39

Figure 3.4 Distribution of turbulent intensity of the circumferential velocity in a round jet without swirl………………………………………………… 39

Figure 3.5 Radial distribution of turbulent shear stress in a round jet without swirl... 40

Figure 3.6 Radial distribution of turbulent kinetic energy in a round jet without swirl……………………………………………………………………. 40

Figure 3.7 Radial distribution of turbulent kinetic energy dissipation rate in a round jet without swirl…………………………………………………………….. 41

Figure 3.8 Comparison of jet half-width…………………………………………….. 41

Figure 3.9 Distribution of turbulent intensity of the axial velocity in a swirl jet……. 42

Figure 3.10 Distribution of turbulent intensity of the radial velocity in a swirl jet…… 42

Figure 3.11 Distribution of turbulent intensity of the circumferential velocity in a swirl jet………………………………………………………………… 44

Figure 3.12 Radial distribution of turbulent kinetic energy in a swirl jet…………….. 44

Figure 3.13 Radial distribution of turbulent shear stress in a swirl jet……………….. 45

Figure 3.14 Distribution of turbulent intensity for different swirl numbers (a) for axial velocity (b) for radial velocity (c) for circumferential velocity……. 46

Chapter 4

Figure 4.1 Sketch of a coherent vortex in plane mixing layer……………………… 52

Figure 4.2 Contour of streamlines for Stuart vortex with different eccentricity: (a) A=0 (b) A=-1/2 (c) A=-3/4 (d) A=-1.0 (e) two vortices with A=-1/2……. 58

Figure 4.3 Streamline contour at vortex center (focus) of Stuart vortex approximated by Taylor function………………………………………… 59

Figure 4.4 Turbulent structures by approximate solution for vortex point (Run-1): (a) turbulent kinetic energy, k (b) turbulent energy dissipation rate, ε (c) turbulent normal stress in x direction, $\overline{u_1u_1}$ (d) turbulent normal stress in y direction, $\overline{u_2u_2}$ (e) turbulent normal stress in z direction, $\overline{u_3u_3}$ (f) turbulent shear stress in xy plane, $\overline{u_1u_2}$ ………………………………… 60

Figure 4.5 Profiles of $c_\mu(S, \Omega)$ in the vortex field for Run-1 and Run-2………….. 63

Figure 4.6 Turbulent structures by approximate solution for vortex point (Run-2): (a) turbulent kinetic energy, k (b) turbulent energy dissipation rate, ε (c) turbulent normal stress in x direction, $\overline{u_1u_1}$ (d) turbulent normal stress in y direction, $\overline{u_2u_2}$ (e) turbulent normal stress in z direction, $\overline{u_3u_3}$ (f) turbulent shear stress in xy plane, $\overline{u_1u_2}$ ………………………………… 64

Figure 4.7 Turbulent structures by numerical simulation for vortex point (Run-1): (a) turbulent kinetic energy, k (b) turbulent energy dissipation rate, ε (c) turbulent normal stress in x direction, $\overline{u_1u_1}$ (d) turbulent normal stress in y direction, $\overline{u_2u_2}$ (e) turbulent normal stress in z direction, $\overline{u_3u_3}$ (f) turbulent shear stress in xy plane, $\overline{u_1u_2}$ ………………………………… 66

Figure 4.8 Turbulent structures by numerical simulation for vortex point (Run-2): (a) turbulent kinetic energy, k (b) turbulent energy dissipation rate, ε (c) turbulent normal stress in x direction, $\overline{u_1u_1}$ (d) turbulent normal stress in y direction, $\overline{u_2u_2}$ (e) turbulent normal stress in z direction, $\overline{u_3u_3}$ (f) turbulent shear stress in xy plane, $\overline{u_1u_2}$ ………………………………… 67

Figure 4.9 Turbulent structures by numerical simulation using standard k-ε model: (a) turbulent kinetic energy, k (b) turbulent energy dissipation rate, ε (c) turbulent normal stress in x direction, $\overline{u_1u_1}$ (d) turbulent normal stress in *y* direction, $\overline{u_2u_2}$ (e) turbulent normal stress in *z* direction, $\overline{u_3u_3}$ (f) turbulent shear stress in xy plane, $\overline{u_1u_2}$ ……………………………… 67

Figure 4.10 Saddle point of Stuart vortex approximated by Taylor function………… 68

Figure 4.11 Turbulent structures by approximate solution for Saddle point (Run-1): (a) turbulent kinetic energy, *k* (b) turbulent energy dissipation rate, ε (c) turbulent normal stress in *x* direction, $\overline{u_1u_1}$ (d) turbulent normal stress in *y* direction, $\overline{u_2u_2}$ (e) turbulent normal stress in *z* direction, $\overline{u_3u_3}$ (f) turbulent shear stress in xy plane, $\overline{u_1u_2}$ ……………………………… 72

Chapter 5

Figure 5.1 Sketch of 3D flow structure in a compound channel (Shiono and Knight, 1991)………………………………………………………………….. 77

Figure 5.2 Arrangements of variables in a staggered grid in the 3D computations…. 80

Figure 5.3 Cross-section of compound open channel…………………………….. 81

Figure 5.4 Plan view of flow pattern (case-A1, t=110 sec, a part of domain is shown)…………………………………………………………………. 83

Figure 5.5 Water surface distribution near the interface for the flow field shown in Fig. 5.4 (b) (case-A1, Run NLKEV, t=110 sec)……………………….. 84

Figure 5.6 Temporal change in the plan view of flow pattern for case-A1, Run NLKEV (a) t=110 sec (b) t=140 sec (c) t=170 sec (d) t=220 sec (e) t=320 sec (half of the computational domain is shown)………………… 85

Figure 5.7 Depth variation along the downstream distance for (a) case-A1, (b) case-A2 , and (c) case-A3…………………………………………… 87

Figure 5.8 The instantaneous profiles of secondary currents at different sections of a single vortex (Case-A2)…………………………………………….. 91

Figure 5.9 Spatially averaged cross-sectional flow pattern of secondary currents: (a)

Case-A1, 2nd order model (b) Case-A1, 3rd order model (c) Case-A1, 3rd order model without considering horizontal vortex (d) Case-A2, 3rd order model (e) Case-A3, 3rd order model……………………………………… 92

Figure 5.10 Discharges computed by different models for (a) case-A1, (b) case-A2, and (c) case-A3…………………………………………………………….. 94

Figure 5.11 Comparison of normalized compound roughness coefficient for different depth ratios ……………………………………………………………. 94

Figure 5.12 Spatial averaged cross-sectional profiles for (a) stream-wise velocity for case B1 (b) boundary shear stress profile for case B1 (c) stream-wise velocity for case B2 (d) boundary shear stress profile for case B2………. 97

Figure 5.13 Comparison of spatial averaged cross-sectional profiles with Abe et al.(1997) for (a) stream-wise velocity for case B1 (b) boundary shear stress profile for case B1…………………………………………………. 98

Figure 5.14 Temporal change in the plan view of flow pattern for the case of two flood plain of case-A3: (a) t=100 sec (b) t=120 sec (c) t=230 sec………. 100

Figure 5.15 Comparison of depth averaged velocity profile for case A3 (two flood plain), calculation is made using 3rd order model………………………. 101

Figure 5.16 Comparison of spatial averaged secondary current for case C1 (two flood plain case, calculation is made using 3rd order model): (a) Experimental (Shiono and Knight, 1991) (b) Simulation result……… 101

Figure 5.17 Comparison of spatially averaged boundary shear stress profile for case C1 compared with the experimental results by Shiono and Knight (1991) 102

Figure 5.18 Plan view of flow vectors showing the horizontal vortices at the interface of main channel and flood plan (case A1, t =300 sec)……….. 103

Figure 5.19 Turbulent structures near the center of a vortex (x =200~380 cm): (a) plan view of flow vectors (b) k (c) ε (d) $\overline{u_1u_1}$ (e) $\overline{u_2u_2}$ (f) $\overline{u_3u_3}$ (g) $\overline{u_1u_2}$ ……………………………………………………………… 104

Figure 5.20 Turbulent structures near the center of a vortex (x =760~920 cm): (a) plan view of flow vectors (b) k (c) ε (d) $\overline{u_1u_1}$ (e) $\overline{u_2u_2}$ (f) $\overline{u_3u_3}$ (g) $\overline{u_1u_2}$ …………………………………………………………….. 106

Figure 5.21 Turbulent structures at the saddle point (x = 400~450 cm): (a) plan view of flow vectors (b) k (c) ε (d) $\overline{u_1u_1}$ (e) $\overline{u_2u_2}$ (f) $\overline{u_3u_3}$ (g) $\overline{u_1u_2}$ ……………………………………………………………………… 108

Figure 5.22 Contour of turbulence production: (a) near the center of a vortex for x =200~380 cm (b) near the center of a vortex for x =760~920 cm (c) at saddle point for x……………………………………………………..... 109

Chapter 6

Figure 6.1 Velocity distribution in (a) solid body rotation (b) potential vortex (c) Rankine vortex………………………………………………………… 114

Figure 6.2 Pressure distribution in (a) solid body rotation (b) potential vortex (c) Rankine vortex………………………………………………………… 114

Figure 6.3 Types of Rankine vortex based on far-field behavior (Uberoi, 1979); here, u_θ and u_z represent the tangential and axial velocity respectively….. 115

Figure 6.4 Photograph of a wing-tip vortex from an agriculture aircraft…………… 116

Figure 6.5 Distribution of (a) circumferential velocity (b) Axial velocity and (c) pressure at t =3.72T…………………………………………………… 125

Figure 6.6 Radial distribution of tangential velocity and its decay with time (Non-linear k-ε model)………………………………………………… 126

Figure 6.7 Radial distribution of normalized circulation for different times (Non-linear k-ε model)………………………………………………… 127

Figure 6.8 Time decay of radial distribution of axial velocity (Non-linear k-ε model)…………………………………………………………….. 127

Figure 6.9 Radial distribution of tangential velocity and its decay with time (Standard *k-ε* model)………………………………………………….. 128

Figure 6.10 Radial distribution of normalized circulation for different times (Standard *k-ε* model)………………………………………………………… 128

Figure 6.11 Radial distribution of axial velocity and its decay with time (Standard *k–ε* model)……………………………………………………......... 129

Figure 6.12 Comparison between time decay of axial velocity and tangential velocity 129

Figure 6.13 Self-similar profile of circumferential velocity compared with Phillips' model……………………………………………………………….. 130

Figure 6.14 Self-similarity in the circulation profile compared with Phillips' model… 130

Figure 6.15 Non-linear k-ε model prediction of (a) vortex flow field and (b) instability in the flow field (t = 7.01T)…………………………………. 133

Figure 6.16 Growth of turbulent kinetic energy with different time periods (Non-linear *k-ε* model)…………………………………………………… 134

Figure 6.17 Radial distribution of turbulent intensities at three directions at (a) t =3.72 T (b) t =5.0 T (c) t=7.013T …………………………………….. 136

Figure 6.18 *k-ε* model prediction of circumferential velocity profile compared with Qin's DNS results (t = 3.72T)…………………………………………… 137

Figure 6.19 *k-ε* model prediction of circulation profile compared with Qin's DNS results (t = 3.72T)……………………………………………………... 138

Figure 6.20 *k-ε* model prediction of axial velocity profile compared with Qin's DNS results (t = 3.72T)…………………………………………………….. 138

Figure 6.21 *k-ε* model prediction of turbulent kinetic energy with Qin's DNS results (t = 3.72T)…………………………………………………………….. 139

Figure 6.22 Non-linear *k-ε* model prediction of Tangential velocity profile compared with DNS results of Duraisamy and Lele (2006) for q = 0.5…………….. 140

Figure 6.23 Non-linear k-ε model prediction of Axial velocity profile compared with DNS results of Duraisamy and Lele (2006) for q = 0.5………………….. 140

Figure 6.24 Non-linear *k-ε* model prediction of normalized circulation compared with DNS results of Duraisamy and Lele (2006) for q = 0.5…………….. 141

Figure 6.25 Time decay of maximum tangential velocity (at $r=r_0(t)$) compared with DNS results of Duraisamy and Lele (2006) for q = 0.5………………….. 141

Figure 6.26 Time decay of maximum axial velocity (at r = 0) compared with DNS results of Duraisamy and Lele (2006) for q = 0.5……………………….. 142

Figure 6.27 Comparison of time decay in maximum axial and maximum tangential velocities (the velocities are normalized by their initial maximum values)………………………………………………………………. 142

Figure 6.28 Comparison of Time decay of Tangential velocity for different swirl numbers; The DNS results of Duraisamy and Lele (2006) for no axial flow case is also shown to compare with calculated decay profile……… 143

Figure 6.29 Comparison of temporal fluctuations of velocity at a point by RANS and LES simulations. 144

Figure 6.30 Plan view of flow vectors at t = 40 sec by (a) RANS and (b) LES simulations 145

Figure 6.31 Radial distribution of tangential velocity calculated by RANS and LES (t = 3.06T)……………………………………………………………... 146

Figure 6.32 Radial distribution of tangential velocity calculated by RANS and LES (t = 3.06T and 4.48 T)……………………………………………………. 147

Figure 6.33 Radial distribution of depth calculated by RANS and LES (Symbols show LES prediction, and lines show corresponding RANS prediction) 147

Figure 6.34 Time decay of maximum tangential velocity calculated by RANS and LES………………………………………………………………… 148

Figure 6.35 Pattern of secondary current at t = 40 sec by (a) RANS and (b) LES simulations………………………………………………………….. 148

Chapter 7

Figure 7.1 Embayment with rock dykes in Yodo river, Japan (Muto et. al., 2002)…. 154

Figure 7.2 Arrangements of variables in a staggered grid in the 3D computations (Curvilinear coordinate system)………………………………………. 157

Figure 7.3 Diagram of flow domain………………………………………………. 158

Figure 7.4 Time averaged velocity vectors……………………………………….. 158

Figure 7.5 Comparison of Time averaged velocity profile along T_0-T_1...................... 158

Figure 7.6 Temporal change of velocity vectors at 0.2 sec intervals………………… 161

Figure 7.7 Temporal change of instability vortices at 0.2 sec intervals……………... 162

Figure 7.8 Temporal change of water depth distribution at 0.2 sec intervals……….. 163

Figure 7.9 Temporal change of water depth distribution near the interface region…. 164

Figure 7.10 Temporal change of water depth distribution along S-S section……….. 164

Figure 7.11 Temporal variations of water surface at A and B……………………… 165

Figure 7.12 Temporal variations in stream-wise velocity (u) at point D (a) Experiment (b) Calculation…………………………………………………………. 165

Figure 7.13 Temporal variation of transverse-velocity component (v) at the interface (x =5 cm)…………………………………………………………………. 166

Figure 7.14 Pattern of secondary current at (a) S-S section (b) T_0-T_1 section (c) adjacent grid just before T_0-T_1 section (d) adjacent grid just after T_0-T_1 section (t = 57.2 sec)…………………………………………………... 167

Figure 7.15 Pattern of time-averaged secondary current in transverse section (T-T section)………………………………………………………................. 169

Figure 7.16 Pattern of time-averaged secondary current in dead-zone (S-S section)…………………………………………………......................... 170

List of Tables

Table 2.1 Estimated values for the coefficients of c_μ and c_β 15

Table 4.1 Estimated and trial values of model constants for the coefficients of c_μ and c_β..54

Table 5.1 Channel properties and hydraulic conditions of compound channel…………..82

Table 7.1 Hydraulic parameters for the simulation of open channel with dead-zone…..157

Chapter 1

INTRODUCTION

1.1 Preliminaries

Most natural and industrial flows are turbulent. Therefore, Turbulent flow is of central importance to many engineering applications in the field of hydraulic engineering, aerospace industry, process engineering, internal combustion engines, environmental engineering etc. Such flow phenomena observed in atmosphere and oceanic flows includes most of the terrestrial atmospheric circulations and atmospheric mixing layers, the intense oceanic currents, the mixing of cold and warm air in the atmosphere by wind, the external flow over all kinds of vehicles (such as cars, airplanes, ships, submarines) etc. The industrial application includes the flow through equipments, such as pipes, ducts, precipitators, gas scrubbers, etc; and through machines such as internal combustion engines, gas turbines, etc. In hydraulic engineering applications, some of the turbulent dominated flows are: turbulent jets, flow through hydraulic and flood control structures (e.g. barrages), flows past an obstacle such as bridge piers, flows behind spur/dykes, compound channel flows, flows in a step-pool system, open channel flows with vegetation zone or with an abrupt expansion, flows with side cavity or dead zones etc. From theoretical consideration, the turbulent flow is differentiated from laminar by Reynolds number (= ud/ν) of the flow. Since, the kinematic viscosity of water (ν) is an order of 10^{-6}

m^2/sec, the Reynolds number becomes high and the flow becomes turbulent even for a small value of velocity and water depth. Due to the application in a wide variety of flows, in the last decades, turbulence has become a very lively area of scientific research, attracting many scientists and researchers to this subject.

The method of investigation of this subject is divided into three categories: Analytical, Numerical and Experimental. In this study, Analytical and Numerical approaches are used to study the application of unsteady turbulent flows. In this chapter, the available numerical methods are explained followed by the objectives and scopes of this thesis.

1.2 Numerical Methods

For so many years, the experimental studies were the only technique for investigation of hydraulic engineering problems. The advent of computers and their rapid advancement brought an opportunity to the engineers to analyze those problems with less simplified assumptions. As the computer capabilities are increasing, the less assumptions are made and more complicated problems are possible to solve more accurately. In Computational Fluid Dynamics (CFD), the term numerical method is referred to those methods, which are to be used to solve the so called conservation equations. These equations are continuity, momentum or Navier-Stokes and Energy equations. In order to solve these equations numerically, they should be discretized and solved by appropriate iterative methods.

As long as the flow is laminar, the only problem is to solve this system of discretized equations. The accuracy of results depends on both the grid and descritization scheme. The moment that the flow becomes turbulent, a chaotic, random motion is observable. In this case, the instantaneous flow values at a fixed location in the flow field show a fluctuating behavior. Turbulence, intermittently, is a three dimensional, time dependent phenomenon. So, in order to study such flows numerically, different approaches have been proposed that have different accuracies which sometimes are flow dependent. The three major approaches are Reynolds Averaged Navier-Stokes (RANS), Large Eddy Simulation (LES) and Direct Numerical Simulation (DNS). Considerable effort has been made to develop these methods in the recent decades and an important advancement has been achieved.

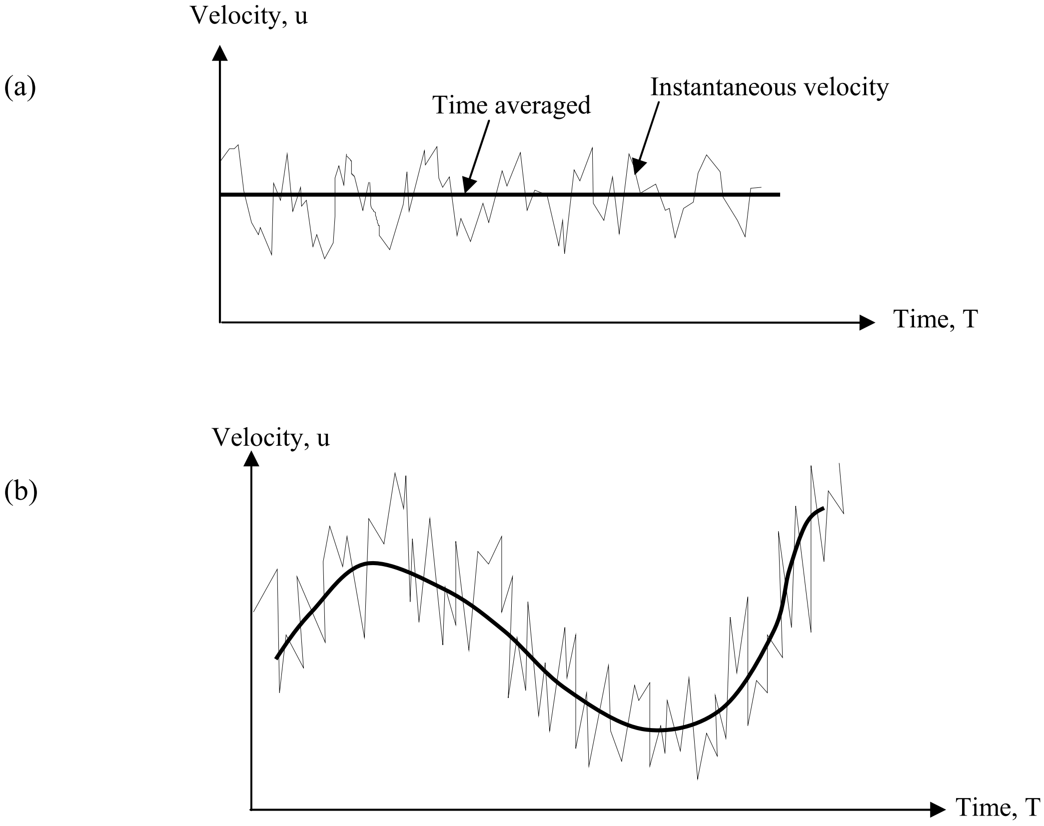

Fig. 1.1 Time averaging of velocity in RANS method (a) Steady RANS (b) Unsteady RANS

1.2.1 RANS Model

Study of stationary turbulent flows has shown that fluctuating flow quantities have a constant mean value (Fig.1.1). This fact inspired Reynolds to decompose the dependent variables into an average and a fluctuating part and take a time integral average of the equations. Doing so, introduced new unknown parameters which are called Reynolds stresses. No longer the system of equations can be considered closed. This problem is referred to as turbulence closure problem which means that the numbers of unknown parameters are more than the number of equations. The models to solve the problem is called turbulence model. In the models, the Boussinesq approximation is used to determine the turbulent stresses that consider an isotropic turbulent viscosity. However, from experiments, it is confirmed that the assumption is valid only for some limited flows.

Unsteady turbulent flow is of interest to researchers both because of its practical importance and its potential to provide additional insight into fundamental aspects of turbulence. In such flows certain fundamental aspects of turbulence are exposed which although present in steady turbulent flows, are not apparent. In addition, due to the effect of inertia, some additional features of turbulence specific to transient flows can be present.

From Fig. 1.1, it is observed that in a steady RANS the averaging time should be much greater (towards infinity) than the fluctuation time scale, however in a unsteady RANS the averaging time period should be short enough to capture the large scale structures.

1.2.2 Large Eddy Simulation

There are many different length scales observed in a turbulent flow. These length scales are representative of eddies' scales in the motion. It is believed that the large scales, receive the energy from the main flow that is delivered via smaller eddies to the smallest scales where it is dissipated. The phenomenon is called cascade process.

The idea of LES comes from this fact that the small scales, regardless of the type of flow and boundary conditions, show an isotropic behavior. So, if the large scales are resolved, it is accurate enough to model the small scales which are called the subgrid scale or SGS. In order to get reasonable good accuracy it is reported that the grid should be fine to some extent (Hinterberger et al. 2007). Important difference between RANS and LES governing equations is the method of filtering. While in RANS the filtering is performed in time, in LES the filtering is performed in space. Another difference compared to RANS is that as turbulence is a time dependent three-dimensional phenomenon, the governing equations in LES also need to solve in unsteady three-dimensional format. Another fact regarding LES is that the grid is supposed to be fine enough to cover some part of scales in the inertial sub-range. These differences make the LES much more expensive than RANS models.

1.2.3 Direct Numerical Simulation

In this method even the small scale of turbulence is simulated. It means that a very fine mesh whose size is in the range of Kolmogorov micro-scales should be implemented. Although it gives most accurate results, the draw back with this method is that it needs very powerful computers with high memory capacities even for a very simple geometries and flows.

1.3 Objectives and justification of the Study

Since LES and DNS require high computer memory and much more CPU time than RANS, the methods are not suitable for practical applications. That is why the RANS type turbulence models, such as two equation model or Reynolds stress model, are still the popular tool used for practical engineering applications (Jaw & Chen, 1998). Therefore, the clarification of the possibility, the limitations and areas of improvement of RANS models should still be paid attention to.

Among the turbulence models, k–ε eddy viscosity model is the simplest ‘complete’ model that can be used on modern personal computers. Due to its simplicity, it became one of the most popular models and found to be adopted frequently. This is a two equation model obtained by solving the turbulent kinetic energy (k) and its dissipation rate (ε) from two differential transport equations. Although this type of model has been applied for prediction of many turbulent flows with high degree of success, it is unable to predict satisfactorily some fundamental flows containing strong streamline curvature, vortices and rotations (Rodi, 1979). This deficiency of this model is due to the isotropic assumption of eddy viscosity that causes mostly a linear relationship between stress and strain rate throughout the turbulent flow field. Thus, the non-linear k–ε model is thought to be a superior tool for predicting such complex flows. However, some draw-backs are reported for existing non-linear model.

Therefore the objective of this study is the refinement of existing non-linear k–ε model and examine its performance for different turbulent flows. Introduction to some turbulent flows are given below, which are considered as the subject of research in this thesis.

Turbulent flows with large scale vortices are often observed in many natural flows and man-made engineering applications. One of the common examples is a compound channel, where coherent vortices are formed at the interface of main channel and flood plain (Fig. 1.2). The more complicated turbulent flow is observed in the flow field of an open channel with side cavity. In addition to coherent vortices, its interaction with the flow circulation and water surface oscillation in the dead zone makes the flow field more complex. Therefore, these are the subtopics chosen for this study as turbulent flow.

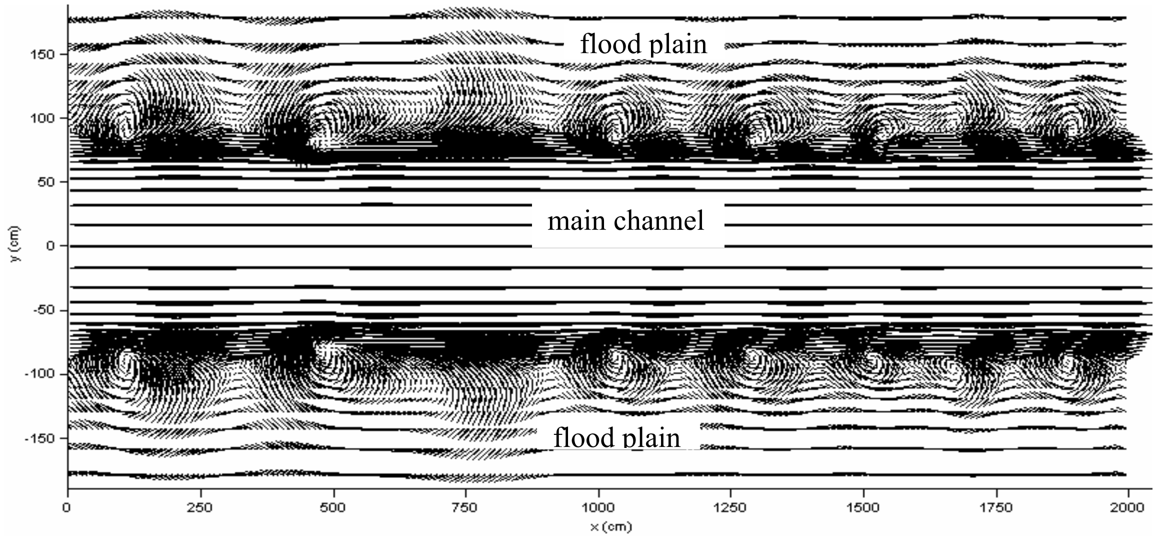

Fig. 1.2 Plan view of flow vector in a compound channel showing the coherent vortices at the interface of main channel and flood plain (simulated flow field in the present study)

Since, the coherent vortices are the important element that controls the turbulent flow fields, the change of turbulent structures with spatial and temporal changes is necessary to investigate. A coherent vortex is composed of two critical points; the maximum vorticity exists at vortex center (focus) and minimum vorticity at saddle point. The Stuart vortex is such a vortex that contains both the critical points in its vorticity field, is considered as an ideal vortex to study the spatial change of turbulent structures with singular points. To study the temporal decay of vorticity, Rankine vortex is considered. This vortex has been used extensively in various studies; for instance, to predict the decay of wing-tip vortices, to estimate the noise level produced by vortices and vibrations, to model the natural phenomena such as hurricanes and tornados.

Some basic turbulent flows, such as, plane shear layer, turbulent jets with and without swirl are also studied using analytical approach based on the proposed non-linear k–ε model.

1.4 Scope of the Research

The manuscript consists of eight chapters including the Introduction and the Conclusions. Chapter 1 describes the basics of different turbulence models and clarifies the objectives of the study.

In Chapter 2, the details of k–ε model for 3D flow both in Cartesian and Curvilinear coordinate system is described. The existing models are discussed and the drawback of the models are highlighted. Some refinements in the second order non-linear model are proposed, where the coefficient of eddy viscosity is derived as a function of strain and rotation parameters. The model constants in the functional forms are estimated considering the realizability conditions and anisotropy of turbulence for different baseline flows.

In Chapter 3, the approximate solutions are presented for the fundamental properties of a swirl jet such as spreading rate, distribution of turbulence intensities, turbulent shear stress, turbulent kinetic energy etc., derived by using the modified non-linear k–ε model. The derived approximate solutions are useful to understand the distributions of turbulent characteristics, the sensitivity of model constants to the distributions of turbulent energy among the turbulent normal stresses, the relation between spreading rate and model constants, etc. Neglecting the swirl parameters from the derived solution, the spreading rate and turbulent properties are also calculated for a round jet without swirl. Tuning the model constants, the derived solutions are compared with the previous experimental results.

In Chapter 4, the spatial distributions and topological change of turbulent structures in an idealized vortex street are investigated using analytical approach, and the applicability of the non-linear k–ε model to large scale vortices are examined. The Stuart vortex, which contains both vortex and saddle patterns in its vorticity contour, is considered for this analysis. The sensitivity of turbulent structures of the vortex street to the coefficient of eddy viscosity are examined. The turbulent structures are also compared with the previous experimental results of free shear flows.

In Chapter 5, the three-dimensional flow field is generated for different hydraulic conditions using standard as well as non-linear k–ε models, where the governing equations of mean velocities and turbulent flow fields are discretized with the finite volume method based on a staggered grid system. The interactions of horizontal vortices with secondary currents, and its consequent effect to the prediction of flow as well as to the compound roughness of the channel, are explained through the interpretation of simulated results with different models.

The turbulent characteristics of the large scale vortices in the compound channel are studied. The formations of singular points (i.e. vortex and saddle patterns) in the coherent structures, and the topological change of turbulent structures with the singular points are investigated. The turbulent structures are compared with the results presented in Chapter 4.

The work presented in Chapter 6 can be classified into twofold. In the first part, 2D numerical simulation with 3D velocity field is carried out for a trailing vortex (axial vortex) for different swirl numbers using standard and Non-linear k–ε models. The temporal decay of tangential and axial velocity, the effect of swirl numbers on vortex decay process, different time-zones of generation and decay of turbulence, distribution of turbulent intensities etc. are studied. The simulated results are compared with previous experimental and DNS results. In the second part, the 3D numerical simulation is carried out for an idealized Rankine vortex using Non-linear k–ε model and large eddy simulation (LES). The temporal changes in vortex simulated by both the models are compared.

In Chapter 7, the three–dimensional numerical simulation is carried out to study the fundamental properties of an open channel flow with a rectangular side cavity. A curvilinear coordinate with a variable grid system is used in this study. The formation of coherent vortices at the interface of mainstream and dead zone, as well as its interaction with the circulation and water surface oscillation in the cavity are studied. The flow pattern and velocity profiles are compared with previous experiments. Finally, Chapter 8 summarizes all the contributions of this study.

1.5 References

1) Hinterberger, C., Frohlich, J. and Rodi, W., Three dimensional and depth averaged Large-eddy simulations of some shallow water flows, *J. Hyd. Engg., ASCE.* 123, pp.857-872, 2007.

2) Jaw, S.Y. and Chen, C. J., Present status of second order closure turbulence models. I: overview, *J. Engg. Mech., ASCE.* 124, pp.485-501, 1998.

3) Rodi, W., Turbulence models for environmental problems, in *Prediction Methods for Turbulent Flows (edited by W. Kollmann)*, pp.259, 1979.

Chapter 2

NON-LINEAR *k–ε* MODEL

2.1 Introduction

It is well known that the RANS (Reynolds Averaged Navier Stokes) type turbulence models, such as two equation model or Reynolds stress model, are the most popular tool used for practical engineering applications (Kimura & Hosoda, 2003; Jaw & Chen, 1998). Because it requires less CPU time and computer memory compared to LES and DNS. Therefore, the clarification of the possibility, the limitation and areas of improvement of RANS models should be still paid attention to. To resolve the Reynolds stress term appeared in the averaged Navier-Stokes equations, the k–ε model is one of the most frequently adopted one (Jaw & Chen, 1998). However, the standard k–ε model cannot produce satisfactory results for the flow field having high rate of strain and rotation because of its isotropic assumption of eddy viscosity (Rodi, 1979). On the other hand, a non-linear model predicts superior result by capturing the anisotropic turbulence.

The non-linear k–ε model is a generalized eddy viscosity model, where additional non-linear terms of mean strain rate are added in the Reynolds stress equation. In standard k–ε model, the value of the coefficient of eddy viscosity (c_μ) is assumed constant throughout the turbulent flow field, that over predicts its value, especially in the case of large rate of strain and rotation. If the strain is sufficiently large, the model may produce negative normal stresses (Shih et al., 1996). Moreover, comparing the non-linear quadratic term in the Reynolds stress equation proposed by Youshizawa (1986) with its another form proposed by Gatski and Spezile (1991), it can be proved (shown in next section) that c_μ is a function of strain and rotation parameters. The non-linear *k–ε* model used in this study differs from the standard *k–ε* model in two important ways: i) the eddy viscosity coefficient (c_μ) is not a constant; and ii) non-linear terms are added in the Reynolds stress equation to account the anisotropy of normal stresses. Kimura and Hosoda (2003) proposed some refinements in the model functions considering the realizability conditions for different types of 2D basic flow patterns. They adopted the model to calculate the 3D flows around a cube, and the complex flow features with separation and reattachment at each surface are qualitatively simulated. Hosoda et al. (1999) and Ali et al. (2007) calculated 3D flow field in compound channels using non-linear model, and pointed out that the functional form of c_μ affects the generation of horizontal vortices. However, the functional model developed by Kimura and Hosoda (2003) contains some physical drawbacks (shown latter), and hence it requires further refinement.

In this chapter, refinement of second order non-linear *k–ε* model is proposed incorporating some new functions for the coefficient of eddy viscosity as well as for that of quadratic term. For tuning model constants, the flow field of a *Simple Shear* is considered first. The conditions of realizability are derived for plane shear layer to determine the constrains of the functional form of c_μ . The coefficients in the non-linear quadratic terms are determined considering the anisotropy in turbulent normal stresses for shear layer. The anisotropy of turbulence is also derived for some other basic flows including *Plane strain*, *Axisymmetric Contraction* and *Axisymmetric Expansion* to tune the model constants as well as to ensure the realizability conditions for these flows.

2.2 Mathematical Formulation in 3D Cartesian Coordinate

2.2.1 *Basic equations*

The basic equations in a *k–ε* model for an unsteady incompressible flow are as follows.

Continuity equation:

$$\frac{\partial U_i}{\partial x_i} = 0 \tag{2.1}$$

Momentum equation:

$$\frac{\partial U_i}{\partial t} + \frac{\partial U_j U_i}{\partial x_j} = g_i - \frac{1}{\rho}\frac{\partial P}{\partial x_i} + \frac{\partial}{\partial x_j}\left(-\overline{u_i u_j}\right) + \nu \frac{\partial^2 U_i}{\partial {x_j}^2} \tag{2.2}$$

k - equation:

$$\frac{\partial k}{\partial t} + \frac{\partial k U_j}{\partial x_j} = -\overline{u_i u_j}\frac{\partial U_i}{\partial x_j} + \frac{\partial}{\partial x_j}\left\{\left(\frac{\nu_t}{\sigma_k} + \nu\right)\frac{\partial k}{\partial x_j}\right\} - \varepsilon \tag{2.3}$$

ε - equation:

$$\frac{\partial \varepsilon}{\partial t} + \frac{\partial \varepsilon U_j}{\partial x_j} = -c_{\varepsilon 1}\frac{\varepsilon}{k}\overline{u_i u_j}\frac{\partial U_i}{\partial x_j} + \frac{\partial}{\partial x_j}\left\{\left(\frac{\nu_t}{\sigma_\varepsilon} + \nu\right)\frac{\partial \varepsilon}{\partial x_j}\right\} - c_{\varepsilon 2}\frac{\varepsilon^2}{k} \tag{2.4}$$

where, x_i : the spatial coordinates, U_i and u_i : the average and turbulent velocities respectively in x_i direction, P : the pressure, ρ : the density of fluid, ν : the kinematic viscosity, k : the averaged turbulent energy, ε : the averaged turbulent energy dissipation rate, ν_t : the eddy viscosity, σ_k, σ_ε , $c_{\varepsilon 1}$, $c_{\varepsilon 2}$: the model constants. Standard values (σ_k= 1.0, σ_ε= 1.3, $c_{\varepsilon 1}$ = 1.44 and $c_{\varepsilon 2}$ = 1.92) are used for these model constants.

2.2.2 *Turbulence models*

(a) Standard k–ε model

In the standard *k–ε* model, the Reynolds stress tensor $\overline{u_i u_j}$ is solved by linear constitutive equations derived from Boussinesq eddy viscosity concept, which does not take into account the anisotropy effect.

$$-\overline{u_i u_j} = \nu_t S_{ij} - \frac{2}{3} k \delta_{ij}\,, \quad S_{ij} = \frac{\partial U_i}{\partial x_j} + \frac{\partial U_j}{\partial x_i} \tag{2.5}$$

Here, ν_t is determined from the dimensional consideration of k and ε and approximated by

$$\nu_t = c_\mu \frac{k^2}{\varepsilon} \quad . \tag{2.6}$$

Here, c_μ is the coefficient of eddy viscosity bears a constant value of 0.09.

(b) Non-linear $k-\varepsilon$ model

Including the non-linear anisotropy term in the Reynolds stress equation introduced by Yoshizawa (1984), the constitutive equations can be expressed in the following forms

$$-\overline{u_i u_j} = \nu_t S_{ij} - \frac{2}{3} k \delta_{ij} - \frac{k}{\varepsilon} \nu_t \sum_{\beta=1}^{3} c_\beta \left(S_{\beta ij} - \frac{1}{3} S_{\beta\alpha\alpha} \delta_{ij} \right) \tag{2.7}$$

$$S_{1ij} = \frac{\partial U_i}{\partial x_\gamma}\frac{\partial U_j}{\partial x_\gamma}, \quad S_{2ij} = \frac{1}{2}\left(\frac{\partial U_\gamma}{\partial x_i}\frac{\partial U_j}{\partial x_\gamma} + \frac{\partial U_\gamma}{\partial x_j}\frac{\partial U_i}{\partial x_\gamma} \right), \quad \text{and} \quad S_{3ij} = \frac{\partial U_\gamma}{\partial x_i}\frac{\partial U_\gamma}{\partial x_j}\,. \tag{2.8}$$

here, c_β (= c_1, c_2, c_3) is the coefficient of non-linear quadratic term. In this equation, ν_t is also determined by equation (2.6), but c_μ is no longer a constant but a function of strain and rotation parameters.

The quadratic term in equation (2.7) is equivalent to the following non-linear viscosity model derived by Pope (1976), and Gatski & Spezile (1993).

$$\alpha_1 (S_{il}\Omega_{lj} + \Omega_{li}S_{jl}) + \alpha_2 (S_{il}S_{lj} - \frac{1}{3} S_{km}S_{mk}\delta_{ij}) + \alpha_3 (\Omega_{il}\Omega_{lj} - \frac{1}{3}\Omega_{km}\Omega_{mk}\delta_{ij}\ ) \tag{2.9}$$

where, the strain and rotation tensors are defined as

$$S_{ij} = \frac{\partial U_i}{\partial x_j} + \frac{\partial U_j}{\partial x_i}\,, \quad \Omega_{ij} = \frac{\partial U_i}{\partial x_j} - \frac{\partial U_j}{\partial x_i} \tag{2.10}$$

From Eqs. (2.7) and (2.9), the relations between the coefficients of two forms of non-linear terms can be derived as

$$c_1 = -2\alpha_1 + \alpha_2 - \alpha_3 \;, \quad c_2 = 2(\alpha_2 + \alpha_3) \;, \; c_3 = 2\alpha_1 + \alpha_2 - \alpha_3 \tag{2.11}$$

The comparison between two forms of non-linear terms (the quadratic term in Eq. (2.7) and Eq.(2.9)) inferred that the coefficient of eddy viscosity c_μ is a function of strain and rotation parameters. The strain parameter *(S*) and rotation parameter (Ω) are defined in Eq. (2.12), as used in the previous studies of Pope (1976), and Gatski and Speziale (1993).

$$S = \frac{k}{\varepsilon}\sqrt{\frac{1}{2}S_{ij}S_{ij}} \;, \quad \Omega = \frac{k}{\varepsilon}\sqrt{\frac{1}{2}\Omega_{ij}\Omega_{ij}} \tag{2.12}$$

For the coefficients of c_β, following constant values are used in previous studies for flows around bluff bodies (Kimura & Hosoda, 2003) :

$$c_1 = 0.40, \; c_2 = 0.40, \; c_3 = -0.13 \tag{2.13}$$

Comparing the analytical results for diagonal components of the anisotropic tensors with that of experiments for simple shear flows, it is observed that the functional form of c_β gave better results instead of taking their constant values (shown later).Therefore, the coefficient of quadratic term c_β is also considered as a function of strain and rotation parameters.

Many kinds of model functions have been proposed for these coefficients. Some of them consider only strain parameter, and rotation parameter is neglected (such as, Cotton and Ismail, 1993; Kato and Launder, 1993). Craft et al. (1993) and Kimura and Hosoda (2003) consider one dominant parameter of two (either S or Ω). Authors have also proposed a new function for the coefficients, which is more generalized than the previous forms. The comparative features are explained below in conjunction with the recent functional model of Kimura and Hosoda (2003).

i) Functional form by Kimura & Hosoda (2003)

The functional form for the model coefficients proposed by Kimura and Hosoda (2003) are described as:

$$c_\mu = \min\left(c_{\mu_0} , \frac{0.3}{1 + 0.09\,\Phi^2} \right) \tag{2.14a}$$

$$c_\beta = \frac{c_{\beta_0}}{1+0.02\Phi^2} \tag{2.14b}$$

where,

$$\Phi = \max(S,\Omega),\ c_{\mu_0} = 0.09,\quad c_{1_0} = 0.40,\ c_{2_0} = 0.0,\ c_{3_0} = -0.13 \tag{2.15}$$

The model takes into account one dominant parameter of two (either S or Ω). Moreover, the model of c_μ is a discontinuous function that may cause sudden change of its values.

ii) Functional form used in this study

The model proposed a continuous function for c_μ, and the strain (S) and rotation (Ω) — both the parameters are taken activated in the functional form. The proposed functional model is expressed as

$$c_\mu = \frac{c_{\mu o}\,(1+c_{ns}S^2 + c_{n\Omega}\Omega^2)}{1+c_{ds}S^2 + c_{d\Omega}\Omega^2 + c_{ds\Omega}S\Omega + c_{ds1}S^4 + c_{d\Omega 1}\Omega^4 + c_{ds\Omega 1}S^2\Omega^2} \tag{2.16a}$$

$$c_\beta = \frac{c_{\beta o}}{1+m_{ds}S^2 + m_{d\Omega}\Omega^2},\ \beta = 1,2,3 \tag{2.16b}$$

Here, c_{ns}, $c_{n\Omega}$, c_{ds}, $c_{d\Omega}$, $c_{ds\Omega}$, c_{ds1}, $c_{d\Omega 1}$, $c_{ds\Omega 1}$, m_{ds} and $m_{d\Omega}$ are the model constants. The values of $c_{\beta 0}$ in Eq.(2.16b) are same as given in Eq.(2.15). The functional form of c_μ assumed by Gatski and Speziale (1993) can be obtained from the above equation [Eq.(2.16a)] simply neglecting some higher order terms i.e. substituting $c_{n\Omega}$, $c_{ds\Omega}$, c_{ds1}, and $c_{d\Omega 1}$ as zero. The more simplified functional form of c_μ, suggested by Pope(1975) for two dimensional flows, can be obtained neglecting some more terms from the above equation. Moreover, when the strain and rotation effects are neglected i.e. S=Ω=0, c_μ becomes equal to the standard value of 0.09. Neglecting quadratic term, the model reduces to the standard $k-\varepsilon$ model.

Table 2.1. Estimated values for the coefficients of c_μ and c_β

Model Const.	$c_{\mu 0}$	c_{ns}	$c_{n\Omega}$	c_{ds}	$c_{ds\Omega}$	$c_{d\Omega}$	c_{ds1}	$c_{d\Omega 1}$	$c_{ds\Omega 1}$	m_{ds}	$m_{d\Omega}$
values	0.09	0.005	0.0068	0.008	-0.003	0.004	0.00005	0.00005	0.00025	0.01	0.003

2.3 Tuning of Model Constants

2.3.1 Tuning of coefficients in c_β

The coefficients of non-linear quadratic term, c_β (c_1, c_2, c_3) in Eq.(2.6), should be determined carefully because they are expected to influence the physical accuracy and numerical performance of the model. In this study, these model constants are tuned considering the anisotropy of turbulent normal stresses in simple shear flows.

For simple shear flow, the flow can be described as

$$U_1 = U_1(y),\quad U_2 = U_3 = 0,\quad \frac{dU_1}{dy} > 0 \tag{2.17}$$

The strain and rotation parameters are defined as

$$S = \Omega = M = \frac{k}{\varepsilon}\frac{dU_1}{dy} \tag{2.18}$$

The diagonal components of the non-dimensional Reynolds stress tensors are

$$\frac{\overline{u_1 u_1}}{k} = \frac{2}{3} + \frac{c_\mu (2c_1 - c_3)}{3} M^2 \tag{2.19}$$

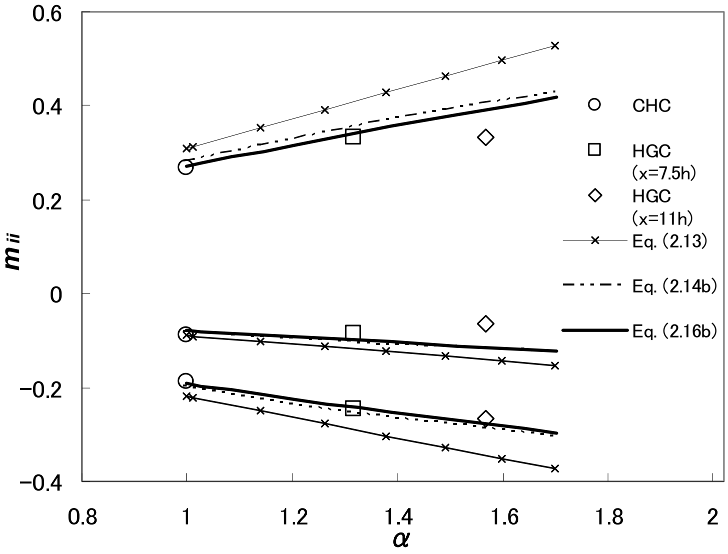

Fig. 2.1. Comparison of anisotropy of turbulence in plane shear layer using Eqs. (2.22) and (2.23) for the coefficient c_β

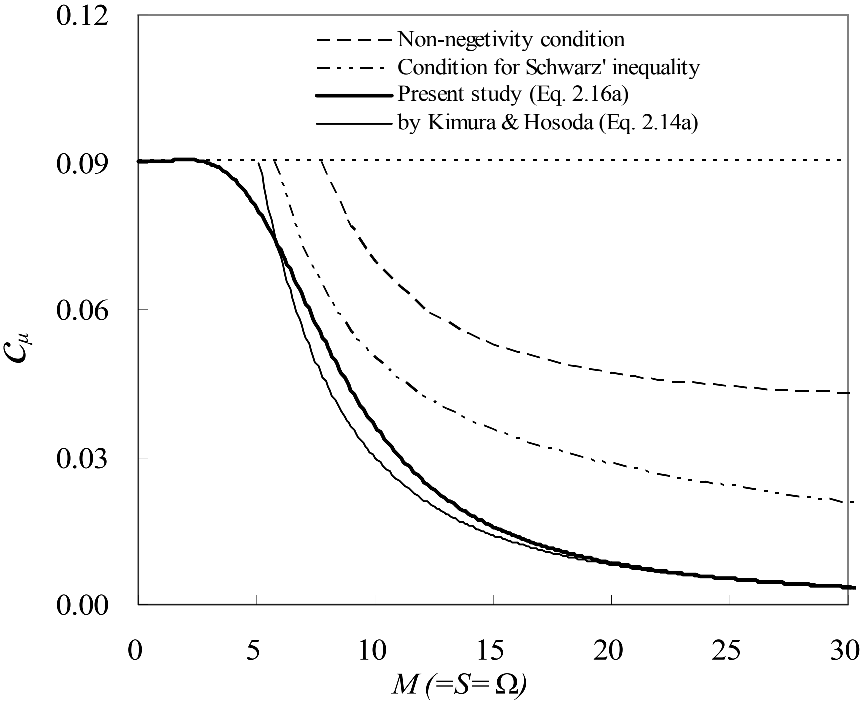

Fig. 2.2 Relation between c_μ and M in a simple shear layer

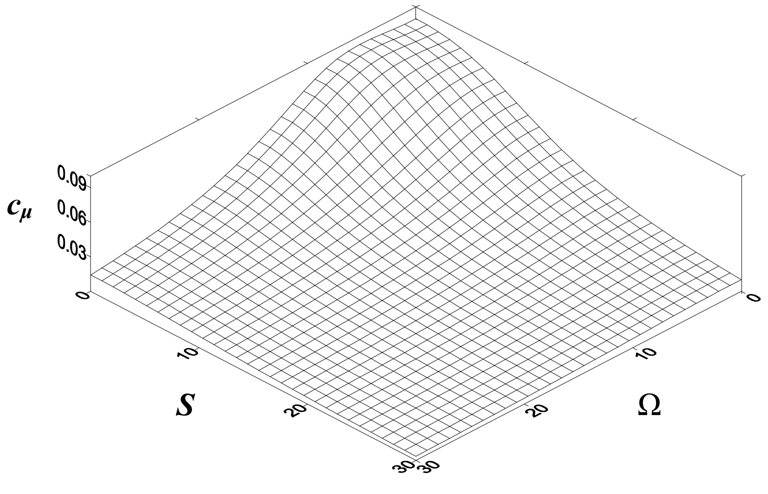

Fig. 2.3 Profile of c_μ (S, Ω) on an S – Ω plane [Eq. (2.16a)]

$$\frac{\overline{u_2u_2}}{k}=\frac{2}{3}+\frac{c_\mu(2c_3-c_1)}{3}M^2 \tag{2.20}$$

$$\frac{\overline{u_3u_3}}{k}=\frac{2}{3}-\frac{c_\mu(c_3+c_1)}{3}M^2 \tag{2.21}$$

The anisotropic tensor m_{ij} are defined by

$$m_{ij} = \frac{\overline{u_i u_j}}{k} - \frac{2}{3}\delta_{ij} \tag{2.22}$$

The ratio of the turbulent energy production term P_k to the dissipation rate ε is

$$\alpha = \frac{P_k}{\varepsilon} = -\frac{\overline{u_1 u_2}}{\varepsilon}\frac{dU_1}{dy} = c_\mu M^2 \tag{2.23}$$

The comparison between the experimental results and analytical solutions for the anisotropy of turbulent normal stresses (m_{ii}) in plane shear layer is shown in Fig. 2.1 (α = the ratio of turbulent production and dissipation rate). In the figure, CHC and HGC denote the experimental results by Champagne et al. (1970) and Harris et al. (1977), respectively. The bold line indicates the functional form for c_β [Eq. (2.16b)], which gives better comparison with experiments than Eq. (2.13). Eq. (2.13) shows the values of c_β bearing constant values, where the effects of strain and rotation parameters are neglected. The functional form by Kimura and Hosoda (2003) is also shown in figure as dotted line.

2.3.2 Consideration of realizability for plane shear layer

Realizability can be defined as the requirement of the non-negativity of turbulent normal stresses and Schwarz' inequality between any turbulent velocity correlations. It is a basic physical and mathematical principle that the solution of any turbulence model equation should obey (Shih et al., 1996). The realizability inequalities for 3D turbulent flows are:

$$\overline{u_i u_i} \geq 0 \tag{2.24}$$

$$\overline{u_i u_i} \cdot \overline{u_j u_j} \geq \overline{u_i u_j}^2 \quad (i \neq j) \tag{2.25}$$

$$\det\begin{bmatrix} \overline{u_1 u_1} & \overline{u_1 u_2} & \overline{u_1 u_3} \\ \overline{u_2 u_1} & \overline{u_2 u_2} & \overline{u_2 u_3} \\ \overline{u_3 u_1} & \overline{u_3 u_2} & \overline{u_3 u_3} \end{bmatrix} \geq 0 \tag{2.26}$$

Einstein's summation rule is not applied in above Equations. In a two dimensional averaged flow, Eq. (2.25) coincides with Eq. (2.26). In this study, the restrictions on c_μ are derived from the mentioned realizability equations for simple shear flow.

Applying Eq. (2.24) to plane shear layer, following two equations are derived for the diagonal components of the Reynolds stress tensor (non-negativity condition)

$$\frac{\overline{u_1u_1}}{k}=\frac{2}{3}+\frac{c_\mu(2c_1-c_3)}{3}M^2\geq 0 \tag{2.27}$$

$$\frac{\overline{u_2u_2}}{k}=\frac{2}{3}+\frac{c_\mu(2c_3-c_1)}{3}M^2\geq 0 \tag{2.28}$$

For plane shear layer, M=S=Ω.

Applying Eq. (2.25), the following inequality equation can be derived for Reynolds stress component, $\overline{u_1u_2}$ (Schwarz' inequality condition).

$$c_\mu^2\left\{9M^2+(2c_1^2+2c_3^2-5c_1c_3)M^4\right\}-2c_\mu(c_1+c_3)M^2-4\leq 0 \tag{2.29}$$

Since the value of c_1 is positive and c_3 is negative, Eq. (2.27) is satisfied regardless of M. Thus, the restrictions on c_μ, derived from Eqs. (2.28) and (2.29), are as follows:

$$c_\mu\leq\frac{2}{(c_1-2c_3)M^2} \tag{2.30}$$

$$c_\mu\leq\frac{(c_1+c_3)M+\sqrt{(c_1+c_3)^2M^2+4\left\{9+(2c_1^2+2c_3^2-5c_1c_3)M^2\right\}}}{9M+(2c_1^2+2c_3^2-5c_1c_3)M^3} \tag{2.31}$$

The model constants in the functional form of c_μ in Eq. (2.16a) are tuned to satisfy the realizability conditions derived in Eqs. (2.30) and (2.31).

For plane shear layer, the realizability conditions [Eqs. (2.30) and (2.31)] as well as the proposed functional form of c_μ [Eq. (2.16a)] are plotted in Fig. 2.2. The calculations are made with the following values of model constants.

$$c_{\mu0}=0.09,\quad c_{ns}+c_{n\Omega}=0.0118,\quad c_{ds}+c_{d\Omega}+c_{ds\Omega}=0.009,\quad c_{ds1}+c_{d\Omega1}+c_{ds\Omega1}=0.00035,$$
$$m_{ds}+m_{d\Omega}=0.013 \tag{2.32}$$

Using these estimated values, the analytical solutions are derived for the anisotropy of turbulence in some other bench-mark flows and the individual values of model constants are determined to satisfy the realizability limit (see section *2.3.4*). The approximate solutions for swirl jet (in Chapter 3) are compared with the previous experimental results and the values of model constants are finally determined by tuning their values for best-fitted comparison. Table-2.1 shows the final values of constants obtained by such a trial and error method, and Fig. 2.2 confirms that the model obeys the realizability conditions with these values of constants.

In the log-law region, the assumed functional form of c_μ shows almost a constant value of 0.09. It can be noted that, instead of functional form, if a constant value of c_μ (=0.09) is used through out the turbulent flow field, it fails to satisfy the realizability conditions. Fig. 2.3 shows the distribution of assumed functional form of c_μ in S – Ω plane.

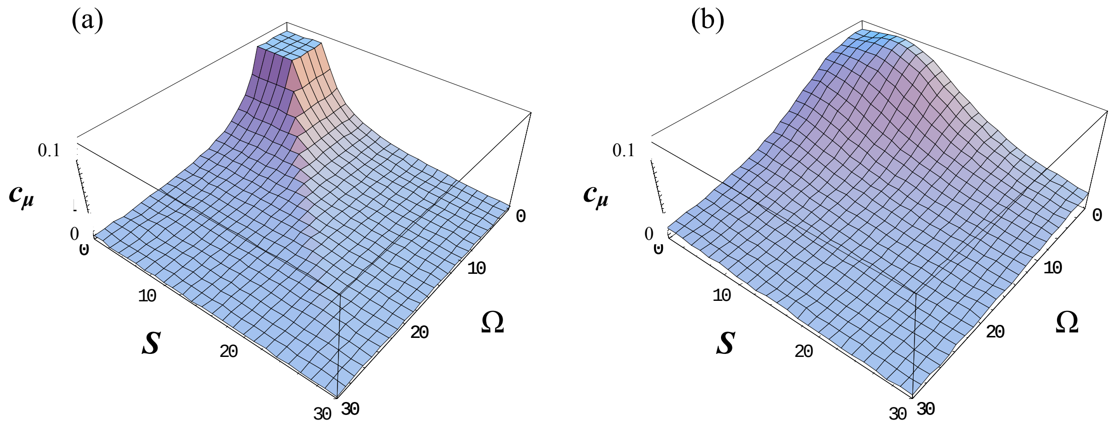

Fig. 2.4. Profile of c_μ (S, Ω) on S – Ω plane for the function in (a) Eq. 2.14a (by Kimura and Hosoda, 2003), (b) Eq. 2.16a (proposed function)

2.3.3 Distribution of c_μ in S – Ω plane

Figure 2.2 shows the comparison of c_μ profiles by Kimura & Hosoda (2003) and the proposed function. Since the profiles are calculated along the line of S = Ω, two profiles seem to be very similar except the sharp change of Kimura & Hosoda’s profile at about S=5. However, the 2D profiles of those two functions on S - Ω plane are considerably different as shown in figures 2.4(a) and 2.4(b). Because, in these figures the effects of both the parameters (S and Ω) are activated. The profile proposed by Kimura & Hosoda (2003) shows sharp edges around the region of S = Ω, which means that the value of the function changes suddenly around that region. These features seem to be physically unsound. A typical flow which satisfies S = Ω is plane shear layer. Therefore, the functional model by Kimura & Hosoda (2003) expressed in Eq. (2.14a) is not suitable for flows with vortex formation from a shear layer due to K-H instability. Another limitation in Craft et al. as well as Kimura & Hosoda's functional form is that c_μ has no dependency on Ω/S as shown by Gatski & Speziale..

2.3.4 Model performance in homogeneous strain

The anisotropy of turbulence is also derived for some other baseline flows including *Plane strain*, *Axisymmetric Contraction* and *Axisymmetric Expansion* to tune the model constants as well as to ensure the realizability conditions for these flows. The flow fields can be defined as follows:

(i) Pure Shear Strain : $U_1 = a X_2$, $U_2 = U_3 = 0$

(ii) Plane Strain: $U_1 = a X_1$, $U_2 = -a X_2$, $U_3 = 0$

(iii) Axisymmetric Contraction: $U_1 = a X_1$, $U_2 = -(a/2) X_2$, $U_3 = -(a/2) X_3$ $(a > 0)$

(iv) Axisymmetric Expansion: $U_1 = a X_1$, $U_2 = -(a/2) X_2$, $U_3 = -(a/2) X_3$ $(a < 0)$

Since in pure shear strain $S = \Omega$, the influence of individual model constants are not active; and that's why, tuning the model constants for plane shear the values of model constants are determined in groups as shown in Eq. (2.32). The analytical solutions of other three baseline flows are given below, in which the influence of individual model constants will be considered through their predictability of anisotropic turbulent stresses to satisfy the realizability constrains. Here, the anisotropic tensors are defined as

$$b_{ij} = \frac{\overline{u_i u_j}}{2k} - \frac{1}{3}\delta_{ij} \tag{2.33}$$

For plane strain:

$$b_{11} = -\frac{1}{2}c_\mu S + \frac{1}{24}c_\mu(c_1 + c_3)S^2 \tag{2.34}$$

$$b_{22} = \frac{1}{2}c_\mu S + \frac{1}{24}c_\mu(c_1 + c_3)S^2 \tag{2.35}$$

$$b_{33} = -\frac{1}{12}c_\mu(c_1 + c_3)S^2 \tag{2.36}$$

For Axisymmetric Contraction:

$$b_{11} = -\frac{1}{\sqrt{3}}c_\mu S + \frac{5}{36}c_\mu(c_1 + c_3)S^2 \tag{2.37}$$

$$b_{22} = b_{33} = \frac{1}{2\sqrt{3}}c_\mu S - \frac{1}{24}c_\mu(c_1 + c_3)S^2 \tag{2.38}$$

For Axisymmetric Expansion:

$$b_{11} = \frac{1}{\sqrt{3}}c_\mu S + \frac{5}{36}c_\mu(c_1 + c_3)S^2 \tag{2.39}$$

$$b_{22} = b_{33} = -\frac{1}{2\sqrt{3}}c_\mu S - \frac{1}{24}c_\mu(c_1 + c_3)S^2 \tag{2.40}$$

The analytical solutions are plotted in Fig. 2.5 including the realizability limit along with the solutions by Abe et al. (1997). It is observed that both for shear straining (Fig. a) and normal straining [Figs. (b)–(d)], the normal stress separation is realistic and the realizability is obeyed even at high strain rates. The present model shows better prediction than Abe's model. It can be noted that although the functional form for c_μ by Abe et al. (1997) accounts both the strain and rotation parameters, the form is similar to Pope's model which is based on a two-dimensional flows. The ability of that model in predicting 3D flows is shown in Chapter 5 for simulation of compound channel flows.

The solutions are also prepared for standard k-ε model and non-linear model with the constant values of c_β [Eq. (2.13)], and the plots are shown in Fig. 2.6. The deficiency of standard model is clearly seen in the figure. Comparing with Fig. 2.5, it is observed that the functional form of c_β shows much sensible anisotropic behavior than their constant values for all the basic flows.

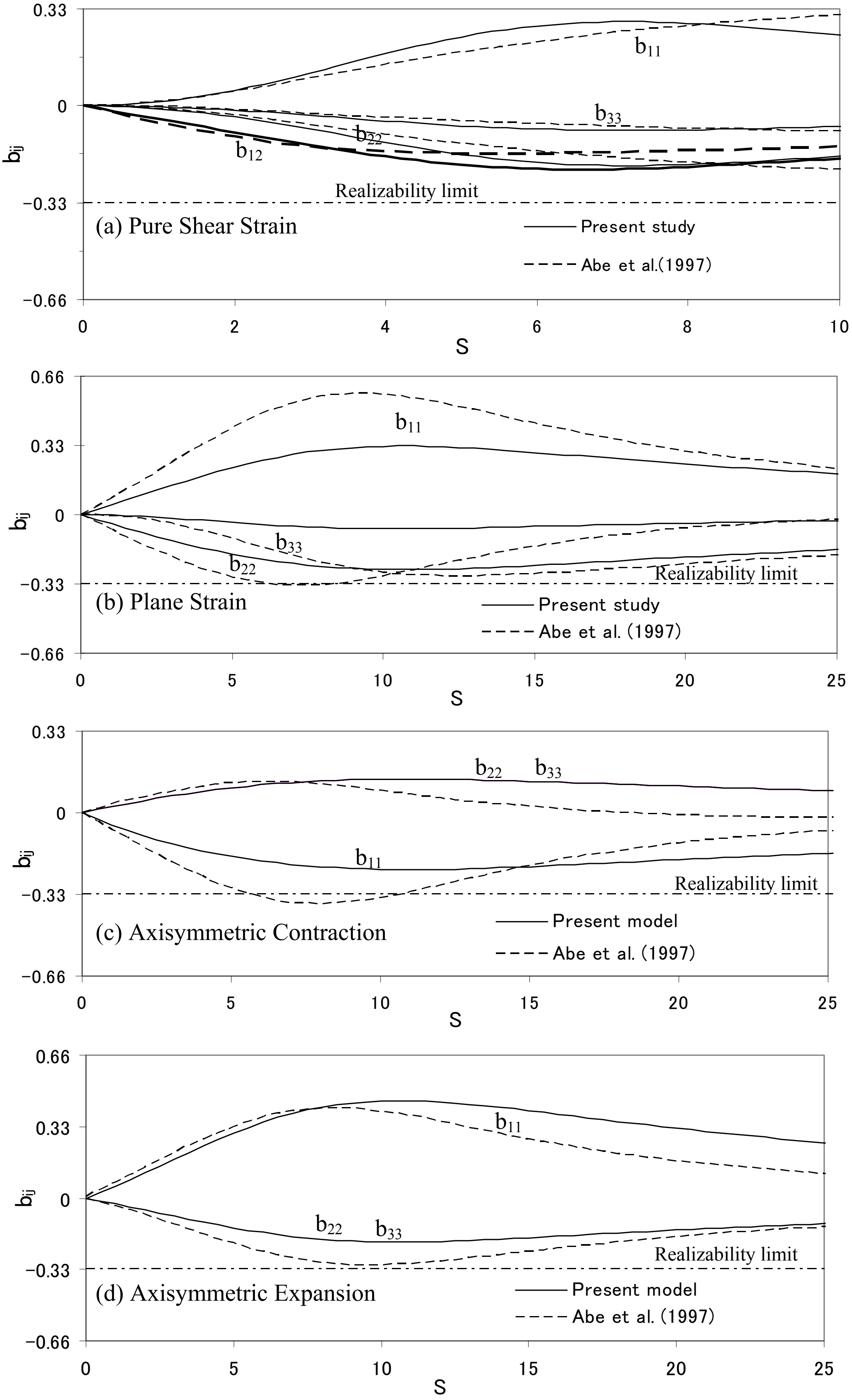

Fig. 2.5. Model performance in homogeneous strain considering the anisotropy of turbulence and realizability limit.

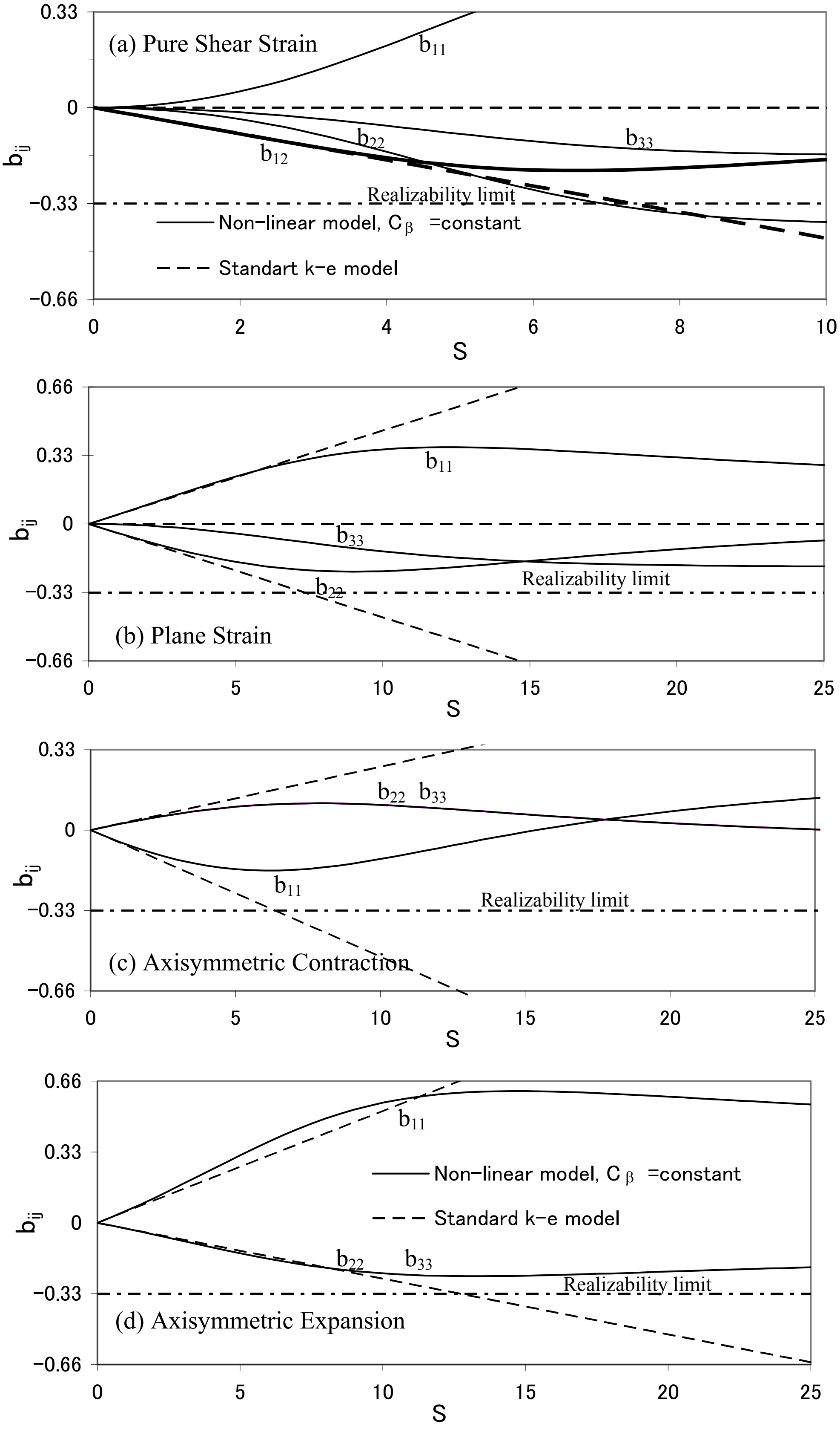

Fig. 2.6. The anisotropy of turbulence for the baseline flows in homogeneous strain predicted by (i) Non-linear k-ε model with c_β=constant and (ii) Standard *k–ε* model.

2.4 Mathematical Formulation in 3D Curvilinear Coordinate

2.4.1 *Basic equations*

The 3D flow equations in a *k–ε* model for an unsteady incompressible flow with contravariant components of velocity vectors on an orthogonal curvilinear coordinate system can be written as follows.

Continuity Equations:

$$\frac{1}{\sqrt{g}}\frac{\partial V^{\alpha}\sqrt{g}}{\partial \xi^{\alpha}} = 0 \tag{2.41}$$

Momentum equation:

$$\frac{\partial V^i}{\partial t} + \nabla_j\left[V^i(V^j - W^j)\right] + V^i\nabla_j W^j + V^j\nabla_j W^i = F^i - \frac{1}{\rho}g^{ij}\nabla_j p + \nabla_j\left[-\overline{v^i v^j}\right] + 2\nu\nabla_j e^{ij} \tag{2.42}$$

k-equation:

$$\frac{\partial k}{\partial t} + \nabla_j\left[k(V^j - W^j)\right] + k\nabla_j W^j = -g_{il}\overline{v^l v^j}\nabla_j V^i - \varepsilon + \nabla_j\left\{\left(\frac{D_t}{\sigma_k} + \nu\right)g^{ij}\nabla_i k\right\} \tag{2.43}$$

ε-equation:

$$\frac{\partial \varepsilon}{\partial t} + \nabla_j\left[\varepsilon(V^j - W^j)\right] + \varepsilon\nabla_j W^j = -C_{\varepsilon 1}\frac{\varepsilon}{k}g_{il}\overline{v^l v^j}\nabla_j V^i - C_{\varepsilon 2}\frac{\varepsilon^2}{k} + \nabla_j\left\{\left(\frac{D_t}{\sigma_k} + \nu\right)g^{ij}\nabla_i \varepsilon\right\} \tag{2.44}$$

Here, V^j is the contravarient component of velocity vector of the flow and W^j is that of the grid motion. g_{ij} and g^{ij} are covariant and contravatiant component of metric tensor.

The covariant derivative is defined as

$$\nabla_i A^k = \frac{\partial A^k}{\partial \xi^i} + A^j\Gamma_{ij} \tag{2.45}$$

Where, $\Gamma_{ij}^{\ k}$ is the Christoffed symbol defined as

$$\Gamma_{i\,j}^{\;k} = \begin{Bmatrix} k \\ i\,j \end{Bmatrix} = \frac{1}{2} g^{km} \left(\frac{\partial g_{jm}}{\partial \xi^i} + \frac{\partial g_{im}}{\partial \xi^j} - \frac{\partial g_{ij}}{\partial \xi^m} \right) = \frac{\partial \xi^k}{\partial x^p} \frac{\partial^2 x^p}{\partial \xi^i \partial \xi^j} \tag{2.46}$$

2.4.2 Constitutive equations

The constitutive equation for 2nd-order non-linear *k–ε* model described in Eq.(2.7) can be written in the following form

$$-\overline{v'^i\, v'^j} = D_t S^{ij} - \frac{2}{3} k \delta_s^i g^{sj} - \frac{k}{\varepsilon} D_t \left[\alpha_1 Q_1 + \alpha_2 Q_2 + \alpha_3 Q_3 \right] \;,\;\; D_t = C_\mu \frac{k^2}{\varepsilon} \tag{2.47}$$

here,

$$Q_1 = S^{i\alpha} g_{\alpha l} \Omega^{lj} + S^{j\beta} g_{\beta l} \Omega^{li} \,, \quad Q_2 = S^{i\alpha} g_{\alpha l} S^{lj} - \frac{1}{3} S^{k\alpha} g_{\alpha m} S^{m\beta} g_{\beta k} \delta_l^i g^{lj} \,,$$

$$Q_3 = \Omega^{i\alpha} g_{\alpha l} \Omega^{lj} - \frac{1}{3} \Omega^{k\alpha} g_{\alpha m} \Omega^{m\beta} g_{\beta k} \delta_l^i g^{lj} \tag{2.48}$$

Strain and rotation tensors are defined as

$$S^{ij} = g^{j\alpha} \nabla_\alpha V^i + g^{i\alpha} \nabla_\alpha V^j \,, \quad \Omega^{ij} = g^{j\alpha} \nabla_\alpha V^i - g^{i\alpha} \nabla_\alpha V^j \tag{2.49}$$

Considering the coefficients of non-linear terms as a function of strain and rotation parameters, their values can be determined from Eqs.(2.11) and (2.13). Eq.(2.11) can be written as

$$\alpha_1 = \frac{1}{4}\left(-c_1 + c_3 \right) , \quad \alpha_2 = \frac{1}{4}(c_1 + c_2 + c_3) \,, \; \alpha_3 = \frac{1}{4}(-c_1 + c_2 - c_3) \tag{2.50}$$

Substituting the functional form from Eq.(2.16b) with the values of $c_{\beta 0}$ from eq. (2.15), the above equation shows the following from

$$\alpha_1 = -0.1325 f_M \,, \; \alpha_2 = 0.0675 f_M \,, \; \alpha_3 = -0.0675 f_M \,, \; f_M = \frac{1}{1 + m_{ds} S^2 + m_{d\Omega} \Omega^2} \tag{2.51}$$

Here, the functional form of c_μ is unchanged as Eq.(2.16a)

$$c_\mu = \frac{c_{\mu o} \,(1 + c_{ns} S^2 + c_{n\Omega} \Omega^2)}{1 + c_{ds} S^2 + c_{d\Omega} \Omega^2 + c_{ds\Omega} S\Omega + c_{ds1} S^4 + c_{d\Omega 1} \Omega^4 + c_{ds\Omega 1} S^2 \Omega^2} \tag{2.52}$$

However, the strain and rotation parameters are defined as

$$S = \frac{k}{\varepsilon} \sqrt{\frac{1}{2} S^{i\alpha} g_{\alpha j} S^{j\beta} g_{\beta i}} \;,\;\; \Omega = \frac{k}{\varepsilon} \sqrt{\frac{1}{2} \Omega^{i\alpha} g_{\alpha j} \Omega^{j\beta} g_{\beta i}} \;. \tag{2.53}$$

2.5 Summary

The standard *k–ε* model has the deficiency of isotropic assumption of eddy viscosity. In this chapter, a second order non-linear *k–ε* model is proposed incorporating some new functions for the model coefficients to explore the model applicability to complex turbulent flows. Considering the realizability principle and anisotropy of turbulence in some baseline flows , the coefficient of eddy viscosity (c_μ) and the coefficients of non-linear quadratic term (c_β) are derived as a function of strain and rotation parameters. It is observed that the functional form of the coefficient of quadratic term shows better comparison than their constant values.

2.6 References

1) Ali, M. S., Hosoda, T., Kimura, I., Effect of empirical functions of non-linear k–ε model on the prediction of flow resistance in a compound channel, *International Conference on Water and Flood Management*, 12-14 March, Dhaka, Bangladesh. vol. 2, pp. 735-743, 2007.
2) Abe, K., Kondoh, T., Nagano, Y., On Reynolds-stress expressions and near-wall scaling parameters for predicting wall and homogeneous turbulent shear flows, *Int. J. Heat and Fluid Flow.* 18, pp.266-282, 1997.
3) Craft, T.J., Launder, B.E. and Suga, K., Extending the applicability of eddy viscosity models through the use of deformation invariants and non-linear elements. *Proc. 5th IAHR Conf. on Refined –Flow Modeling and Measurement*, Paris. pp.125-132, 1993.
4) Cotton, M. A. and Ismail, J.O., Development of a two equation turbulence model with reference to a strain parameter, *Proc. 5th IAHR Conf. on Refined-Flow Modeling and Measurement, Paris,* pp. 117-124, 1993.
5) Champagne, F.H., Harris, V.G. and Corrsin, S., 1970. Experiments on nearly homogeneous

turbulent shear flows. *J. Fluid Mech.,* 41, 81.

6) Gatski, T. B. and Speziale, C. G., On explicit algebraic stress models for complex turbulent flows, *J. Fluid Mech.,* 254, pp.59-78, 1993.
7) Harris V.G., Graham, J.A.H., and Corrsin, S., Further experiments in nearly homogeneous turbulent shear flows, *J. Fluid Mech.* 81, 657, 1977.
8) Hosoda, T., Sakurai, T., Kimura, I. and Muramoto, Y., 3-D computations of compound open channel flows with horizontal vortices and secondary currents by means of non-linear k–ε model, *Journal of Hydroscience and Hydraulic Engineering*, *JSCE*, Vol.17, No.2, 87-96, 1999.
9) Jaw, S.Y. and Chen, C. J., Present status of second order closure turbulence models. I: overview, *J. Engg. Mech., ASCE.* 124, pp.485-501, 1998.
10) Kato, M. and Launder, B.E., The modeling of turbulent flow around stationary and vibrating square cylinder, *Proc. 9th Symp. on Turbulent Shear Flows, Kyoto Vol. 1,* 10-4-4~10-46, 1993.
11) Kimura, I. and Hosoda, T., A non-linear k–ε model with realizability for prediction of flows around bluff bodies, *Int. J. Numer. Meth. Fluids.,* 42, pp.813-837, 2003.
12) Pope, S. B., A more general effective viscosity hypothesis, *J. Fluid Mech.,* 72, pp.331-340, 1975.
13) Rodi, W., Turbulence models for environmental problems, in *Prediction Methods for Turbulent Flows (edited by W. Kollmann)*, pp.259, 1979.
14) Shih,T. H., Zhu, J. and Lumley, J. L., Calculation of bounded complex flows and free shear flows, *Int. J. Numer. Meth. Fluids*., 33, pp.1133-1144, 1996.
15) Yoshizawa, A., Statistical analysis of the deviation of the Reynolds stress from its eddy viscosity representation, *Phys. Fluids,* 27, pp.1377-1387, 1984.

Chapter 3

TURBULENT ROUND JET WITH AND WITHOUT SWIRL

3.1 Introduction

Due to the circumferential motion of jet, the flow field of a swirling jet is more complex than that of a non-swirling one. However, this type of flow is observed in many natural geophysical as well as anthropogenic activities. Tornado is an example of natural swirling flow. Since the geometry, coherent structure, spreading, and dilutions of the jet fluid are highly influenced by the presence of swirl in a jet, it is sometimes imparted to the flow to control its development. The practical examples include flow through combustors, propulsion devices, cyclone separators etc. Swirl jet can also be used in any environmental mixing devices, where a faster spreading or rapid mixing of jet fluid is necessary.

Most of the previous experimental as well as computational works on swirl jet mainly focused on the region close to the source. Examples are the experimental investigations conducted by Panda and Mclaughin (1994), Billant et al.(1998), Ribeiro and Whitelaw (1980) as well as Paschereit et al. (1999), where the interaction of coherent structures of swirl jet just downstream of the nozzle was the main concern. On the other hand, Pratte and Keffer (1972) performed the experiments to study the turbulent field of the jet up to a well downstream distance of 30 jet diameters. Although some numerical studies have been performed on near nozzle region of turbulent swirling flows using Reynolds stress model (e. g. Gibson and Younis, 1986) and Large eddy simulation (e.g. Mcllwain and Pollard, 2002; Wang et al., 2004), to the best of author's knowledge, the *k–ε* model is yet to be applied successfully.

In this chapter, the approximate solutions are presented for the fundamental properties of a swirl jet, such as spreading rate, distribution of turbulence intensities, turbulent shear stress, turbulent kinetic energy etc., derived by using a non-linear *k–ε* model. Neglecting the swirl parameters from the derived solutions, the spreading rate and turbulent properties are calculated for a round jet without swirl. The results are compared with the previous experiments. The model constants in the assumed functional forms for the coefficients of eddy viscosity and quadratic term, estimated in previous chapter considering 2D shear flow, will be determined by tuning their values for best fitted comparison with previous experimental results. Finally, the turbulent properties of swirl jet are predicted for different swirl numbers.

3.2 Governing Equations

The equations for 2nd order non-linear *k–ε* model can be rewritten as follows:

Continuity equation: $$\frac{\partial U_i}{\partial x_i} = 0 \tag{3.1}$$

Momentum equation: $$\frac{\partial U_i}{\partial t} + \frac{\partial U_j U_i}{\partial x_j} = g_i - \frac{1}{\rho}\frac{\partial P}{\partial x_i} + \frac{\partial}{\partial x_j}\left(-\overline{u_i u_j}\right) + \nu \frac{\partial^2 U_i}{\partial {x_j}^2} \tag{3.2}$$

k - equation: $$\frac{\partial k}{\partial t} + \frac{\partial k U_j}{\partial x_j} = -\overline{u_i u_j}\frac{\partial U_i}{\partial x_j} + \frac{\partial}{\partial x_j}\left\{\left(\frac{\nu_t}{\sigma_k} + \nu\right)\frac{\partial k}{\partial x_j}\right\} - \varepsilon \tag{3.3}$$

ε - equation: $$\frac{\partial \varepsilon}{\partial t} + \frac{\partial \varepsilon U_j}{\partial x_j} = -c_{\varepsilon 1}\frac{\varepsilon}{k}\overline{u_i u_j}\frac{\partial U_i}{\partial x_j} + \frac{\partial}{\partial x_j}\left\{\left(\frac{\nu_t}{\sigma_\varepsilon} + \nu\right)\frac{\partial \varepsilon}{\partial x_j}\right\} - c_{\varepsilon 2}\frac{\varepsilon^2}{k} \tag{3.4}$$

Turbulence model (Non-linear): $$-\overline{u_i u_j} = \nu_t S_{ij} - \frac{2}{3}k\delta_{ij} - \frac{k}{\varepsilon}\nu_t \sum_{\beta=1}^{3} c_\beta \left(S_{\beta ij} - \frac{1}{3}S_{\beta\alpha\alpha}\delta_{ij}\right) \tag{3.5}$$

Here,

$$\nu_t = c_\mu \frac{k^2}{\varepsilon},\quad S_{ij} = \frac{\partial U_i}{\partial x_j} + \frac{\partial U_j}{\partial x_i},\quad \Omega_{ij} = \frac{\partial U_i}{\partial x_j} - \frac{\partial U_j}{\partial x_i}, S = \frac{k}{\varepsilon}\sqrt{\frac{1}{2} S_{ij} S_{ij}}\,, \Omega = \frac{k}{\varepsilon}\sqrt{\frac{1}{2}\Omega_{ij}\Omega_{ij}} \qquad (3.6)$$

In Equation (3.5),

$$S_{1ij} = \frac{\partial U_i}{\partial x_\gamma}\frac{\partial U_j}{\partial x_\gamma},\quad S_{2ij} = \frac{1}{2}\left(\frac{\partial U_\gamma}{\partial x_i}\frac{\partial U_j}{\partial x_\gamma} + \frac{\partial U_\gamma}{\partial x_j}\frac{\partial U_i}{\partial x_\gamma}\right),\quad S_{3ij} = \frac{\partial U_\gamma}{\partial x_i}\frac{\partial U_\gamma}{\partial x_j}\,. \qquad (3.7)$$

$$c_\mu = \frac{c_{\mu o}\,(1 + c_{ns}S^2 + c_{n\Omega}\Omega^2)}{1 + c_{ds}S^2 + c_{d\Omega}\Omega^2 + c_{ds\Omega}S\Omega + c_{ds1}S^4 + c_{d\Omega 1}\Omega^4 + c_{ds\Omega 1}S^2\Omega^2} \qquad (3.8)$$

$$c_\beta = c_{\beta o}\frac{1}{1 + m_{ds}S^2 + m_{d\Omega}\Omega^2} \qquad (3.9)$$

The value of the model constants are: $c_{\mu 0}$ = 0.09, c_{ns} = 0.005, $c_{n\Omega}$ = 0.0068, c_{ds} = 0.008, $c_{d\Omega}$ = 0.004, $c_{ds\Omega}$ = -0.003, c_{ds1} = 0.00005, $c_{d\Omega 1}$ = 0.00005, $c_{ds\Omega 1}$ = 0.00025, c_{10} =0.40, c_{20} =0.0, c_{30} = -0.13, m_{ds} = 0.01, $m_{d\Omega}$ = 0.003, σ_k = 1.0, σ_ε = 1.3, $c_{\varepsilon 1}$ = 1.44 and $c_{\varepsilon 2}$ = 1.92. In standard $k - \varepsilon$ model, c_μ = 0.09 and c_β = 0.0.

For turbulent shear flows, the following assumptions are made (Jaw and Chen, 1998):

a) The pressure gradient is small i.e. $\frac{\partial P}{\partial x} \approx 0$

b) Viscous shear stress is much smaller than the turbulent shear stress, and can be neglected.

c) Diffusion in the direction normal to the flow (y- and z-directions) is much larger than the diffusion in the direction of flow (x-direction).

Thus, the momentum equation in x-direction as well as the k and ε equations can be presented in a simplified form as follows.

The momentum equation in x-direction:

$$U_x\frac{\partial U_x}{\partial x} + U_y\frac{\partial U_x}{\partial y} + U_z\frac{\partial U_x}{\partial z} = \frac{\partial}{\partial x}\left(-\overline{u_x u_x}\right) + \frac{\partial}{\partial y}\left(-\overline{u_x u_y}\right) + \frac{\partial}{\partial z}\left(-\overline{u_x u_z}\right) \qquad (3.10)$$

k - equation:

$$U_x\frac{\partial k}{\partial x} + U_y\frac{\partial k}{\partial y} + U_z\frac{\partial k}{\partial z} = -\overline{u_x u_x}\frac{\partial U_x}{\partial x} - \overline{u_x u_y}\frac{\partial U_x}{\partial y} - \overline{u_x u_z}\frac{\partial U_x}{\partial z} - \overline{u_y u_x}\frac{\partial U_y}{\partial x} - \overline{u_y u_y}\frac{\partial U_y}{\partial y}$$

$$-\overline{u_y u_z}\frac{\partial U_y}{\partial z}-\overline{u_z u_x}\frac{\partial U_z}{\partial x}-\overline{u_z u_y}\frac{\partial U_z}{\partial y}-\overline{u_z u_z}\frac{\partial U_z}{\partial z}+\frac{\partial}{\partial y}\left(\frac{\nu_t}{\sigma_k}\frac{\partial k}{\partial y}\right)+\frac{\partial}{\partial z}\left(\frac{\nu_t}{\sigma_k}\frac{\partial k}{\partial z}\right)-\varepsilon \tag{3.11}$$

ε- equation:

$$U_x\frac{\partial \varepsilon}{\partial x}+U_y\frac{\partial \varepsilon}{\partial y}+U_z\frac{\partial \varepsilon}{\partial z}=c_{\varepsilon 1}\frac{\varepsilon}{k}\left[-\overline{u_x u_x}\frac{\partial U_x}{\partial x}-\overline{u_x u_y}\frac{\partial U_x}{\partial y}-\overline{u_x u_z}\frac{\partial U_x}{\partial z}-\overline{u_y u_x}\frac{\partial U_y}{\partial x}-\overline{u_y u_y}\frac{\partial U_y}{\partial y}\right.$$
$$\left.-\overline{u_y u_z}\frac{\partial U_y}{\partial z}-\overline{u_z u_x}\frac{\partial U_z}{\partial x}-\overline{u_z u_y}\frac{\partial U_z}{\partial y}-\overline{u_z u_z}\frac{\partial U_z}{\partial z}\right]+\frac{\partial}{\partial y}\left(\frac{\nu_t}{\sigma_\varepsilon}\frac{\partial k}{\partial y}\right)+\frac{\partial}{\partial z}\left(\frac{\nu_t}{\sigma_\varepsilon}\frac{\partial k}{\partial z}\right)-c_{\varepsilon 2}\frac{\varepsilon^2}{k}$$

(3.12)

3.3 Procedure for the Solution

The functional forms of velocities and *k–ε* distributions are assumed as a first approximation. Using the integral equation of momentum conservation, the parameter accounted for swirl (introduced in assumed velocity distributions in *section 3.4.1*) is derived as function of non-dimensional swirl number, S_N. Substituting the mathematical expressions of the assumed distributions into the continuity, momentum and non-linear *k–ε* equations, a set of algebraic equations are derived considering the relation of lowest order with respect to the power of 1/*x*. Solving these simultaneous algebraic equations, the unknown coefficients in the assumed distributions are determined as the function of the non-linear *k–ε* model constants. Approximate solutions for the distributions of turbulence characteristics such as distribution of turbulence intensities, turbulent shear stress, etc. are derived using the constitutive equations of the model. Neglecting the swirl parameters, the derived solutions for swirl jet are applied for a round jet without swirl.

In the previous chapter, the coefficients in the functional forms of c_μ and c_β are initially estimated considering realizability conditions and anisotropy of turbulence in plane shear layer. In this chapter, the approximate solution for a round jet with and without swirl are compared with the previous experiments, and the model constants are finally determined by tuning their values for best fitted comparison. The fundamental properties are then predicted for a jet with different swirl numbers.

3.4 Approximate Solution for Turbulent Swirling Jet

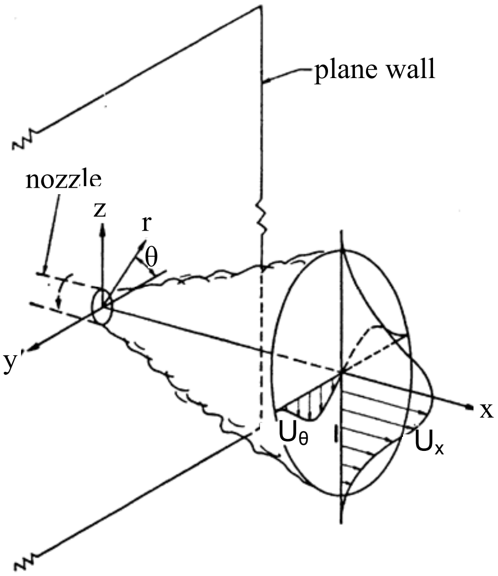

Fig. 3.1 Definition sketch of swirl jet (Pratte and Keffer, 1972)

Figure 3.1 shows the definition sketch of a swirl jet with Cartesian and Cylindrical coordinate systems. Consider, U_x, U_y, and U_z are the jet velocities in axial (x), lateral (y), and transverse (z) directions in Cartesian coordinate system and U_x, U_r, and U_θ are the velocities in axial (x), radial (r), and azimuthal (θ) directions in Cylindrical coordinate system respectively.

3.4.1 Assumed profiles

In the self-similar region, the following relations can be obtained for the attenuation rate of hydraulic variables of an axisymmetric swirl jet (Rajaratnam, 1976; Hosoda et. al., 1984).

$$B \propto x, \quad U_m \propto \frac{1}{x}, \quad k_0 \propto \frac{1}{x^2}, \quad \varepsilon_0 \propto \frac{1}{x^4} \tag{3.13}$$

Here, B is the jet width; U_m is the centerline maximum velocity of the jet; k_0 and ε_0 are the centerline values of turbulent kinetic energy and its dissipation rate respectively.

The following assumptions are made for the functional forms of velocity and k–ε

distributions, which are compatible with the decaying power law of velocity and k–ε along the centerline of jet.

$$U_x = \frac{a_1}{x}\exp\left(-\frac{y^2+z^2}{\gamma^2 x^2}\right) + \frac{a_3}{x}\frac{y^2+z^2}{\gamma^2 x^2}\exp\left(-\frac{y^2+z^2}{\gamma^2 x^2}\right) \tag{3.14}$$

$$U_y = \frac{b}{x}\frac{y}{\gamma x}\exp\left(-\frac{y^2+z^2}{\gamma^2 x^2}\right) + \frac{\alpha z}{\gamma x^3}\exp\left(-\frac{y^2+z^2}{\gamma^2 x^2}\right) \tag{3.15}$$

$$U_z = \frac{b}{x}\frac{z}{\gamma x}\exp\left(-\frac{y^2+z^2}{\gamma^2 x^2}\right) - \frac{\alpha y}{\gamma x^3}\exp\left(-\frac{y^2+z^2}{\gamma^2 x^2}\right) \tag{3.16}$$

$$k = \frac{1}{x^2}\left(k_0 + k_2\frac{y^2+z^2}{\gamma^2 x^2}\right)\exp\left(-2\frac{y^2+z^2}{\gamma^2 x^2}\right) \tag{3.17}$$

$$\varepsilon = \frac{1}{x^4}\left(\varepsilon_0 + \varepsilon_2\frac{y^2+z^2}{\gamma^2 x^2}\right)\exp\left(-3\frac{y^2+z^2}{\gamma^2 x^2}\right) \tag{3.18}$$

Where, a_1, a_3, b, α, and γ are the unknown coefficients of the velocity profile; and k_0, k_2, ε_0, and ε_2 are that of the k-ε distributions.

3.4.2 Swirl parameter

To define the swirl parameter, the cylindrical coordinate system is considered. Rajaratnam (1976) showed that for the circular jet with swirl, integral of the pressure plus momentum (W) as well as angular momentum (T) are preserved. They are defined by

$$W = \int_0^\infty \left(U_x^2 - \frac{U_\theta^2}{2}\right) r\,dr \tag{3.19}$$

and $$T = \int_0^\infty r^2 U_x U_\theta\,dr \tag{3.20}$$

respectively.

Considering $U_x >> U_\theta$, Eq. (3.19) can be reduced to

$$W = \int_0^\infty U_x^2 \, r dr \tag{3.21}$$

Substituting the assumed velocity distributions into Eqs. (3.20) and (3.21), the following relations are obtained (U_θ is calculated from U_y and U_z).

$$W = \frac{\gamma^2}{8}\left(2a_1^2 + 2a_1 a_3 + a_3^2\right) \tag{3.22}$$

$$T = \frac{\alpha\gamma^3}{8}\left(a_1 + a_3\right) \tag{3.23}$$

A non-dimensional parameter combining W and T is used to represent the relative amount of swirl present in the flow, called swirl number (S_N).

$$S_N = \frac{T}{W r_0} \tag{3.24}$$

where, r_0 is the radius of the jet nozzle.

Using Eqs. (3.22) to (3.24), the swirl number can be defined as

$$S_N = \frac{6\alpha\gamma^2}{25 b r_0} \tag{3.25}$$

Hence,

$$\alpha = \frac{25 S_N b r_0}{6\gamma^2} \tag{3.26}$$

3.4.3 Derived solutions

Substituting the assumed velocity distributions [Eqs. (3.14) to (3.18)] into the continuity equation, the following algebraic relations are derived.

$$a_1 = \frac{2b}{\gamma}, \quad a_3 = \frac{2}{3}\frac{b}{\gamma} \tag{3.27-a, b}$$

The integral equation for conservation of momentum flux also results as Eq. (3.28).

$$M_0 = U_0{}^2 A_0 = 2\pi\left(\frac{a_1^2\gamma^2}{4} + 2\frac{a_1 a_3\gamma^2}{8} + \frac{a_3^2\gamma^2}{8}\right) \tag{3.28}$$

Where, A_0, U_0, and M_0 are the area, velocity, and initial momentum flux of the jet at inlet respectively.

Substituting Eq. (3.27) into Eq. (3.28), the coefficient of attenuation of radial velocity '*b'* is determined as a function of inlet conditions.

$$b = \frac{3}{5}\sqrt{\frac{M_0}{\pi}} \ . \tag{3.29}$$

For the assumed velocity and *k–ε* distributions, using the Reynolds equation in the *x*-direction and *k–ε* equations, the following three algebraic expressions are derived as the relations of lowest order with respect to the power of 1/*x*.

Reynolds equation in *x*-direction:

$$\frac{1}{x^3}: \quad -a_1^2\left\{\varepsilon_0^2 + \frac{1}{2}c_{ds}k_0^2\left(4a_1^2 + 8\frac{b^2}{\gamma^2}\right)\right\}$$

$$= 2c_{\mu_0}\varepsilon_0 k\left\{\varepsilon_0{}^2 + \frac{1}{2}c_{ns}\frac{k_0^2}{\varepsilon_0^2}\left(4a_1^2 + 8\frac{b^2}{\gamma^2}\right)\right\}\left(\frac{2a_3}{\gamma^2} - \frac{2a_1}{\gamma^2} - \frac{2b}{\gamma}\right)_0^2 \tag{3.30}$$

k-equation:

$$\frac{1}{x^4}: \quad \left(-2a_1k_0 + \varepsilon_0\right)\left\{\varepsilon_0^2 + \frac{1}{2}c_{ds}k_0^2\left(4a_1^2 + 8\frac{b^2}{\gamma^2}\right)\right\}$$

$$= \frac{c_{\mu_0}}{\sigma_k}\varepsilon_0 k_0^2\left(\frac{4k_2}{\gamma^2} - \frac{8k_0}{\gamma^2}\right)\left\{\varepsilon_0^2 + \frac{1}{2}c_{ns}\frac{k_0^2}{\varepsilon_0^2}\left(4a_1^2 + 8\frac{b^2}{\gamma^2}\right)\right\} \tag{3.31}$$

ε-equation:

$$\frac{1}{x^6}: \quad \left(-4a_1\varepsilon_0 k_0 + c_{\varepsilon 2}\varepsilon_0^2\right)\left\{\varepsilon_0^2 + \frac{1}{2}c_{ds}k_0^2\left(4a_1^2 + 8\frac{b^2}{\gamma^2}\right)\right\}$$

$$= \frac{c_{\mu_0}}{\sigma_\varepsilon}\varepsilon_0 k_0^3\left(\frac{4\varepsilon_2}{\gamma^2} - \frac{8\varepsilon_0}{\gamma^2}\right)\left\{\varepsilon_0^2 + \frac{1}{2}c_{ns}\frac{k_0^2}{\varepsilon_0^2}\left(4a_1^2 + 8\frac{b^2}{\gamma^2}\right)\right\} \tag{3.32}$$

The values of b, a_1 and a_3 are determined from Eqs. (3.27) and (3.29). Substituting the values of k_0 and ε_0, which are the k and ε values at centerline, the development rate of swirl jet (γ) can be estimated by Eq. (3.30). For any known value of swirl number S_N, the value of 'α' can be easily determined using Eq. (3.26). The coefficients of k and ε distributions are determined by solving Eqs. (3.31) and (3.32).

The radial distribution of turbulent intensities as well as turbulent shear stresses are derived using non-linear constitutive equations. The derived equations are shown in Appendix-3.A.

3.5 Results and Discussions

Tuning the model constants (estimated from realizability considerations), the approximate solutions are compared with the previous experimental results, and the values of model constants are determined for best fitted comparison. Eliminating swirl parameter i.e. taking swirl number (S_N) and hence the swirl parameter (α) as zero, the derived solutions for swirl jet is applied to a round jet without swirl. The comparisons of results for swirl and non-swirl jets with experiments are presented below.

3.5.1 Round jet without swirl

Figures 3.2, 3.3, and 3.4 show the radial distributions of turbulent intensities for axial, radial and circumferential velocities. The results are compared with the experimental data by Wygnanski and Fielder (1969), and Wang and Law (2002). In Fig. 3.5, the calculated shear stress profile is compared with the range of experimental results by Fukushima et al. (2000), where two experimental profiles represent the lower and upper boundary of a number of measured profiles for different downstream distances.

The distribution of turbulent kinetic energy (k) normalized by U_m^2 is favorably compared with the experiment of Wygnanski and Fielder, and shown in Fig.3.6. The approximate solution for normalized turbulent energy dissipate rate ($\varepsilon x/U_m^3$) , compared with the experimental data of Wygnanski & Fielder (1969) as well as with that of Sami (1967), is shown in Fig. 3.7. The available experimental data on turbulent kinetic energy dissipation rate are quite scattered. The present prediction coincides with the Wygnanski & Fielders' data near the central region of jet, and it is close to Sami's data for higher radial distances. In comparison to experimental results, a little deviation is observed in the spreading of ε profile; it can be noted that this deficiency may be due to the simple assumptions made in the exponential part of ε distributions in Eq. (3.18). The values of k_0 and ε_0, which are the center line values of k and ε, are estimated by tuning their values for best fitted comparison with experimental results.

Approximate solutions are also derived by using standard k–ε model and shown in the figures by dotted line.

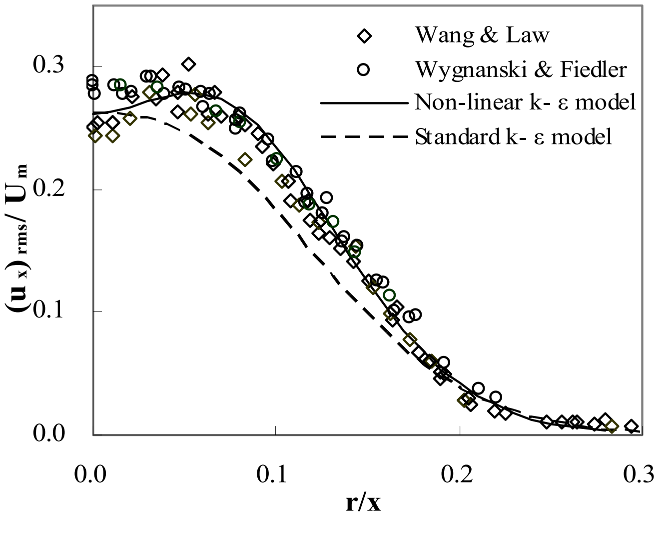

Fig. 3.2 Distribution of turbulent intensity of the axial velocity in a round jet without swirl

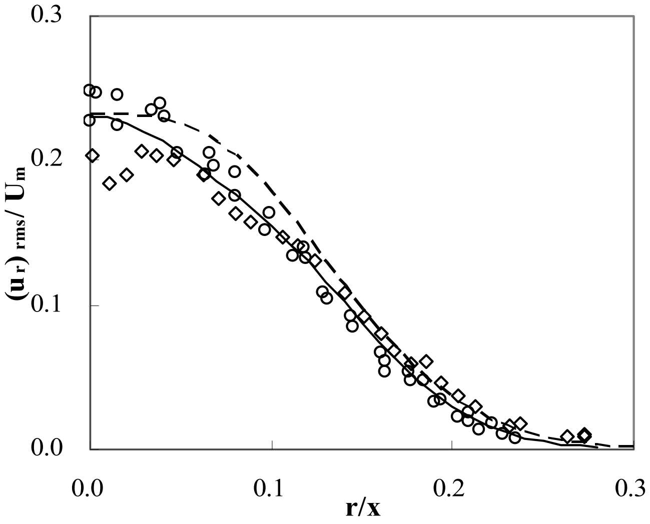

Fig. 3.3 Distribution of turbulent intensity of the radial velocity in a round jet without swirl

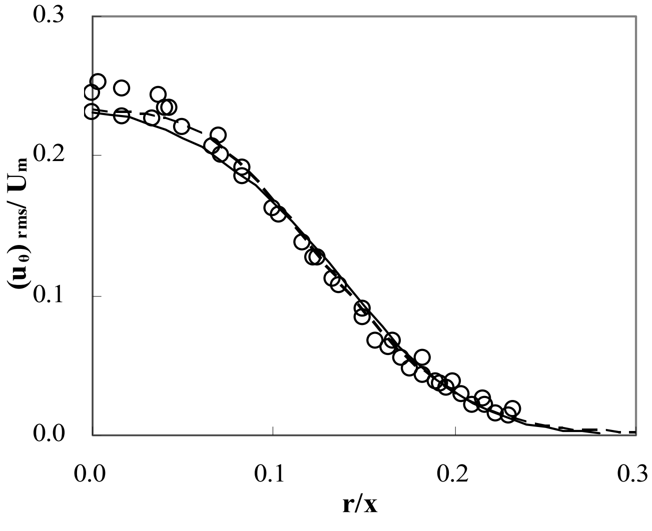

Fig. 3.4 Distribution of turbulent intensity of the circumferential velocity in a round jet without swirl

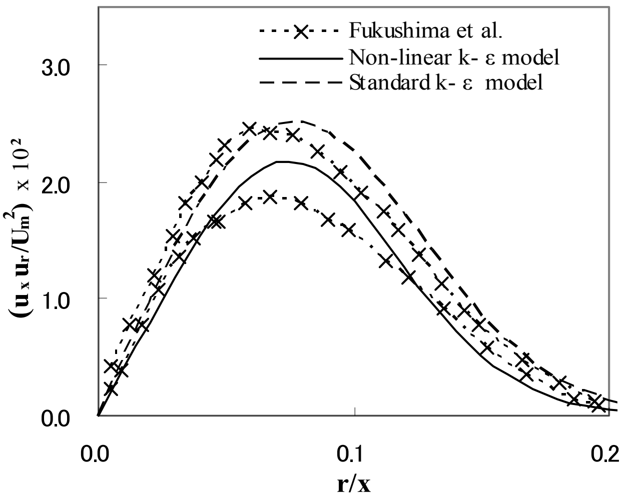

Fig. 3.5 Radial distribution of turbulent shear stress in a round jet without swirl

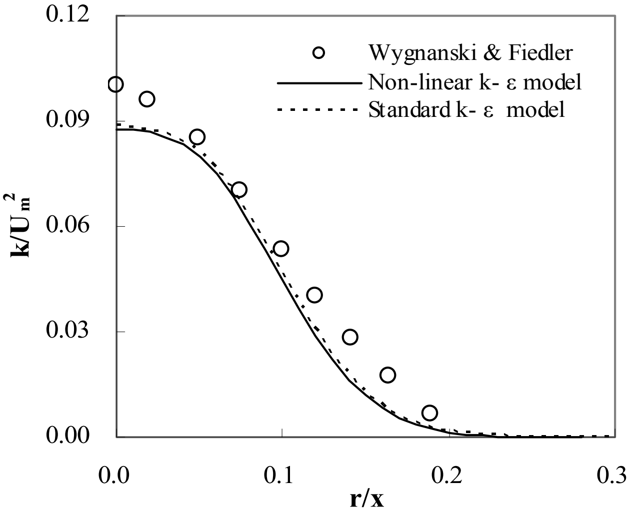

Fig. 3.6 Radial distribution of turbulent kinetic energy in a round jet without swirl

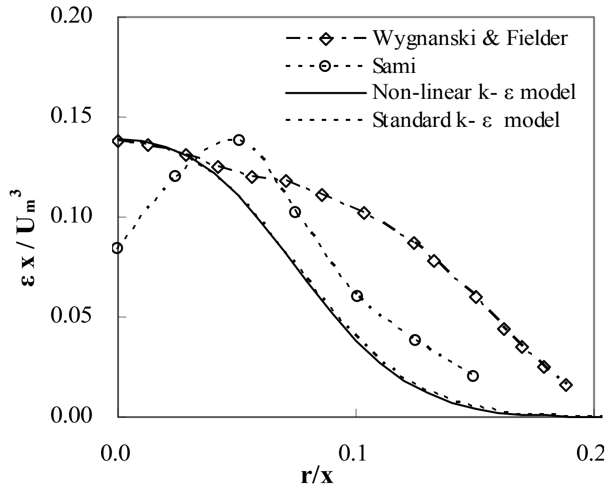

Fig. 3.7 Radial distribution of turbulent kinetic energy dissipation rate in a round jet without swirl

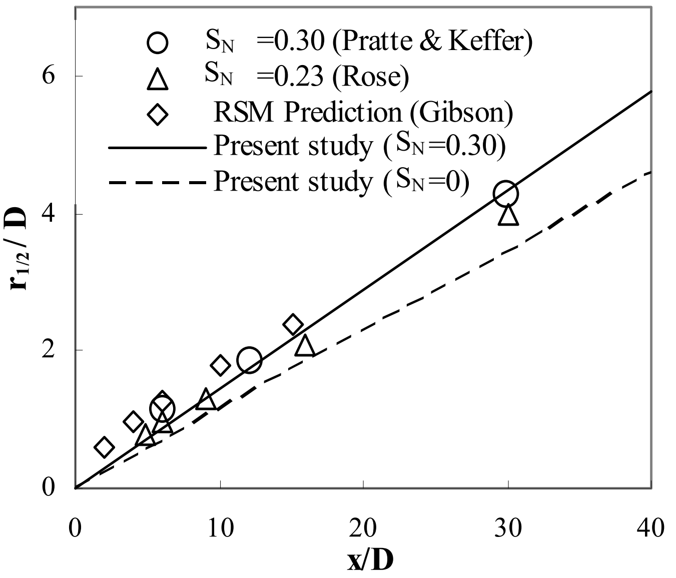

Fig. 3.8 Comparison of jet half-width

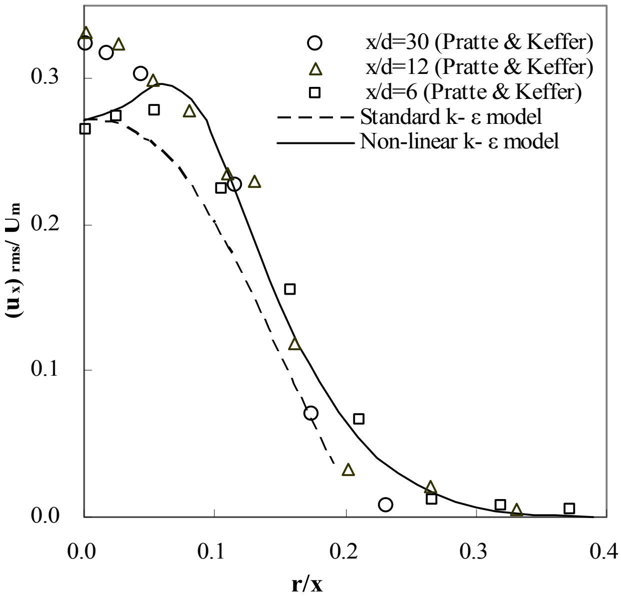

Fig. 3.9 Distribution of turbulent intensity of the axial velocity in a swirl jet

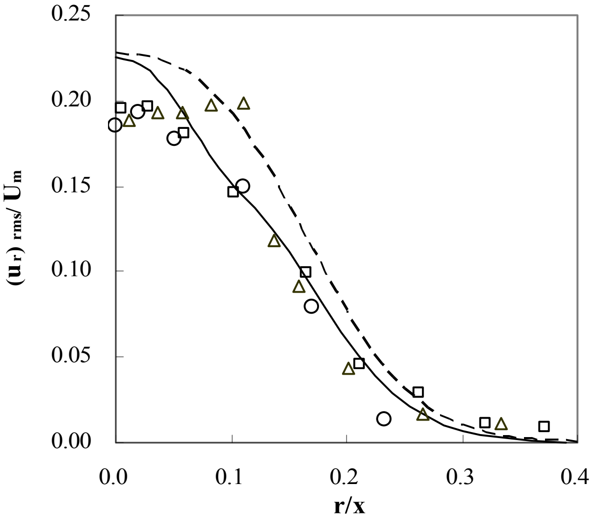

Fig. 3.10 Distribution of turbulent intensity of the radial velocity in a swirl jet

3.5.2 Swirl jet

In Fig. 3.8, the estimated jet half-width for a moderate swirl of S_N =0.3 is plotted against downstream distances; both are normalized with initial jet diameter *D*. Here, the jet half-width

($r_{1/2}$) is defined as the radial distance (r), where the axial velocity is half of the maximum centerline velocity. The present prediction shows a good agreement with the previous experimental data by Pratte and Keffer (S_N=0.3) as well as with that of Rose (1962) (S_N=0.23). The prediction of Reynolds Stress Model (RSM) by Gibson and Younis (1986), which is limited to 15 jet diameters of downstream distances, are also shown for comparison. The swirl jet reasonably spreads faster than the round jet. The value of jet half-width for swirl jet evaluated by approximate solution is 0.144, which is about 21% higher than the estimated half-width of a round jet without swirl. Gibson and Younis (1986) also reported similar comparison with a difference of 25% between the jet-half width of swirl and non-swirl round jets.

The turbulent intensities for axial, lateral and circumferential velocities are calculated for the swirl number of S_N=0.3. The results are compared with experimental data by Pratte and Keffer (1972) in Figs. 3.9 to 3.11. In Fig. 3.12, the distribution of normalized turbulent kinetic energy $\left(\overline{q^2}\right)^{\frac{1}{2}}/U_m$ (where, $\overline{q^2}$ is twice the turbulent kinetic energy), is favorably compared with the previous experiment. Figure 3.13 shows the radial distribution of turbulent Reynolds stress, $\overline{u_x u_r}$; due to unavailability of experimental data, this result is not compared with experiments.

The figurers show that the non-linear model well compared with experiments results. In comparison to experimental results as well as non-linear model prediction, the standard k–ε model under predicts the turbulent intensities for axial direction and over predicts for radial and circumferential directions. The discrepancy is higher for swirl jet case. Reasonably, the non-linear model showed better comparison than standard one.

The distributions of turbulent intensities are found to be changed significantly depending on swirl number. For different swirl numbers of S_N = 0.3, 1.5 and 2.5, the turbulent intensities are calculated. The radial distributions of turbulent intensities for axial, radial and circumferential velocities are shown in Figs. 3.14(a), (b), and (c) respectively. It is observed that, with increasing swirl number the turbulent intensity is decreased for axial velocity component and increased for lateral and circumferential velocity components. Also the pattern of profiles, especially for axial velocity, are changed significantly with the swirl numbers.

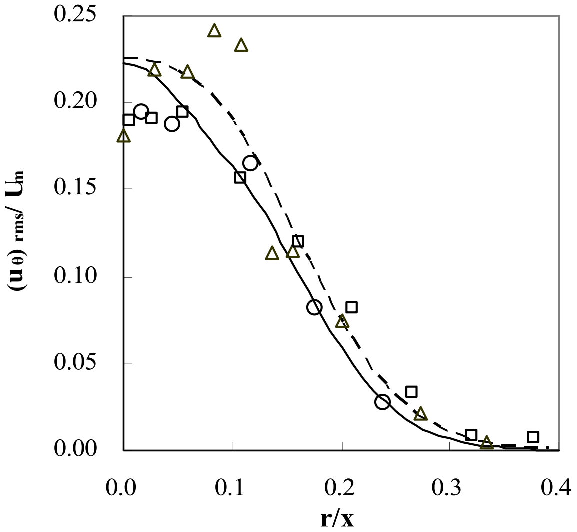

Fig. 3.11 Distribution of turbulent intensity of the circumferential velocity in a swirl jet

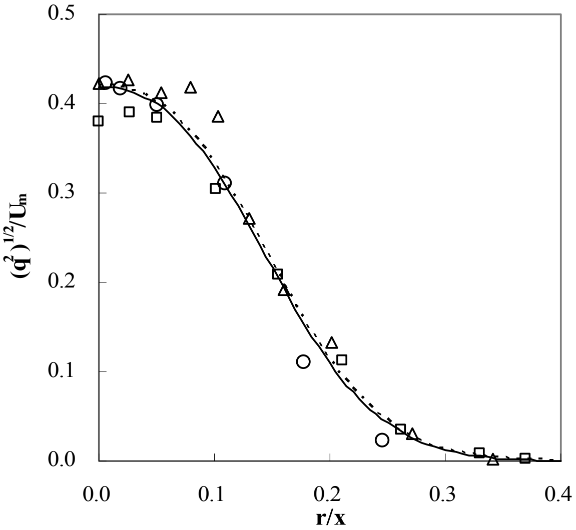

Fig. 3.12 Radial distribution of turbulent kinetic energy in a swirl jet

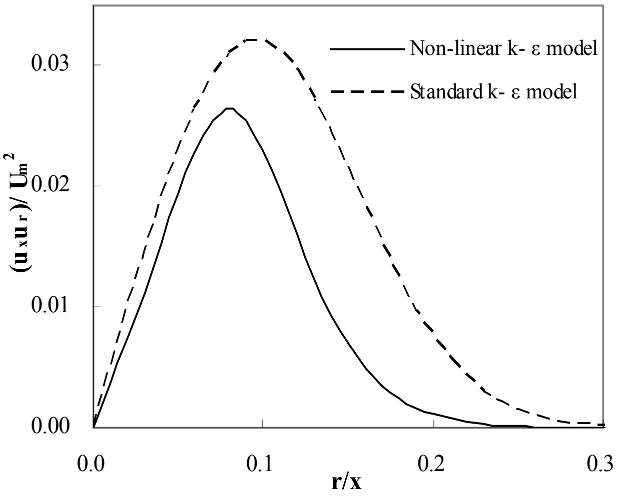

Fig. 3.13 Radial distribution of turbulent shear stress in a swirl jet

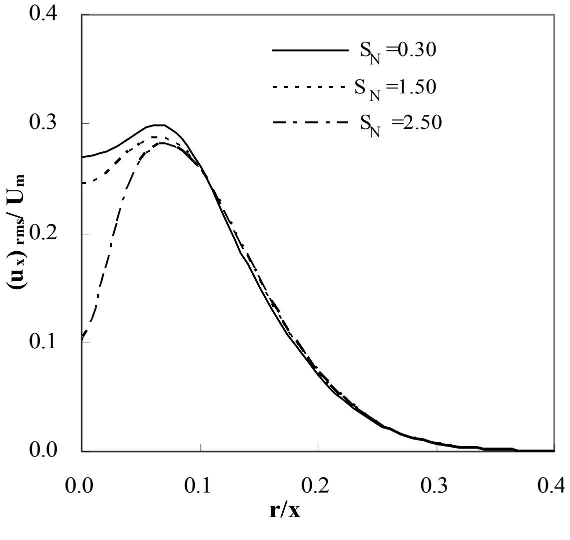

(a)

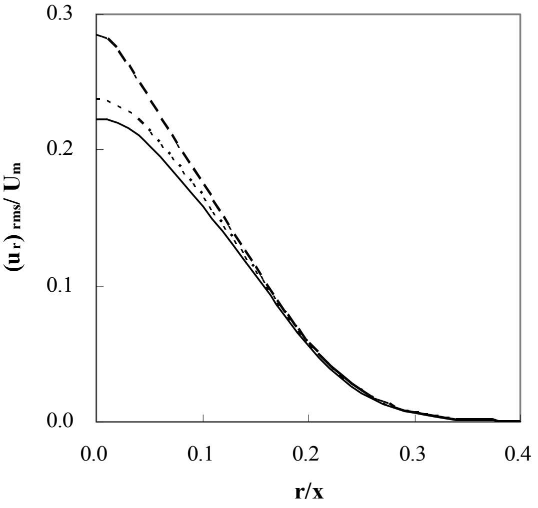

(b)

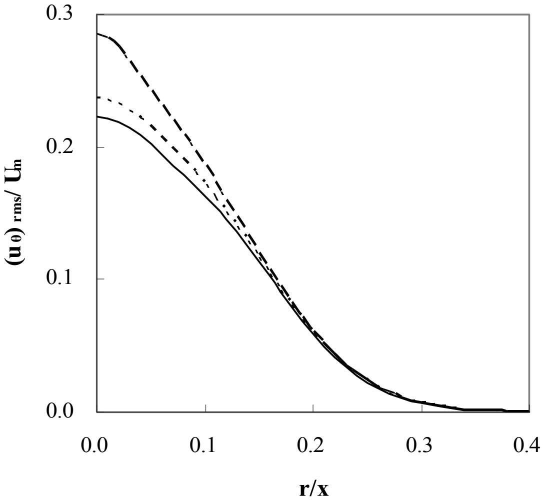

(c)

Fig. 3.14 Distribution of turbulent intensity for different swirl numbers (a) for axial velocity (b) for radial velocity and (c) for circumferential velocity of jet

3.6 Summary

The model constants in a turbulence model are of major concern to its applicability. In this chapter, approximate solutions for the fundamental properties of swirl and non-swirl jets are derived based on the non-linear *k–ε* model. Tuning the model constants (estimated from realizability considerations) the approximate solutions are compared with the previous experimental results, and the values of model constants are determined for best fitted comparison. The solutions of standard *k–ε* model is also presented. Reasonably, the non-linear model showed better comparison than the standard one.

The distribution of turbulent intensity is significantly influenced by the swirl number. It is observed that, with increasing swirl number the turbulent intensity is decreased for axial velocity component and increased for lateral and circumferential velocity components.

Appendix-3A: Derived Equations

Derived equations for the distributions of turbulent intensities in a swirl jet are given below.

$$
\begin{aligned}
\overline{u_x u_x} = {} & \left\{2a_1 - \frac{r^2}{x^2}\left(\frac{4a_1}{\gamma^2} - \frac{6a_3}{\gamma^2}\right)\right\}\frac{c_\mu k'^2}{\varepsilon'}\frac{1}{x^2}\exp\left(-2\frac{r^2}{\gamma^2 x^2}\right) + c_\mu \frac{k'^3}{\varepsilon'^2}\frac{1}{x^2}\exp\left(-2\frac{r^2}{\gamma^2 x^2}\right) \\
& \times\Biggl[(c_1 + c_2 + c_3)\left(\frac{2}{3}a_1{}^2 - \frac{2}{3}\frac{b^2}{\gamma^2}\right) - (c_1 - c_2 + c_3)\frac{1}{x^2}\left(\frac{2}{3}\frac{\alpha^2}{\gamma^2}\right) + \frac{r^2}{x^2}\Biggl\langle c_1\Biggl\{\frac{2}{3}\left(\frac{2a_3}{\gamma^2} - \frac{2a_1}{\gamma^2}\right)^2 \\
& - \frac{4}{3}\left(\frac{2a_1{}^2}{\gamma^2} - \frac{3a_1 a_3}{\gamma^2}\right) - \frac{4}{3}\frac{b^2}{\gamma^2} + \frac{4}{3}\frac{b^2}{\gamma^4} + \frac{1}{x^2}\left(\frac{4}{3}\frac{\alpha^2}{\gamma^4} - \frac{3\alpha^2}{\gamma^2}\right) \\
& + c_2\left\{-\frac{4}{3}\left(\frac{2a_1{}^2}{\gamma^2} - \frac{3a_1 a_3}{\gamma^2}\right) - \frac{2}{3}\frac{b}{\gamma}\left(\frac{2a_3}{\gamma^2} - \frac{2a_1}{\gamma^2}\right) + \frac{4}{3}\frac{b^2}{\gamma^4} - \frac{1}{x^2}\left(\frac{4}{3}\frac{\alpha^2}{\gamma^4}\right)\right\} + c_3\Biggl\{-\frac{1}{3}\left(\frac{2a_3}{\gamma^2} - \frac{2a_1}{\gamma^2}\right)^2 \\
& - \frac{4}{3}\left(\frac{2a_1{}^2}{\gamma^2} - \frac{3a_1 a_3}{\gamma^2}\right) + \frac{8}{3}\frac{b^2}{\gamma^2} + \frac{4}{3}\frac{b^2}{\gamma^4} + \frac{1}{x^2}\left(\frac{4}{3}\frac{\alpha^2}{\gamma^4} + \frac{6\alpha^2}{\gamma^2}\right)\Biggr\}\Biggr\rangle + \frac{r^4}{x^4}\Biggl\langle c_1\Biggl\{\frac{2}{3}\left(\frac{2a_1}{\gamma^2} - \frac{3a_3}{\gamma^2}\right)^2 \\
& - \frac{8}{3}\frac{a_3}{\gamma^4}\left(\frac{2a_3}{\gamma^2} - \frac{2a_1}{\gamma^2}\right) - \frac{4}{3}\frac{b^2}{\gamma^6} + \frac{8}{3}\frac{b^2}{\gamma^4}\Biggr\} + c_2\Biggl\{\frac{2}{3}\left(\frac{2a_1}{\gamma^2} - \frac{3a_3}{\gamma^2}\right)^2 + \frac{2}{3}\frac{b}{\gamma^3}\left(\frac{2a_3}{\gamma^2} - \frac{2a_1}{\gamma^2}\right) - \frac{4}{3}\frac{b^2}{\gamma^6} \\
& + \frac{4}{3}\frac{a_3 b}{\gamma^5}\Biggr\} + c_3\left\{\frac{2}{3}\left(\frac{2a_1}{\gamma^2} - \frac{3a_3}{\gamma^2}\right)^2 + \frac{4}{3}\frac{a_3}{\gamma^4}\left(\frac{2a_3}{\gamma^2} - \frac{2a_1}{\gamma^2}\right) - \frac{4}{3}\frac{b^2}{\gamma^6} - \frac{16}{3}\frac{b^2}{\gamma^4}\right\}\Biggr\rangle\Biggr] \\
& + \frac{2}{3}\frac{1}{x^2}\left(k_0 + k_2\frac{r^2}{\gamma^2 x^2}\right)\exp\left(-2\frac{r^2}{\gamma^2 x^2}\right)
\end{aligned}
\tag{3.A1}
$$

$$
\overline{u_r u_r} = \left\{-2\frac{b}{\gamma} + \frac{4b}{\gamma^3}\frac{r^2}{x^2}\right\}c_\mu \frac{k'^2}{\varepsilon'}\frac{1}{x^2}\exp\left(-2\frac{r^2}{\gamma^2 x^2}\right) + c_\mu \frac{k'^3}{\varepsilon'^2}\frac{1}{x^2}\exp\left(-2\frac{r^2}{\gamma^2 x^2}\right)
$$

$$
\begin{aligned}
&\times\Bigg[(c_1+c_2+c_3)\left(\frac{1}{3}\frac{b^2}{\gamma^2}-\frac{1}{3}a_1{}^2\right)+(c_1-c_2+c_3)\frac{1}{x^2}\left(\frac{1}{3}\frac{\alpha^2}{\gamma^2}\right)+\frac{r^2}{x^2}\Bigg\langle c_1\Bigg\{-\frac{1}{3}\left(\frac{2a_3}{\gamma^2}-\frac{2a_1}{\gamma^2}\right)^2\\
&+\frac{2}{3}\left(\frac{2a_1{}^2}{\gamma^2}-\frac{3a_1a_3}{\gamma^2}\right)-\frac{4}{3}\frac{b^2}{\gamma^2}+\frac{4}{3}\frac{b^2}{\gamma^4}+\frac{1}{x^2}\left(\frac{4}{3}\frac{\alpha^2}{\gamma^4}-\frac{3\alpha^2}{\gamma^2}\right)\Bigg\}+c_2\Bigg\{\frac{2}{3}\left(\frac{2a_1{}^2}{\gamma^2}-\frac{3a_1a_3}{\gamma^2}\right)\\
&+\frac{4}{3}\frac{b}{\gamma}\left(\frac{2a_3}{\gamma^2}-\frac{2a_1}{\gamma^2}\right)+\frac{4}{3}\frac{b^2}{\gamma^4}-\frac{4}{3}\frac{b^2}{\gamma^2}\Bigg\}+\frac{1}{x^2}\left(\frac{2}{3}\frac{\alpha^2}{\gamma^4}\right)+c_3\Bigg\{-\frac{1}{3}\left(\frac{2a_3}{\gamma^2}-\frac{2a_1}{\gamma^2}\right)^2+\frac{2}{3}\left(\frac{2a_1{}^2}{\gamma^2}-\frac{3a_1a_3}{\gamma^2}\right)\\
&-\frac{4}{3}\frac{b^2}{\gamma^2}+\frac{4}{3}\frac{b^2}{\gamma^4}-\frac{1}{x^2}\left(\frac{8}{3}\frac{\alpha^2}{\gamma^4}+\frac{3\alpha^2}{\gamma^2}\right)\Bigg\}\Bigg\rangle+\frac{r^2}{x^2}\Bigg\langle c_1\Bigg\{4\frac{b^2}{\gamma^2}-4\frac{b^2}{\gamma^4}\Bigg\}+c_2\Bigg\{-2\frac{b}{\gamma}\left(\frac{2a_3}{\gamma^2}-\frac{2a_1}{\gamma^2}\right)-4\frac{b^2}{\gamma^4}\Bigg\}\\
&+c_3\Bigg\{\left(\frac{2a_3}{\gamma^2}-\frac{2a_1}{\gamma^2}\right)^2-4\frac{b^2}{\gamma^4}\Bigg\}\Bigg\rangle+\frac{r^4}{x^4}\Bigg\langle c_1\Bigg\{-\frac{1}{3}\left(\frac{2a_1}{\gamma^2}-\frac{3a_3}{\gamma^2}\right)^2+\frac{4}{3}\frac{a_3}{\gamma^4}\left(\frac{2a_3}{\gamma^2}-\frac{2a_1}{\gamma^2}\right)-\frac{4}{3}\frac{b^2}{\gamma^6}+\frac{8}{3}\frac{b^2}{\gamma^4}\Bigg\}\\
&+c_2\Bigg\{-\frac{1}{3}\left(\frac{2a_1}{\gamma^2}-\frac{3a_3}{\gamma^2}\right)^2-\frac{2}{3}\frac{b}{\gamma^3}\left(\frac{2a_3}{\gamma^2}-\frac{2a_1}{\gamma^2}\right)-\frac{8}{3}\frac{a_3b}{\gamma^5}\Bigg\}+c_3\Bigg\{-\frac{1}{3}\left(\frac{2a_1}{\gamma^2}-\frac{3a_3}{\gamma^2}\right)^2+\frac{4}{3}\frac{a_3}{\gamma^4}\left(\frac{2a_3}{\gamma^2}-\frac{2a_1}{\gamma^2}\right)\\
&-\frac{4}{3}\frac{b^2}{\gamma^6}+\frac{8}{3}\frac{b^2}{\gamma^4}\Bigg\}\Bigg\rangle\Bigg]+\frac{r^4}{x^4}\Bigg\langle c_1\Bigg\{4\frac{b^2}{\gamma^6}-8\frac{b^2}{\gamma^4}\Bigg\}+c_2\Bigg\{2\frac{b}{\gamma}\left(\frac{4a_3}{\gamma^4}-\frac{2a_1}{\gamma^4}\right)+4\frac{b^2}{\gamma^6}\Bigg\}\\
&+c_3\Bigg\{-\frac{4a_3}{\gamma^4}\left(\frac{2a_3}{\gamma^2}-\frac{2a_1}{\gamma^2}\right)+4\frac{b^2}{\gamma^6}\Bigg\}\Bigg\rangle+\frac{2}{3}\frac{1}{x^2}\left(k_0+k_2\frac{r^2}{\gamma^2x^2}\right)\exp\left(-2\frac{r^2}{\gamma^2x^2}\right)
\end{aligned}
\tag{3.A2}
$$

$$
\begin{aligned}
\overline{u_\theta u_\theta}&=\Bigg\{-2\frac{b}{\gamma}\Bigg\}c_\mu\frac{k'^2}{\varepsilon'}\frac{1}{x^2}\exp\left(-2\frac{r^2}{\gamma^2x^2}\right)+c_\mu\frac{k'^3}{\varepsilon'^2}\frac{1}{x^2}\exp\left(-2\frac{r^2}{\gamma^2x^2}\right)\times\Big[(c_1+c_2+c_3)\\
&\left(\frac{1}{3}\frac{b^2}{\gamma^2}-\frac{1}{3}a_1{}^2\right)+(c_1-c_2+c_3)\frac{1}{x^2}\left(\frac{1}{3}\frac{\alpha^2}{\gamma^2}\right)+\frac{r^2}{x^2}\Bigg\langle c_1\Bigg\{-\frac{1}{3}\left(\frac{2a_3}{\gamma^2}-\frac{2a_1}{\gamma^2}\right)^2+\frac{2}{3}\left(\frac{2a_1{}^2}{\gamma^2}-\frac{3a_1a_3}{\gamma^2}\right)\\
&-\frac{4}{3}\frac{b^2}{\gamma^2}+\frac{4}{3}\frac{b^2}{\gamma^4}+\frac{1}{x^2}\left(\frac{4}{3}\frac{\alpha^2}{\gamma^4}-\frac{3\alpha^2}{\gamma^2}\right)\Bigg\}+c_2\Bigg\{\frac{2}{3}\left(\frac{2a_1{}^2}{\gamma^2}-\frac{3a_1a_3}{\gamma^2}\right)+\frac{4}{3}\frac{b}{\gamma}\left(\frac{2a_3}{\gamma^2}-\frac{2a_1}{\gamma^2}\right)+\frac{4}{3}\frac{b^2}{\gamma^4}-\frac{4}{3}\frac{b^2}{\gamma^2}\Bigg\}\\
&+\frac{1}{x^2}\left(\frac{2}{3}\frac{\alpha^2}{\gamma^4}\right)+c_3\Bigg\{-\frac{1}{3}\left(\frac{2a_3}{\gamma^2}-\frac{2a_1}{\gamma^2}\right)^2+\frac{2}{3}\left(\frac{2a_1{}^2}{\gamma^2}-\frac{3a_1a_3}{\gamma^2}\right)-\frac{4}{3}\frac{b^2}{\gamma^2}+\frac{4}{3}\frac{b^2}{\gamma^4}-\frac{1}{x^2}\left(\frac{8}{3}\frac{\alpha^2}{\gamma^4}+\frac{3\alpha^2}{\gamma^2}\right)\Bigg\}\Bigg\rangle\\
&+\frac{r^4}{x^4}\Bigg\langle c_1\Bigg\{-\frac{1}{3}\left(\frac{2a_1}{\gamma^2}-\frac{3a_3}{\gamma^2}\right)^2+\frac{4}{3}\frac{a_3}{\gamma^4}\left(\frac{2a_3}{\gamma^2}-\frac{2a_1}{\gamma^2}\right)-\frac{4}{3}\frac{b^2}{\gamma^6}+\frac{8}{3}\frac{b^2}{\gamma^4}\Bigg\}+c_2\Bigg\{-\frac{1}{3}\left(\frac{2a_1}{\gamma^2}-\frac{3a_3}{\gamma^2}\right)^2\\
&-\frac{2}{3}\frac{b}{\gamma^3}\left(\frac{2a_3}{\gamma^2}-\frac{2a_1}{\gamma^2}\right)-\frac{8}{3}\frac{a_3b}{\gamma^5}\Bigg\}+c_3\Bigg\{-\frac{1}{3}\left(\frac{2a_1}{\gamma^2}-\frac{3a_3}{\gamma^2}\right)^2+\frac{4}{3}\frac{a_3}{\gamma^4}\left(\frac{2a_3}{\gamma^2}-\frac{2a_1}{\gamma^2}\right)-\frac{4}{3}\frac{b^2}{\gamma^6}\\
&+\frac{8}{3}\frac{b^2}{\gamma^4}\Bigg\}\Bigg\rangle\Bigg]+\frac{2}{3}\frac{1}{x^2}\left(k_0+k_2\frac{r^2}{\gamma^2x^2}\right)\exp\left(-2\frac{r^2}{\gamma^2x^2}\right)
\end{aligned}
\tag{3.A3}
$$

The derived equation for the turbulent shear stress is as follows.

$$\begin{aligned}
\overline{u_x u_r} = {} & \Biggl\{\biggl(\frac{2a_1}{\gamma^2}-\frac{2a_3}{\gamma^2}+\frac{3b}{2\gamma}\biggr)\frac{r}{x}\Biggr\} c_\mu \frac{k'^2}{\varepsilon'}\frac{1}{x^2}\exp\biggl(-2\frac{r^2}{\gamma^2 x^2}\biggr)+c_\mu \frac{k'^3}{\varepsilon'^2}\frac{1}{x^2}\exp\biggl(-2\frac{r^2}{\gamma^2 x^2}\biggr) \\
& \times\Biggl[\frac{r}{x}\Biggl\langle c_1\Biggl\{\frac{b}{\gamma}\biggl(\frac{2a_3}{\gamma^2}-\frac{2a_1}{\gamma^2}+2a_1\biggr)+c_2\Biggl\{\frac{1}{2}\frac{b}{\gamma}\biggl(\frac{2a_3}{\gamma^2}-\frac{2a_1}{\gamma^2}\biggr)+\frac{a_1 b}{\gamma}-\frac{a_1}{2}\biggl(\frac{2a_3}{\gamma^2}-\frac{2a_1}{\gamma^2}\biggr)-\frac{b^2}{\gamma^2}+\biggl(\frac{3}{2}\frac{\alpha^2}{x^2\gamma^2}\biggr)\Biggr\} \\
& +c_3\Biggl\{-a_1\biggl(\frac{2a_3}{\gamma^2}-\frac{2a_1}{\gamma^2}\biggr)-2\frac{b^2}{\gamma^2}-3\frac{\alpha^2}{x^2\gamma^2}\Biggr\}\Biggr\rangle+\frac{r^3}{x^3}\Biggl\langle c_1\Biggl\{-2\frac{b}{\gamma}\biggl(\frac{3a_1}{\gamma^2}-\frac{3a_3}{\gamma^2}\biggr)-\frac{2a_3 b}{\gamma^5}-2\frac{b}{\gamma^3}\biggl(\frac{2a_3}{\gamma^2}-\frac{2a_1}{\gamma^2}\biggr)\Biggr\} \\
& +c_2\Biggl\{-\frac{b}{\gamma}\biggl(\frac{2a_1}{\gamma^2}-3\frac{a_3}{\gamma^2}\biggr)-\frac{a_1 b}{\gamma}-\frac{b}{\gamma^3}\biggl(\frac{2a_3}{\gamma^2}-\frac{2a_1}{\gamma^2}\biggr)\quad+\frac{1}{2}\biggl(\frac{2a_1}{\gamma^2}-\frac{3a_3}{\gamma^2}\biggr)\biggl(\frac{2a_3}{\gamma^2}-\frac{2a_1}{\gamma^2}\biggr)+\frac{a_1 a_3}{\gamma^4}+\frac{3b^2}{\gamma^4}\Biggr\} \\
& +c_3\Biggl\{\biggl(\frac{2a_1}{\gamma^2}-\frac{3a_3}{\gamma^2}\biggr)\biggl(\frac{2a_3}{\gamma^2}-\frac{2a_1}{\gamma^2}\biggr)+\frac{2a_1 a_3}{\gamma^4}+\frac{2b^2}{\gamma^4}\Biggr\}\Biggr\rangle\Biggr] \qquad (3.A4)
\end{aligned}$$

Here, $\varepsilon' = \left(\varepsilon_0 + \varepsilon_2 \frac{r^2}{\gamma^2 x^2}\right)$ and $k' = \left(k_0 + k_2 \frac{r^2}{\gamma^2 x^2}\right)$

3.7 References

1) Billiant, P., Chomaz J. M., Huerre, P., Experimenttal study of vortex breakdown in swirling jet, *J. Fluid Mech.,* 376, pp.183-219, 1998.

2) Fukushima, C., Aanen, L. and Westerweel, J., Investigation of the mixing process in an axisymmetric turbulent jet using PIV and LIF, *Proc. Int. Symp. on Application of Laser Techniques to Fluid Mechanics (Lisbon, Portugal)*, paper 11.1, July 10-13, 2000.

3) Gibson, M. M. and Younis, B. A., Calculation of swirling jets with a Reynolds stress model, *Phys. Fluids*, 29, pp.38-48, 1986.

4) Hosoda, T., Iwasa, Y. and Yokosi, S., Hydraulic analysis of turbulent jets by means of *k* - ε models, *Research Report no. 84-HY-01, School of Civil Engineering, Kyoto University*, Japan, 1984.

5) Jaw, S.Y. and Chen, C. J., Present status of second order closure turbulence models. I: overview, *J. Engg. Mech., ASCE*, 124, pp.485-501,1998.

6) Mcllwain, S. and Pollard, A., Large eddy simulation of the effects of mild swirl on the near

field of a round free jet, *Phys. Fluids*. 14, pp.653-661, 2002.

7) Panda, J. and Mclaughin, D. K., Experiments in the instabilities of a swirling jet, *Phys. Fluids.,* 6, pp.263-276, 1994.
8) Paschereit, C. O., Gutmark, K. E. and Weisenstein, W., Coherent structures in swirling flows and their role in acoustic combustion control, *Phys. Fluids.,* 11, pp.2667, 1999.
9) Pratte, B. D. and Keffer, J. F., The swirling turbulent jet, *J. Basic Engg., Trans. ASME*, pp. 739-748, 1972.
10) Ribeiro, M. M. and Whitelaw, J. H., Coaxial jets with and without swirl, *J. Fluid Mech.,* 96, pp.769-795, 1980.
11) Rajaratnam, N., *Turbulent Jets,* Elsevier scientific publishing company, 1976.
12) Rose, W. G., A swirling round turbulent jet, *J. Appl. Mech., Trans. ASME*, 29, pp.615-625, 1962.
13) Sami, S., Balance of turbulence energy in the region of jet flow establishment, *J. Fluid. Mech.*, 29, pp.81-92, 1967.
14) Wang, H. and Law, A. W. K., Second-order integral model for a round turbulent jet, *J. Fluid Mech*., 459, pp.397-428, 2002.
15) Wang, P., Bai, X. S., Wessman. M. and Klingmann, J., Large eddy simulation and experimental studies of a turbulent swirling jet, *Phys. Fluids*., 16, pp.3303-3324, 2004.
16) Wygnanski, I. and Fielder, H., Some measurements in the self-preserving jet, *J. Fluid Mech.*, 38, pp.577-612, 1969.

Chapter 4

SPATIAL DISTRIBUTION AND TOPOLOGICAL CHANGE OF TURBULENT STRUCTURES IN AN IDEALIZED VORTEX STREET

4.1 Introduction

The large scale vortical structures, also referred to as coherent structures, are an intrinsic feature of many turbulent flows. In turbulent shear flows, they play a vital role in the overall development of flow through the entrainment, mixing and momentum exchange between fast and slow speed fluids. Flows with large scale vortices caused by shear layer instability are often observed in many natural, geophysical as well as anthropogenic activities. From engineering application perspective, some examples are: turbulent jets, flow through hydraulic and flood control structures (e.g. barrages), flows past an obstacle such as bridge piers, flows behind spur/dykes, compound channel flows, open channel flows with vegetation zone or with an abrupt expansion, flows with side cavity or dead zones etc. Considering the importance of understanding the basics of vortical structures, the free shear flows has been given attention in numerous research efforts since the past decades (Brown & Roshko, 1974; Browand & Weidman, 1976; Hossain, 1986; Panides & Chevray, 1990). Hossain (1986) reviewed the studies of coherent structures in several free shear flows, and focused on the state of understanding from the view point of their spatial details of turbulence structures and dynamic significance.

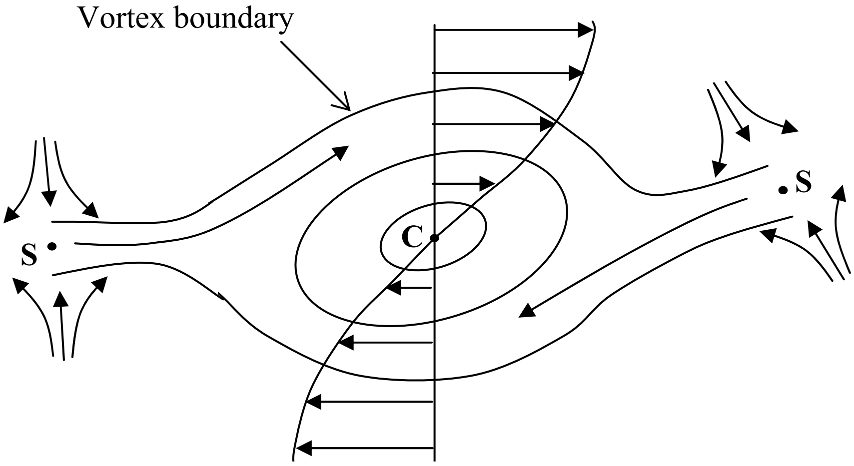

Fig. 4.1. Sketch of a coherent vortex in plane mixing layer

Fig. 4.1 shows an example of the span wise cut of coherent structure, in particular in the plane mixing layer (Hossain, 1986). The outer contour of coherent vorticity denotes the structure boundary. It shows that there are two critical points in the structure: the saddle (S) characterized by negligible spanwise vorticity, and the center of vortex (C) characterized by peak spanwise vorticity. Based on the experimental results on turbulent structures of a plane shear layer, Hossain (1986) reported that the structures of turbulent normal stresses at vortex point are elliptical in shape; on the other hand, the turbulent shear stresses show hyperbolic profile. The same patterns are also confirmed in further studies with turbulent axisymmetric jets and wakes.

It is reported that the standard k–ε model cannot produce satisfactory results for the flow field having high rate of strain and rotation because of its isotropic assumption of eddy viscosity (Rodi, 1979). On the other hand, a non-linear model predicts superior result by capturing the anisotropic turbulence. It is reported that the generation of coherent vortices in a shear layer is influenced by the functional form of c_μ. For compound channel, it is observed that the flow resistance in the channel is influenced by this function (chapter 5). Since this type of model has been using in calculating many turbulent flows that contain vorticity in the flow field, it is worth to examine the model's applicability to predict the spatial details of turbulent structures in an idealized vortex street.

In this chapter, an approximate solution is derived for turbulent characteristics of an ideal vortex street. The Stuart vortex, which contains both vortex and saddle patterns in its vorticity contour, is considered for this analysis. The aim is to explore the model applicability to large scale vortices, and to investigate the spatial distribution and topological change of turbulent structures with singular points. The turbulent structures are also compared with the previous experimental results of free shear flows.

4.2 Governing Equations

The equations for standard and 2nd order non-linear k–ε model are rewritten as follows :

Continuity equation: $$\frac{\partial U_i}{\partial x_i} = 0 \tag{4.1}$$

Momentum equation: $$\frac{\partial U_i}{\partial t} + \frac{\partial U_j U_i}{\partial x_j} = g_i - \frac{1}{\rho}\frac{\partial P}{\partial x_i} + \frac{\partial}{\partial x_j}\left(-\overline{u_i u_j}\right) + \nu \frac{\partial^2 U_i}{\partial {x_j}^2} \tag{4.2}$$

k - equation: $$\frac{\partial k}{\partial t} + \frac{\partial k U_j}{\partial x_j} = -\overline{u_i u_j}\frac{\partial U_i}{\partial x_j} + \frac{\partial}{\partial x_j}\left\{\left(\frac{\nu_t}{\sigma_k} + \nu\right)\frac{\partial k}{\partial x_j}\right\} - \varepsilon \tag{4.3}$$

ε - equation: $$\frac{\partial \varepsilon}{\partial t} + \frac{\partial \varepsilon U_j}{\partial x_j} = -c_{\varepsilon 1}\frac{\varepsilon}{k}\overline{u_i u_j}\frac{\partial U_i}{\partial x_j} + \frac{\partial}{\partial x_j}\left\{\left(\frac{\nu_t}{\sigma_\varepsilon} + \nu\right)\frac{\partial \varepsilon}{\partial x_j}\right\} - c_{\varepsilon 2}\frac{\varepsilon^2}{k} \tag{4.4}$$

Turbulence model (linear): $$-\overline{u_i u_j} = \nu_t S_{ij} - \frac{2}{3}k\delta_{ij}\,,\ \nu_t = c_\mu \frac{k^2}{\varepsilon}\,,\ c_\mu{=}0.09 \tag{4.5}$$

Turbulence model (Non-linear): $$-\overline{u_i u_j} = \nu_t S_{ij} - \frac{2}{3}k\delta_{ij} - \frac{k}{\varepsilon}\nu_t \sum_{\beta=1}^{3} c_\beta \left(S_{\beta ij} - \frac{1}{3}S_{\beta\alpha\alpha}\delta_{ij}\right) \tag{4.6}$$

Here,

$$\nu_t = c_\mu \frac{k^2}{\varepsilon},\ \ S_{ij} = \frac{\partial U_i}{\partial x_j} + \frac{\partial U_j}{\partial x_i},\ \ \Omega_{ij} = \frac{\partial U_i}{\partial x_j} - \frac{\partial U_j}{\partial x_i}, S = \frac{k}{\varepsilon}\sqrt{\frac{1}{2}S_{ij}S_{ij}}\,, \Omega = \frac{k}{\varepsilon}\sqrt{\frac{1}{2}\Omega_{ij}\Omega_{ij}} \tag{4.7}$$

In Equation (4.6),

$$S_{1ij}=\frac{\partial U_i}{\partial x_\gamma}\frac{\partial U_j}{\partial x_\gamma},\quad S_{2ij}=\frac{1}{2}\left(\frac{\partial U_\gamma}{\partial x_i}\frac{\partial U_j}{\partial x_\gamma}+\frac{\partial U_\gamma}{\partial x_j}\frac{\partial U_i}{\partial x_\gamma}\right),\quad S_{3ij}=\frac{\partial U_\gamma}{\partial x_i}\frac{\partial U_\gamma}{\partial x_j}. \tag{4.8}$$

$$c_\mu=\frac{c_{\mu o}\,(1+c_{ns}S^2+c_{n\Omega}\Omega^2)}{1+c_{ds}S^2+c_{d\Omega}\Omega^2+c_{ds\Omega}S\Omega+c_{ds1}S^4+c_{d\Omega 1}\Omega^4+c_{ds\Omega 1}S^2\Omega^2} \tag{4.9}$$

$$c_\beta=c_{\beta o}\frac{1}{1+m_{ds}S^2+m_{d\Omega}\Omega^2} \tag{4.10}$$

Here, σ_k= 1.0, σ_ε= 1.3, $c_{\varepsilon 1}$ = 1.44 $c_{\varepsilon 2}$ = 1.92, c_{10}=0.40, c_{20}=0.0 and c_{30}= -0.13, have their standard values.

Table 4.1 shows two sets of model constants. The value of model constants determined in previous chapter are given in Run-1. Run-2 shows a set of trial values that will be used to investigate the sensitivity of empirical functions to the structural change of turbulent properties in the vortex point (focus).

Table 4.1 Estimated and trial values of model constants

Model Const.	$c_{\mu 0}$	c_{ns}	$c_{n\Omega}$	c_{ds}	$c_{ds\Omega}$	$c_{d\Omega}$	c_{ds1}	$c_{d\Omega 1}$	$c_{ds\Omega 1}$	m_{ds}	$m_{d\Omega}$
Run-1	0.09	0.005	0.0068	0.008	-0.003	0.004	0.00005	0.00005	0.00025	0.01	0.003
Run-2	0.09	0.01	0.007	0.008	-0.003	0.004	0.00005	0.00005	0.00025	0.01	0.003

4.3 Methods of Investigations

4.3.1 Stuart vortices

The stream function of Stuart vortex can be expressed as follows:

$$\psi=\log(\cosh y+A\ \cos x) \tag{4.11}$$

here, $0 \geq A \geq -1$ is a constant and indicates the eccentricity of the elliptic streamline of the vortex. If $A=0$, the hyperbolic-tangent mixing layer is recovered; whereas $A=-1$ shows a single row of co-rotating vortices, with circulation of *-4*π, periodically spaced along the x axis with a period of *2*π. Fig. 4.2 shows the streamlines of Stuart vortices with various values of A.

In this study, we examine the Stuart vortex as a simple model of Vortex Street. Eq. (4.11) is substituted into k–ε equations to derive the spatial distributions of turbulent intensities. Although Stuart vortex is a solution of Euler equation, it is shown that the turbulence can be generated in the fixed flow field of the vortex. A moderate eccentricity of A=- *0.5* is used to calculate the turbulent characteristics of the vortex at vortex center and saddle point.

4.3.2 Approximations solution

For the approximate analysis of Stuart vortices, the viscous shear stress is assumed much smaller than the turbulent shear stress. Therefore, the k and ε equations [Eqs. (4.3) and (4.4)] can be simplified for a steady 2-D flow in the following forms.

k - equation:

$$U_x \frac{\partial k}{\partial x} + U_y \frac{\partial k}{\partial y} = -\overline{u_x u_x}\frac{\partial U_x}{\partial x} - \overline{u_x u_y}\frac{\partial U_x}{\partial y} - \overline{u_y u_x}\frac{\partial U_y}{\partial x} - \overline{u_y u_y}\frac{\partial U_y}{\partial y} + \frac{\partial}{\partial y}\left(\frac{\nu_t}{\sigma_k}\frac{\partial k}{\partial y}\right) + \frac{\partial}{\partial x}\left(\frac{\nu_t}{\sigma_k}\frac{\partial k}{\partial x}\right) - \varepsilon \tag{4.12}$$

ε - equation:

$$U_x \frac{\partial \varepsilon}{\partial x} + U_y \frac{\partial \varepsilon}{\partial y} = c_{\varepsilon 1}\frac{\varepsilon}{k}\left[-\overline{u_x u_x}\frac{\partial U_x}{\partial x} - \overline{u_x u_y}\frac{\partial U_x}{\partial y} - \overline{u_y u_x}\frac{\partial U_y}{\partial x} - \overline{u_y u_y}\frac{\partial U_y}{\partial y}\right] + \frac{\partial}{\partial y}\left(\frac{\nu_t}{\sigma_\varepsilon}\frac{\partial k}{\partial y}\right)$$

$$+\frac{\partial}{\partial x}\left(\frac{\nu_t}{\sigma_\varepsilon}\frac{\partial k}{\partial x}\right) - c_{\varepsilon 2}\frac{\varepsilon^2}{k} \tag{4.13}$$

Here, the Reynolds stresses are determined using the constitutive equations of the turbulence model.

Two separate solutions are derived for turbulent characteristics at vortex center and saddle point using the stream-function of Stuart vortex to investigate the spatial distribution of turbulent structures in a large-scale vortex. The stream function of Stuart vortex is expanded using the

Taylor's function, near the origin (0, 0) and at a periodic distance of (π, 0), for the flow field of vortex center and saddle point respectively. The functional forms of k and ε distributions are assumed as a first approximation. Substituting the assumed distributions into the non-linear k and ε equations, a set of algebraic equations are derived considering the relation among the coefficients with respect to the same power of variables (x and y). Solving these simultaneous algebraic equations, the unknown coefficients in the assumed distributions are determined as the function of the non-linear k–ε model constants. The distributions of turbulent stresses for vortex and saddle points are derived using the constitutive equations of the model. The turbulent structures are compared to previous experiments of large scale coherent vortices in free shear flows reported by Hossain (1986).

4.3.3 Numerical simulation

Using the model constants estimated by approximate solution, the numerical simulation is carried out to determine the turbulent characteristics of Stuart vortices, and the structures are compared with approximate solution.

The flow field of Stuart vortices is given as input to calculate the turbulent characteristics. The code solves the k, ε and constitutive equations discretized with the finite volume method. The hybrid central upwind scheme is used for k and ε equations. Time advancement is achieved by Adam-Bashforth scheme of second-order accuracy, in each equation. The equations are discretized as fully explicit forms and solved successively with the time increment step by step. The wall functions are employed as the wall boundary conditions for k and ε. Periodic boundary conditions are used in upstream and downstream ends of the flow domain.

4.4 Turbulent Structures at Vortex Center (Focus)

4.4.1 Approximate solution

The equation of Stuart vortex expressed in Eq. (4.11) is expanded using Taylor function near the origin, and the approximated stream function for the vortex point is expressed as follows (eccentricity, A=- 0.5 is used):

$$\psi = \ln\left(1/2\right) + \frac{1}{2}x^2 + y^2 - \frac{1}{6}x^4 - \frac{1}{2}x^2y^2 - \frac{5}{12}y^4 + \ldots\ldots\ldots \tag{4.14}$$

The corresponding velocity field is approximated as

$$U_x = \frac{\partial \psi}{\partial y} = 2y - x^2y - \frac{5}{3}y^3 \tag{4.15}$$

$$U_y = -\frac{\partial \psi}{\partial x} = -x + xy^2 + \frac{2}{3}x^3 \tag{4.16}$$

The contour of streamlines for vortex point approximated by Taylor function near the origin (Eq. 4.14) is shown in Fig. 4.3.

As a first approximation, the following polynomial functional forms are assumed for the distributions of k and ε

$$k = k_{00} + k_{01}x + k_{10}y + +k_{02}x^2 + k_{20}y^2 + k_{11}xy \tag{4.17}$$

$$\varepsilon = \varepsilon_{00} + \varepsilon_{01}x + \varepsilon_{10}y + +\varepsilon_{02}x^2 + \varepsilon_{20}y^2 + \varepsilon_{11}xy \tag{4.18}$$

where, $k_{00}, k_{01}, k_{10}, k_{02}, k_{20}, k_{11}$ are the unknown coefficients for k; and $\varepsilon_{00}, \varepsilon_{01}, \varepsilon_{10}, \varepsilon_{02}, \varepsilon_{20}, \varepsilon_{11}$ are that for ε distributions respectively.

Substituting the assumed k and ε distributions [Eqs. (4.17) and (4.18)], into k–ε equations [Eqs. (4.12) and (4.13)], the following algebraic expressions are derived considering the relations of coefficients for the same power of variables (x, y) in each equation. To avoid complexity in solving a large number of equations, the higher order terms of k_{01}, k_{10}, k_{02}, k_{20}, k_{11}, ε_{01}, ε_{10}, ε_{02}, ε_{20} and ε_{11} are neglected to form a set of linear equations.

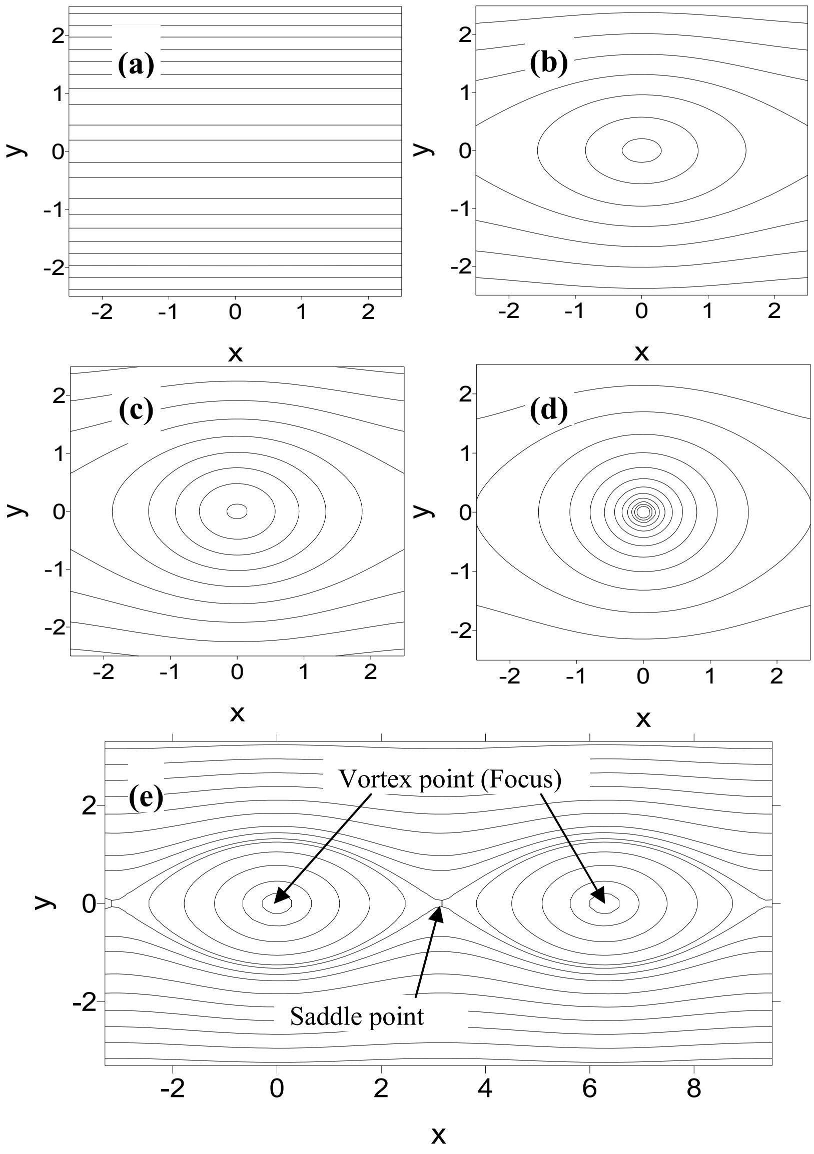

Fig. 4.2 Contour of streamlines for Stuart vortex with different eccentricity: (a) A=0 (b) A=-1/2 (c) A=-3/4 (d) A=-1.0 (e) two vortices with A=-1/2

k-equation:

$$0: \quad c_{\mu_0} k_{00}^2 (1)_0 - (2)_0 + \frac{c_{\mu_0}}{\sigma_k} k_{00}^2 \{2k_{02} + 2k_{20}\}(1)_0 = 0 \tag{4.19}$$

$$x: \quad -k_{10} = A_f k_{01} + B_f \varepsilon_{01} \tag{4.20}$$

$$y: \quad 2k_{01} = A_f k_{10} + B_f \varepsilon_{10} \tag{4.21}$$

$$x^2: \quad -k_{11} = A_f k_{02} + B_f \varepsilon_{02} + C_{f5}\left(k_{02} + k_{20}\right) + C_{f1} \tag{4.22}$$

$$y^2: \quad 2k_{11} = A_f k_{20} + B_f \varepsilon_{20} - C_{f_6}\left(k_{02} + k_{20}\right) + C_{f2} \tag{4.23}$$

$$xy: \quad 4k_{02} - 2k_{20} = A_f k_{11} + B_f \varepsilon_{11} \tag{4.24}$$

<u>ε -equation</u>:

$$0: \quad c_{\varepsilon_1} c_{\mu_0} k_{00}^2 \varepsilon_{00}^2 (1)_0 - c_{\varepsilon_2} \varepsilon_{00}^2 (2)_0 + \frac{c_{\mu_0}}{\sigma_\varepsilon} k_{00}^3 \left\{2k_{02} + 2k_{20}\right\}(1)_0 = 0 \tag{4.25}$$

$$x: \quad -\varepsilon_{10} = C_f k_{01} + D_f \varepsilon_{01} \tag{4.26}$$

$$y: \quad 2\varepsilon_{01} = C_f k_{10} + D_f \varepsilon_{10} \tag{4.27}$$

$$x^2: \quad -\varepsilon_{11} = C_f k_{02} + D_f \varepsilon_{02} + C_{f_7}\left(\varepsilon_{02} + \varepsilon_{20}\right) + C_{f3} \tag{4.28}$$

$$y^2: \quad 2\varepsilon_{11} = C_f k_{20} + D_f \varepsilon_{20} - C_{f8}\left(\varepsilon_{02} + \varepsilon_{20}\right) + C_{f4} \tag{4.29}$$

$$xy: \quad 4\varepsilon_{02} - 2\varepsilon_{20} = C_f k_{11} + D_f \varepsilon_{11} \tag{4.30}$$

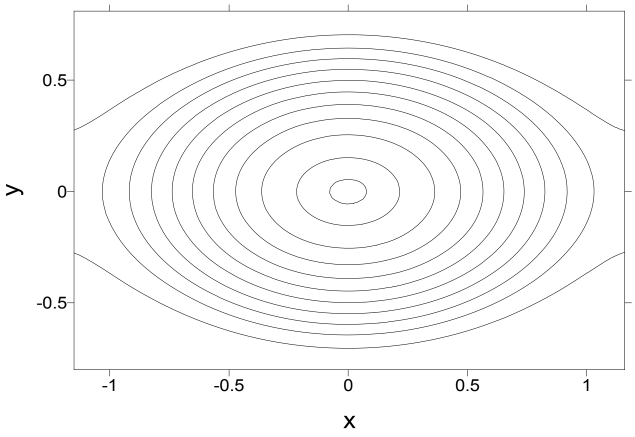

Fig. 4.3 Streamline contour at vortex center (focus) of Stuart vortex approximated by Taylor function

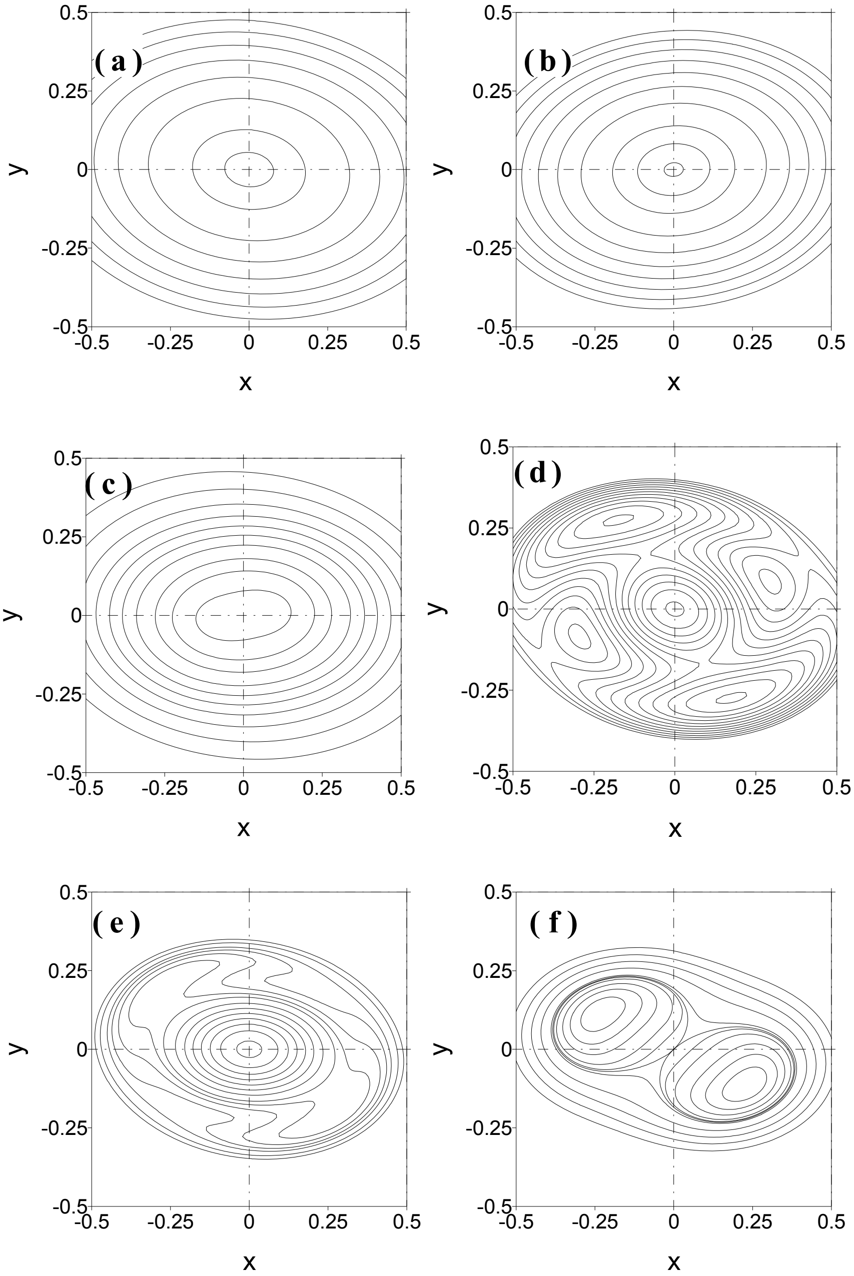

Fig. 4.4 Turbulent structures by approximate solution for vortex point (Run-1): (a) turbulent kinetic energy, k (b) turbulent energy dissipation rate, ε (c) turbulent normal stress in x direction, $\overline{u_1 u_1}$ (d) turbulent normal stress in y direction, $\overline{u_2 u_2}$ (e) turbulent normal stress in z direction, $\overline{u_3 u_3}$ (f) turbulent shear stress in xy plane, $\overline{u_1 u_2}$

Here,

$$\begin{aligned}A_f =& \big[c_{\mu_0}\varepsilon_{00}k_{00}^3\{(1)_0(2m_{ds}+18m_{d\Omega})+(4)_0(2c_{ns}+18c_{n\Omega})\}+2c_{\mu_0}\varepsilon_{00}k_{00}(1)_0(4)_0\\ &-\varepsilon_{00}k_{00}(2)_0(2m_{ds}+18m_{d\Omega})-\varepsilon_{00}k_{00}(4)_0\{\varepsilon_{00}^2(2c_{ds}+6c_{ds\Omega}+18c_{d\Omega})\\ &+4k_{00}^2(c_{ds1}+9c_{ds\Omega 1}+81c_{d\Omega 1})\}\big]/\{(2)_0(4)_0\}\end{aligned}$$

$$\begin{aligned}B_f =& \big[2c_{\mu_0}\varepsilon_{00}^2k_{00}^2\{(1)_0+(4)_0\}+c_{\mu_0}k_{00}^2(1)_0(4)_0-\{2(2)_0\varepsilon_{00}^2+4\varepsilon_{00}^4(4)_0\\ &+\varepsilon_{00}^2k_{00}^2(4)_0(2c_{ds}+6c_{ds\Omega}+18c_{d\Omega})+(2)_0(4)_0\}\big]/\{(2)_0(4)_0\}\end{aligned}$$

$$\begin{aligned}C_f =& \big[c_{\mu_0}c_{\varepsilon_1}\varepsilon_{00}^2k_{00}^3\{(1)_0(2m_{ds}+18m_{d\Omega})+(4)_0(2c_{ns}+18c_{n\Omega})\}+2c_{\mu_0}c_{\varepsilon_1}\varepsilon_{00}^2k_{00}(1)_0(4)_0\\ &-c_{\varepsilon_2}\varepsilon_{00}^2k_{00}(2)_0(2m_{ds}+18m_{d\Omega})-c_{\varepsilon_2}\varepsilon_{00}^2k_{00}(4)_0\{\varepsilon_{00}^2(2c_{ds}+6c_{ds\Omega}+18c_{d\Omega})\\ &+4k_{00}^2(c_{ds1}+9c_{ds\Omega 1}+81c_{d\Omega 1})\}\big]/\{(2)_0(4)_0k_{00}\}\end{aligned}$$

$$\begin{aligned}D_f =& \big[2c_{\mu_0}c_{\varepsilon_1}\varepsilon_{00}^3k_{00}^2\{(1)_0+(4)_0\}+2c_{\mu_0}c_{\varepsilon_1}\varepsilon_{00}k_{00}^2(1)_0(4)_0-c_{\varepsilon_2}\{2(2)_0\varepsilon_{00}^3+4\varepsilon_{00}^5(4)_0\\ &+\varepsilon_{00}^3k_{00}^2(4)_0(2c_{ds}+6c_{ds\Omega}+18c_{d\Omega})+2\varepsilon_{00}(2)_0(4)_0\}\big]/\{(2)_0(4)_0k_{00}\}\end{aligned}$$

$$\begin{aligned}C_{f1} =& \big[-\varepsilon_{00}k_{00}^2\{(2)_0(2m_{ds}-18m_{d\Omega})+\varepsilon_{00}^2(4)_0(2c_{ds}-18c_{d\Omega})\}+2c_{\mu_0}\varepsilon_{00}k_{00}^2(1)_0(4)_0\\ &+c_{\mu_0}\varepsilon_{00}k_{00}^4(1)_0(2m_{ds}-18m_{d\Omega})+\varepsilon_{00}k_{00}^4(4)_0\{c_{\mu_0}(2c_{ns}-18c_{n\Omega})-4(c_{ds1}-81c_{d\Omega 1})\}\big]/\{(2)_0(4)_0\}\end{aligned}$$

$$\begin{aligned}C_{f2} =& \big[-\varepsilon_{00}k_{00}^2\{(2)_0(-8m_{ds}-36m_{d\Omega})-\varepsilon_{00}^2(4)_0(8c_{ds}+36c_{d\Omega}+18c_{ds\Omega})\}-8c_{\mu_0}\varepsilon_{00}k_{00}^2(1)_0(4)_0\\ &+c_{\mu_0}\varepsilon_{00}k_{00}^4(1)_0(-8m_{ds}-36m_{d\Omega})+\varepsilon_{00}k_{00}^4(4)_0\{c_{\mu_0}(-8c_{ns}-36c_{n\Omega})\\ &+4(4c_{ds1}+162c_{d\Omega 1}+27c_{ds\Omega 1})\}\big]/\{(2)_0(4)_0\}\end{aligned}$$

$$\begin{aligned}C_{f3} =& \big[-c_{\varepsilon_2}\varepsilon_{00}^2k_{00}^2\{(2)_0(2m_{ds}-18m_{d\Omega})+\varepsilon_{00}^2(4)_0(2c_{ds}-18c_{ds\Omega})\}+2c_{\mu_0}c_{\varepsilon_1}\varepsilon_{00}^2k_{00}^2(1)_0(4)_0\\ &+c_{\mu_0}c_{\varepsilon_1}\varepsilon_{00}^2k_{00}^4(1)_0(2m_{ds}-18m_{d\Omega})+\varepsilon_{00}^2k_{00}^4(4)_0\{c_{\varepsilon_1}c_{\mu_0}(2c_{ns}-18c_{n\Omega})\\ &-4c_{\varepsilon_2}(c_{ds1}-81c_{d\Omega 1})\}\big]/\{(2)_0(4)_0\}\end{aligned}$$

$$\begin{aligned}C_{f4} =& \big[-c_{\varepsilon_2}\varepsilon_{00}^2k_{00}^2\{(2)_0(-8m_{ds}-36m_{d\Omega})-\varepsilon_{00}^2(4)_0(8c_{ds}+36c_{d\Omega}+18c_{ds\Omega})\}\\ &-8c_{\mu_0}c_{\varepsilon_1}\varepsilon_{00}^2k_{00}^2(1)_0(4)_0+c_{\mu_0}c_{\varepsilon_1}\varepsilon_{00}^2k_{00}^4(1)_0(-8m_{ds}-36m_{d\Omega})\\ &+\varepsilon_{00}^2k_{00}^4(4)_0\{c_{\mu_0}c_{\varepsilon_1}(-8c_{ns}-36c_{n\Omega})+4c_{\varepsilon_2}(4c_{ds1}+162c_{d\Omega 1}+27c_{ds\Omega 1})\}\big]/\{(2)_0(4)_0k_{00}\}\end{aligned}$$

$$C_{f5} = \left[\frac{2c_{\mu_0}}{\sigma_k} \varepsilon_{00} k_{00}^4 \left\{ (1)_0 \left(2m_{ds} - 18m_{d\Omega} \right) + (4)_0 \left(2c_{ns} - 18c_{n\Omega} \right) \right\} \right] \Big/ \left\{ (2)_0 (4)_0 \right\}$$

$$C_{f6} = \left[\frac{2c_{\mu_0}}{\sigma_k} \varepsilon_{00} k_{00}^4 \left\{ (1)_0 \left(8m_{ds} + 36m_{d\Omega} \right) + (4)_0 \left(8c_{ns} + 36c_{n\Omega} \right) \right\} \right] \Big/ \left\{ (2)_0 (4)_0 \right\}$$

$$C_{f7} = \left[\frac{2c_{\mu_0}}{\sigma_\varepsilon} \varepsilon_{00} k_{00}^4 \left\{ (1)_0 \left(2m_{ds} - 18m_{d\Omega} \right) + (4)_0 \left(2c_{ns} - 18c_{n\Omega} \right) \right\} \right] \Big/ \left\{ (2)_0 (4)_0 \right\}$$

$$C_{f8} = \left[\frac{2c_{\mu_0}}{\sigma_\varepsilon} \varepsilon_{00} k_{00}^4 \left\{ (1)_0 \left(8m_{ds} + 36m_{d\Omega} \right) + (4)_0 \left(8c_{ns} + 36c_{n\Omega} \right) \right\} \right] \Big/ \left\{ (2)_0 (4)_0 \right\}$$

$$(1)_0 = \varepsilon_{00}^2 + c_{ns} k_{00}^2 + 9c_{n\Omega} k_{00}^2$$

$$(2)_0 = \varepsilon_{00}^2 \left(\varepsilon_{00}^2 + c_{ds} k_{00}^2 + 3c_{ds\Omega} k_{00}^2 + 9c_{d\Omega} k_{00}^2 \right) + k_{00}^4 \left(c_{ds1} + 9c_{ds\Omega 1} + 81c_{d\Omega 1} \right)$$

$$(4)_0 = \varepsilon_{00}^2 + m_{ds} k_{00}^2 + 9m_{d\Omega} k_{00}^2$$

Solving the twelve equations from Eqs. (4.19) to (4.30), twelve unknowns are determined in terms of model constants. Substituting the obtained values of unknown coefficients into Eqs. (4.17) and (4.18), the k and ε profiles are calculated. The distributions of turbulent intensities and shear stresses are obtained by constitutive equations.

Figure 4.4 shows the turbulent structures at the center of vortex determined by approximate solution using the model constants of Run-1. It is observed that, the profiles for turbulent kinetic energy (k), dissipation rate (ε) [Figs. (a) and (b)] as well as the turbulent normal stresses in x, y and z directions (expressed as $\overline{u_1 u_1}$, $\overline{u_2 u_2}$, $\overline{u_3 u_3}$ and shown in Figs. (c), (d) and (e) respectively) show elliptical structures. On the other hand, the turbulent shear stress in xy plane ($\overline{u_1 u_2}$) shows hyperbolic (saddle pattern) profile [Fig. (f)] . These features of turbulent structures at the center of vortex are consistent with the previous experimental results reported for free shear flows.

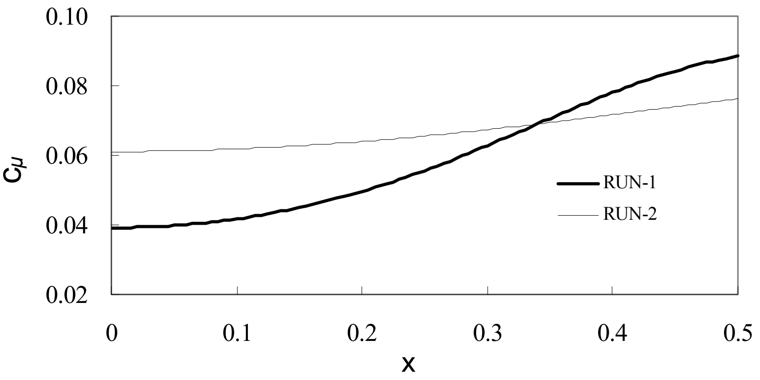

Fig. 4.5 Profiles of c_μ (S, Ω) in the vortex field for Run-1 and Run-2.

The model constants for Run-2 are a trial set of model constants to investigate the influence of functional form of c_μ on turbulent structures at the vortex center. The variation of c_μ between two sets of model constants, plotted against the spatial distance from vortex center (*x*), is shown in Fig. 4.5. Fig. 4.6 shows the turbulent structures at vortex center predicted by Run-2. It is found that the turbulent kinetic energy (*k*), and turbulent intensities, $\overline{u_1 u_1}$ and $\overline{u_2 u_2}$, show hyperbolic profile instead of elliptical structures. This means that Run-2 failed to predict the actual turbulent structures that are observed in the previous experimental studies. By comparing the results for two sets of model constants, it can be concluded that the turbulent structures in a vortex is sensitive to the functional form of c_μ.

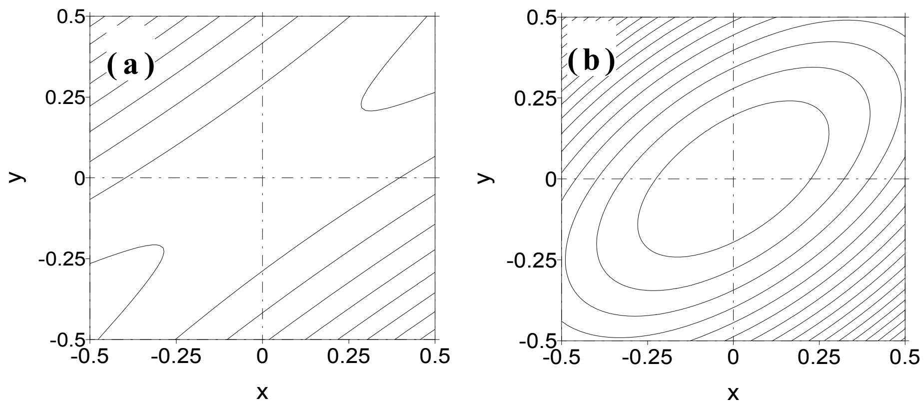

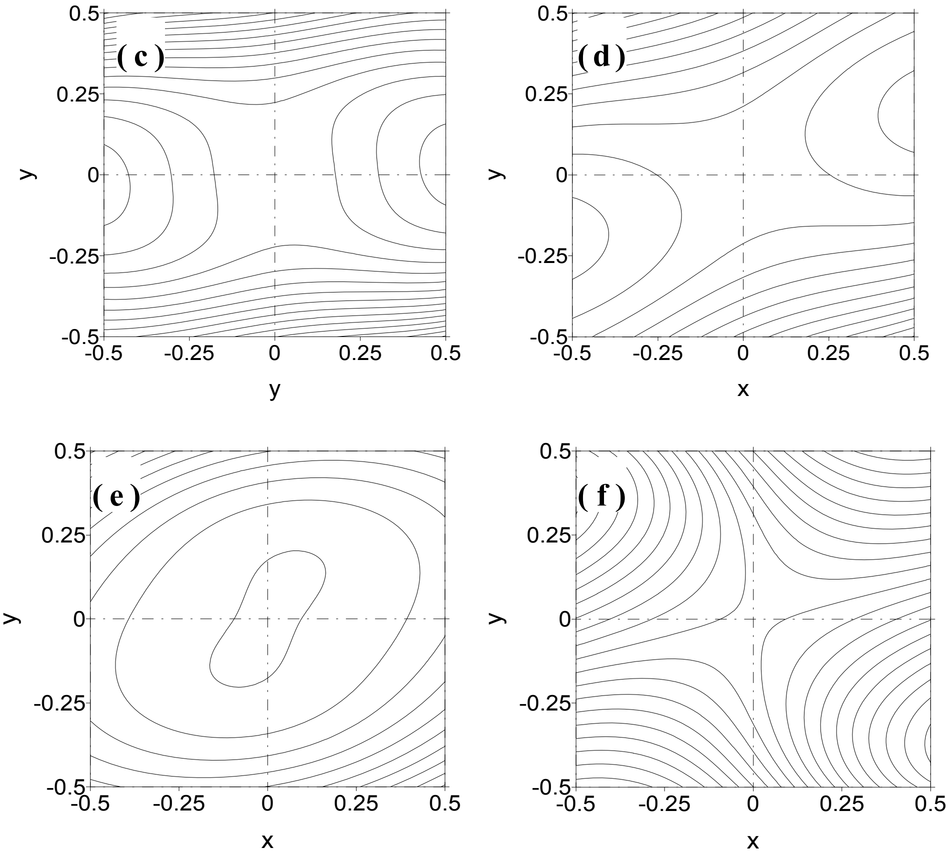

Fig. 4.6 Turbulent structures by approximate solution for vortex point (Run-2): (a) turbulent kinetic energy, k (b) turbulent energy dissipation rate, ε (c) turbulent normal stress in x direction, $\overline{u_1u_1}$ (d) turbulent normal stress in y direction, $\overline{u_2u_2}$ (e) turbulent normal stress in z direction, $\overline{u_3u_3}$ (f) turbulent shear stress in xy plane, $\overline{u_1u_2}$

4.4.2 Numerical simulation

In the previous section, approximate solutions are derived for the vortex point and the turbulent characteristics are predicted. In this section, numerical simulations are carried out for the same flow field, and the results are compared to approximate solution to assess the effectiveness of the approximate approach.

The equation of actual Stuart vortex expressed in Eq. (4.11) gives the following velocity field.

$$U_x = \frac{\partial \psi}{\partial y} = \frac{\sinh y}{\cosh y + A\cos x} \tag{4.31}$$

$$U_y = -\frac{\partial \psi}{\partial x} = \frac{A\sin x}{\cosh y + A\cos x} \tag{4.32}$$

For this velocity field, the turbulent stresses as well as k and ε profiles are determined. As shown in Fig. 4.2(e), two vortices are considered in the flow domain with a periodic boundary condition at upstream and downstream end.

The periodic turbulent structures simulated for Run-1 are shown in Fig. 4.7. Turbulent kinetic energy (k), its dissipation rate (ε) and turbulent normal stresses in x, y and z directions (expressed as $\overline{u_1u_1}$,$\overline{u_2u_2}$ and $\overline{u_3u_3}$ respectively) are showing the contours in elliptical shape at the vortex center. On the other hand, the turbulent shear stress in xy plane ($\overline{u_1u_2}$) is showing hyperbolic profile (saddle pattern). The results satisfy the approximate solution, and prove that the conditions derived for the constitutive law with the estimated model constants are applicable to simulate large scale vortices.

In the approximate solution it is shown that, the turbulent structure is changed with the change of the values of model constants; the evidence is also presented using the model constants of Run-2. The simulation results for Run-2 are presented in Fig. 4.8. Considering turbulent kinetic energy and turbulent normal stresses as shown in Fig. 4.8 (a), (c) and (d), the hyperbolic profiles (saddle pattern) are observed instead of elliptical one. The results of numerical simulation fully satisfy the approximate solution.

Figure 4.5 shows that at the center of vortex, where the strain and rotation parameters are large, the value of c_μ is less than 1/2 of its far field value. However, in the standard k-ε model, the coefficient c_μ has no dependency on the rate of strain and rotation, and bears a constant value (=0.09) throughout the turbulent flow field. This deficiency of standard k-ε model causes an inconsistent prediction of turbulent structures at the center of vortex. Fig. 4.9 shows the results simulated by standard k-ε model. The model failed to generate the elliptical structures (focus pattern) for *k,* ε and turbulent normal stresses. The result is consistent with Run-2 (Figs. 4.6 and 4.8), where the value of c_μ is not sufficient to count the effect of strain and rotation rates.

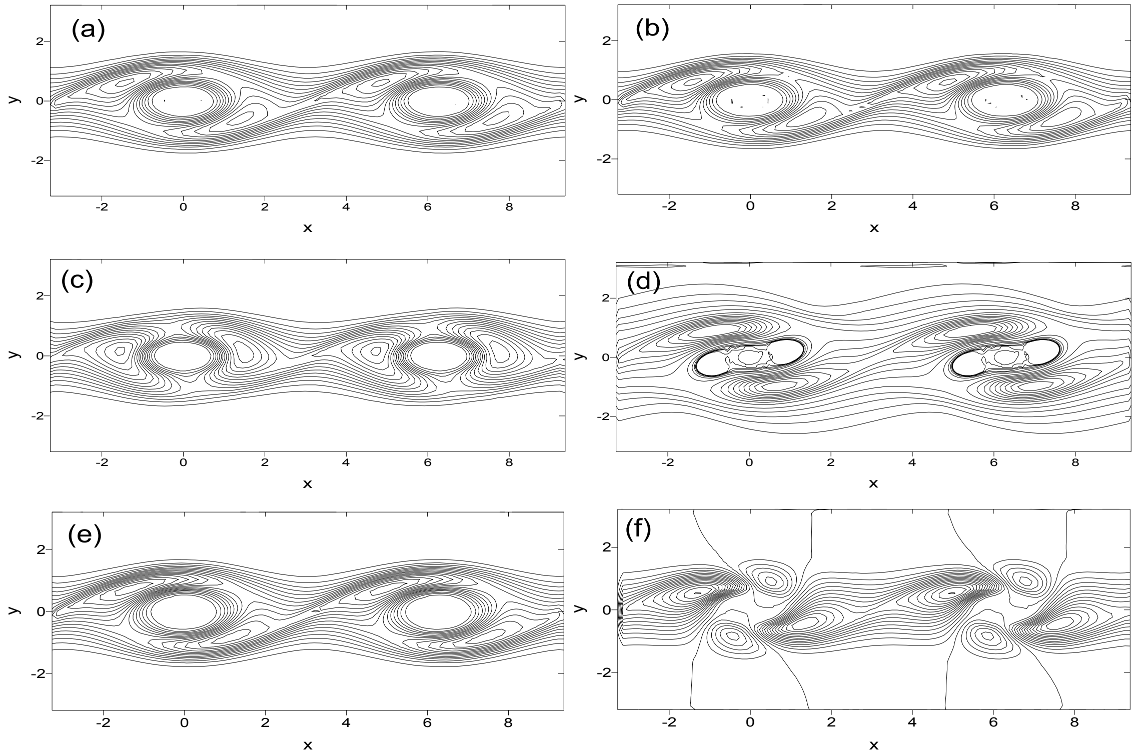

Fig. 4.7 Turbulent structures by numerical simulation (Run-1): (a) turbulent kinetic energy, *k* (b) turbulent energy dissipation rate, ε (c) turbulent normal stress in *x* direction, $\overline{u_1 u_1}$ (d) turbulent normal stress in *y* direction, $\overline{u_2 u_2}$ (e) turbulent normal stress in *z* direction, $\overline{u_3 u_3}$ (f) turbulent shear stress in *xy* plane, $\overline{u_1 u_2}$

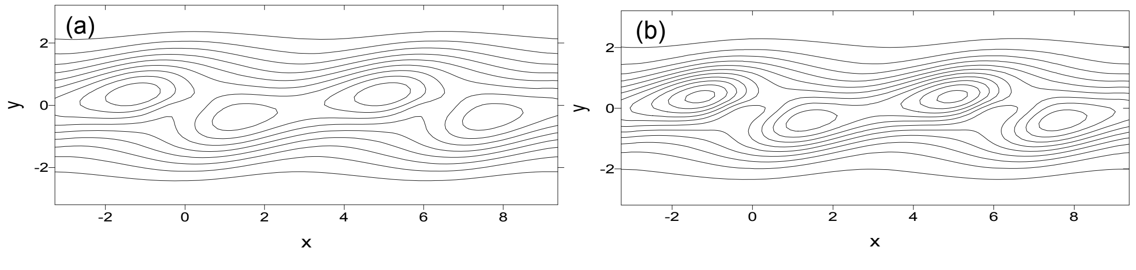

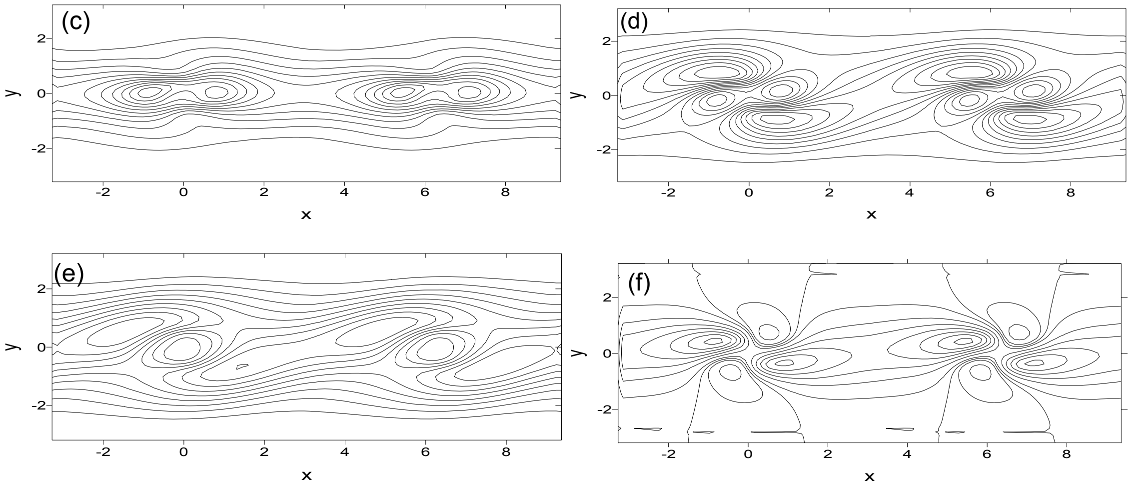

Fig. 4.8 Turbulent structures by numerical simulation (Run-2): (a) turbulent kinetic energy, *k* (b) turbulent energy dissipation rate, *ε* (c) turbulent normal stress in *x* direction, $\overline{u_1 u_1}$ (d) turbulent normal stress in *y* direction, $\overline{u_2 u_2}$ (e) turbulent normal stress in *z* direction, $\overline{u_3 u_3}$ (f) turbulent shear stress in *xy* plane, $\overline{u_1 u_2}$

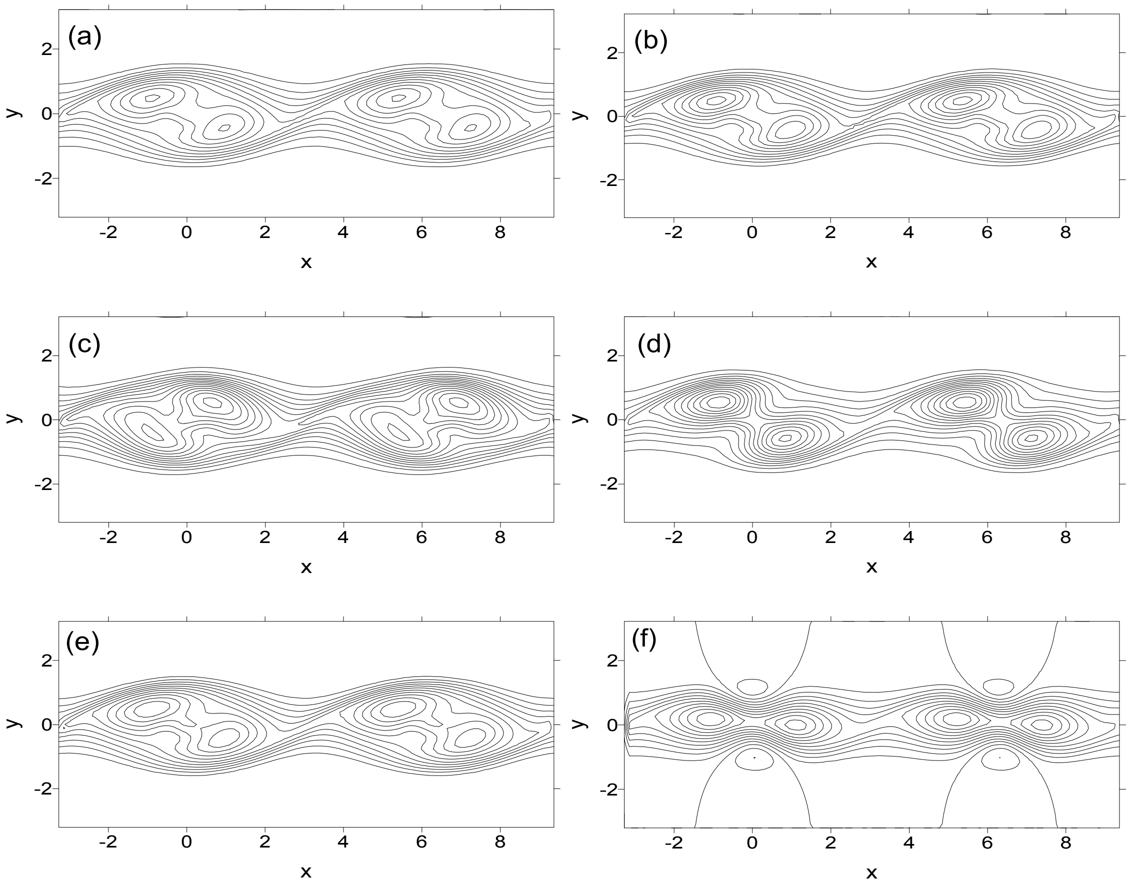

Fig. 4.9 Turbulent structures by numerical simulation by Standard *k*-*ε* model: (a) turbulent

kinetic energy, k (b) turbulent energy dissipation rate, ε (c) turbulent normal stress in x direction, $\overline{u_1u_1}$ (d) turbulent normal stress in y direction, $\overline{u_2u_2}$ (e) turbulent normal stress in z direction, $\overline{u_3u_3}$ (f) turbulent shear stress in xy plane, $\overline{u_1u_2}$

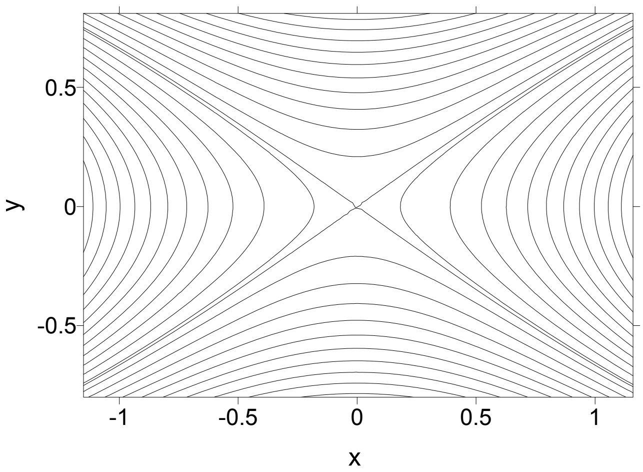

Fig. 4.10 Saddle point of Stuart vortex approximated by Taylor function

4.5 Turbulent Structures at Saddle Point

In a Stuart vortex, two vortices are separated in the saddle point at a periodic distance of π from the vortex point [Fig. 4.2(e)]. Therefore, the equation of Stuart vortices expressed in Eq.(4.11) is expanded using Taylor function at a periodic distance of (π,0), and the approximated stream function for the saddle point is expressed as follows (eccentricity, A=- 0.5 is used)

$$\psi = \ln\left(\frac{1}{2}\right) - \frac{1}{6}x^2 + \frac{1}{3}y^2 + \frac{1}{18}x^2y^2 - \frac{1}{36}y^4 + \ldots\ldots\ldots \tag{4.33}$$

The corresponding velocity field is approximated as

$$U_x = \frac{\partial\psi}{\partial y} = \frac{2}{3}y + \frac{1}{9}x^2y - \frac{1}{9}y^3 \tag{4.34}$$

$$U_y = -\frac{\partial\psi}{\partial x} = \frac{1}{3}x - \frac{1}{9}xy^2 \tag{4.35}$$

The contour of streamlines for saddle point approximated by Taylor function (Eq. 4.33) is shown in Fig. 4.10.

Similar to previous analysis for vortex center, the following polynomial functional forms are assumed for the distributions of k and ε in saddle point

$$k = k_{00} + k_{01}x + k_{10}y + +k_{02}x^2 + k_{20}y^2 + k_{11}xy \tag{4.36}$$

$$\varepsilon = \varepsilon_{00} + \varepsilon_{01}x + \varepsilon_{10}y + +\varepsilon_{02}x^2 + \varepsilon_{20}y^2 + \varepsilon_{11}xy \tag{4.37}$$

Applying the same procedure as vortex point, the following algebraic expressions are derived considering the relations of coefficients for the same power of variables (x, y) in k and ε equations [Eqs. (4.12) and (4.13)].

<u>*k*-equation</u>:

$$0: \quad c_{\mu_0} k_{00}^2 (1)_0 - (2)_0 + \frac{c_{\mu_0}}{\sigma_k} k_{00}^2 \{2k_{02} + 2k_{20}\}(1)_0 = 0 \tag{4.38}$$

$$x: \quad k_{10} = A_s k_{01} + B_s \varepsilon_{01} \tag{4.39}$$

$$y: \quad 2k_{01} = A_s k_{10} + B_s \varepsilon_{10} \tag{4.40}$$

$$x^2: \quad k_{11} = A_s k_{02} + B_s \varepsilon_{02} + C_{s5}(k_{02} + k_{20}) + C_{s1} \tag{4.41}$$

$$y^2: \quad 2k_{11} = A_s k_{20} + B_s \varepsilon_{20} + C_{s6}(k_{02} + k_{20}) + C_{s2} \tag{4.42}$$

$$xy: \quad 4k_{02} + 2k_{20} = A_s k_{11} + B_s \varepsilon_{11} \tag{4.43}$$

<u>ε -equation</u>:

$$0: \quad c_{\varepsilon_1} c_{\mu_0} k_{00}^2 \varepsilon_{00} (1)_0 - c_{\varepsilon_2} \varepsilon_{00} (2)_0 + \frac{c_{\mu_0}}{\sigma_\varepsilon} k_{00}^3 \{2\varepsilon_{02} + 2\varepsilon_{20}\}(1)_0 = 0 \tag{4.44}$$

$$x: \quad \varepsilon_{10} = C_s k_{01} + D_s \varepsilon_{01} \tag{4.45}$$

$$y: \quad 2\varepsilon_{01} = C_s k_{10} + D_s \varepsilon_{10} \tag{4.46}$$

$$x^2: \quad \varepsilon_{11} = C_s k_{02} + D_s \varepsilon_{02} + C_{s7}(\varepsilon_{02} + \varepsilon_{20}) + C_{s3} \tag{4.47}$$

$$y^2: \quad 2\varepsilon_{11} = C_s k_{20} + D_s \varepsilon_{20} + C_{s8}(\varepsilon_{02} + \varepsilon_{20}) + C_{s4} \tag{4.48}$$

$$xy: \quad 4\varepsilon_{02} + 2\varepsilon_{20} = C_s k_{11} + D_s \varepsilon_{11} \tag{4.49}$$

Here,

$$A_s = \Biggl[c_{\mu_0} \varepsilon_{00} k_{00}^3 \biggl\{ (1)_0 \biggl(2m_{ds} + \frac{2}{9} m_{d\Omega} \biggr) + (4)_0 \biggl(2c_{ns} + \frac{2}{9} c_{n\Omega} \biggr) \biggr\} + 2c_{\mu_0} \varepsilon_{00} k_{00} (1)_0 (4)_0$$

$$- \varepsilon_{00} k_{00} (2)_0 \biggl(2m_{ds} + \frac{2}{9} m_{d\Omega} \biggr) - \varepsilon_{00} k_{00} (4)_0 \biggl\{ \varepsilon_{00}^2 \biggl(2c_{ds} + \frac{2}{3} c_{ds\Omega} + \frac{2}{9} c_{d\Omega} \biggr)$$

$$+ 4k_{00}^2 \biggl(c_{ds1} + \frac{1}{9} c_{ds\Omega 1} + \frac{1}{81} c_{d\Omega 1} \biggr) \biggr\} \Biggr] 3.0 / \{ (2)_0 (4)_0 \}$$

$$B_s = \lfloor 2c_{\mu_0} \varepsilon_{00}^2 k_{00}^2 \{ (1)_0 + (4)_0 \} + c_{\mu_0} k_{00}^2 (1)_0 (4)_0 - \{ 2(2)_0 \varepsilon_{00}^2 + 4\varepsilon_{00}^4 (4)_0$$

$$+ \varepsilon_{00}^2 k_{00}^2 (4)_0 \biggl(2c_{ds} + \frac{2}{3} c_{ds\Omega} + \frac{2}{9} c_{d\Omega} \biggr) + (2)_0 (4)_0 \biggr\} \Biggr] 3.0 / \{ (2)_0 (4)_0 \}$$

$$C_s = \Biggl[c_{\mu_0} c_{\varepsilon_1} \varepsilon_{00}^2 k_{00}^3 \biggl\{ (1)_0 \biggl(2m_{ds} + \frac{2}{9} m_{d\Omega} \biggr) + (4)_0 \biggl(2c_{ns} + \frac{2}{9} c_{n\Omega} \biggr) \biggr\} + 2c_{\mu_0} c_{\varepsilon_1} \varepsilon_{00}^2 k_{00} (1)_0 (4)_0$$

$$- c_{\varepsilon_2} \varepsilon_{00}^2 k_{00} (2)_0 \biggl(2m_{ds} + \frac{2}{9} m_{d\Omega} \biggr) - c_{\varepsilon_2} \varepsilon_{00}^2 k_{00} (4)_0 \biggl\{ \varepsilon_{00}^2 \biggl(2c_{ds} + \frac{2}{3} c_{ds\Omega} + \frac{2}{9} c_{d\Omega} \biggr)$$

$$+ 4k_{00}^2 \biggl(c_{ds1} + \frac{1}{9} c_{ds\Omega 1} + \frac{1}{81} c_{d\Omega 1} \biggr) \biggr\} \Biggr] 3.0 / \{ (2)_0 (4)_0 k_{00} \}$$

$$D_s = \lfloor 2c_{\mu_0} c_{\varepsilon_1} \varepsilon_{00}^3 k_{00}^2 \{ (1)_0 + (4)_0 \} + 2c_{\mu_0} c_{\varepsilon_1} \varepsilon_{00} k_{00}^2 (1)_0 (4)_0 - c_{\varepsilon_2} \{ 2(2)_0 \varepsilon_{00}^3 + 4\varepsilon_{00}^5 (4)_0$$

$$+ \varepsilon_{00}^3 k_{00}^2 (4)_0 \biggl(2c_{ds} + \frac{2}{3} c_{ds\Omega} + \frac{2}{9} c_{d\Omega} \biggr) + 2\varepsilon_{00} (2)_0 (4)_0 \} \Biggr] 3.0 / \{ (2)_0 (4)_0 k_{00} \}$$

$$C_{s1} = \Biggl[- \varepsilon_{00} k_{00}^2 \biggl\{ (2)_0 \biggl(\frac{2}{9} m_{ds} + \frac{2}{27} m_{d\Omega} \biggr) + 2\varepsilon_{00}^2 (4)_0 \biggl(\frac{1}{9} c_{ds} + \frac{1}{27} c_{d\Omega} + \frac{2}{27} c_{ds\Omega} \biggr) \biggr\}$$

$$+ \frac{2}{9} c_{\mu_0} \varepsilon_{00} k_{00}^2 (1)_0 (4)_0 + c_{\mu_0} \varepsilon_{00} k_{00}^4 (1)_0 \biggl(\frac{2}{9} m_{ds} + \frac{2}{27} m_{d\Omega} \biggr)$$

$$+ \varepsilon_{00} k_{00}^4 (4)_0 \biggl\{ c_{\mu_0} \biggl(\frac{2}{9} c_{ns} + \frac{2}{27} c_{n\Omega} \biggr) - \biggl(\frac{4}{9} c_{ds1} + \frac{4}{243} c_{d\Omega 1} + \frac{8}{81} c_{ds\Omega 1} \biggr) \biggr\} \Biggr] 3.0 / \{ (2)_0 (4)_0 \}$$

$$C_{s2} = \Biggl[- \varepsilon_{00} k_{00}^2 \biggl\{ (2)_0 \biggl(- \frac{8}{9} m_{ds} - \frac{4}{27} m_{d\Omega} \biggr) + 2\varepsilon_{00}^2 (4)_0 \biggl(- \frac{4}{9} c_{ds} - \frac{2}{27} c_{d\Omega} - \frac{5}{27} c_{ds\Omega} \biggr) \biggr\}$$

$$- \frac{8}{9} c_{\mu_0} \varepsilon_{00} k_{00}^2 (1)_0 (4)_0 + c_{\mu_0} \varepsilon_{00} k_{00}^4 (1)_0 \biggl(- \frac{8}{9} m_{ds} - \frac{4}{27} m_{d\Omega} \biggr)$$

$$+\varepsilon_{00}k_{00}^{4}(4)_0\left\{c_{\mu_0}\left(-\frac{8}{9}c_{ns}-\frac{4}{27}c_{n\Omega}\right)+4\left(\frac{4}{9}c_{ds1}+\frac{2}{243}c_{d\Omega 1}+\frac{5}{81}c_{ds\Omega 1}\right)\right\}\Bigg]3.0/\{(2)_0(4)_0\}$$

$$C_{s3}=\Bigg[-c_{\varepsilon_2}\varepsilon_{00}^{2}k_{00}^{2}\left\{(2)_0\left(\frac{2}{9}m_{ds}+\frac{2}{27}m_{d\Omega}\right)+2\varepsilon_{00}^{2}(4)_0\left(\frac{1}{9}c_{ds}+\frac{1}{27}c_{d\Omega}+\frac{2}{27}c_{ds\Omega}\right)\right\}$$

$$+\frac{2}{9}c_{\mu_0}c_{\varepsilon_1}\varepsilon_{00}^{2}k_{00}^{2}(1)_0(4)_0+c_{\mu_0}c_{\varepsilon_1}\varepsilon_{00}^{2}k_{00}^{4}(1)_0\left(\frac{2}{9}m_{ds}+\frac{2}{27}m_{d\Omega}\right)$$

$$+\varepsilon_{00}^{2}k_{00}^{4}(4)_0\left\{c_{\varepsilon_1}c_{\mu_0}\left(\frac{2}{9}c_{ns}+\frac{2}{27}c_{n\Omega}\right)-c_{\varepsilon_2}\left(\frac{4}{9}c_{ds1}+\frac{4}{243}c_{d\Omega 1}+\frac{8}{81}c_{ds\Omega 1}\right)\right\}\Bigg]\ 3.0/\{(2)_0(4)_0\}$$

$$C_{s4}=\Bigg[-c_{\varepsilon_2}\varepsilon_{00}^{2}k_{00}^{2}\left\{(2)_0\left(-\frac{8}{9}m_{ds}-\frac{4}{27}m_{d\Omega}\right)+2\varepsilon_{00}^{2}(4)_0\left(-\frac{4}{9}c_{ds}-\frac{2}{27}c_{d\Omega}-\frac{5}{27}c_{ds\Omega}\right)\right.$$

$$-\frac{8}{9}c_{\mu_0}c_{\varepsilon_1}\varepsilon_{00}^{2}k_{00}^{2}(1)_0(4)_0+c_{\mu_0}c_{\varepsilon_1}\varepsilon_{00}^{2}k_{00}^{4}(1)_0\left(-\frac{8}{9}m_{ds}-\frac{4}{27}m_{d\Omega}\right)$$

$$+\varepsilon_{00}^{2}k_{00}^{4}(4)_0\left\{c_{\mu_0}c_{\varepsilon_1}\left(-\frac{8}{9}c_{ns}-\frac{4}{27}c_{n\Omega}\right)+4c_{\varepsilon_2}\left(\frac{4}{9}c_{ds1}+\frac{2}{243}c_{d\Omega 1}+\frac{5}{81}c_{ds\Omega 1}\right)\right\}\Bigg]3.0/\{(2)_0(4)_0k_{00}\}$$

$$C_{s5}=\left[\frac{2c_{\mu_0}}{\sigma_k}\varepsilon_{00}k_{00}^{4}\left\{(1)_0\left(\frac{2}{9}m_{ds}+\frac{2}{27}m_{d\Omega}\right)+(4)_0\left(\frac{2}{9}c_{ns}+\frac{2}{27}c_{n\Omega}\right)\right\}\right]3.0\Big/\{(2)_0(4)_0\}$$

$$C_{s6}=\left[\frac{2c_{\mu_0}}{\sigma_k}\varepsilon_{00}k_{00}^{4}\left\{(1)_0\left(-\frac{8}{9}m_{ds}-\frac{4}{27}m_{d\Omega}\right)+(4)_0\left(-\frac{8}{9}c_{ns}-\frac{4}{27}c_{n\Omega}\right)\right\}\right]3.0\Big/\{(2)_0(4)_0\}$$

$$C_{s7}=\left[\frac{2c_{\mu_0}}{\sigma_\varepsilon}\varepsilon_{00}k_{00}^{4}\left\{(1)_0\left(\frac{2}{9}m_{ds}+\frac{2}{27}m_{d\Omega}\right)+(4)_0\left(\frac{2}{9}c_{ns}+\frac{2}{27}c_{n\Omega}\right)\right\}\right]3.0\Big/\{(2)_0(4)_0\}$$

$$C_{s8}=\left[\frac{2c_{\mu_0}}{\sigma_\varepsilon}\varepsilon_{00}k_{00}^{4}\left\{(1)_0\left(-\frac{8}{9}m_{ds}-\frac{4}{27}m_{d\Omega}\right)+(4)_0\left(-\frac{8}{9}c_{ns}-\frac{4}{27}c_{n\Omega}\right)\right\}\right]3.0\Big/\{(2)_0(4)_0\}$$

$$(1)_0=\varepsilon_{00}^{2}+c_{ns}k_{00}^{2}+\frac{1}{9}c_{n\Omega}k_{00}^{2}$$

$$(2)_0=\varepsilon_{00}^{2}\left(\varepsilon_{00}^{2}+c_{ds}k_{00}^{2}+\frac{1}{9}c_{d\Omega}k_{00}^{2}+\frac{1}{3}c_{ds\Omega}k_{00}^{2}\right)+k_{00}^{4}\left(c_{ds1}+\frac{1}{9}c_{ds\Omega 1}+\frac{1}{81}c_{d\Omega 1}\right)$$

$$(4)_0=\varepsilon_{00}^{2}+m_{ds}k_{00}^{2}+\frac{1}{9}m_{d\Omega}k_{00}^{2}$$

Solving twelve equations from Eqs. (4.38) to (4.49), twelve unknowns are determined in terms of model constants. The calculated profiles for *k*, *ε* and turbulent stresses are shown in Fig.

4.11. It demonstrates that the turbulent energy and dissipation rate as well as turbulent normal stresses show hyperbolic profile (saddle pattern) in a saddle point. However, the shear stress shows elliptic structure.

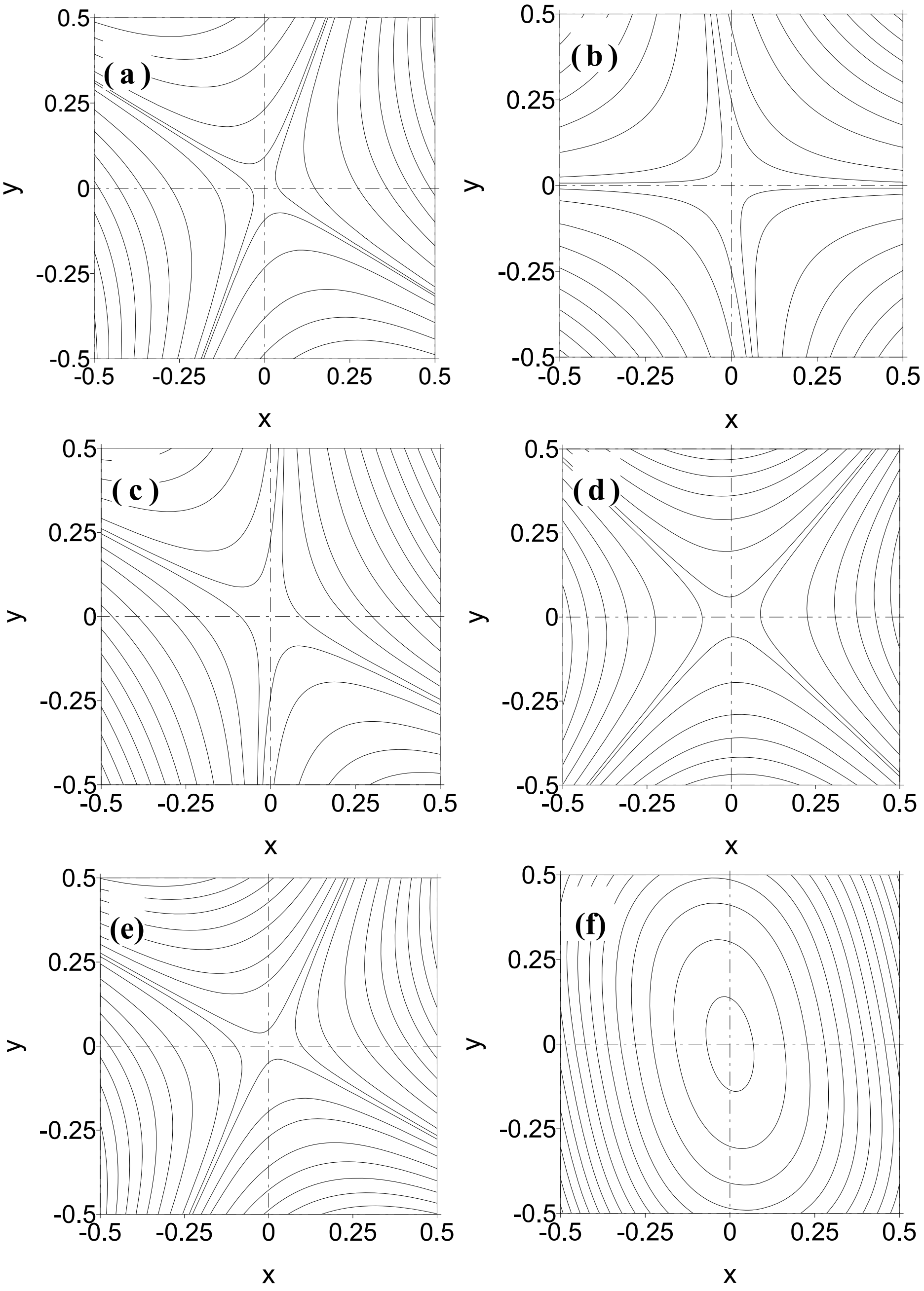

Fig. 4.11 Turbulent structures by approximate solution for Saddle point (Run-1): (a) turbulent kinetic energy, k (b) turbulent energy dissipation rate, ε (c) turbulent normal stress in x

direction, $\overline{u_1 u_1}$ (d) turbulent normal stress in *y* direction, $\overline{u_2 u_2}$ (e) turbulent normal stress in *z* direction, $\overline{u_3 u_3}$ (f) turbulent shear stress in xy plane, $\overline{u_1 u_2}$

From the analytical solution, it can be concluded that the turbulent structures are changed with the spatial distance depending on the structures of singular points. The turbulent normal stresses show elliptical structure near the vortex center, which are changed to hyperbolic profile near saddle point at a stream-wise periodic distance of π. On the other hand, the shear stresses show hyperbolic structures at vortex center and changed to elliptical at saddle point. The spatial change of turbulent structures for turbulent kinetic energy and dissipation rates are found similar to turbulent normal stresses. These features are consistent with the previous experiments of coherent vortices in plane shear layer and turbulent jets (Hossain, 1986).

Coherent vortices are generated due to shear layer caused by velocity gradient. In a river flow, such velocity gradient is observed when the water flows in an out of bank condition, which is a common feature of a natural river. Generally, the velocity in the flood plain is lower than that in the main channel. Therefore, the coherent vortices are formed at the junction between the main channel and the flood plain. Due to shear layer instability, the vortices are generated with the vertical axis at the interface. In the next chapter, the spatial distributions and topological changes of turbulent structures in coherent vortices at the interface of a compound open channel will be investigated and compared with the present findings in an ideal vortex street.

4.6 Summary

Based on a realizable non-linear *k–ε* model, approximate solutions are derived for the turbulent properties of an idealized vortex street to explore the predictability of the model for large scale vortices. The spatial changes of turbulent structures with singular points in the vortices are investigated. The qualitative results are compared to previous experiments to assess the models applicability. The findings are summarized below :

(i) The Stuart vortex, which contains both vortex and saddle patterns in its vorticity contour, is considered as an ideal simple vortex street. The turbulent structures at vortex center and saddle point obtained by approximate solution are found to be consistent with the previous experimental results of large scale coherent vortices in free shear flows.

(ii) The turbulent structures of the vortex street are found to be sensitive to the functional form of the coefficient of eddy viscosity, c_μ.

(iii) The numerical simulation verifies the accuracy of approximate solution, and reveals that the conditions derived for the constitutive law with the estimated model constants are applicable to simulate large scale vortices.

(iv) In the standard k-ε model, the coefficient c_μ has no dependency on the rate of strain and rotation, and bears a constant value (=0.09) throughout the turbulent flow field. That's why it is observed that, the standard model fails to predict the turbulent structures accurately at the center of vortex.

(v) The turbulent structures are found to be changed with the spatial distance depending on the structures of singular points. It is observed that the turbulent normal stresses show elliptical structure near vortex center, which changed to hyperbolic profile near saddle point at a stream-wise periodic distance of π. However, the shear stress show hyperbolic structure at vortex center, and the structure changes to elliptical at saddle point.

(vi) The topological changes of turbulent kinetic energy and dissipation rate with stream-wise spatial distance are found similar to turbulent normal stresses.

In the next chapter, the spatial distributions and topological changes of turbulent structures in coherent vortices at the interface of a compound open channel will be investigated and compared with the present findings of an ideal vortex case.

4.7 References

1) Brown, G. L., and Roshko, A., On density effects and large structures in turbulent mixing layers, *J. Fluid. Mech.*, 64, pp.755, 1974.
2) Browand, F. K., and Weidman, P. D., Large scales in the developing mixing layer, *J. Fluid. Mech.*, 76, pp.127, 1976.
3) Hossain, A. K. M. F., Coherent structures and turbulence, *J. Fluid. Mech.,* 173, pp.303, 1986.
4) Panides, E., and Chevray, R., Vortex dynamics in a plane moderate-Reynolds-number shear layer, *J. Fluid. Mech.*, 214, pp.411, 1990.
5) Rodi, W., Turbulence models for environmental problems, in *Prediction Methods for Turbulent Flows* (edited by W. Kollmann), pp.259, 1979.

Chapter 5

UNSTEADY 3D COMPUTATION OF COMPOUND OPEN CHANNEL FLOWS

5.1 Introduction

Compound channel is a common feature of natural rivers, where the water in main channel flows in an out-of-bank condition. Since the water level in flood plain is shallower and the roughness is higher (due to more vegetation) than the main channel, the flow velocity in the flood plain is generally lower than that in the main channel. Because of this velocity gradient, a shear layer is observed at the junction, and large-scale vortices are generated with the vertical axis at the interface of main channel and flood plain. The vortex formation causes momentum transfer in the lateral direction from the main channel to the flood plains, resulting a decrease in channel conveyance, and hence, the flow resistance in the channel is increased. The vortices also significantly distort the velocity and shear stress pattern. A sketch of flow pattern in a compound channel by Shiono and Knight (1991) is shown in Fig. 5.1. In addition to the coherent vortices at interface, the generation of secondary currents due to anisotropy of turbulence makes the flow very complex, and the flow field shows strong three dimensional characteristics.

A single channel method, in which the compound channel is considered as a single channel, gives an under predicted discharge; on the other hand, the divided channel method predicts a higher discharge than the actual. Thus it is necessary to estimate effect of horizontal vortices on the flow resistance that directly affects the channel conveyance. Since the turbulent characteristics of this type of flows are highly non-linear, the nonlinear terms and empirical functions in a non-linear k–ε model plays an important role to generate the horizontal vortices and secondary currents by accounting the anisotropic turbulent behaviors. In this study, the flow field in a compound channel is generated using standard as well as non-liner (2nd and 3rd order) k–ε models. The interaction of horizontal vortices with secondary currents and its effect on the prediction of compound roughness are investigated. The contribution of vortices and secondary currents evaluated by different models are assessed from the view point of calculated discharge, secondary flow pattern and predicted roughness coefficients. The model is validated by comparing the depth averaged velocity and shear stress profiles as well as

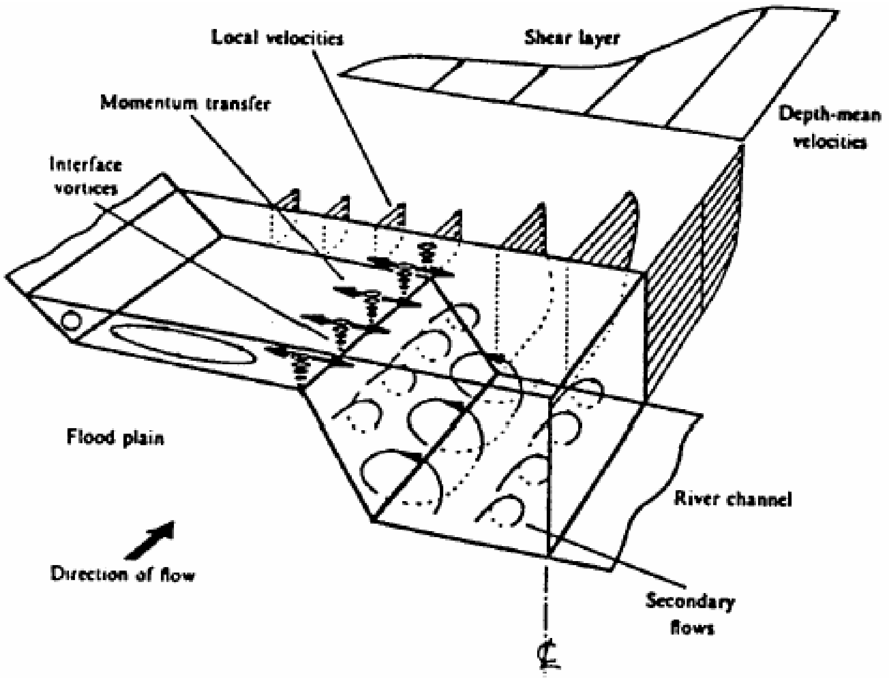

Fig. 5.1 Sketch of 3D flow structure in a compound channel (Shiono and Knight, 1991)

secondary flow patterns with previous experiments.

Although the vortex characteristics in a compound channel are studied by many researchers both in experimental and numerical means, all are concentrated mainly on the effect of vortices to the cross-sectional flow or turbulence profiles, or to the channel resistance properties. However, as far as in author's knowledge, the spatial change of turbulent structures with the singular points of large scale vortices are not reported for compound channel flows. In this study, in addition to general flow features, the formations of singular points (i.e. vortex and saddle patterns) in the coherent structures, and the topological changes of turbulent structures with the singular points are investigated and compared with the results of the ideal vortex street presented in previous chapter.

5.2 Governing Equations

The 3D unsteady flow equations for open channel with linear, 2nd order and 3rd order non-linear *k–ε* model are given below, which are used to simulate the compound channel flows in this study.

Continuity equation: $$\frac{\partial U_i}{\partial x_i} = 0 \tag{5.1}$$

Momentum equation: $$\frac{\partial U_i}{\partial t} + \frac{\partial U_j U_i}{\partial x_j} = g_i - \frac{1}{\rho}\frac{\partial P}{\partial x_i} + \frac{\partial}{\partial x_j}\left(-\overline{u_i u_j}\right) + \nu \frac{\partial^2 U_i}{\partial {x_j}^2} \tag{5.2}$$

k - equation: $$\frac{\partial k}{\partial t} + \frac{\partial k U_j}{\partial x_j} = -\overline{u_i u_j}\frac{\partial U_i}{\partial x_j} + \frac{\partial}{\partial x_j}\left\{\left(\frac{\nu_t}{\sigma_k} + \nu\right)\frac{\partial k}{\partial x_j}\right\} - \varepsilon \tag{5.3}$$

ε - equation: $$\frac{\partial \varepsilon}{\partial t} + \frac{\partial \varepsilon U_j}{\partial x_j} = -c_{\varepsilon 1}\frac{\varepsilon}{k}\overline{u_i u_j}\frac{\partial U_i}{\partial x_j} + \frac{\partial}{\partial x_j}\left\{\left(\frac{\nu_t}{\sigma_\varepsilon} + \nu\right)\frac{\partial \varepsilon}{\partial x_j}\right\} - c_{\varepsilon 2}\frac{\varepsilon^2}{k} \tag{5.4}$$

(a) Standard *k–ε* model

$$-\overline{u_i u_j} = \nu_t S_{ij} - \frac{2}{3} k \delta_{ij}\,, \quad \nu_t = c_\mu \frac{k^2}{\varepsilon}\,, \quad c_\mu = 0.09 \tag{5.5}$$

(b) 2nd order non-linear *k–ε* model

$$-\overline{u_i u_j} = \nu_t S_{ij} - \frac{2}{3} k \delta_{ij} - \frac{k}{\varepsilon} \nu_t \sum_{\beta=1}^{3} c_\beta \left(S_{\beta ij} - \frac{1}{3} S_{\beta\alpha\alpha} \delta_{ij} \right) \tag{5.6}$$

(c) 3rd order non-linear *k–ε* model

$$-\overline{u_i u_j} = \nu_t S_{ij} - \frac{2}{3} k \delta_{ij} - \frac{k}{\varepsilon} \nu_t \sum_{\beta=1}^{3} c_\beta \left(S_{\beta ij} - \frac{1}{3} S_{\beta\alpha\alpha} \delta_{ij} \right)$$

$$-\frac{k^2}{\varepsilon^2} \nu_t c_4 \left(\Omega_{ik} S_{kl} S_{lj} - S_{ik} S_{kl} \Omega_{lj} \right) - \frac{k^2}{\varepsilon^2} \nu_t c_5 \left(\Omega_{ik} S_{kl} S_{lj} + S_{ik} \Omega_{kl} \Omega_{lj} - \frac{2}{3} S_{mn} \Omega_{no} \Omega_{om} \delta_{ij} \right) \tag{5.7}$$

Here,

$$\nu_t = c_\mu \frac{k^2}{\varepsilon}\,, \quad S_{ij} = \frac{\partial U_i}{\partial x_j} + \frac{\partial U_j}{\partial x_i}\,, \quad \Omega_{ij} = \frac{\partial U_i}{\partial x_j} - \frac{\partial U_j}{\partial x_i}\,, S = \frac{k}{\varepsilon} \sqrt{\frac{1}{2} S_{ij} S_{ij}}\,, \Omega = \frac{k}{\varepsilon} \sqrt{\frac{1}{2} \Omega_{ij} \Omega_{ij}} \tag{5.8}$$

In Equation (5.6) and (5.7),

$$S_{1ij} = \frac{\partial U_i}{\partial x_\gamma} \frac{\partial U_j}{\partial x_\gamma}\,, \quad S_{2ij} = \frac{1}{2} \left(\frac{\partial U_\gamma}{\partial x_i} \frac{\partial U_j}{\partial x_\gamma} + \frac{\partial U_\gamma}{\partial x_j} \frac{\partial U_i}{\partial x_\gamma} \right), \quad S_{3ij} = \frac{\partial U_\gamma}{\partial x_i} \frac{\partial U_\gamma}{\partial x_j}\,. \tag{5.9}$$

$$c_\mu = \frac{c_{\mu o}\,(1 + c_{ns} S^2 + c_{n\Omega} \Omega^2)}{1 + c_{ds} S^2 + c_{d\Omega} \Omega^2 + c_{ds\Omega} S \Omega + c_{ds1} S^4 + c_{d\Omega 1} \Omega^4 + c_{ds\Omega 1} S^2 \Omega^2} \tag{5.10}$$

$$c_\beta = \frac{c_{\beta o}}{1 + m_{ds} S^2 + m_{d\Omega} \Omega^2}\,, c_4 = \frac{c_{4o}}{1 + m_{ds} S^2 + m_{d\Omega} \Omega^2}\,, c_5 = \frac{c_{5o}}{1 + m_{ds} S^2 + m_{d\Omega} \Omega^2} \tag{5.11}$$

The used values of the model constants are: $c_{\mu 0} = 0.09$, $c_{ns} = 0.005$, $c_{n\Omega} = 0.0068$, $c_{ds} = 0.008$, $c_{d\Omega} = 0.004$, $c_{ds\Omega} = -0.003$, $c_{ds1} = 0.00005$, $c_{d\Omega 1} = 0.00005$, $c_{ds\Omega 1} = 0.00025$, $c_{10} = 0.40$, $c_{20} = 0.0$, $c_{30} = -0.13$, $c_{40} = -0.02$, $c_{50} = 0.0$, $m_{ds} = 0.01$, $m_{d\Omega} = 0.003$. Standard values are used for other model constants: $\sigma_k = 1.0$, $\sigma_\varepsilon = 1.3$, $c_{\varepsilon 1} = 1.44$, and $c_{\varepsilon 2} = 1.92$.

5.3 Numerical Procedure and Flow Configurations

5.3.1 Numerical schemes and boundary conditions

The code solves the governing equations for mean velocities and turbulent flow field discretized with the finite volume method and is based on a staggered grid system. The arrangements of variables in a staggered grid for 3D computations are shown in Fig. 5.2. For the momentum equation, convection and diffusive fluxes are approximated with Quick and central difference schemes respectively. The hybrid central upwind scheme is used for the k and ε equations. Time advancement is achieved by Adam-Bashforth scheme of second-order accuracy, in each equation. The basic equations are discretized as fully explicit forms and solved successively with the time increment in step by step. The pressure field is solved using iterative procedure at each time step. The free surface elevation is solved by continuity equation integrated over the control volume of the surface layer.

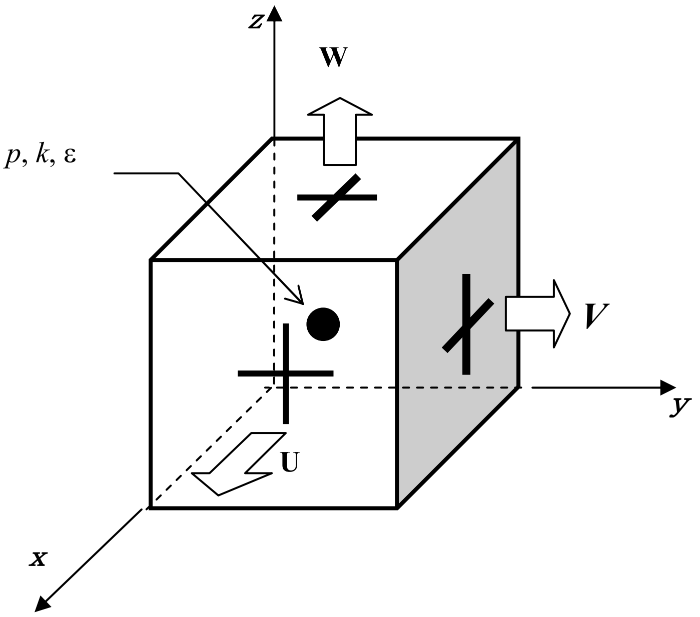

Fig. 5.2 Arrangements of variables in a staggered grid in the 3D computations

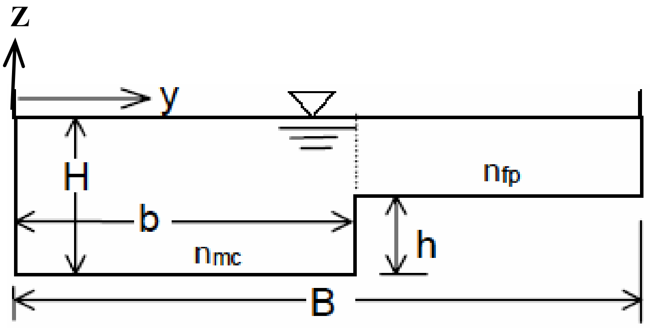

(a) Geometry-A

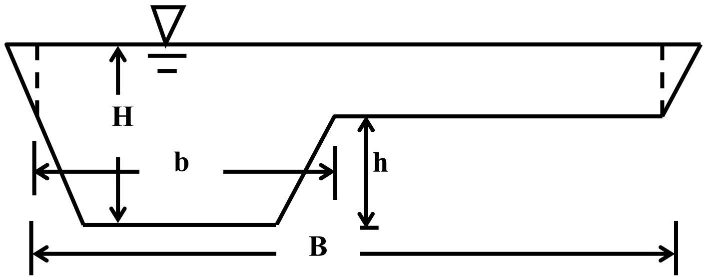

(b) Geometry-B (side slope = 1:1)

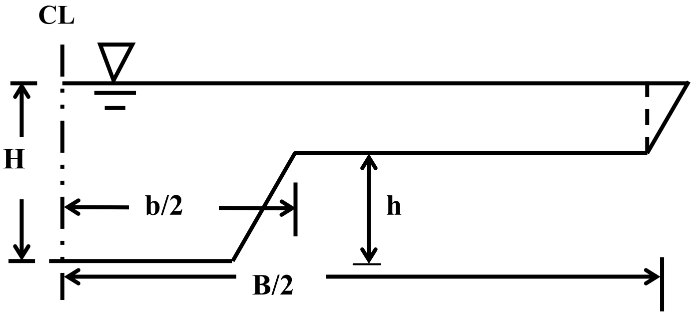

(c) Geometry-C (side slope =1:1)

Fig. 5.3: Cross-section of compound open channel

The wall functions are employed as the wall boundary conditions for *k* and *ε*. The frictions near the bed and side walls are estimated by log-law. Periodic boundary conditions are used in upstream and downstream ends of the flow domain. Near the free surface, the eddy viscosity is multiplied by a damping function for the rapid attenuation of turbulent intensities in the depth wise direction. The turbulent dissipation rate for the surface layer is evaluated by the expression proposed by Sugiyama et al (1995). The damping function (f_s) and the dissipation rate (ε_s) for surface layer are shown in the following equations; the subscript represents the value of surface layer (here, B_s =10).

$$f_s = 1 - \exp\left(- B_s \frac{(h - y)\varepsilon_s}{k_s^{3/2}} \right), \qquad \varepsilon_s = \frac{c_{\mu_0}^{3/4} k_s^{3/2}}{0.4 \nabla y_s} \tag{5.12}$$

Table 5.1: Channel properties and hydraulic conditions of compound channel

Geometry	Cases	B (cm)	b (cm)	H (cm)	h (cm)	Long. slope	n_{mc}	n_{fp}
A	A1	200	75.7	7.5	5.0	0.001	0.01	0.028
	A2			10.0				
	A3			12.5				
B	B1	405	180	19.8	15.0	0.001	0.01106	
	B2			17.6				
C	C1	315 X 2	180	17.7	15.0	0.001	0.01106	

5.3.2 Flow configuration and test models

Considering the availability of experimental data, numerical simulations are performed for three types of geometry. For Geometry-A (having no side slope and different roughness for main channel and flood plain, shown in Fig. 5.3(a)), the laboratory experiments have been performed by Fukuoka at al.(1989) to determine the compound roughness of the channel. For this geometry, the numerical simulations are performed for three cases with different flood plain to main channel depth ratios. The Geometry-B is a trapezoidal section with a side slope of 1:1 (shown in Fig. 5.3(b)). For cases B1 and B2, the laboratory data are available for depth averaged velocity and shear stress profiles (Knight, 1992). All the cases from A1 to B2 consist of single flood plain. In order to compare the secondary currents (considering the availability of experiments), the simulation is performed for Case C1, which contains two flood plains. The details of hydraulic conditions are shown in Table-5.1. The reported experimental results for geometry B and C are from the first phase experiments of Wallingford Flood Channel Facility

(FCF), UK (Shiono and Knight, 1991; Wormleaton, 1996; Bousmar, 2002). Among nine series, Case B1 and B2 belong to series-06, and Case- C1 belongs to series 02 in that phase of experiments.

For geometry-A, the flow domain consists of 200 grids in stream-wise (x), 42 in transverse (y) and 11 in depth-wise (z) directions. For Cases B1 and B2, numbers of grid for x, y and z directions are 200, 50 and 11 respectively; for Case C1, 200 x 72 x 11 grids are used. It can be noted that, since the ratio of depth (H/h) is one of the dominant factor for the formation of vortex at the interface, for case A, the simulation work is performed for three cases of depth ratios varying from 1.5 to 2.5 as shown in Table 5.1.

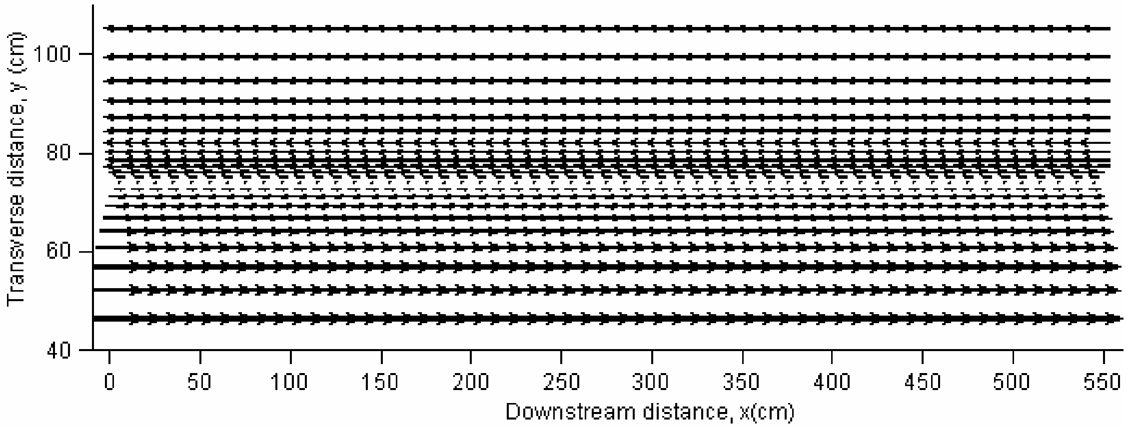

(a) Plan view of flow field without horizontal vortices

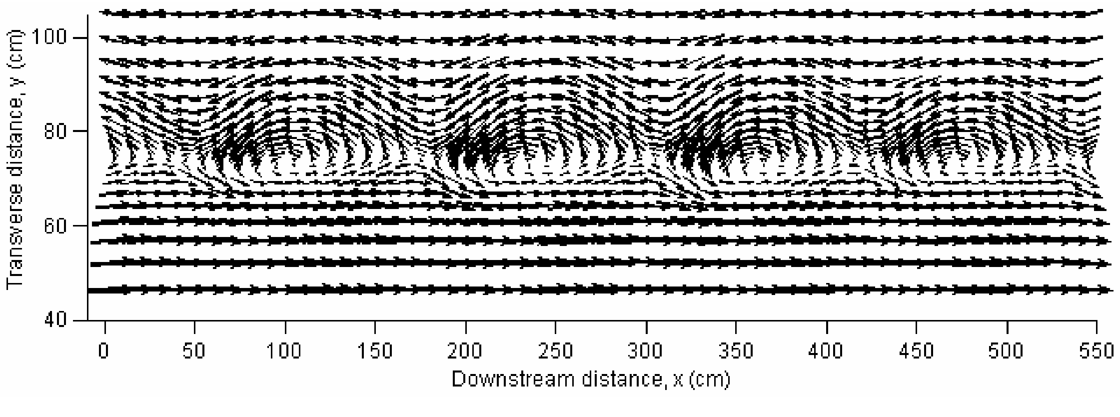

(b) Plan view of flow field after generation of horizontal vortices

Fig. 5.4: Plan view of flow pattern (case-A1, t=110 sec, a part of domain is shown)

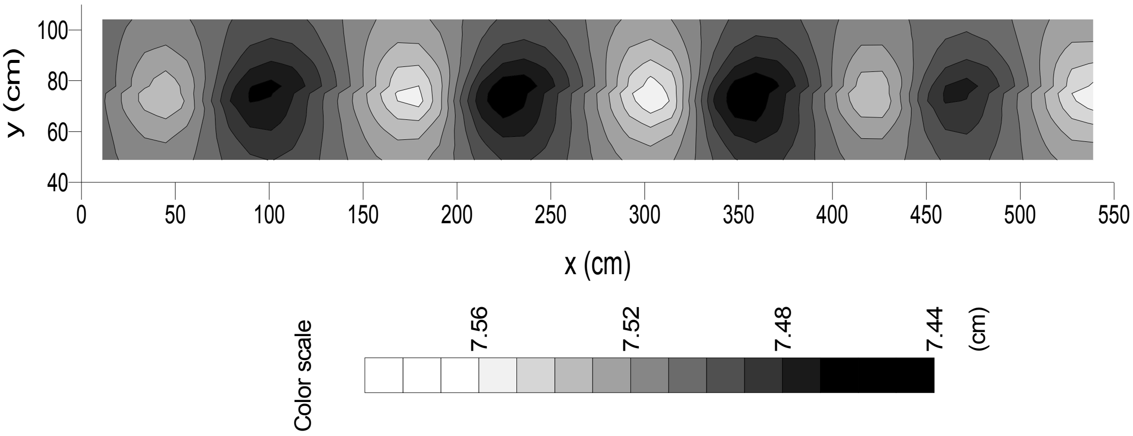

Fig. 5.5: Water surface distribution near the interface for the flow field shown in Fig. 5.4 (b) (case-A1, Run NLKEV, t=110 sec)

The numerical tests are performed using both standard and nonlinear *k–ε* models. The simulations are run both including vortex and excluding vortex conditions to study the effect of vortices in the flow field. To distinguish the effect of nonlinearity of eddy viscosity, the non-linear *k–ε* model without quadratic term is also applied. For all the three different cases of geometry A, as shown in Table 5.1, each of the following models and simulation conditions are used.

(i) 3rd order non-linear *k–ε* model considering horizontal vortices

(ii) 3rd order Non-linear *k–ε* model without considering horizontal vortices

(iii) 2nd order non-linear *k–ε* model considering horizontal vortices (Run NLKEV)

(iv) 2nd order Non-linear *k–ε* model without horizontal vortices (Run NLKE)

(v) Standard *k–ε* model considering horizontal vortices (Run SKEV)

(vi) Standard *k–ε* model without considering horizontal vortices (Run SKE)

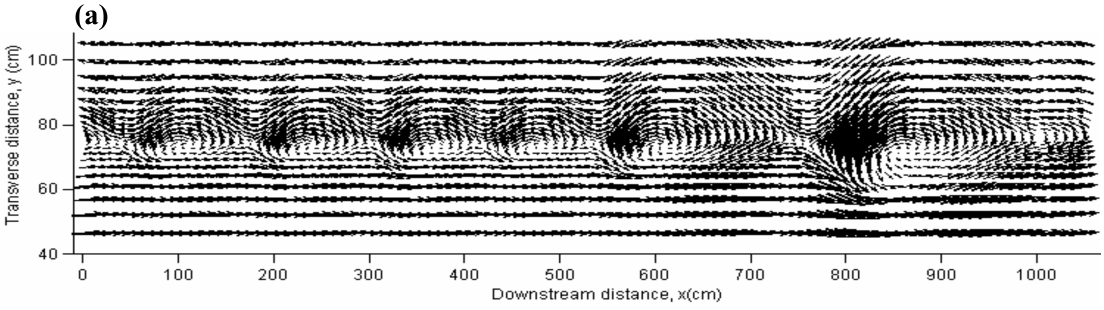

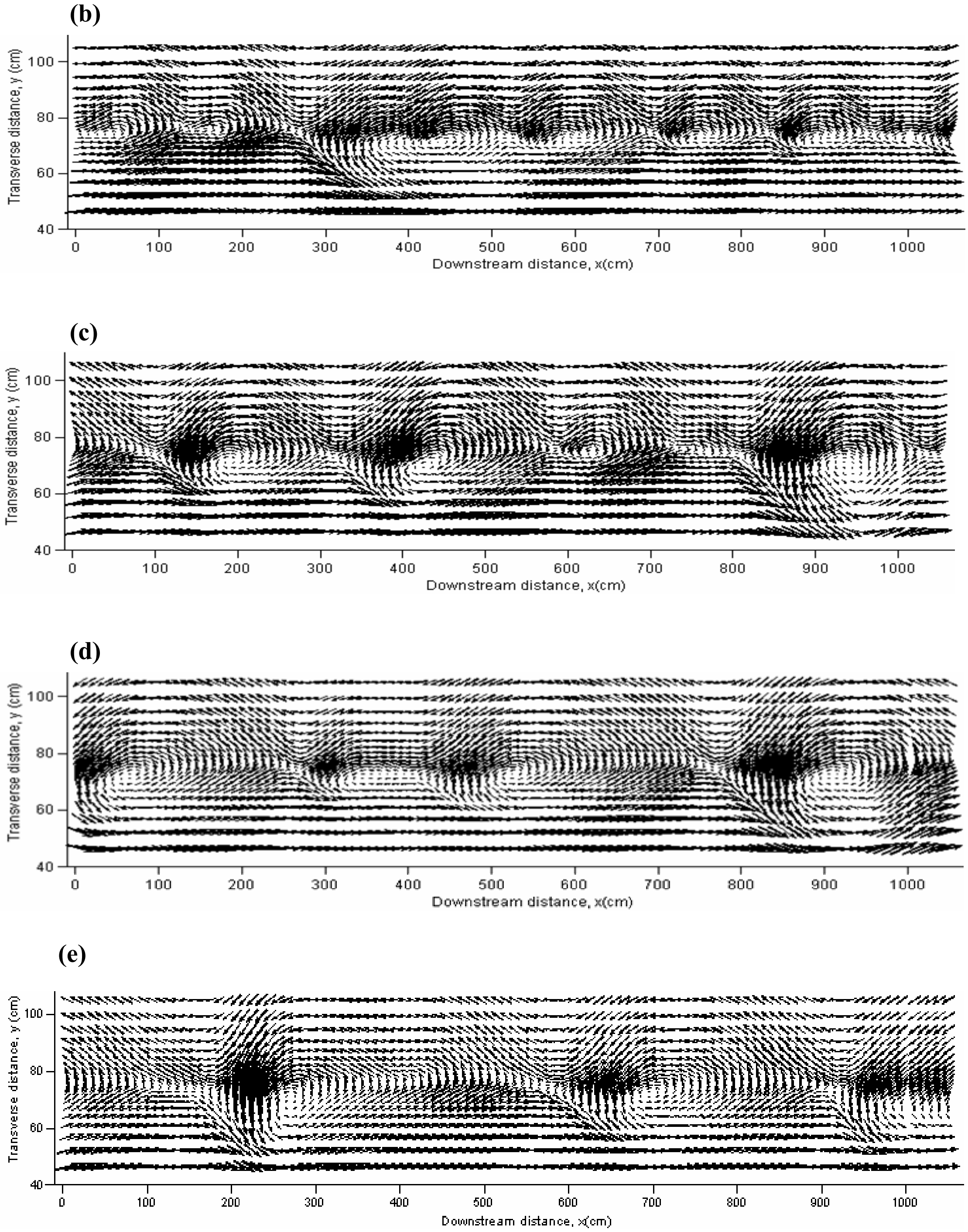

Fig. 5.6: Temporal change in the plan view of flow pattern for case-A1, Run NLKEV (a) t=110 sec (b) t=140 sec (c) t=170 sec (d) t=220 sec (e) t=320 sec (half of the computational domain is shown)

5.4 Results and Discussions

5.4.1 Plan view of flow pattern

Present work is dedicated to the modelling of periodic turbulent structures, such as large scale vortices with vertical axis, which are observed at the interface between the main channel and flood plain of a compound channel. To quantify the effect of these vortices on characteristics of channel flow as well as on its flow resistive properties, the flow fields are also generated by omitting the vortices. For all the cases of geometry A with H/h from 1.5 to 2.5, the horizontal vortices are found to be generated both by standard and nonlinear k- ε models. Figure 5.4(b) shows the plan view of flow pattern generated with the horizontal vortices using 2nd order nonlinear k–ε model for case A1. Fig. 5.4(a) shows the flow field without horizontal vortices. The water surface distribution corresponding to the flow field in Fig.5.4(b) is presented in Fig. 5.5. It demonstrates that a depression in water surface is formed at the centre of each vortex. The depth gradually increases in up- and down-stream of vortex centre and becomes maximum at saddle points of the flow field.

During simulation, the instability in the initial uniform flow is started at about t = 70 to 90 sec, and clear periodic vortices are appeared at about t= 100 to 150 sec. After the initial vortices completely developed, two or thee neighbouring vortices are found to be merged together to form a larger one. However, after about t=250 seconds, the merging process stops and vortices size remains approximately constant with respect to time. Such temporal change in the plan view of flow pattern is shown in Fig. 5.6. For case-A1, flow fields near the interface region is shown for t=110, 140, 170, 220 and 320 secs. Water surface fluctuations in the merged vortices are found higher than the initial small vortices. Such phenomena of vortex merging were also observed by Bousmar (2002) in his numerical simulation. He reported that the non-merged vortices better matched with experimentally observed vortices than the merged one. The variation of water depth along the interface is shown in Fig. 5.7. It is observed that, although water surface variation is very regular for case A1 (Fig. 5.7a), they show some discrepancy for cases A2 and A3 (Fig 5.7 b and 5.7c). This indication reveals that the periodic vortices are not clearly observed as the relative depth (H/h) increases. This feature concerning the relative depth has also pointed out by Fukuoka et al. (1989) in their laboratory tests.

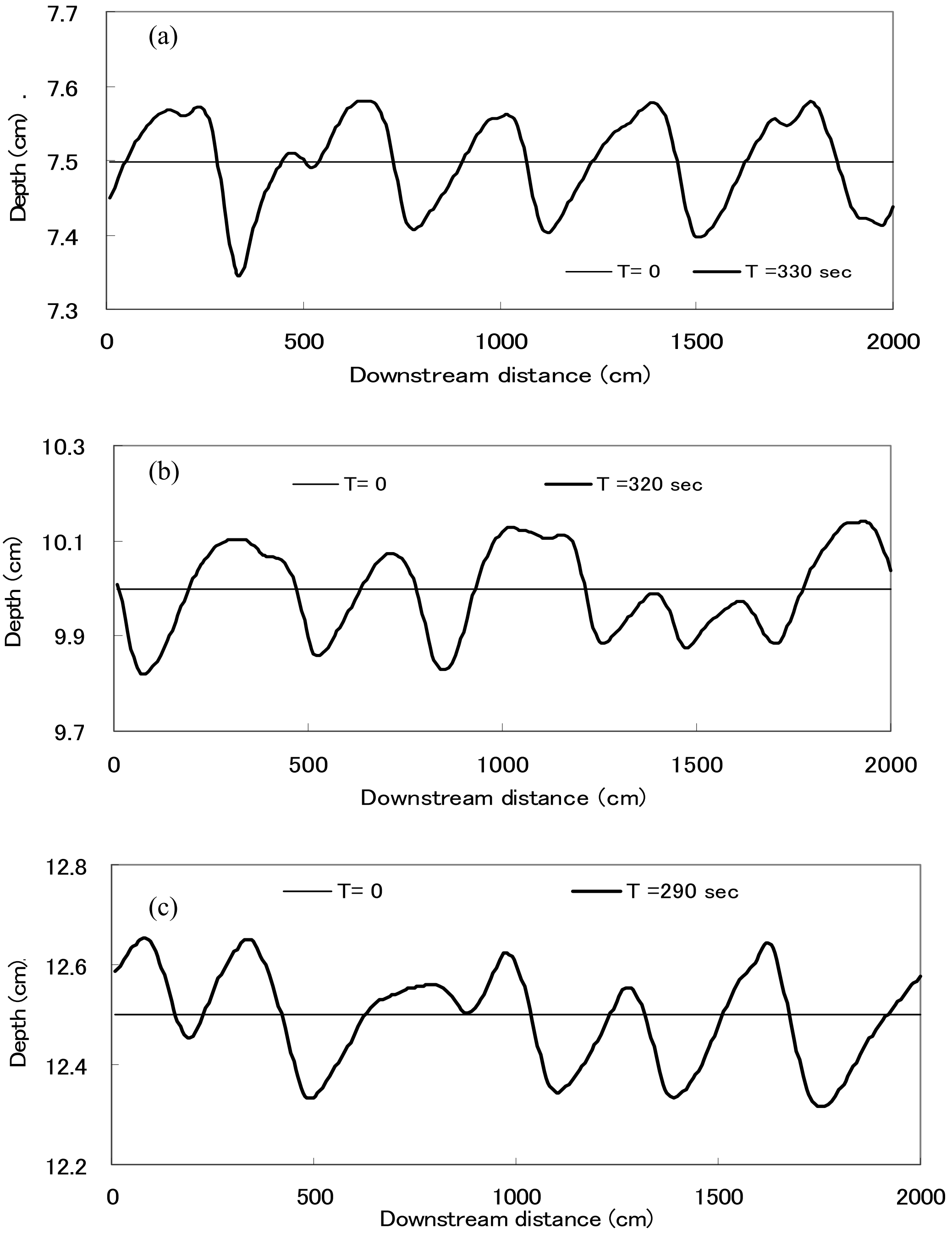

Fig. 5.7: Depth variation along the downstream distance for (a) case-A1, (b) case-A2 , and (c) case-A3

5.4.2 Characteristics of secondary currents

In addition to horizontal vortices, the helical secondary currents are considered to be another main source of momentum transfer on the flood plains. The flow exchange between main channel and flood plain due to the interaction of secondary currents and horizontal vortices are explained in Fig. 5.8. In the figure, the pattern of secondary currents is shown at different sections in a coherent vortex. The plan view of the vortex is shown in Fig. 5.8(a), where the positions of sections are shown. The plan view shows that the vortex lies between 1300 to 1500 centimetres of stream-wise distances. The secondary currents are shown for the sections at x= 1300, 1340, 1360, 1380, 1420, 1440, 1460 and 1500 cm distances. The first and last sections are situated in saddle point region; 4th section is near to vortex centre; sections at x=1340 and 1440 cm contain the maximum tangential velocity with two opposite directional flow; and other sections are transition between adjacent sections. The plan as well as sectional view of vector plots show that, in the sections upstream side of vortex centre (first three sections) the flow is moving from flood plain to main channel. A reverse movement is shown in downstream three sections. This flow exchange between main channel and flood plain is minimum at saddle and vortex center, which gradually increases spatially and reaches its peak in between two critical points. Although the surface and bottom circulation cells in the left end of main channel secondary current are observed as a common feature in all the sections, the secondary circulation at the interface region is observed only in the sections near the vortex centre and saddle points.

Figure 5.9 shows the spatially averaged cross-sectional flow pattern of secondary currents. The pairs of surface vortices as well as the corner vortices in main channel are clearly depicted by all the models. The inclined upwelling currents are generated from the edge of the junction toward the surface. Due to unavailability of experimental results, the calculated secondary currents for these cases are not directly compared with the experimental results. But the qualitative features of the secondary flow patterns are found well comparable with other experimental results such as Tominaga and Nezu (1991).

Comparing the prediction of 3rd order model [Fig. 5.9(b)] with that of 2nd order [Fig. 5.9(a)], it is observed that 3rd order model predicts superior results than 2nd order model. The circulation cell width of both the surface vortices is under predicted by second order model. Although the downward vectors at the centre of main channel predicted by 3rd order model are well agreed with experiments, the 2nd order model shows an upward flow. The direction of secondary flow in the upper part of flood plain simulated by 2nd order model contradicts with previous experiments, however 3rd order one predicts accurately.

The interaction of horizontal vortices with the secondary currents at the interface of subsections is clearly depicted in Figs. 5.9(b) and (c). The magnitude of upwelling secondary currents at the interface, for the flow field having horizontal vortices, is slightly smaller than that of without vortex condition. It indicates that the secondary currents near the junction are suppressed by the influence of flows caused by the vortices. The secondary currents for higher depth ratios (H/h) are found higher in magnitude compared to lower depth ratios. It is seen that with increasing the flood plain depth, the scales of surface vortices are increased. The magnitudes of secondary currents are also increased significantly with the flood plain depth. Compared to case A1, a stronger circulation cell is observed at the right end corner of flood plain for cases A2 and A3 [in Figs. 5.9 (d) and (e)].

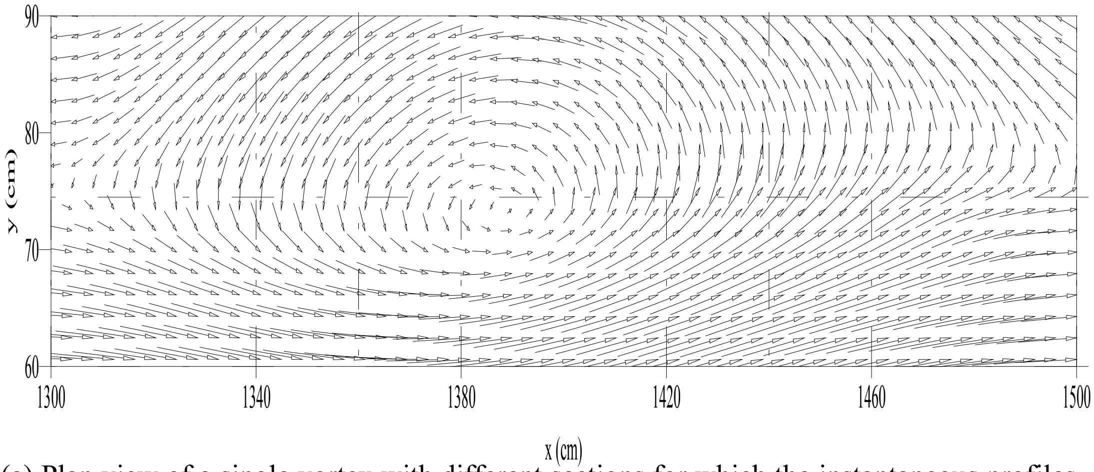

(a) Plan view of a single vortex with different sections for which the instantaneous profiles of secondary currents are given below

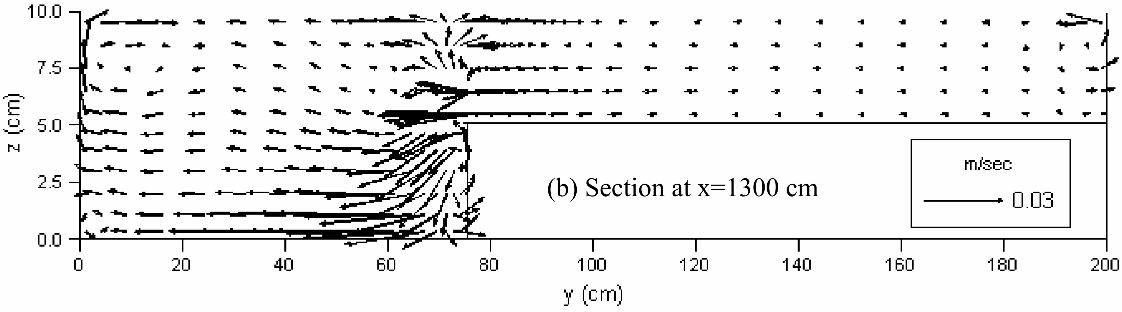

(b) Section at x=1300 cm

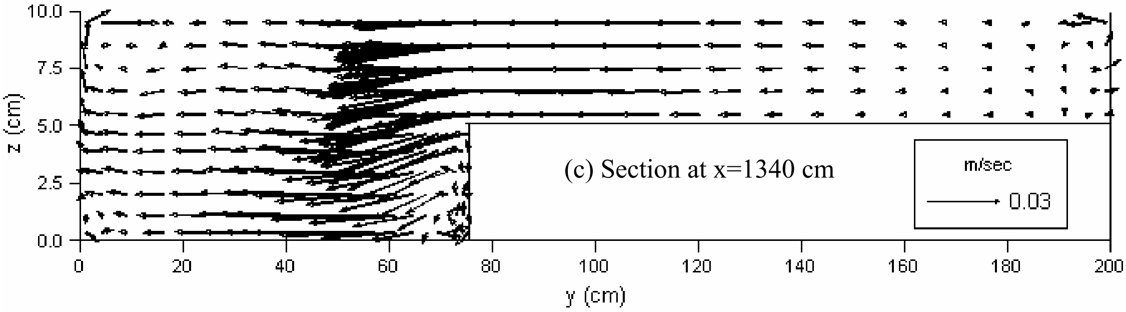

(c) Section at x=1340 cm

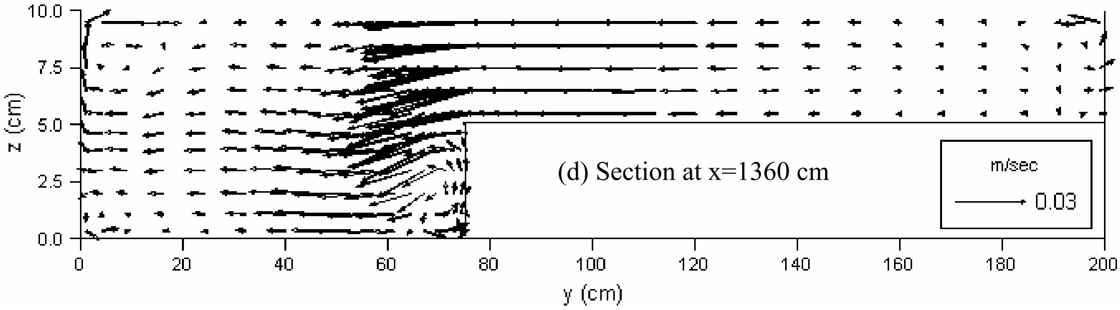

(d) Section at x=1360 cm

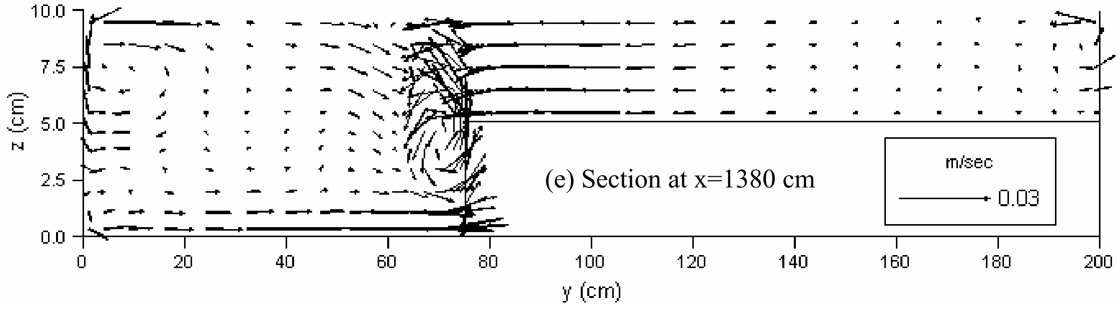

(e) Section at x=1380 cm

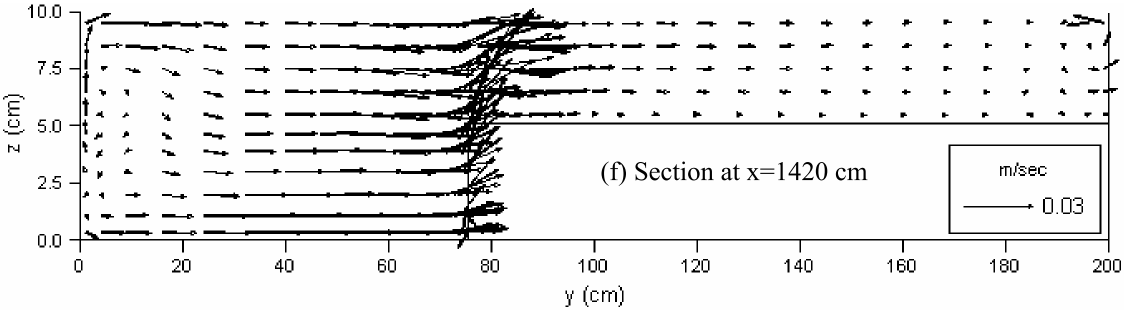

(f) Section at x=1420 cm

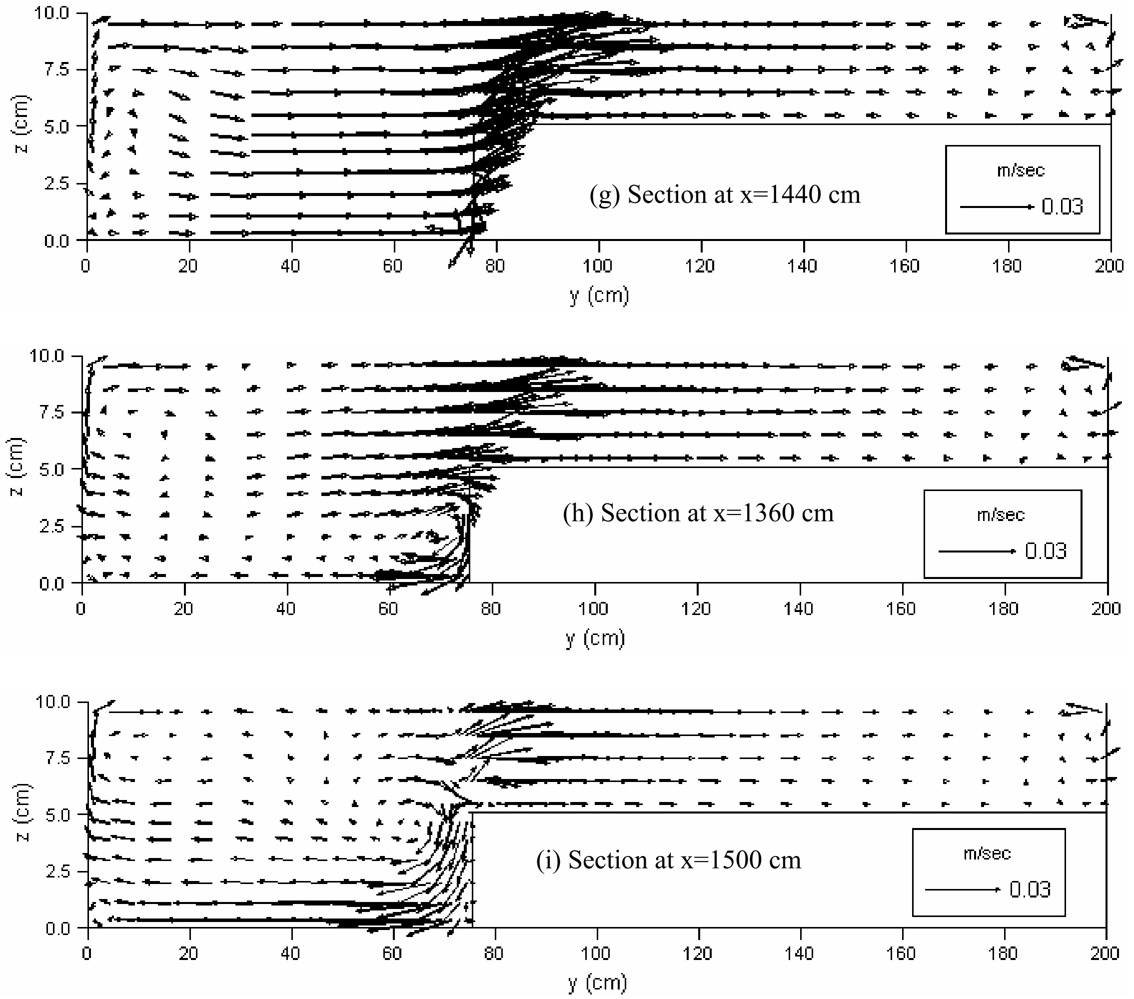

Fig. 5.8: The instantaneous profiles of secondary currents at different sections of a single vortex (Case-A2)

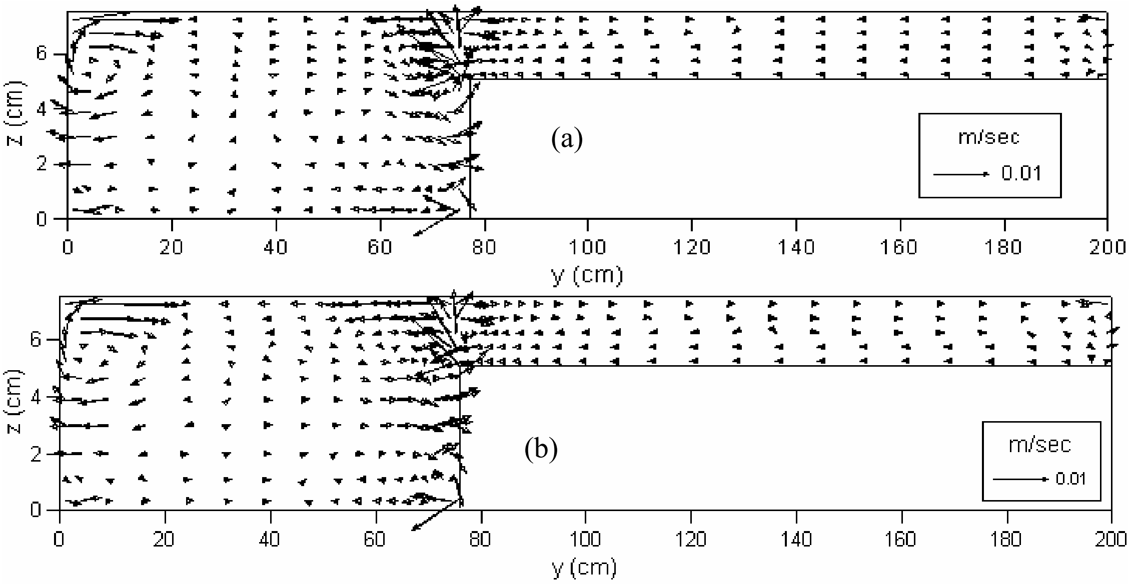

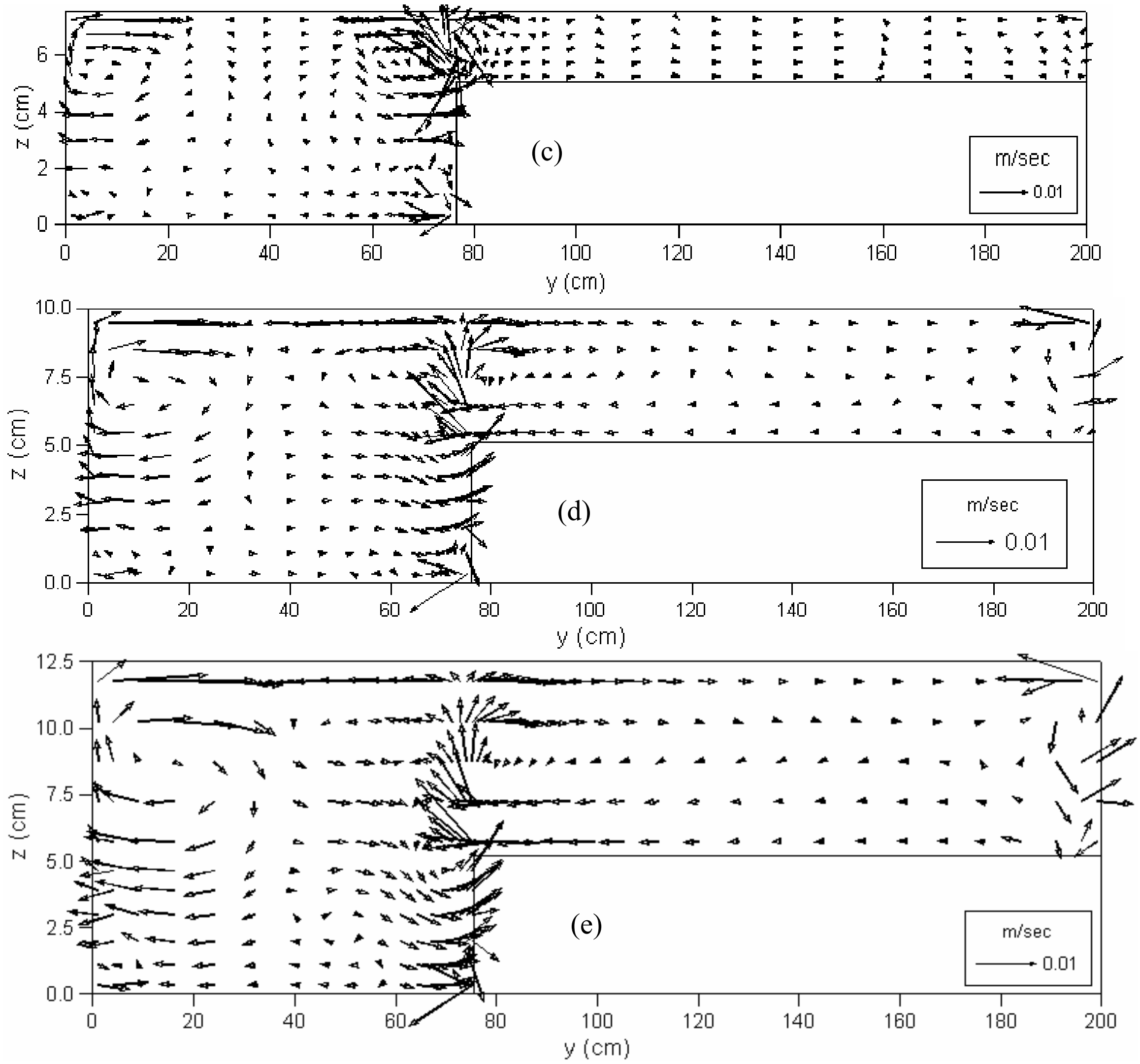

Fig. 5.9: Spatially averaged cross-sectional flow pattern of secondary currents: (a) Case-A1, 2nd order model (b) Case-A1, 3rd order model (c) Case-A1, 3rd order model without considering horizontal vortex (d) Case-A2, 3rd order model (e) Case-A3, 3rd order model

5.4.3 *Prediction of discharge*

The simulated discharge in a compound channel predicted by all the models for all three cases of geometry-A are plotted against time and shown in Fig. 5.10. The predicted discharges with and without including vortices indicate the contribution of vortices. On the other hand, the model performance between standard and non-linear k–ε model are clearly depicted. For all the cases, the linear model predicts higher discharge over non-linear one, and the simulated flow field without vortices also over predicts the discharge compared to a flow field with vortices. Thus the maximum and minimum discharges are predicted by a standard model without vortices and a non-linear model with vortices condition respectively; the comparisons show about 5% to 8% difference in discharge computations for case A1 to case A3 respectively.

(a)

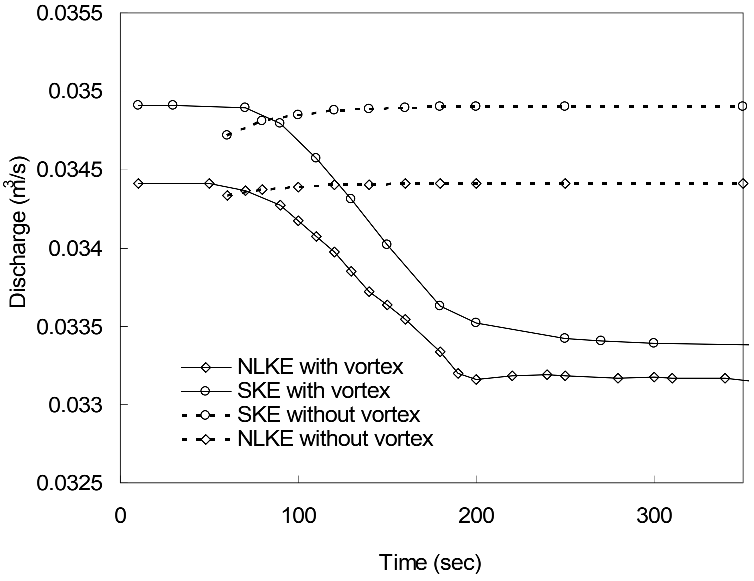

(b)

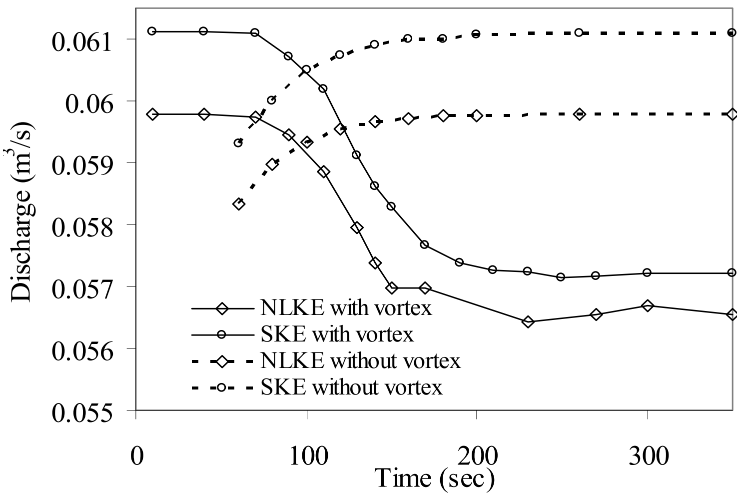

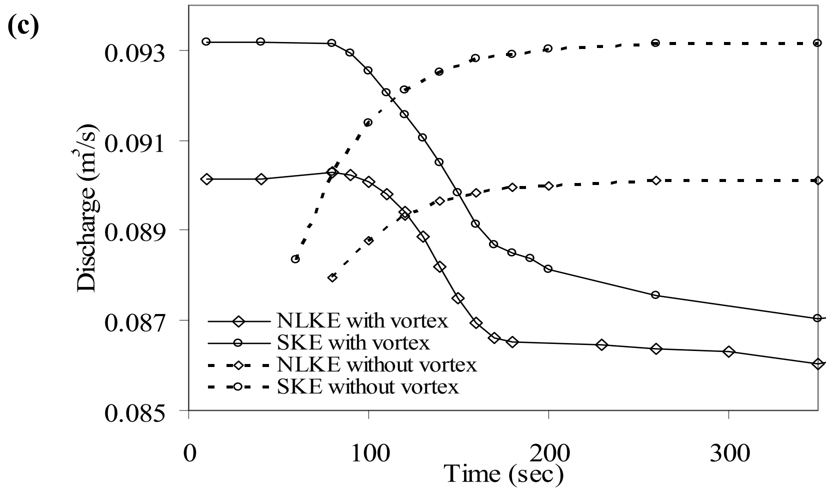

Fig. 5.10: Discharges computed by different models for (a) case-A1, (b) case-A2, and (c) case-A3 (here, NLKE indicates second order model)

5.4.4 *Prediction of flow resistance*

The roughness coefficient for compound channel is calculated by numerical simulation, and compared to experimental as well as other semi-analytical results.

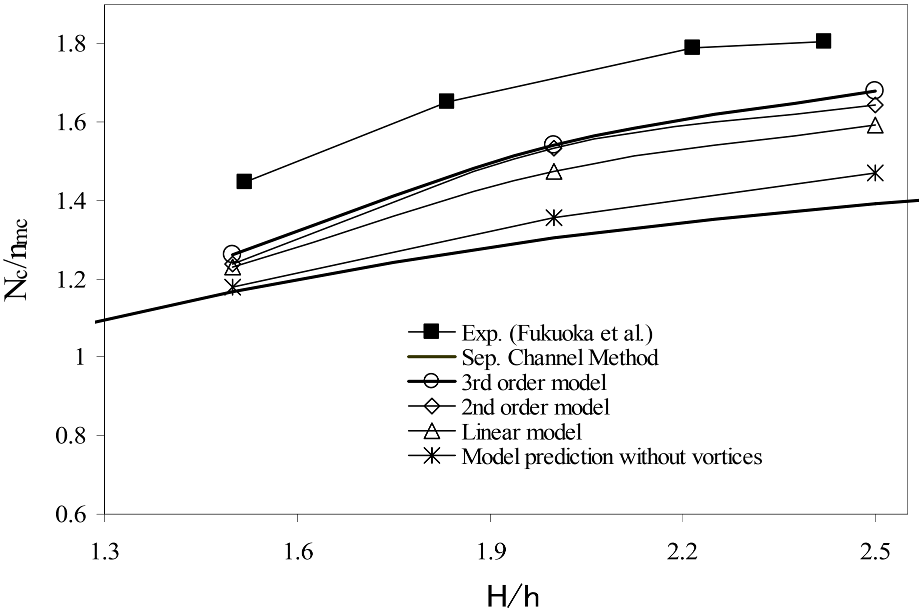

Fig. 5.11: Comparison of normalized compound roughness coefficient for different depth ratios

(a) Prediction Methods

(i) Method 1 (Separate Channel Method): The use of Manning's formula for discharge calculation is restricted to channels with an almost uniform velocity distribution in the cross-section. Thus, to use the equation for a compound channel, the cross-section is divided into two independent sections. Although the dividing line between main channel and flood plain can be either vertical, horizontal or diagonal, a vertical line is used here (dotted line in Fig. 5.3a), which is the most common and practical one. In this method the interaction of flows in two sections are completely neglected. The total discharge is evaluated as summation of the discharges in two sections as

$$Q=\frac{A_{fp}}{n_{fp}}\left(\frac{A_{fp}}{S_{fp}}\right)^{2/3} I_b^{1/2}+\frac{A_{mc}}{n_{mc}}\left(\frac{A_{mc}}{S_{mc}}\right)^{2/3} I_b^{1/2} \qquad (5.13)$$

where, I_b is the bed slope and '*n'* is the Manning's coefficient, A and S are the cross-sectional area and wetted perimeter respectively. The subscripts '*mc*' and '*fp*' are used to denote the parameters for main channel and flood plain respectively.

The magnitude of the flow resistance is estimated as a compound roughness coefficient, N_c, which is defined as follows

$$N_c=\frac{A_{mc}+A_{fp}}{Q}R_c^{2/3}I_b^{1/2}\,,\ \ R_c=\left[\frac{A_{mc}\left(A_{mc}/S_{mc}\right)^{2/3}+A_{fp}\left(A_{fp}/S_{fp}\right)^{2/3}}{A_{mc}+A_{fp}}\right]^{3/2} \qquad (5.14)$$

(ii) Method 2 (Computation with k-ε model): The definition of compound roughness coefficient in equation (5.14) can be written in the following form

$$\frac{N_c}{n_{mc}}=\frac{Q_{mc}}{Q}+\frac{n_{fp}}{n_{mc}}\frac{Q_{fp}}{Q} \qquad (5.15)$$

Using the standard and non-linear *k*- ε model as described in Eqs. (5.1) to (5.7), the discharge in main channel and flood plain are computed to calculate the compound roughness coefficient using the above relations.

(b) Comparison of roughness coefficient

For different depth ratios, the compound roughness coefficients evaluated by different methods and using various models are plotted in Fig. 5.11, along with the experimental results by Fukuoka et al. (1989). It is shown that the separate channel method, where the flow interaction between two subsections is not taken into account, shows the worst comparison with experimental result. The figure indicates that the standard and non-linear *k*–*ε* model can reproduce the increase of roughness coefficient due to lateral momentum transfer. The contribution of vortices in the momentum transfer, and thus to the channel roughness, can be quantified by the difference in their magnitude predicted by the models with and without vortices. The non-linear *k*- ε model shows best result over standard one. Slight improvement is observed in the prediction of third order model over that of second. Comparing the results for case A3, it is observed that the numerical result improves the resistance coefficient by about 21% over the separate channel method, where the vortices contribute about half of that and the rest is due to secondary current and associated three-dimensional turbulent structure. However, the value still about 9% underestimated than the experimental value.

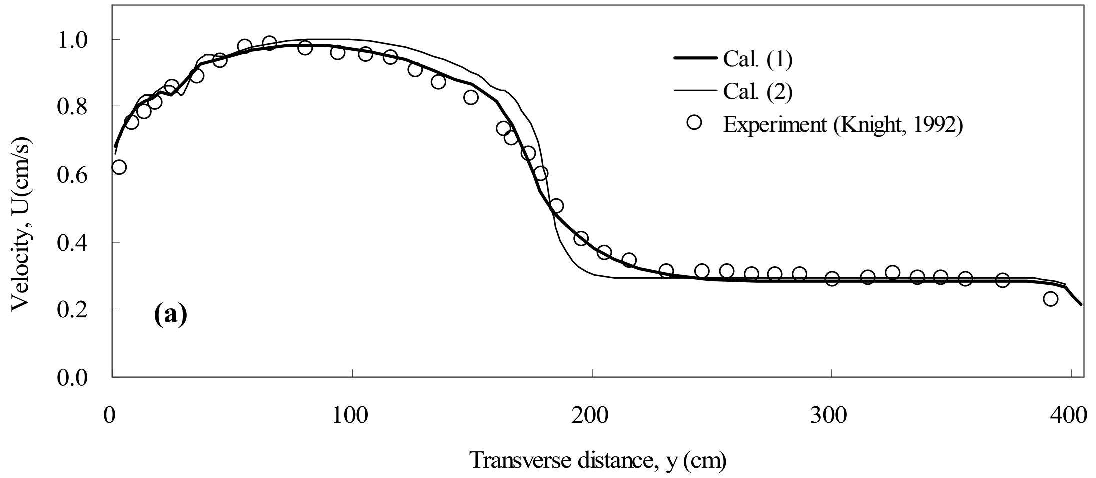

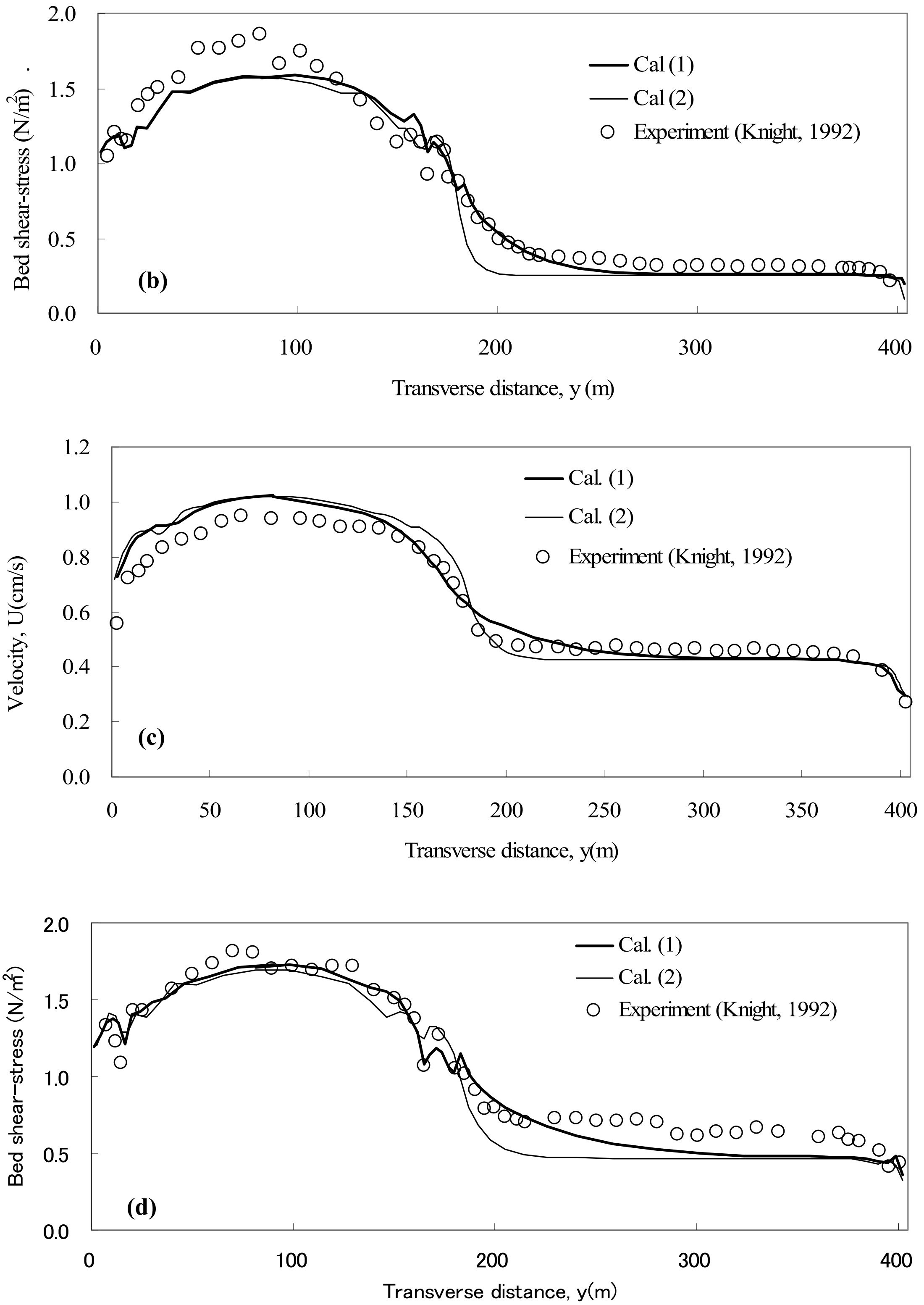

Fig. 5.12: Spatial averaged cross-sectional profiles for (a) stream-wise velocity for case B1 (b) boundary shear stress profile for case B1 (c) stream-wise velocity for case B2 (d) boundary shear stress profile for case B2

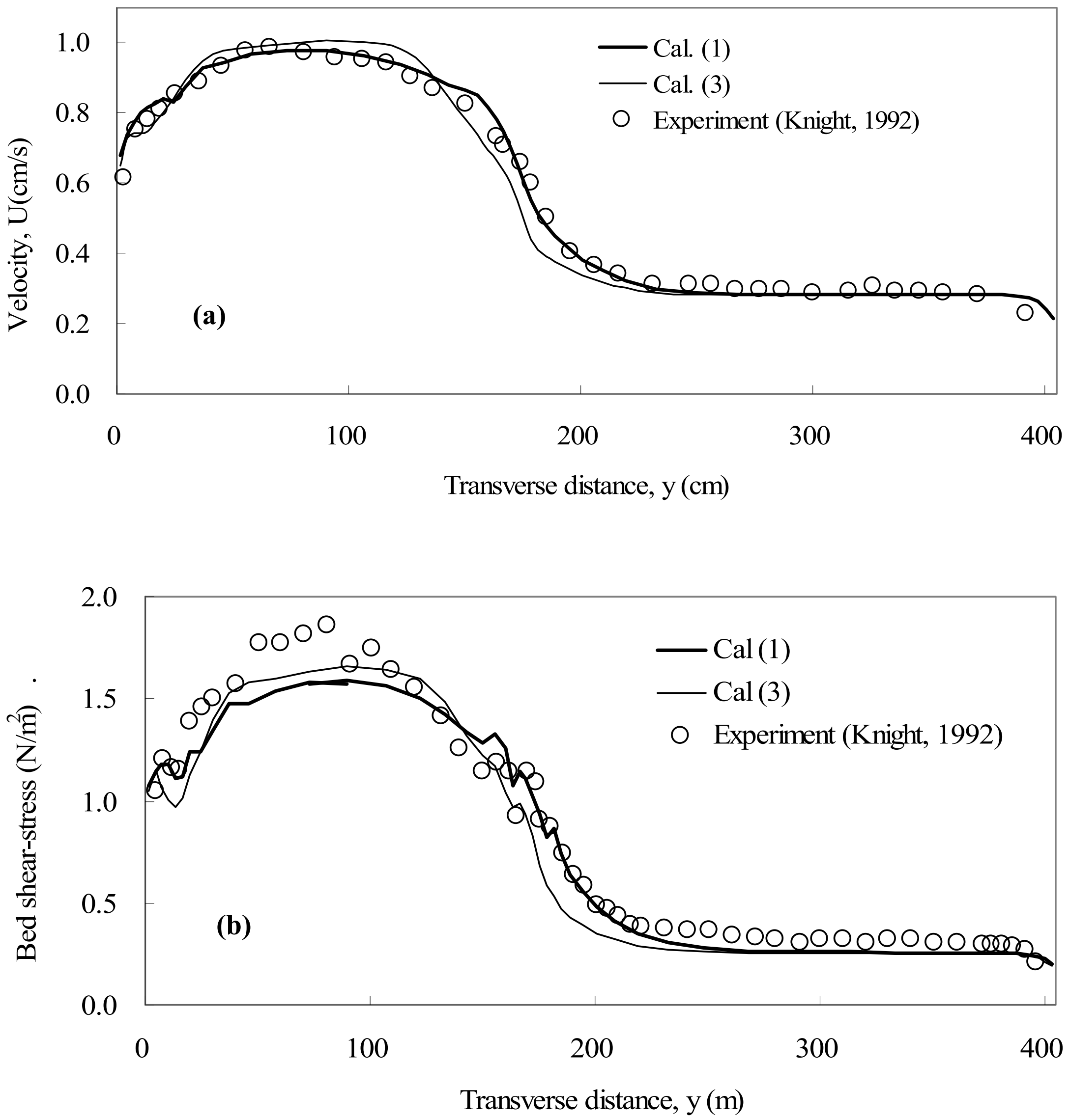

Fig. 5.13: Comparison of spatial averaged cross-sectional profiles with Abe et al.(1997) for (a) stream-wise velocity for case B1 (b) boundary shear stress profile for case B1

5.4.5 Velocity and shear stress profiles

The depth averaged velocity and bed shear stress profiles are computed by 3rd order non-linear model for cases B1 and B2. The calculated profiles are compared with the laboratory experiments of Knight (1992). In Figure 5.12, Cal. (2) represents the profile without considering transverse momentum transfer due to horizontal vortices. It is observed that the simulation results by the non-linear model (Cal.-1) are in good agreement with experiments. However, Cal. (2) under-predicts the velocity and shear-stress values at least near the interface region. The comparison reveals that, the well agreed profiles are obtained when the effects of vortices are considered.

The flow field is also calculated using the model by Abe et al. (1997) and shown in Fig.5.13 as Cal. (3) with comparison to previous experiments as well as the prediction of present model. Present model (Cal. 1) shows better comparison than Abe's model. Cal. (3) under-predicts the velocity and shear-stress values near the interface region.

5.4.6 Compound Channel with two flood plains

Numerical simulation is performed for the same condition of experiments reported by Shiono and Knight (1991) for first phase of FCF-02 experimental series having two-flood plain in the geometry with B/b=4.2 and (H-h)/H=0.157. The temporal change of coherent vortices at interfaces of main channel and flood plains are shown in Fig. 5.14. The vortex merging observed for geometry A is also observed here. For a particular time, the instability vortices at two interfaces are found to form at the same downstream distances.

The spatial and depth averaged velocity profile is compared with experiment in Fig. 5.15. An excellent agreement is observed. In Fig. 5.16, the simulation of spatial averaged secondary current is compared with experiments. The patterns as well the magnitudes are found in close agreement with each other. Near the interface region, three counter rotating secondary flow cells are observed. Among two surface cells, the first one is at the top edge of flood plain, which contains the scale as same as flood plain depth. The bottom secondary flow cell has the size of main channel depth. The comparison of bed shear stress profiles also shows very good agreement in Fig. 5.17.

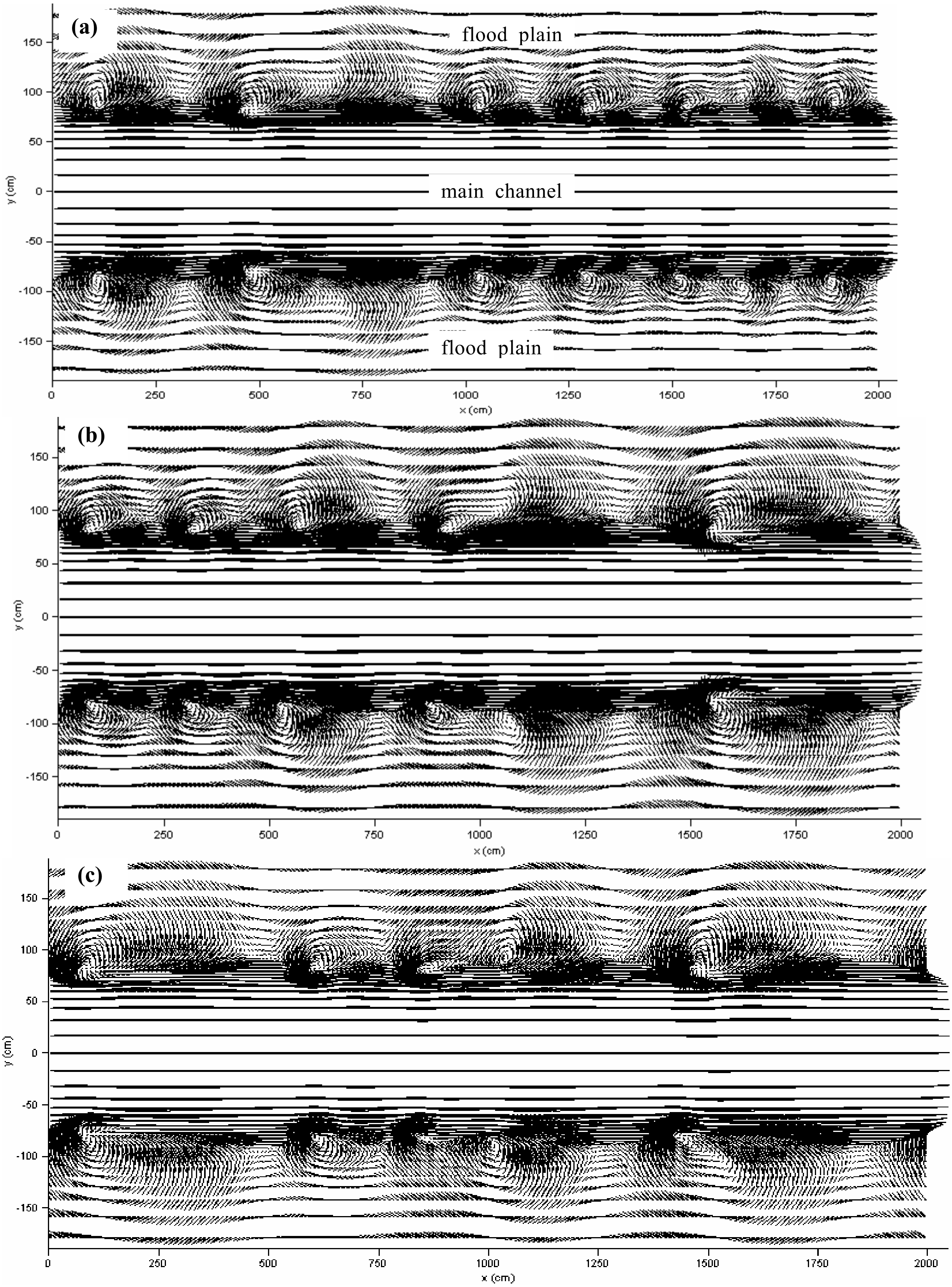

Fig. 5.14: Temporal change in the plan view of flow pattern for the case of two flood plain of case-A3: (a) t=100 sec (b) t=120 sec (c) t=230 sec

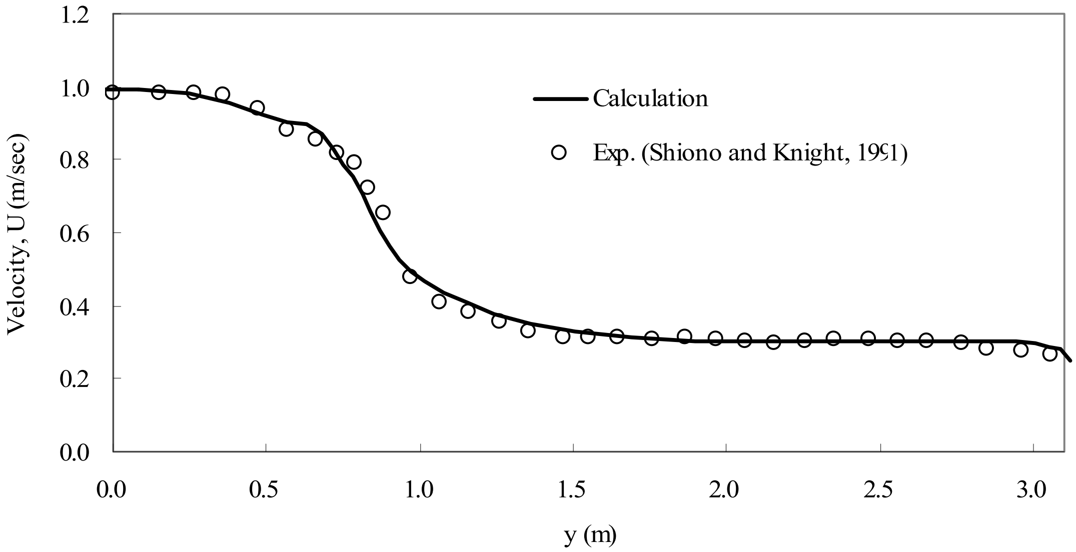

Fig. 5.15 Comparison of depth averaged velocity profile for case C1 (two flood plain), calculation is made using 3rd order model.

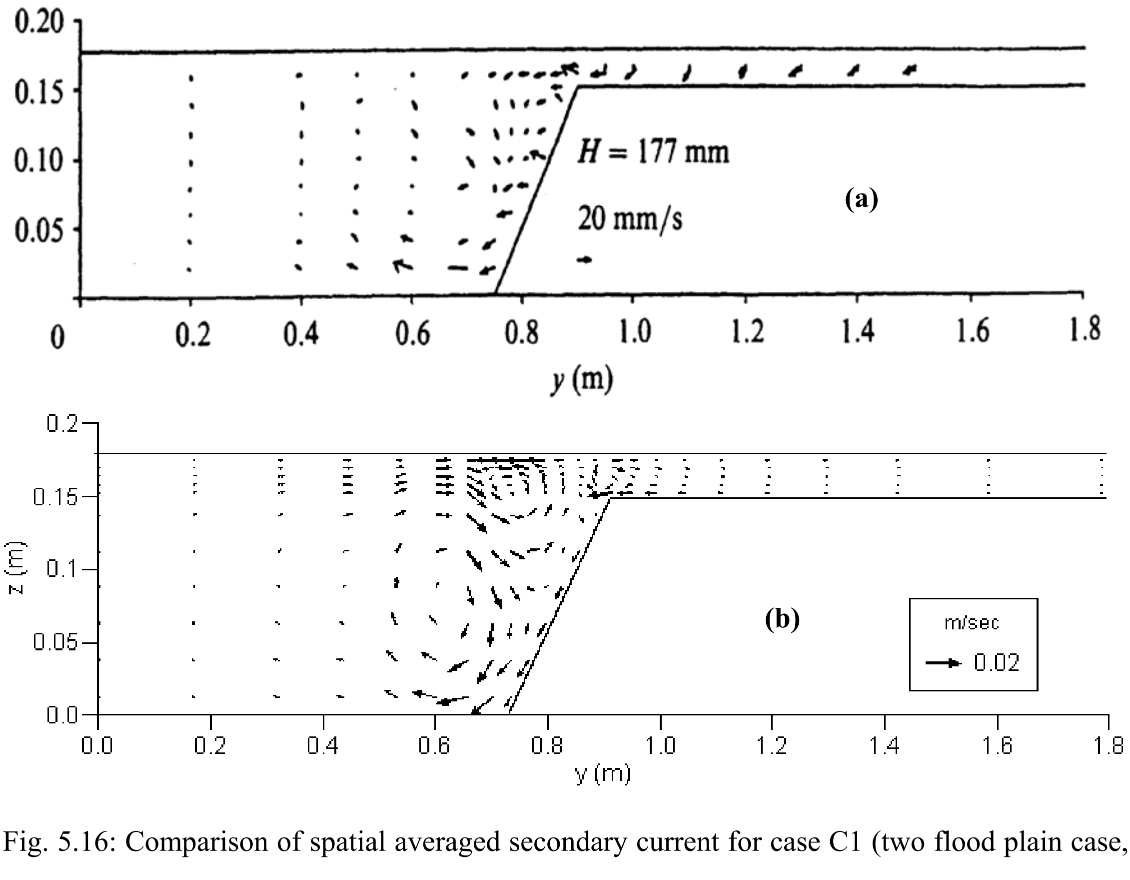

Fig. 5.16: Comparison of spatial averaged secondary current for case C1 (two flood plain case, calculation is made using 3rd order model): (a) Experimental (Shiono and Knight, 1991) (b) Simulation result

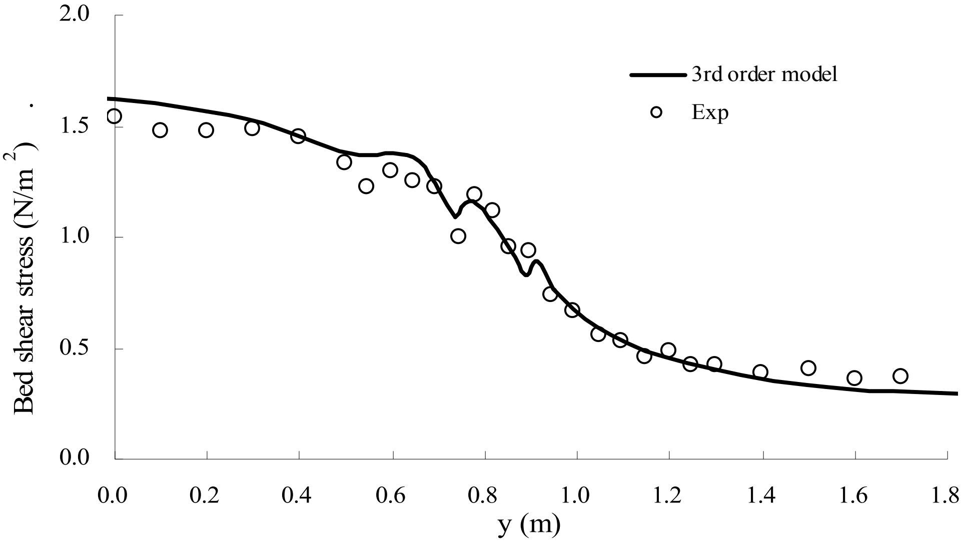

Fig. 5.17: calculated spatially averaged boundary shear stress profile for case C1 compared with the experimental results by Shiono and Knight (1991)

5.4.7 Turbulent properties of coherent vortices in compound channel

In the previous chapter, approximate solutions are derived for the turbulent characteristics of Stuart vortices, and the spatial distributions and topological changes of turbulent structures with singular points are evaluated. In the previous section of this chapter, it is showed that in a compound channel the horizontal vortices are generated at the interface of main channel and flood plain due to turbulent shear layer. In this section, the characteristics of coherent vortices are analyzed from the view point of the formation and spatial change of turbulent structures with respect to singular points. The properties are compared with the approximate analytical solution (presented in chapter 4) as well as with the previous experiments.

Fig. 5.18 shows the plan view of flow patterns for case-A1 at t=300 sec. The generated horizontal vortices are observed in the figure clearly. The turbulent structures near the vortex point at two different spatial distances are shown in Figs. 5.19 and 5.20. The flow vectors of two individual vortices are shown in Figs. 5.19(a) and 5.20(a) for the stream-wise distances of *x*=200 to 380 cm and *x*=760 to 920 cm respectively. The figures indicate that the turbulent normal stresses in *x*, *y* and *z* directions, expressed as $\overline{u_1u_1}$, $\overline{u_2u_2}$ and $\overline{u_3u_3}$ respectively, show the contours in elliptical structure at the vortex center [Figs. (d), (e) and (f) respectively]. The structures of turbulent kinetic energy (*k*) and dissipation rate (ε) [Figs. (b) and (c)] are similar to turbulent normal stresses. On the other hand, the turbulent shear stress in *xy* plane ($\overline{u_1u_2}$) shows hyperbolic profile [Fig. (g)].

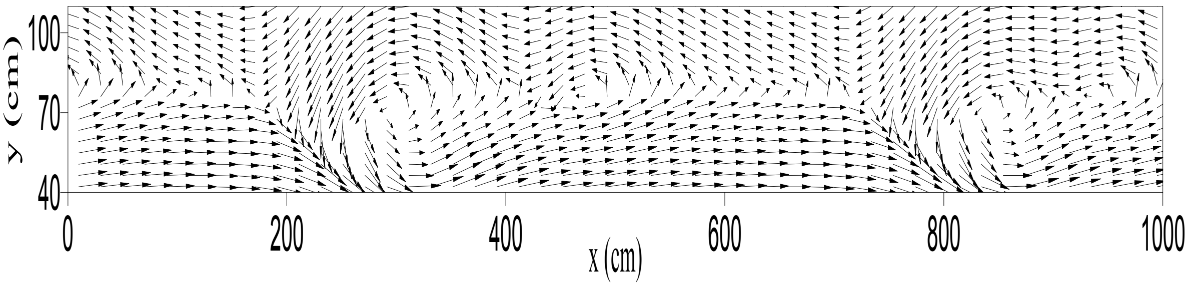

Fig. 5.18 Plan view of flow vectors showing the horizontal vortices at the interface of main channel and flood plan (case A1, t =300 sec)

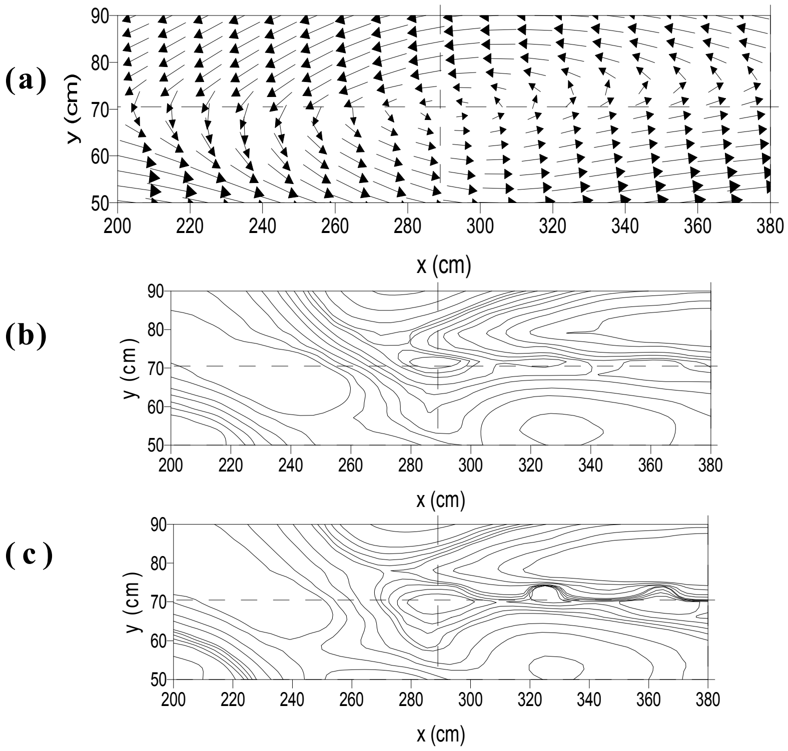

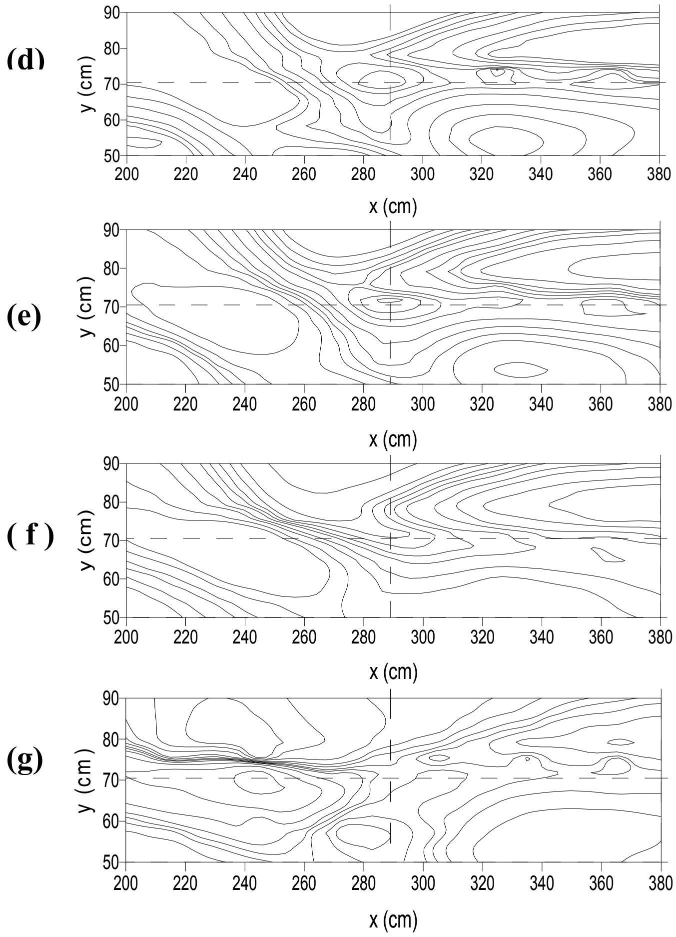

Fig. 5.19 Turbulent structures near the center of a vortex (x =200~380 cm): (a) plan view of flow vectors (b) k (c) ε (d) $\overline{u_1u_1}$ (e) $\overline{u_2u_2}$ (f) $\overline{u_3u_3}$ (g) $\overline{u_1u_2}$

The turbulent structures for saddle point are shown in Fig. 5.21. It is found that the turbulent kinetic energy and dissipation rate as well as turbulent normal stresses show hyperbolic profile (saddle pattern) in the saddle point. However, the shear stress shows elliptical structure.

Therefore, the changes of topological structures of turbulent stresses in the large scale vertices of a compound channel are found compatible with analytical solution of the idealized vortex street. The features are also compatible to the previous experimental results on large scale coherent vortices in free shear flows (Hossain, 1986).

Hossain (1986) reported that the turbulence production is an important criterion to explain the roles of ribs and vortex stretching in a coherent vortex. Fig. 5.22 shows the structures of turbulence production at vortex center [Figs. (a) and (b)] and saddle point [Fig. (c)] for different spatial distances. Comparing the turbulent structures for both the vortex and saddle points with Figs. 5.19 to 5.21, it is found that the turbulence productions follow the structures of turbulent shear stresses. The quantitative comparison indicates that the turbulence production at the vortex center is very small, but is larger in the upstream and downstream directions, being the maximum at the saddle on either side. This feature is also consistent with the measurements of coherent structures in free shear flows.

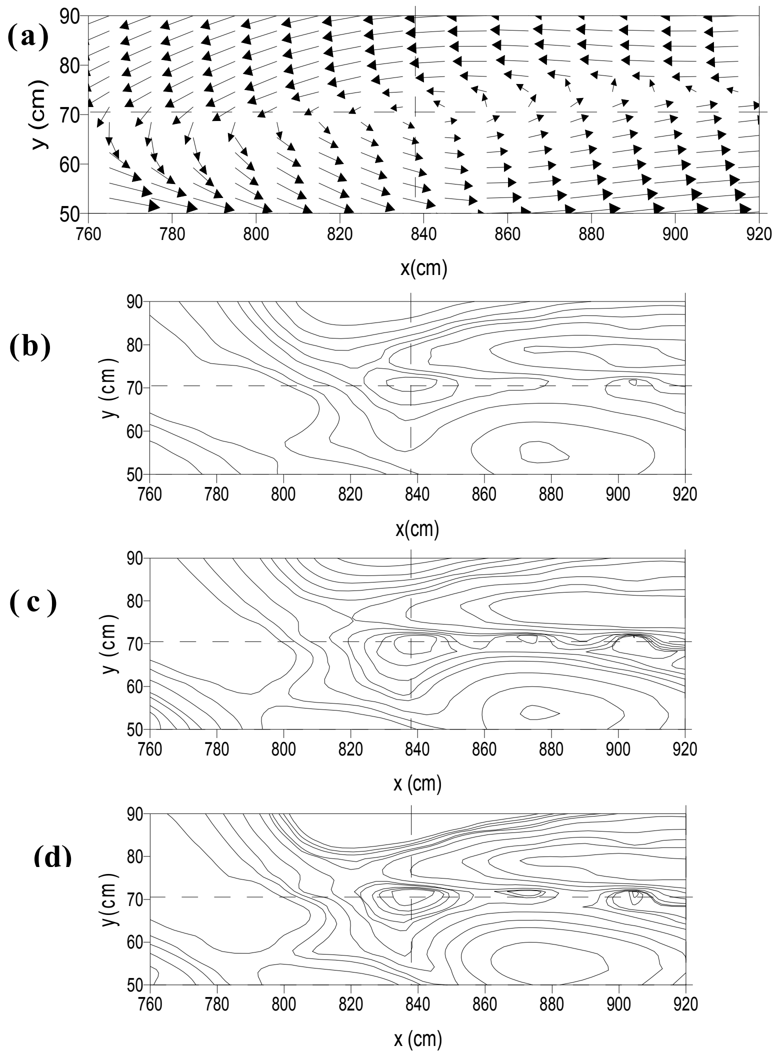

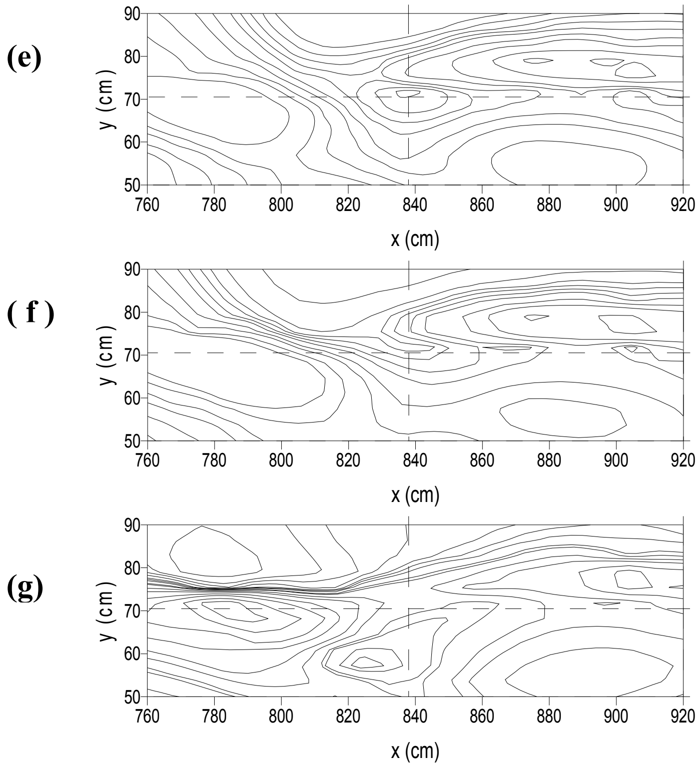

Fig. 5.20 Turbulent structures near the center of a vortex (x =760~920 cm): (a) plan view of flow vectors (b) k (c) ε (d) $\overline{u_1u_1}$ (e) $\overline{u_2u_2}$ (f) $\overline{u_3u_3}$ (g) $\overline{u_1u_2}$

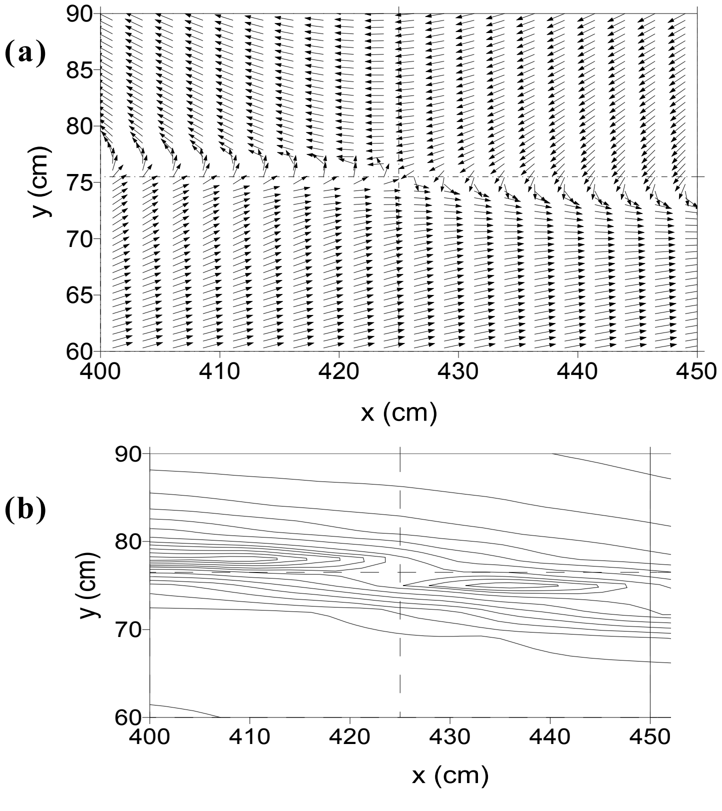

(c)

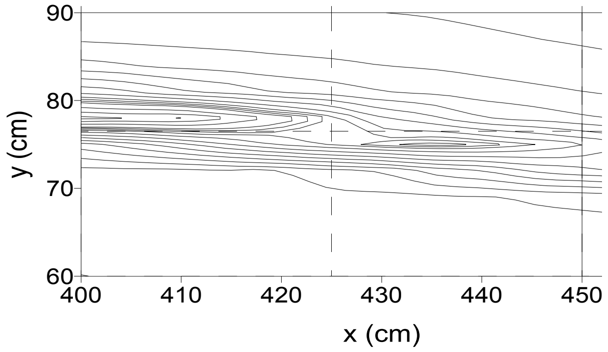
90
80
70
60
y (cm)
400
410
420
430
440
450
x (cm)

(d)

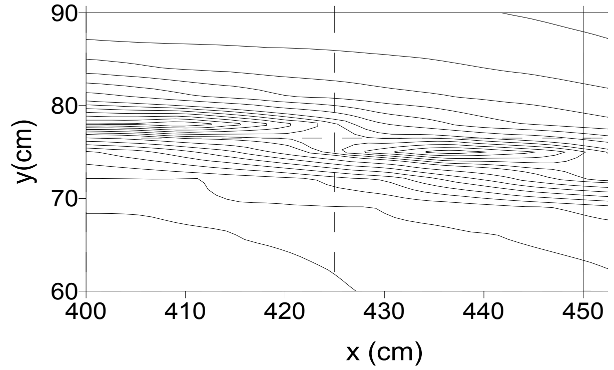
90
80
70
60
y(cm)
400
410
420
430
440
450
x (cm)

(e)

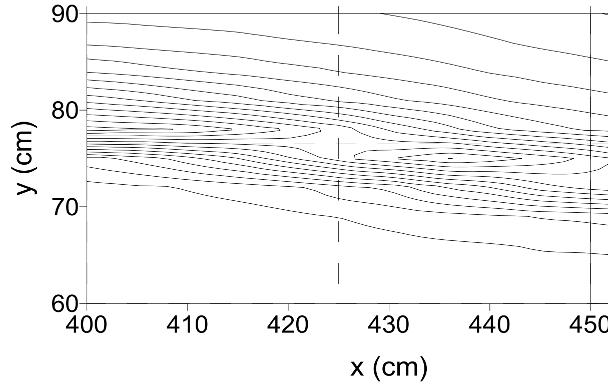
90
80
70
60
y (cm)
400
410
420
430
440
450
x (cm)

(f)

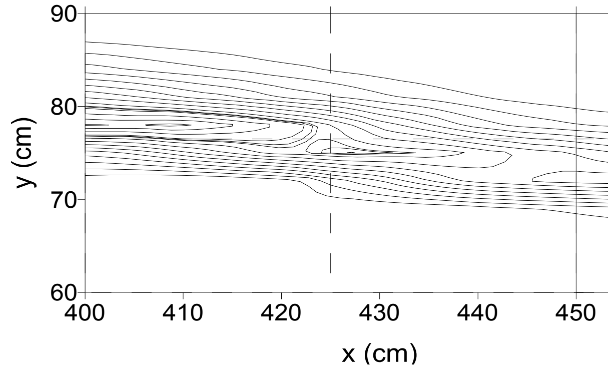
90
80
70
60
y (cm)
400
410
420
430
440
450
x (cm)

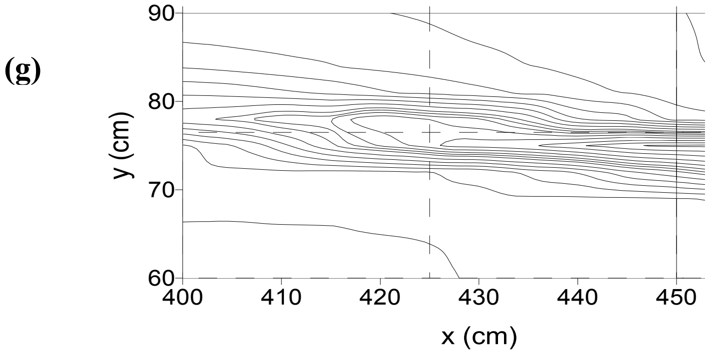

Fig. 5.21 Turbulent structures at the saddle point (x = 400~450 cm): (a) plan view of flow vectors (b) k (c) ε (d) $\overline{u_1u_1}$ (e) $\overline{u_2u_2}$ (f) $\overline{u_3u_3}$ (g) $\overline{u_1u_2}$

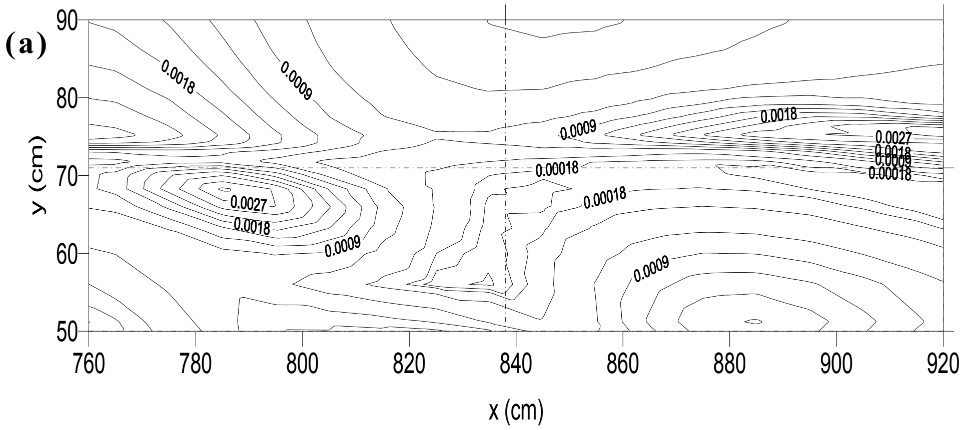

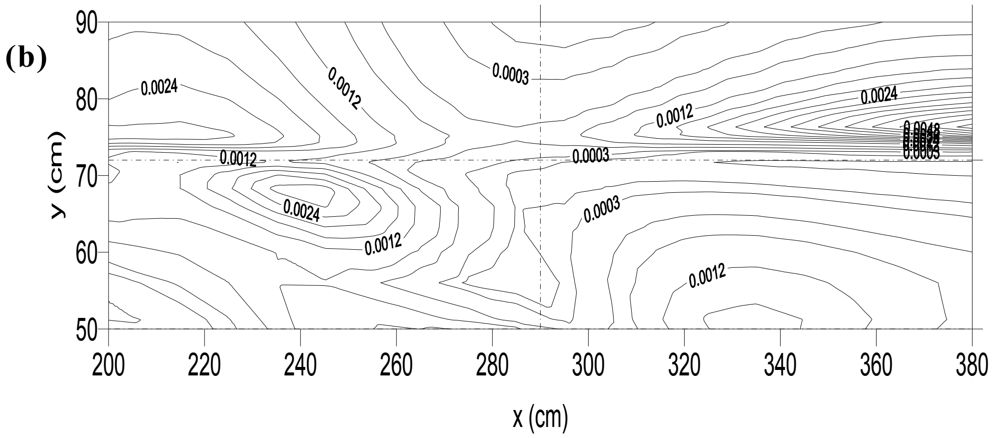

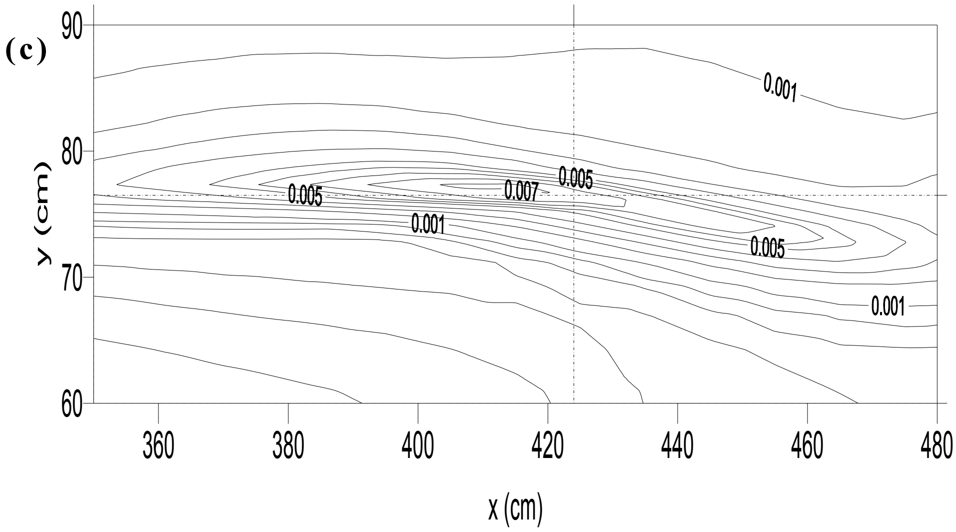

Fig. 5.22 Contour of turbulence production: (a) near the center of a vortex for *x* =200~380 cm (b) near the center of a vortex for *x* =760~920 cm (c) at saddle point for *x* =350~480 cm

5.5 Summary

The flow field in a compound channel is generated using standard as well as non-linear k-ε models with including and omitting the horizontal vortices. The numerical results are assessed from the view point of coherent structures, such as horizontal vortices at the interface of subsections and secondary current of second kind. The predicted discharges by different models are compared and the contribution of eddy viscosity and quadratic term in non-linear model is evaluated. Comparing the predicted roughness coefficients with previous experimental results as well as with other methods, the contribution of vortices and secondary currents to the prediction of roughness coefficients are quantified. Based on simulated results following conclusions are made:

(i) The velocity and shear-stress profiles are found to be distorted significantly due to generation of coherent vortices at the interface of main channel and flood plain. It is observed that the velocity and shear stress values are under-predicted near the interface region, if momentum transfer due to horizontal vortices is not considered. The well agreed profiles are obtained when the effects of vortices are taken into account.

(ii) The magnitudes of secondary currents as well as the qualitative features of the flow patterns are found to be well comparable with previous experimental observations. Although the pairs of surface vortices as well as the corner vortices in main channel are clearly depicted by both the non-linear models, the 3rd order model shows better agreement with experiments than 2nd order model. It is seen that the magnitude of upwelling secondary currents at the interface are suppressed by the influence of flows caused by the coherent vortices. The secondary currents for higher depth ratios (H/h) are found higher in magnitude compared to lower depth ratios. It is noted that with increasing the flood plain depth, the scales of surface vortices are increased. The magnitudes of secondary currents are also increased significantly with the flood plain depth.

(iii) The flow exchange between main channel and flood plain is found to be minimum at saddle point and vortex center, which gradually increases with streamwise distance and being the maximum in between two critical points.

(iv) The resistance of compound channel is increased due to generation of coherent structures. The numerical result improves the prediction of compound resistance coefficient by about 21% over the separate channel method, where the vortices contribute about half of that and the rest is due to secondary currents and associated three-dimensional turbulent structures.

(v) For symmetrical two flood plain case, the instability vortices at two interfaces are generated at the same downstream distances in a particular time. The simulated results of sectional depth averaged velocity and bottom shear stress profiles show an excellent agreement with experiment. The pattern as well as the magnitude of secondary current is also found in close agreement. Near the interface region, three counter rotating secondary flow cells are observed. Among two surface cells, the first one is at the top edge of flood plain, which contains the scale as same as flood plain depth. The bottom secondary flow cell shows the size of bank-full depth of main channel.

(vi) The turbulent structures are found to be changed with the spatial distance depending on the structures of singular points. It is observed that the turbulent normal stresses show elliptical structure near vortex center, which changed to hyperbolic profile near saddle point. However, the shear stresses show hyperbolic structures at vortex center and the structure changes to elliptical at saddle point. The topological change of turbulent kinetic energy and dissipation rates with stream-wise spatial distance are found similar to turbulent normal stresses.

(vii) The turbulent structures of horizontal vortices generated at the interface of main channel and flood plain are well agreed with that of approximate solution of an idealized vortex street. The structures of turbulent stresses at vortex center and saddle point are found consistent with previous experiments of coherent structures in free shear flows.

(viii) Comparing the topology of turbulence production both for vortex center and saddle points, it is seen that they follow the structures of turbulent shear stresses. The quantitative comparison indicates that the turbulence production at the high vorticity point (vortex center) is very small, but is larger in the upstream and downstream directions, being the maximum at the saddle on either side, where the vorticity is minimum. This feature is also consistent with the measurements of coherent structures in free shear flows.

5.6 References

1) Abe, K., Kondoh, T., Nagano, Y., On Reynolds-stress expressions and near-wall scaling parameters for predicting wall and homogeneous turbulent shear flows, *Int. J. Heat and Fluid Flow.* 18, pp.266-282, 1997.

2) Bousmar, S., *Flow Modeling in Compound Channel*, Doctoral thesis, Universite′ Catholeque de Louvain, Belgium, 2002

3) Fukuoka, S. and Fujita, K., Prediction of flow resistance in compound channels and its application to design river courses, *J. Hydr., Coast. and Envir. Engrg.,* No.411/II-12, pp. 63-72, 1989.

4) Hossain, A. K. M. F., Coherent structures and turbulence, *J. Fluid. Mech.,* 173, 303, 1986.

5) Knight, D. W., *SERC-FCF Exp. data phase-A, Report SR314,* HR Wallingford, UK., 1992

6) Shiono, K. and Knight, D. W., Turbulent open channel flows with variable depth across the channel, *J. Fluid Mech.*, 222, pp. 617-646, 1991.

7) Sugiyama, H. Akiyama, M. and Matsubara, T., Numerical simulation of compound open channel flow on turbulence with a Reynold Stress Model, *J. Hydr., Coast. and Envir. Engrg.*, No.515/II-31, pp. 55-65, 1995.

8) Tominaga, A. and Nezu, I, Turbulent structure in compound channel flows, *J. Hydr. Engrg., ASCE*, No.117, pp. 21-41, 1991.

9) Wormleaton, P. R., Floodplain secondary circulation as a mechanism for flow and shear stress redistribution in straight compound channels in *Coherent Flow Structures in Open Channels* (edited by Ashworth, Bennett, Best and McLelland), John wiley and Sons publication, 1996.

Chapter 6

THE STRUCTURE AND DECAY OF TURBULENT RANKINE VORTEX WITH AND WITHOUT AXIAL FLOW

6.1 Introduction

The basic types of plane vortices can be classified into two categories: one with slower velocity at center and maximum at sides; and the other with maximum at center and minimum velocity at edges. The rotary fluid motion of the first one is called the solid body rotation, since it is similar to the fluid motion filled in a rotating hollow box. On the other hand, if a long circular rod rotates in a fluid with constant velocity around its axis, the fluid velocity is found highest and equal to the velocity of rod at the rods surface (due to adhesion); and with increasing distance from the rod, the velocity is diminished in inverse proportional to the distance. Such a fluid motion is called a potential vortex (Fig. 6.1). Fluid motion composed of a potential vortex and solid body rotation is called Rankine vortex after the fluid dynamicist Rankine. The radial distance from the center to the maximum tangential velocity is called the radius of vortex core (Fig. 6.1(c)). For a steady circular motion without a velocity component normal to the plane of rotation, the rankine vortex in the only possible vortex whose velocity is zero at the center as well as far away from it. In addition to these basic vortices, there are other time-dependent rotary motions that have azimuthal velocity component as well as radial and axial components.

The pressure in a vortex is not uniformly constant with the radial distance. We know the distribution of pressure for a solid body rotation, for instance in a rotating box, is parabola (Laugt, 1983). The minimum pressure exists at the center and increases towards the wall of the box [Fig. 6.2(a)]. On the other hand for a potential vortex, the pressure increases from wall to outwards distance in a concave manner [Fig. 6.2(b)]. Therefore, the combination of these two gives the pressure distribution of Rankine vortex as shown in Fig. 6.2(c).

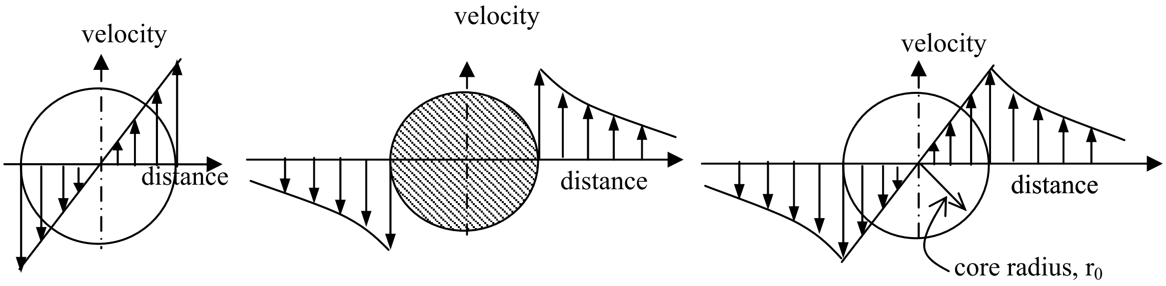

(a) **(b)** **(c)**

Fig. 6.1 Velocity distribution in (a) solid body rotation (b) potential vortex (c) Rankine vortex

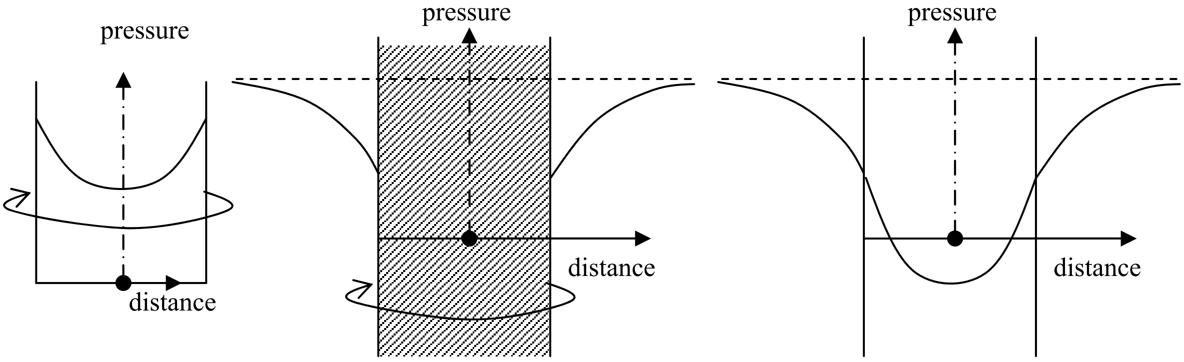

(a) **(b)** **(c)**

Fig. 6.2 Pressure distribution in (a) solid body rotation (b) potential vortex (c) Rankine vortex

The existence of such vortices is not limited to natural phenomena but also in many engineering applications. The Rankine vortex has been used extensively in various studies; for instance, to predict the decay of wing-tip vortices, to estimate the noise level produced by vortices and vibrations, and to model the natural phenomena such as hurricanes and tornados. Current aircraft spacing in and around airports is partially governed by the vortex wake hazard caused by the possible interaction between leading aircraft's trailing wake and vortices and following aircraft. However, the vortex behavior behind a lifting vehicle is still a topic of debate.

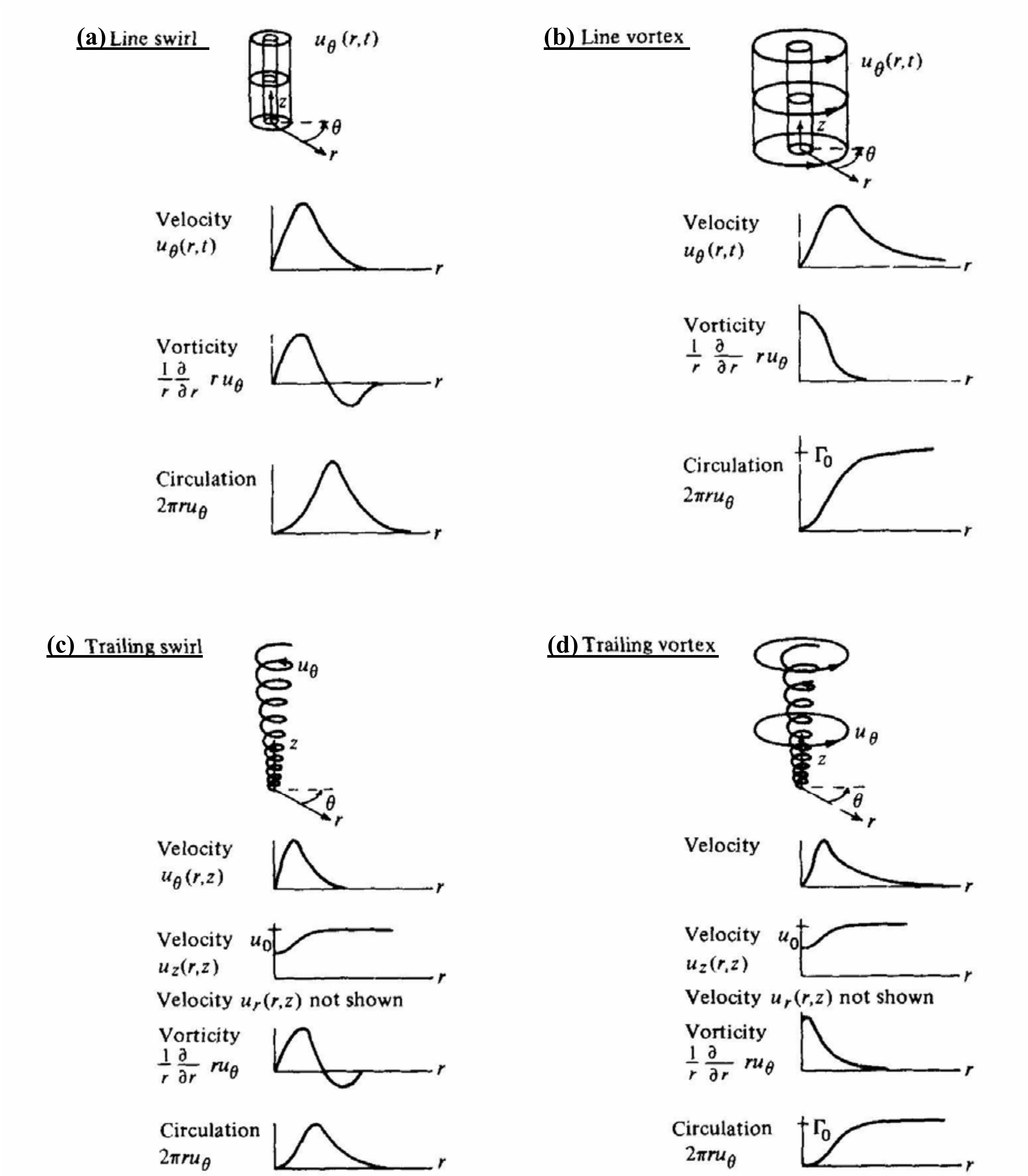

Fig. 6.3 Types of Rankine vortex based on far-field behavior (Uberoi, 1979); here, u_θ and u_z represent the tangential and axial velocity respectively.

The understanding about the internal structure as well as the mechanism of turbulence growth in the vortex core is also debatable. Vortex flows are the major cause of cavitation and underwater acoustics in marine propellers. Cavitation and hollow core due to pressure deficit at vortex center causes air-entraining vortices, which is an important part in hydraulics. Therefore, the emphasis on present topic is not only due to academic interest, but due to its practical importance as well.

Fig. 6.4 A smoke picture of wing-tip vortex observed in the wake of an agricultural aircraft (Courtesy NASA/JPL- Caltech)

Uberoi (1979) reported that in the far field such vortex is nearly independent of initial conditions and may take one of the four forms. Figure 6.3 shows the sketch of four possible flow profiles. Author considered that the line vortex and trailing vortex classification are the most relevant to study their properties. The line vortex is a time dependent, infinitely long region of concentrated vorticity with one non-zero velocity component, V_θ. Here $V_\theta = \Gamma_0/2\pi r$ contains zero circulation at r =0, and non-zero net circulation for large r. A trailing vortex is a time dependent vorticity concentration created at the tip of a semi-infinite wing with two non-zero velocity components, V_θ and Vz , and constant circulation at infinity. Therefore, the main difference between the trailing and line vortex is the presence of axial velocity component. As an example, a photograph of a trailing vortex generated at the wing tip of an agriculture aircraft is shown in Fig. 6.4.

Other two vorticity concentrations, line swirl and trailing swirl, have zero circulation outside of some finite radius. They are unstable by Rayleighs criteria and are not considered in this research.

The work presented in this chapter can be classified into twofold. In the first part, unsteady numerical simulation with 3D velocity field is carried out for turbulent trailing vortex with different swirl numbers using non-linear k–ε model. Although 3D flow equations are solved, the simulation is carried out based on 2D numerical grid. The trailing vortex without axial velocity (i.e. line vortex) is also simulated. The general features of vortex decay as well as the different time periods of turbulence growth/decay captured in simulation result are discussed. The self similarity in radial distribution of tangential velocity and circulation profiles are tested for trailing vortex. Well-grown vortex field is compared with previous DNS data. The simulation is also performed using standard k–ε model, and comparison is shown with non-linear model.

In the second part, the 3D numerical simulation is carried out for an idealized Rankine vortex using non-linear k–ε model and large eddy simulation (LES). 3D staggered grid is used both for RANS and LES. The general flow features such as temporal change of vortex decay, distribution of water surface etc., predicted by both the models are compared.

6.2 Nonlinear k–ε Model

Following 3D flow equations are used in unsteady RANS calculation for all the cases of turbulent trailing and idealized Rankine vortex.

Continuity equation: $$\frac{\partial U_i}{\partial x_i} = 0 \qquad (6.1)$$

Momentum equation: $$\frac{\partial U_i}{\partial t} + \frac{\partial U_j U_i}{\partial x_j} = g_i - \frac{1}{\rho}\frac{\partial P}{\partial x_i} + \frac{\partial}{\partial x_j}\left(-\overline{u_i u_j}\right) + \nu \frac{\partial^2 U_i}{\partial x_j{}^2} \qquad (6.2)$$

k - equation:
$$\frac{\partial k}{\partial t}+\frac{\partial kU_j}{\partial x_j}=-\overline{u_i u_j}\frac{\partial U_i}{\partial x_j}+\frac{\partial}{\partial x_j}\left\{\left(\frac{\nu_t}{\sigma_k}+\nu\right)\frac{\partial k}{\partial x_j}\right\}-\varepsilon \tag{6.3}$$

ε - equation:
$$\frac{\partial \varepsilon}{\partial t}+\frac{\partial \varepsilon U_j}{\partial x_j}=-c_{\varepsilon 1}\frac{\varepsilon}{k}\overline{u_i u_j}\frac{\partial U_i}{\partial x_j}+\frac{\partial}{\partial x_j}\left\{\left(\frac{\nu_t}{\sigma_\varepsilon}+\nu\right)\frac{\partial \varepsilon}{\partial x_j}\right\}-c_{\varepsilon 2}\frac{\varepsilon^2}{k} \tag{6.4}$$

Turbulence model (Non-linear):
$$-\overline{u_i u_j}=\nu_t S_{ij}-\frac{2}{3}k\delta_{ij}-\frac{k}{\varepsilon}\nu_t\sum_{\beta=1}^{3}c_\beta\left(S_{\beta ij}-\frac{1}{3}S_{\beta\alpha\alpha}\delta_{ij}\right) \tag{6.5}$$

Here,

$$\nu_t=c_\mu\frac{k^2}{\varepsilon},\ S_{ij}=\frac{\partial U_i}{\partial x_j}+\frac{\partial U_j}{\partial x_i},\ \Omega_{ij}=\frac{\partial U_i}{\partial x_j}-\frac{\partial U_j}{\partial x_i},S=\frac{k}{\varepsilon}\sqrt{\frac{1}{2}S_{ij}S_{ij}},\Omega=\frac{k}{\varepsilon}\sqrt{\frac{1}{2}\Omega_{ij}\Omega_{ij}} \tag{6.6}$$

In Equation (6.5),

$$S_{1ij}=\frac{\partial U_i}{\partial x_\gamma}\frac{\partial U_j}{\partial x_\gamma},\ S_{2ij}=\frac{1}{2}\left(\frac{\partial U_\gamma}{\partial x_i}\frac{\partial U_j}{\partial x_\gamma}+\frac{\partial U_\gamma}{\partial x_j}\frac{\partial U_i}{\partial x_\gamma}\right),\ S_{3ij}=\frac{\partial U_\gamma}{\partial x_i}\frac{\partial U_\gamma}{\partial x_j}. \tag{6.7}$$

$$c_\mu=\frac{c_{\mu o}\,(1+c_{ns}S^2+c_{n\Omega}\Omega^2)}{1+c_{ds}S^2+c_{d\Omega}\Omega^2+c_{ds\Omega}S\Omega+c_{ds1}S^4+c_{d\Omega 1}\Omega^4+c_{ds\Omega 1}S^2\Omega^2} \tag{6.8}$$

$$c_\beta=c_{\beta o}\frac{1}{1+m_{ds}S^2+m_{d\Omega}\Omega^2} \tag{6.9}$$

The value of the model constants are: $c_{\mu 0}$= 0.09, c_{ns}= 0.005, $c_{n\Omega}$= 0.0068, c_{ds}= 0.008, $c_{d\Omega}$= 0.004, $c_{ds\Omega}$= -0.003, c_{ds1}= 0.00005, $c_{d\Omega 1}$= 0.00005, $c_{ds\Omega 1}$= 0.00025, c_{10}=0.40, c_{20}=0.0, c_{30}= -0.13, m_{ds}= 0.01, $m_{d\Omega}$= 0.003, σ_k= 1.0, σ_ε= 1.3, $c_{\varepsilon 1}$ = 1.44 and $c_{\varepsilon 2}$ = 1.92. In the standard $k-\varepsilon$ model, c_μ= 0.09 and c_β = 0.0.

6.3 Large Eddy Simulation

The basic equations used in LES are three-dimensional, time-dependent, filtered Navier stokes equations. In the model, the grid itself is used as a spatial filter to separate the velocity field into a resolved and sub-grid part. The eddies larger than the mesh size is the resolved part, and the effects of small scale motions on the resolved field are calculated through sub-grid scale model. Therefore, the resolved part, generally denoted with an over-bar, is basically the averaged quantity over the control volume formed by the numerical mesh.

The filtered equations are developed from the Navier-Stokes equations. Consider, U_i is a velocity in i direction contains resolved scale part $\overline{U_i}$ and sub grid scale part u_i, then $U_i = \overline{U}_i + u_i$, similarly for pressure $P = \overline{p} + p'$. Substituting these two decompositions into Navier-Stokes equations, the filtered equations of LES can be obtained as follows

Continuity equation:

$$\frac{\partial \overline{U}_i}{\partial x_i} = 0 \tag{6.10}$$

Momentum equation:

$$\frac{\partial \overline{U}_i}{\partial t} + \frac{\partial \overline{U}_j \overline{U}_i}{\partial x_j} = g_i - \frac{1}{\rho}\frac{\partial \overline{P}}{\partial x_i} + \nu \frac{\partial^2 \overline{U}_i}{\partial x_j{}^2} - \frac{\partial \tau_{ij}}{\partial x_j} \tag{6.11}$$

Here, τ_{ij} is the subgrid scale Reynolds stress defined by

$$\tau_{ij} = \overline{u_i u_j} - \overline{u_i}\,\overline{u_j} \tag{6.12}$$

The most commonly used subgrid-scale turbulence model is Smagorinsky model proposed by Smagorinsky (1963). In this model, the residual stress takes the Boussinesq eddy viscosity form.

$$\tau_{ij} - \frac{1}{3}\tau_{kk}\delta_{ij} = -2\nu_t \overline{S}_{ij} \tag{6.13}$$

Here, the resolved strain rate $\overline{S_{ij}} = \frac{1}{2}\left(\frac{\partial U_i}{\partial x_j} + \frac{\partial U_j}{\partial x_i}\right)$.

The eddy viscosity ν_t is determined by the Smagorinsky model

$$\nu_t = (C_s \Delta)^2 \sqrt{2\overline{S_{ij}}\,\overline{S_{ij}}} \tag{6.14}$$

Δ is the filter width related to grid size calculated as the geometric average of the grid spacing in three directions, $\Delta = (\Delta x_1 \Delta x_2 \Delta x_3)^{1/3}$. C_s is the Smagorinsky model constant, whose value varies from 0.065 to 0.20 (Ferziger & Peric, 1999); 0.15 is used in the present simulation.

6.4 Simulation Details and Flow Configurations of Test Cases

The turbulent trailing vortex formed by the rolling up of vortex sheet have been studied previously both experimentally and numerically. The experimental results and theoretical observations by Phillips (1981), the DNS numerical study by Qin (1998) as well as by Duraisamy and Lele (2006) are used here to compare the non-linear k–ε model predictions. Phillips (1981) described the Rankine vortex as a multi-layered structure. The innermost region is called vortex core (Region-I). The tangential velocity is zero at the center of the core where viscosity produces nearly solid body rotation. The outer most region (Region-III) can be described by the wake diffusion but extended inward to include turbulent diffusion. Region-II is a buffer region between the nearly potential outerflow and the solid body rotation of core. This region contains the point of maximum tangential velocity where the inertial effects are negligible but high strain rate exists. Hoffmann & Joubart (1963) reported that this region is very similar to that of turbulent boundary layer near wall, and is believed to follow a behavior of log law.

In this study, following test cases with different swirl numbers (q) are considered. Non-linear k–ε model is used for all the cases. LES is performed for case-4 to compare with RANS results.

(a) Case-1: trailing vortex with axial velocity for q =1.0

(b) Case-2: trailing vortex with axial velocity for q=0.5

(c) Case-3: trailing vortex without axial velocity, i.e., $q = \propto$

(d) Case-4: 3D simulation of Rankine vortex without axial velocity using both LES and RANS model

6.4.1 Initial conditions

(a) Case-1: For this q-vortex, the direct numerical simulation results are reported by Qin (1998).

The simulation is performed with the same initial conditions of Qin. Since the axial velocity of this vortex is not a function of axial distance but of radial distance, 2D numerical grid becomes applicable to simulate 3D flow field. The details of the flow field is given below.

Tangential velocity, $$\frac{V_\theta}{V_0} = \frac{q_0}{r}\left(1 - e^{-r^2}\right) \tag{6.15}$$

Radial velocity, $$\frac{V_r}{V_0} = 0 \tag{6.16}$$

Axial velocity, $$\frac{V_z}{V_0} = \frac{1}{q_0}\left(1 - e^{-r^2}\right) \tag{6.17}$$

Here, V_0 is the scaling velocity, related to the initial mean tangential flow, defined as

$$V_0 = \frac{M_p \gamma}{q_0\left(1 - e^{-r^2}\right)} \tag{6.18}$$

M_p =0.009 and γ =1.1209 are used in Qin's (1998) DNS simulation. As discussed by Lessen et al. (1974), the stability of q-vortex can be related to the value of swirl number q. They found that for any value of $q_0<\sqrt{2}$, the vortex is initially unstable and the addition or subtraction of a constant velocity to the axial velocity profile, or an inversion of a velocity deficit to a velocity excess, does not change the temporal stability of the vortex. In this case, to make the vortex initially unstable, the initial swirl number q_0 is chosen to be unity.

The time is non-dimensionalized by $T = 2\pi r_0/V_{\theta m}$ at $t = 0$. Here, r_0 is the radial distance where the tangential velocity contains the peak value in the initial flow field (at $t = 0$).

(b) Case-2: For cases-2 and 3, the results of direct numerical simulation are reported by Duraisamy and Lele (2006). The initial condition of the vortex is given below.

Tangential velocity, $$\frac{V_\theta}{V_0} = -\frac{1}{r\sqrt{\alpha}}\left(1 - e^{-\alpha r^2}\right) \tag{6.19}$$

Radial velocity, $$\frac{V_r}{V_0} = 0 \tag{6.20}$$

Axial velocity, $$\frac{V_z}{V_0} = -\frac{1}{q_0}\left(e^{-\alpha r^2}\right) \tag{6.21}$$

Here, $\alpha = 1.25643$ (Lamb's constant), which makes the initial core radius (the radial location of maximum tangential velocity) is $r_0 = 1$. For case 2, $q_0 = 0.5$.

(c) Case-3: This case does not contain any axial velocity. Therefore, it can be considered as line vortex. In consideration of q-vortex, this case has a value of $q_0 = \propto$ in axial velocity distribution (Eq. 6.21).

(d) Case-4: All the three cases explained above are simulated using 3D flow equations with 2D numerical grid. However, in Case-4 simulation is performed using 3D Cartesian grid for an idealized Rankine vortex.

The initial condition of the vortex is given below.

Tangential velocity, $$\frac{V_\theta}{V_0} = -\frac{1}{r}\left(1 - e^{-r^2}\right) \tag{6.22}$$

Radial velocity, $$\frac{V_r}{V_0} = 0 \tag{6.23}$$

Axial velocity, $$\frac{V_z}{V_0} = 0 \tag{6.24}$$

6.4.2 Flow domain and computational schemes

The governing equations for mean velocities and turbulent flows are discretized with the finite volume method based on a staggered grid system. For the momentum equation, convective and diffusive fluxes are approximated with Quick and central difference schemes respectively. The hybrid central upwind scheme is used for the k and ε equations. Time advancement is achieved by Adam-Bashforth scheme of second-order accuracy, in each equation. The basic equations are discretized as fully explicit forms and solved successively with the time increment in step by step. The pressure field is solved using iterative procedure at each time step.

(a) 2D grid (for Cases-1 to 3): The numerical simulations for 3-D unsteady flows are performed under the same conditions of DNS computations (Qin, 1998 for case-1; Duraisamy and Lele, 2006 for next two cases). Variable grid spacing is used with dense grid at centre and coarser towards the boundary. The computational domain consists of 100 grids in each of lateral (*x* and *y*) directions for all the cases. The size of domain is taken sufficiently large ($12\ r_0 \times 12\ r_0$) to overcome the interference of boundary in the vortex decay process. Cartesian grid is used for computation, and the results are presented in cylindrical coordinate using the geometric conversion.

(b) 3D grid (for Case-4): The flow domain consider here is $12\ r_0 \times 12\ r_0$ (in two lateral, *x* and *y* directions) $\times 1\ r_0$ (in axial /depth-wise, z direction). For LES 140×140×15 grids are used in x, y and z directions respectively. For RANS simulation the grid no is reduced to 70×70×10 grids. Variable grid system is used for two lateral directions.

6.5 Simulation of Turbulent Trailing Vortex with Swirl Number q =1.0

The distribution of tangential velocity, axial velocity and corresponding pressure distribution in the vortex are shown in Fig. 6.5 for simulation time t=3.72T. The case of trailing vortex considered here contains the axial velocity with a minimum magnitude at vortex center (at center, $V_z = 0$ at t=0) that gradually increases in outward direction and became constant at a far distance from the center. In the simulated results, the axial velocity in the center region is found to increase with time in order to reduce the gradient with far field. The tangential velocity also decays with time. The details of temporal change in flow characteristics are explained in the next sections.

The basics of pressure distribution in a Rankine vortex are described in Fig. 6.2. The distribution of pressure in a trailing vortex is found similar to the line vortex regardless the presence of axial velocity. The figure shows that the pressure at vortex center is minimum and gradually increases in outward direction and becomes constant at a far distance from the center.

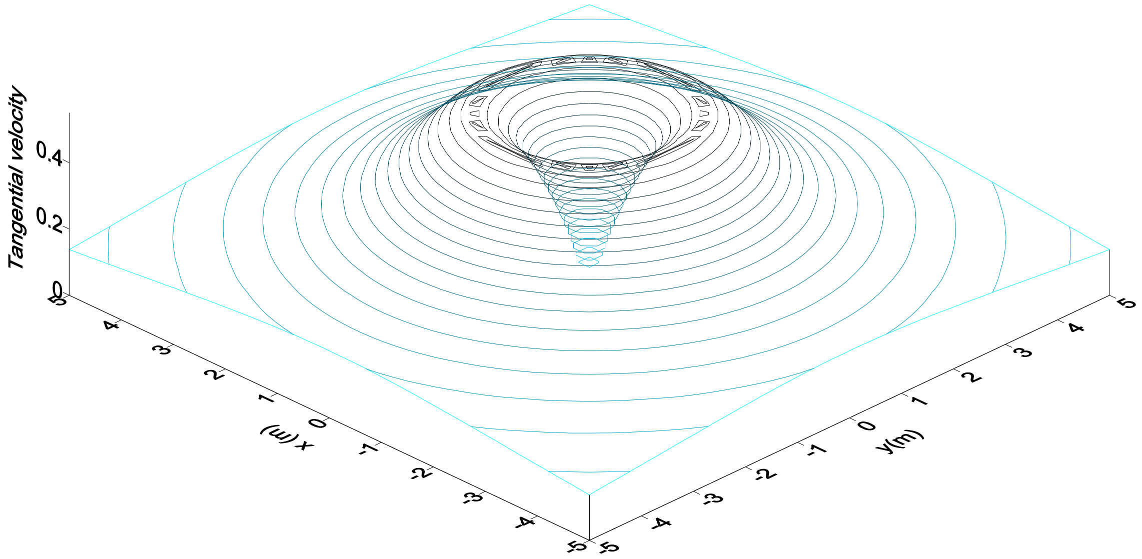

(a) Distribution of tangential velocity

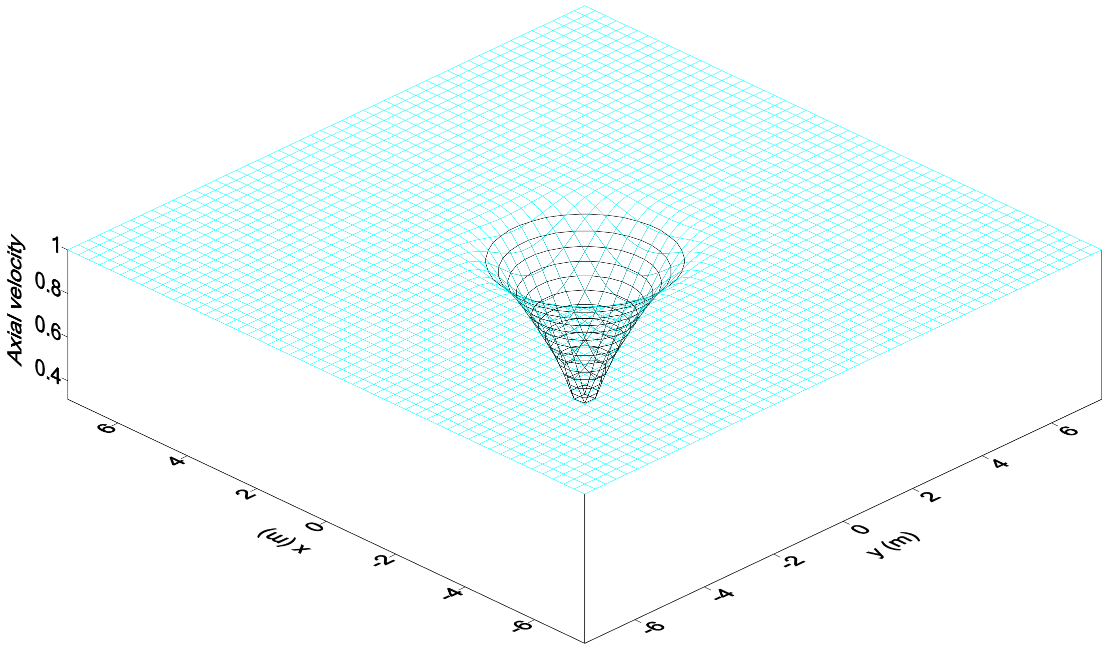

(b) Distribution of axial velocity

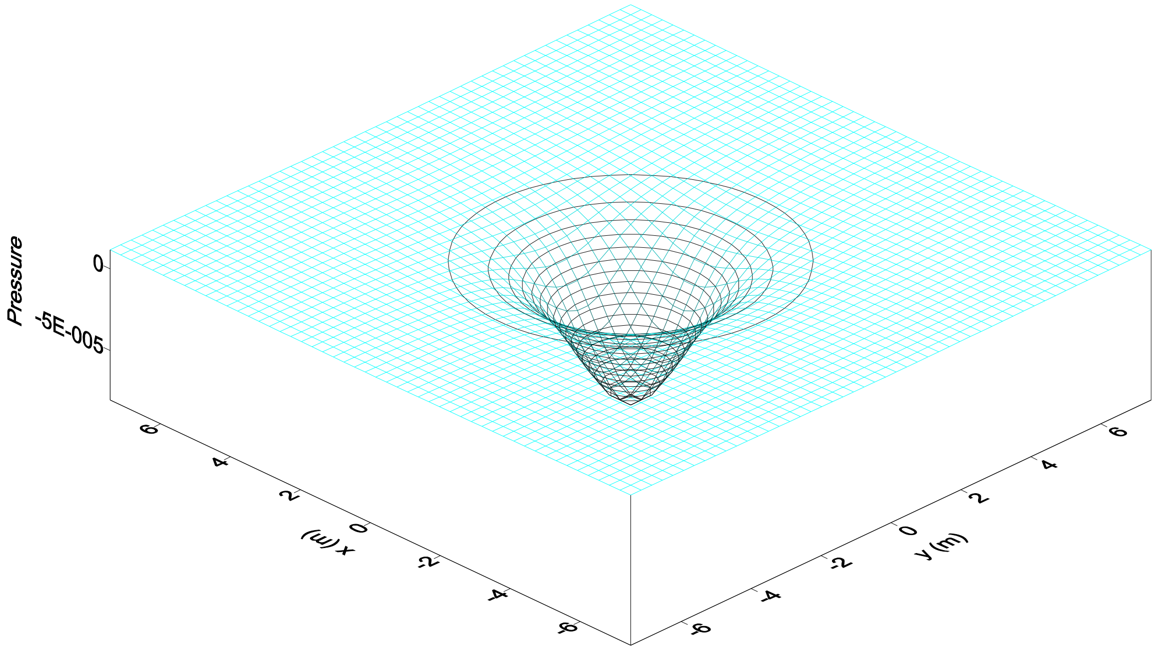

(b) Distribution of pressure

Fig. 6.5 Simulation result for q =1 vortex at t =3.72T

6.5.1 Decay of Trailing vortex

Figs. 6.6, 6.7 and 6.8 show the profiles of tangential velocity, axial velocity and circulation for different times calculated using Non-linear k-ε model. Figs. 6.9, 6.10 and 6.11 show those of the standard k-ε model. It is observed that the standard model shows faster decay of tangential and axial velocity than the non-linear model.

The circulation is zero at the vortex center line and is found to increase toward the radial direction that reached a free stream value at some radius outside the vortex core (at $r\gamma/r_0 > 5$). A circulation overshoot is observed after the adjustment of initial conditions and when the vortex comes in self similar stage (at about t >3.0T). Qin's DNS simulation also shows a brief overshoot after the vortex adjusts itself to the unphysical initial conditions. Saffman (1974) claimed that the circulation overshoot is a general feature of turbulent vortices. However, Phillips argued that the circulation overshoot is unlikely. Some researches pointed out that the overshoot does not appear to be enough to produce a visible instability. Uberoi (1979) added that overshoot is possible if vortex diffusion rate is greater than that for a laminar vortex.

In the tangential velocity, maximum decay occurs at the point of maximum velocity, while for axial velocity the maximum decay is at the center of vortex. Figure 6.12 compares the percentage changes of axial velocity and peak tangential velocity with initial time. It is observed that the decay rate of axial velocity is much higher than the tangential velocity. Since the vortex takes some time to adjust with initial condition, it is observed that the decay rate is small at initial times, approximately t< 1.25T. For both velocities, the high decay rate is observed in intermediate time period of 1.25T> t <4.25T. After that the decay slows down, and the slope of trajectories shows to proceed towards minimum.

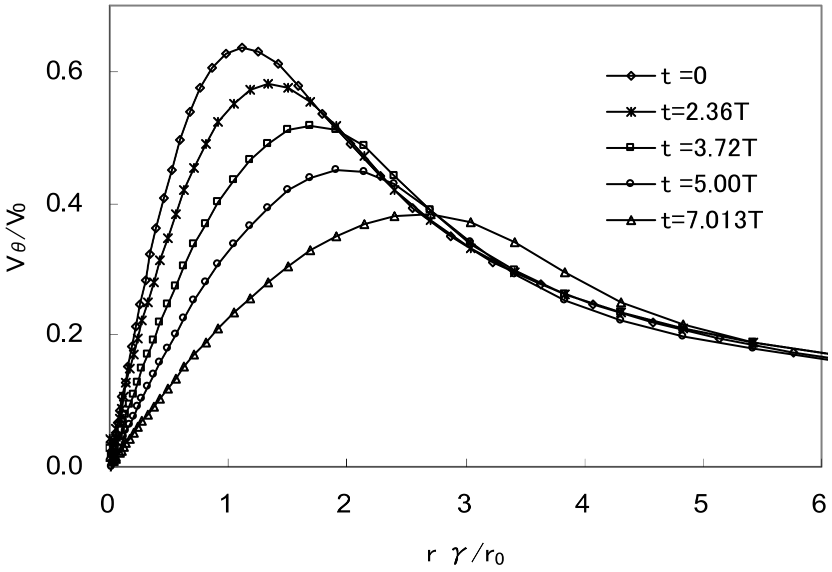

Fig. 6.6 Radial distribution of tangential velocity and its decay with time (Non-linear *k–ε* model)

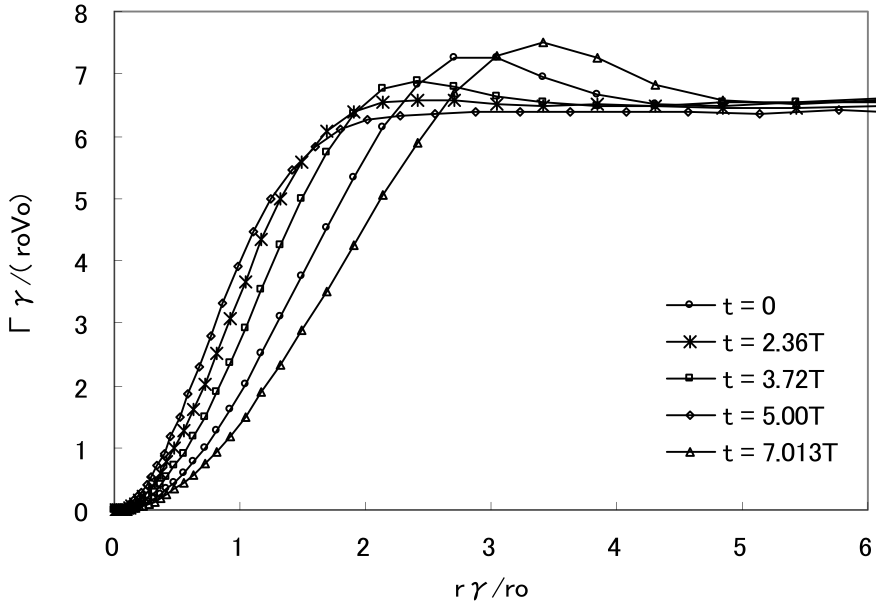

Fig. 6.7 Radial distribution of normalized circulation for different times (Non-linear *k*–*ε* model)

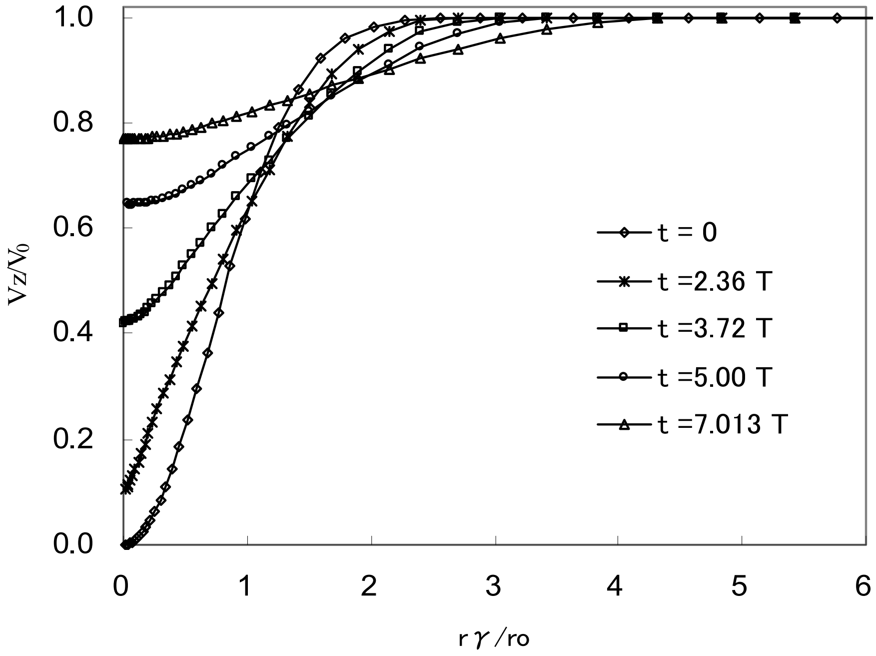

Fig. 6.8 Time decay in radial distribution of axial velocity (Non-linear *k*–*ε* model)

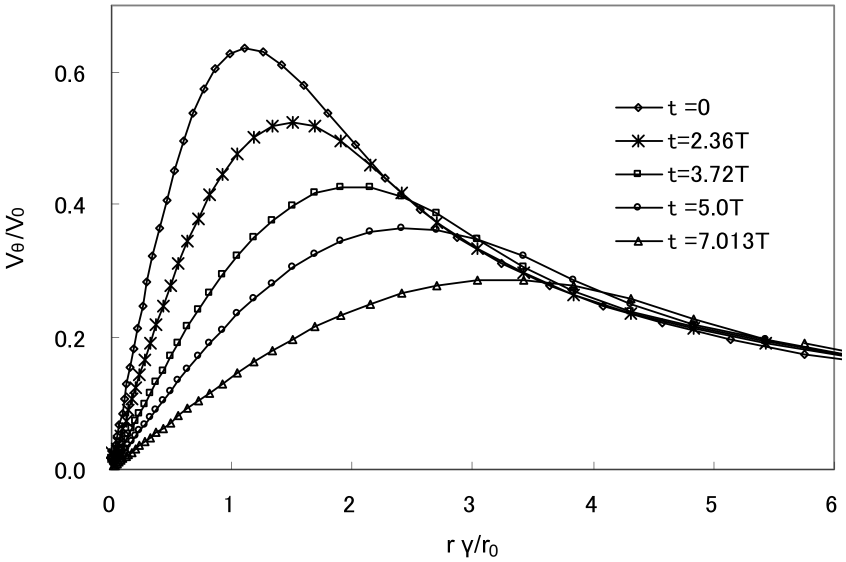

Fig. 6.9 Radial distribution of tangential velocity and its decay with time (Standard *k–ε* model)

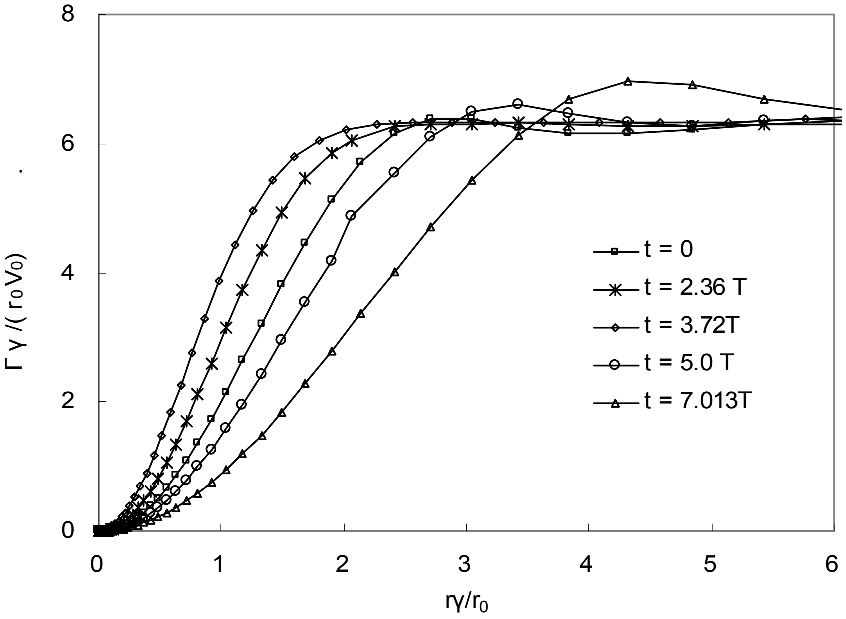

Fig. 6.10 Radial distribution of normalized circulation for different times (Standard *k–ε* model)

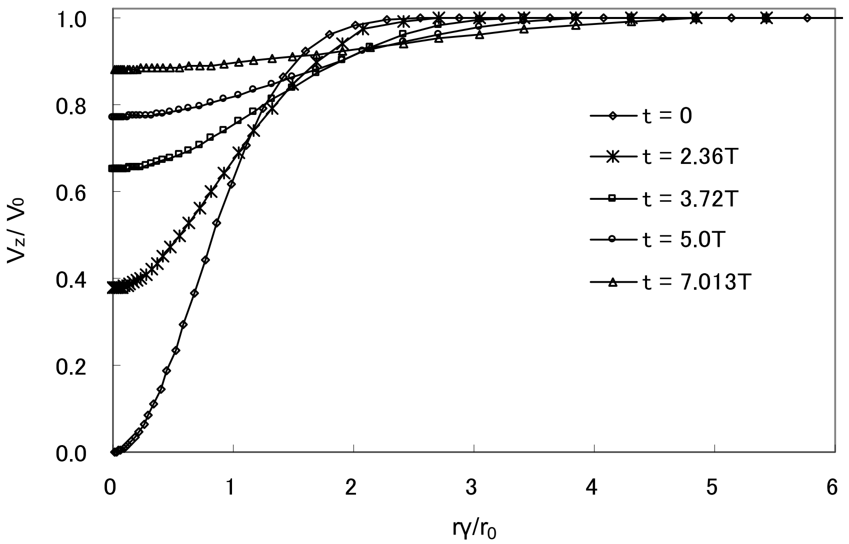

Fig. 6.11 Radial distribution of axial velocity and its decay with time (Standard *k–ε* model)

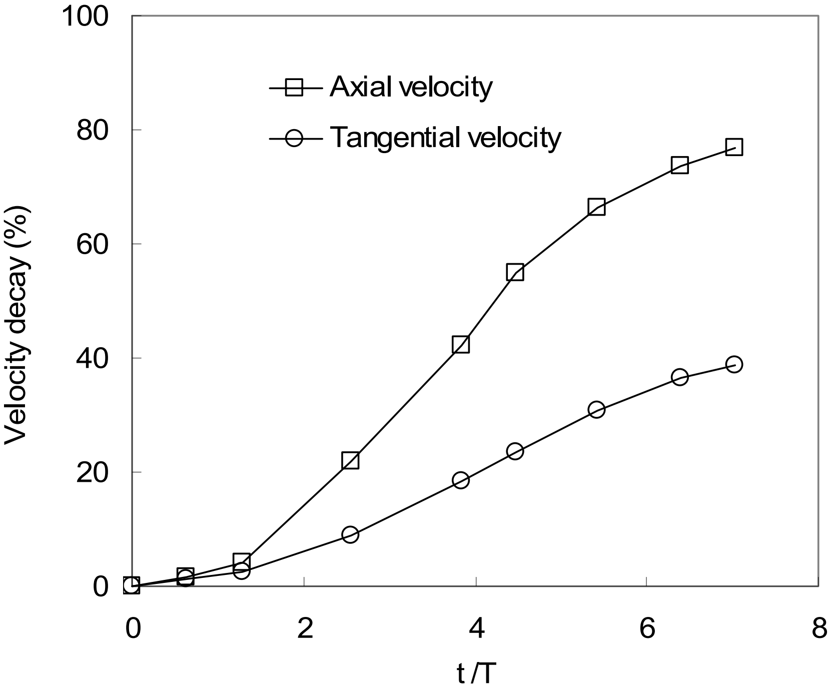

Fig. 6.12 Comparison between time decay of axial velocity and tangential velocity

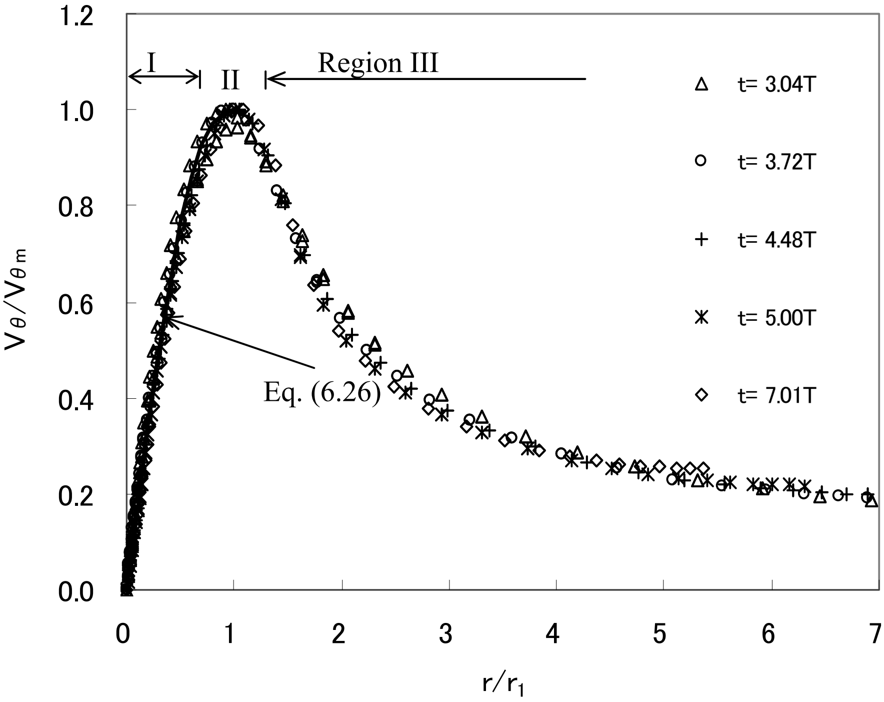

Fig. 6.13 Self-similar profile of tangential velocity compared with Phillips' model

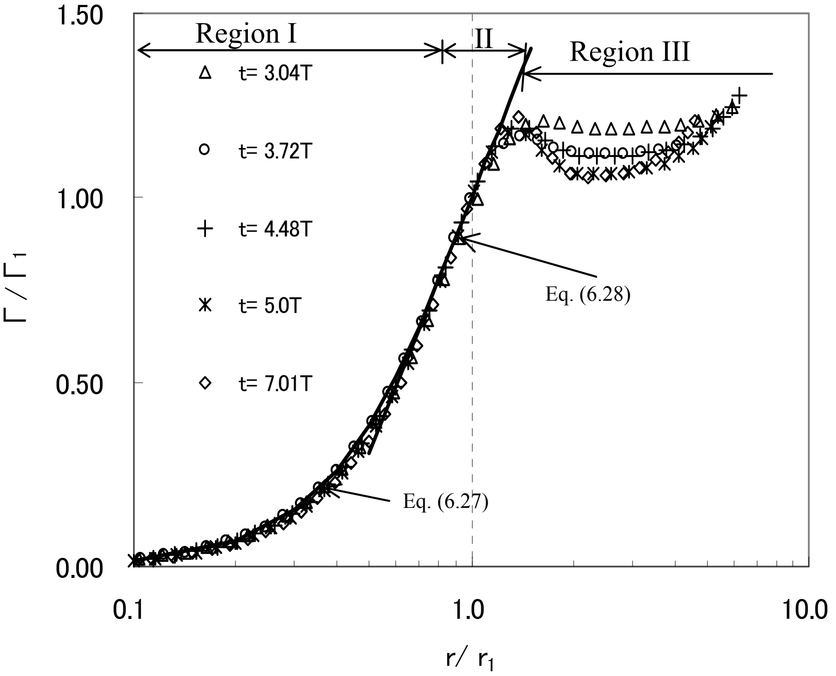

Fig. 6.14 Self-similarity in the circulation profile compared with Phillips' model

6.5.2 Self-similarity of profiles

From dimensional analysis Hoffmann and Joubart (1963) showed that for fully-developed flow

$$\frac{V_\theta}{V_{\theta m}} = f\left(\frac{r}{r_1}\right) \quad \text{or} \quad \frac{\Gamma}{\Gamma_1} = f\left(\frac{r}{r_1}\right) \tag{6.25}$$

Here, r_1 is the radial distance of maximum tangential velocity $V_{\theta m}$. Γ is the circulation defined as $\Gamma = 2\pi r V_\theta$ and Γ_1 is the value at a radial distance of r_1.

By plotting experimental results of $V_\theta / V_{\theta m}$ versus r/r_1, Phillips (1981) also showed that for a fully developed flow the data collapsed in a single curve, and independent of the outer flow characteristics.

Comparing with the experimental results, Phillips proposed the following equations to fit the self-similar profile.

Region-I:

$$\frac{V_\theta}{V_{\theta m}} = 1.7720\left(\frac{r}{r_1}\right) - 1.0467\left(\frac{r}{r_1}\right)^3 + 0.2747\left(\frac{r}{r_1}\right)^5 \tag{6.26}$$

$$\frac{\Gamma}{\Gamma_1} = 1.7720\left(\frac{r}{r_1}\right)^2 - 1.0467\left(\frac{r}{r_1}\right)^4 + 0.2747\left(\frac{r}{r_1}\right)^6 \tag{6.27}$$

Logarithomic part of Region-II:

$$\frac{\Gamma}{\Gamma_1} = \ln\left(\frac{r}{r_1}\right) + 1 \tag{6.28}$$

In Fig. 6.13, it is observed that for tangential velocity the self similarity solution embraces all the regions I, II and III. Here the profiles are shown for t > 3.0T. Eq. (6.26) proposed by Phillips is perfectly fitted with the simulation results by non-linear k-ε model. For t<3.0T, region I and II are found to show self similarity, but region III does not collapse with the data shown in Fig. 6.13. Therefore, region III shows the similarity form only for a particular flow conditions and in the fully developed flow case.

Figure 6.14 shows the self-similar circulation profile. It is seen that although the simulated results for region I and region II collapse in a single curve, region III does not show the self similarity form. Eqs. (6.27) and (6.28) are also showing excellent fitting with the simulated data. From previous studies it is found that region I is weakly dependent on initial and hydraulic conditions. Phillips noted that this self-similar profile exists in region I and II, regardless the presence of axial velocity component. Present result also support the argument and reveals that this region shows self-similarity form for all the times including $t<3.0T$. The logarithmic region near $r/r_1 = 1$ is reported as truly universal region. Dissimilarity in region III is observed in figures also reported in previous studies. Due to circulation overshoot, there does not seem to be any scope for the self-similarity solution in region III.

6.5.3 Instability vortices

The non-linear model shows the occurrence of instability in a well grown vortex field (at $t > 3.0T$ for this case) after the self-similar form of flow field is attained. Figure 6.15 shows the flow field of vortex (fig. a) and the instability vortices (Fig. b) at $t = 7.013T$. Note that the instability vortex field is calculated by subtracting a mean velocity field from the main vortex field. Phillips' multi-layered structure is seen in this figure. Due to tangential velocity gradient between region I and II, as well as between II and III, instability vortices are found to form in those regions. In this figure, the instability vortices are observed at a radial distance of $0.7r_1$ and $1.2\ r_1$ respectively.

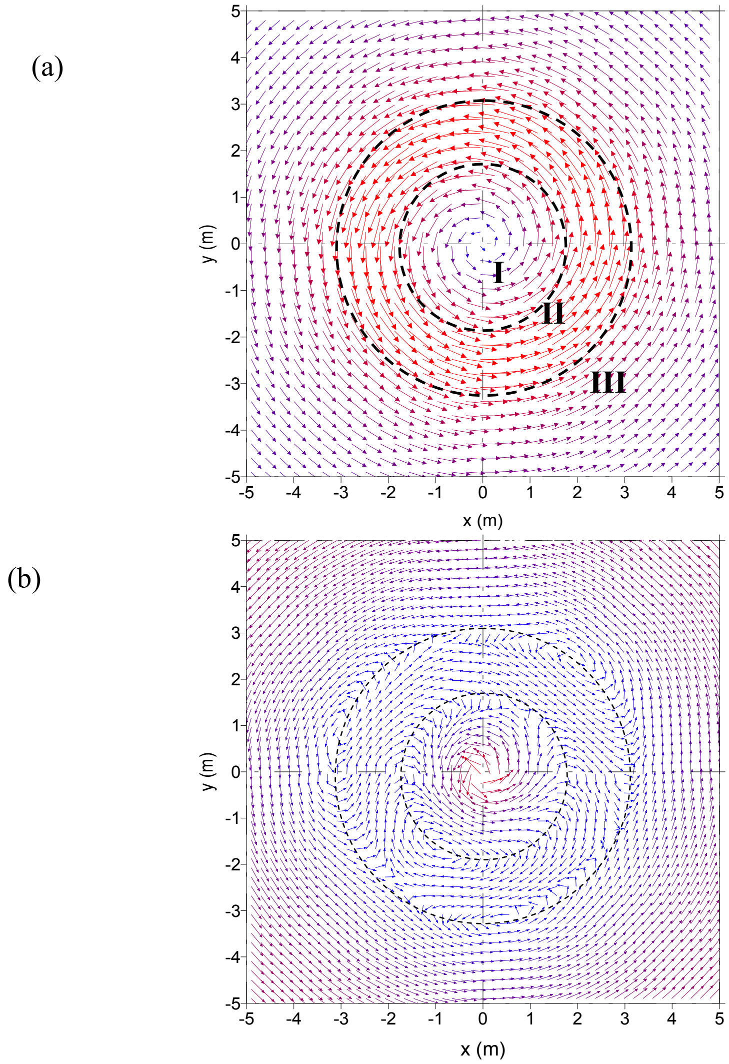

Fig. 6.15 Non-linear *k*–*ε* model prediction of (a) vortex flow field and (b) instability in the flow field (t = 7.01T)

6.5.4 Temporal growth/decay of turbulence

Production of turbulence in the vortex field is due to the tangential and axial velocity gradients. In the vortex lifetime, five different growth/decay rates of turbulent kinetic energy as reported in DNS calculation (Qin, 1998) are also reflected in the simulation of non-linear *k*-*ε* model. Figure 6.16 shows the growth/decay of turbulence kinetic energy with approximated five different time periods. Initially (zone (i)), the vortex changes very slowly, as it requires adjustment of any unphysical nature of initial conditions. In time zone (ii), an exponential growth of turbulent kinetic energy is seen. The growth slows down in the next time period of zone (iii). It is found that the growth of axial velocity is significantly high in time zone (ii) and (iii). The turbulent kinetic energy reaches its peak value and remains about constant throughout the short period of zone (iv). It reveals that in this stabilization period the flow field becomes saturated and cannot support additional turbulence. Finally, the decay of turbulence is started as predicted by most of the previous researches (such as, Uberoi, 1979; Bachelor, 1964; etc.). The logarithmic plot shows that the decay rate in zone (v) is much slower than the growth rate in zone (ii). It shows that the decay of velocity field slows down as the turbulence decay period starts.

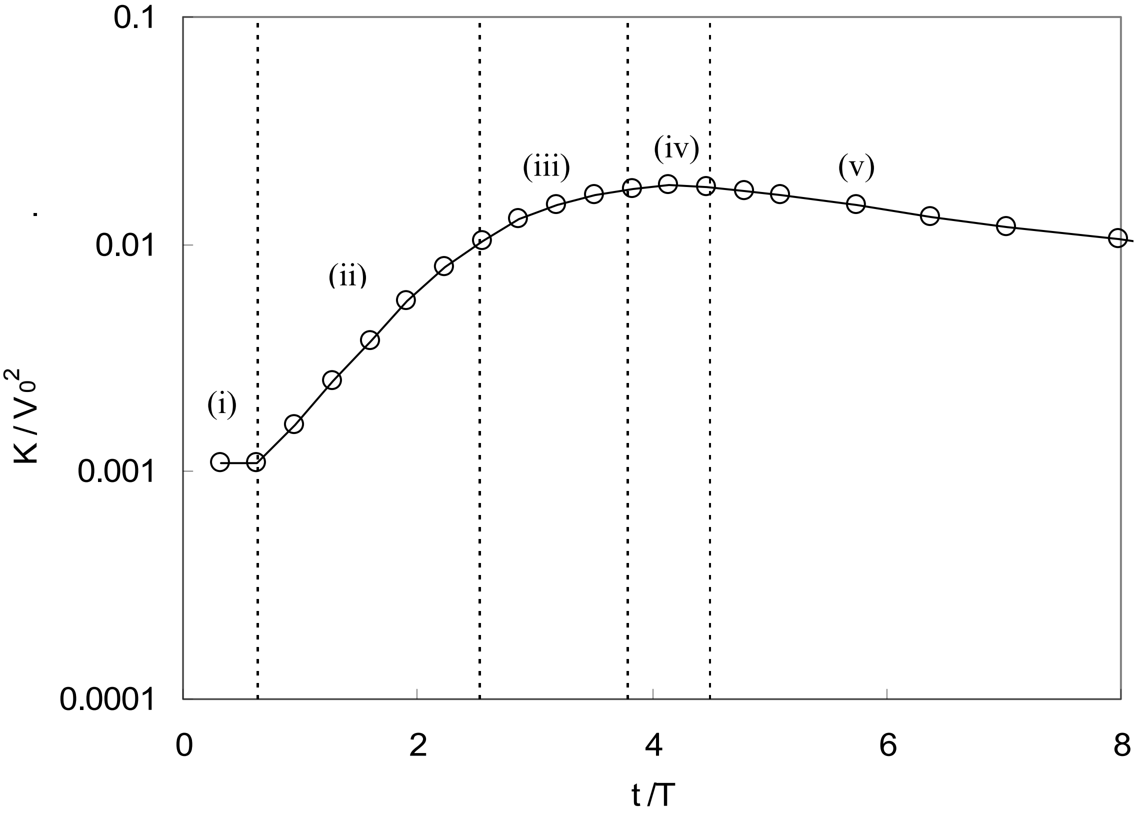

Fig. 6.16 Growth of turbulent kinetic energy with different time periods (Non-linear k–ε model)

Figure 6.17 shows the radial distribution of turbulent normal stresses (R_{ii}) in axial, radial and tangential directions for different times; the stresses are noted as $\overline{u_z u_z}$,$\overline{u_r u_r}$ and $\overline{u_\theta u_\theta}$ respectively. Here, the radial distance is normalized by $r_1 = r_0(t)$, which is the radial distance of maximum tangential velocity. For a round jet in a stagnant surroundings, $\overline{u_z u_z} > \overline{u_\theta u_\theta} \geq \overline{u_r u_r}$ over the radius of jet (Ali et al., 2006; Wygnanski & Fielder, 1969). However, in the matured stage of a trailing vortex, the turbulent normal stresses show two types of anisotropy depending on the radial distance. Inside the vortex core ($r/r_1<1$) up to certain distance from center, the relation is $\overline{u_r u_r} \geq \overline{u_\theta u_\theta} > \overline{u_z u_z}$; and beyond that distance the stresses follows $\overline{u_r u_r} > \overline{u_z u_z} > \overline{u_\theta u_\theta}$. The latter case is the situation where turbulence production is significantly less than diffusion, such as in the central region of an axisymmetric wake. These anisotropic behaviors of turbulence are also reported in previous studies by Devenport et al. (1996) and Phillips & Graham (1984).

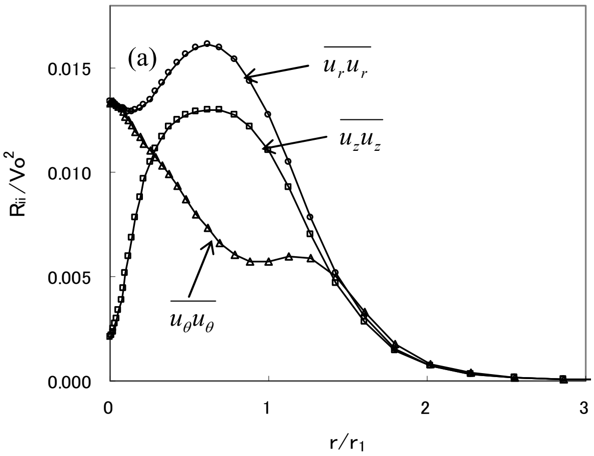

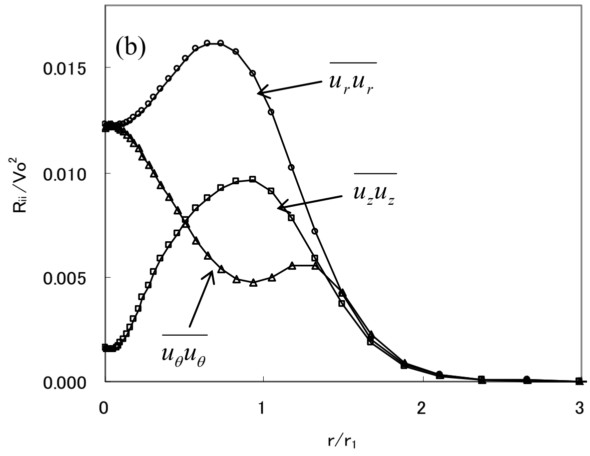

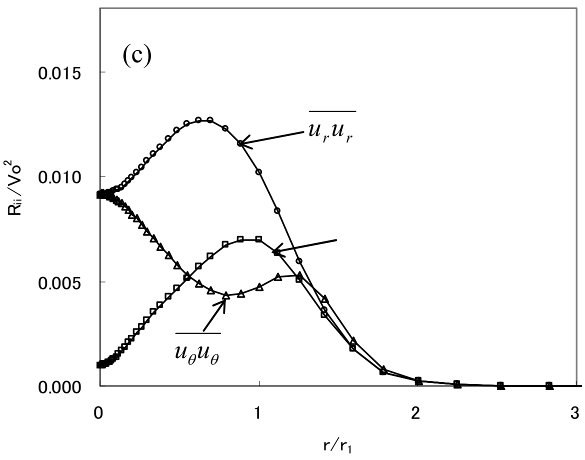

Fig. 6.17 Radial distribution of turbulent intensities at three directions at (a) t =3.72 T (b) t =5.0 T (c) t=7.013T

In the growth stage of time zone (ii), all the normal stresses are found to increase simultaneously. In Fig. 6.17, the distribution of turbulent normal stresses are shown for different times (t= 3.72 T, 5.0 T and 7.13T), those are belongs to time zones (iii), (iv) and (v), respectively. Comparison of turbulent intensities between time zones (iii) and (iv) indicates that only the axial velocity component shows significant decay. On the other hand, comparison between (iv) and (v), shows the simultaneous decay of turbulent intensities in all the velocity components.

It is observed that at the center of vortex (i.e. at r =0), $\overline{u_\theta u_\theta} = \overline{u_r u_r}$ throughout the simulation time. It confirms the axisymmetric condition of the flow field.

6.5.5 Comparison with Qin's DNS data

Circumferential velocity, circulation and axial velocity are compared with the DNS calculation of Qin (1998) at time t =3.72 T as shown in Figs. 6.18, 6.19 and 6.20 respectively. At this stage the vortex already overcame the effect of initial conditions and shows self-similar behavior. Also, the turbulent flow field became saturated and stabilized gaining a peak value of turbulent kinetic energy after passing its growth periods. In the figure, the non-linear model shows well agreement with DNS data. Although the axial velocity decay is fitted well, the magnitude and position of maximum tangential velocity shows slightly faster decay than DNS data. A very high decay rate is found for the standard model in comparison to the non-linear model and DNS simulations. Such discrepancy is also seen in the comparison of circulation profile. By comparing the turbulence kinetic energy in Fig. 6.21, it is observed that the non-linear model shows much better comparison over standard model. However, the model over-predicts the kinetic energy near the maximum point, and this is the cause of faster decay of tangential velocity than DNS as observed in Fig. 6.18.

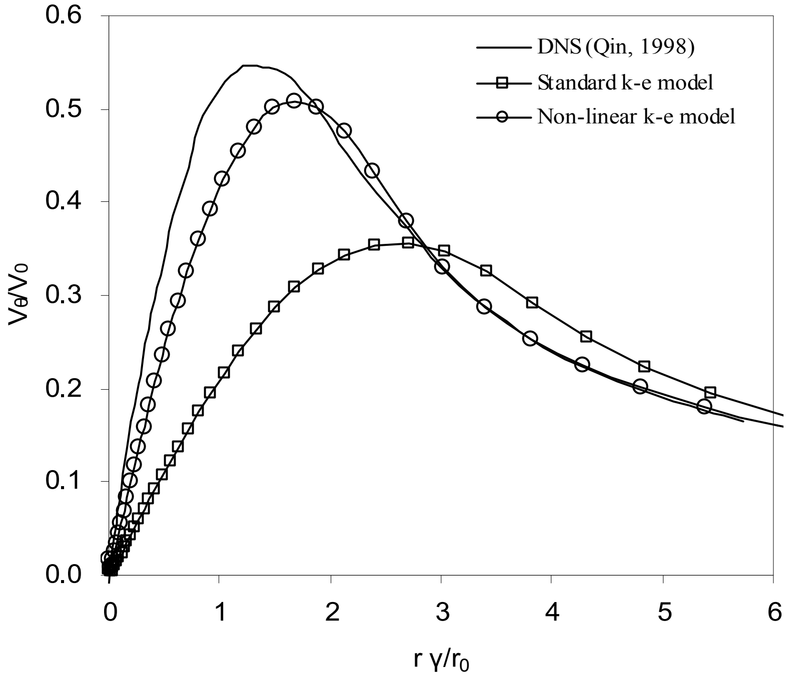

Fig. 6.18 k–ε model prediction of tangential velocity profile compared with Qin's DNS results (t = 3.72T)

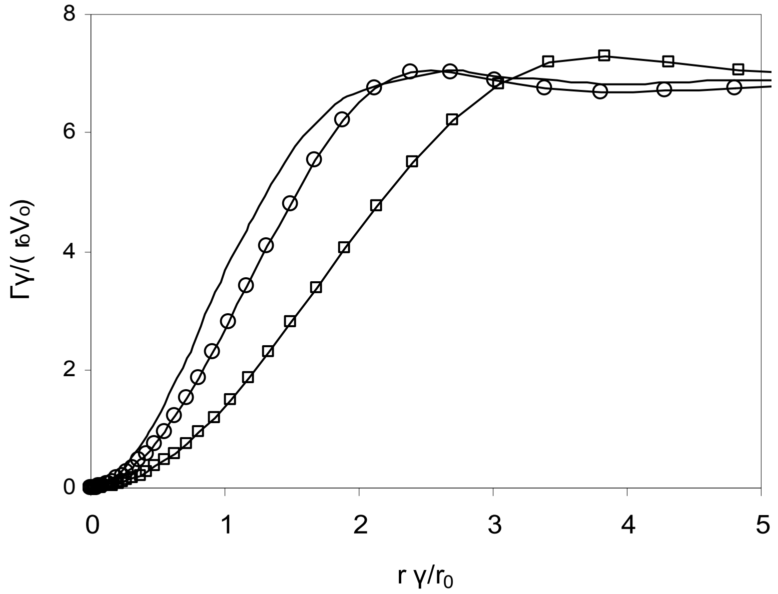

Fig. 6.19 k–ε model prediction of circulation profile compared with Qin's DNS results (t = 3.72T)

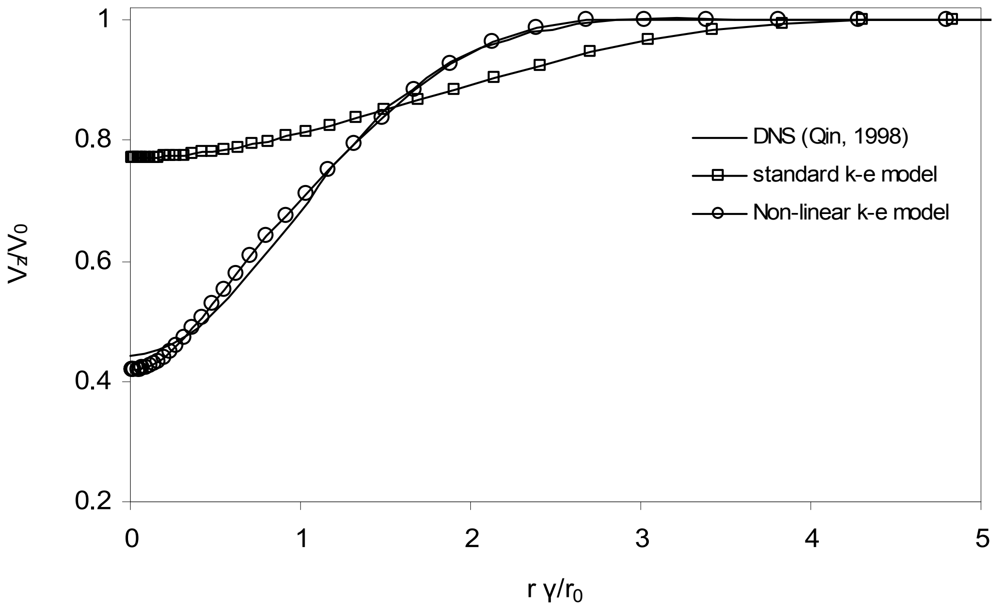

Fig. 6.20 k–ε model prediction of axial velocity profile compared with Qin's DNS results (t = 3.72T)

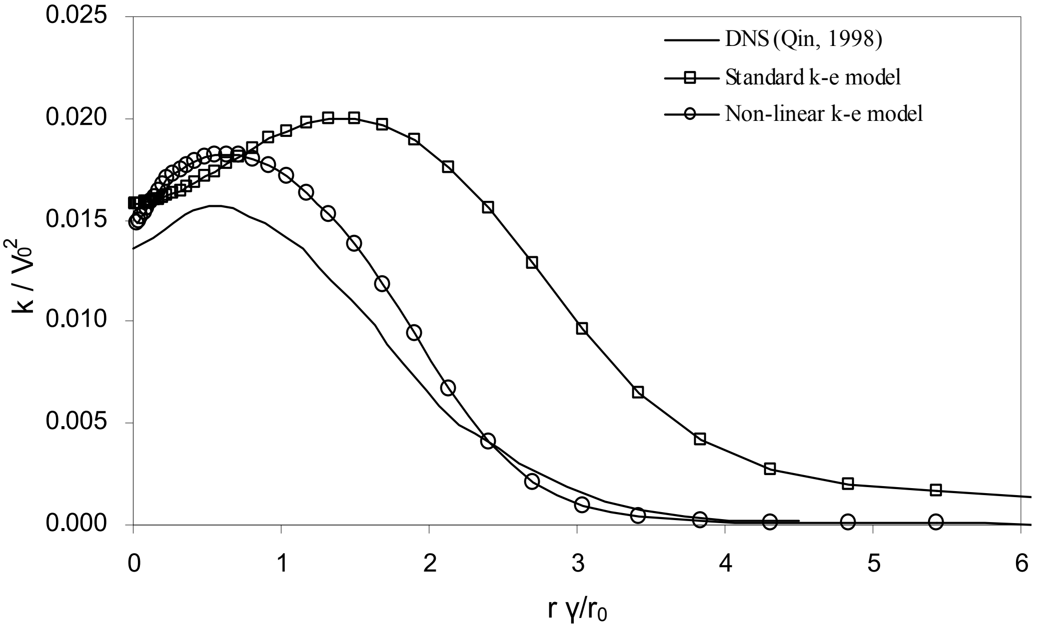

Fig. 6.21 *k–ε* model prediction of turbulent kinetic energy with Qin's DNS results (t = 3.72T)

6.6 Simulation of Turbulent Trailing Vortex with a Swirl Number q = 0.5

Calculated flow profiles for radial distributions of tangential velocity, axial velocity and circulations are shown in Figs. 6.22, 6.23 and 6.24 respectively. Non-linear model is used in these calculations. The initial flow profiles are also included in the figure. It can be noted that the initial radial distribution of axial velocity profile as shown in Fig 6.23 for the case of q = 0.5 is different from that for q=1 (shown in Fig. 6.8). Comparison of results at time t =2.9T is shown in the figures with the DNS calculations of Duraisamy and Lele (2006). At this stage the turbulent flow field became saturated after the exponential growth period of turbulent kinetic energy. The figure indicates that the predicted profiles are well agreed with DNS data. Since the circulations are non-dimensionalized by their initial maximum values, the overshoot is clearly seen in the figure (Fig. 6.4) both in non-linear *k–ε* and DNS simulations.

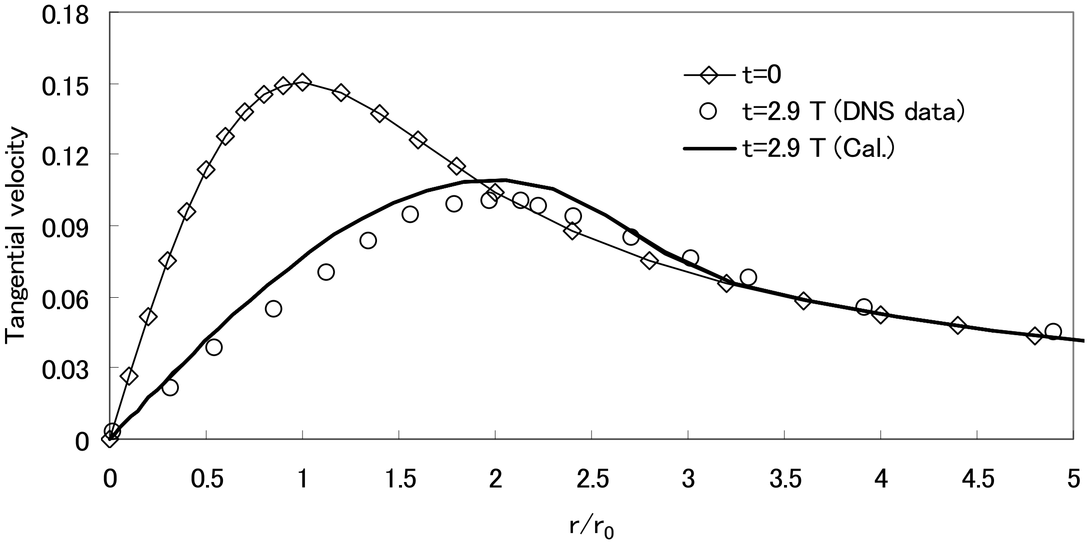

Fig. 6.22 Non-linear *k*–*ε* model prediction of tangential velocity profile compared with DNS results of Duraisamy and Lele (2006) for q = 0.5

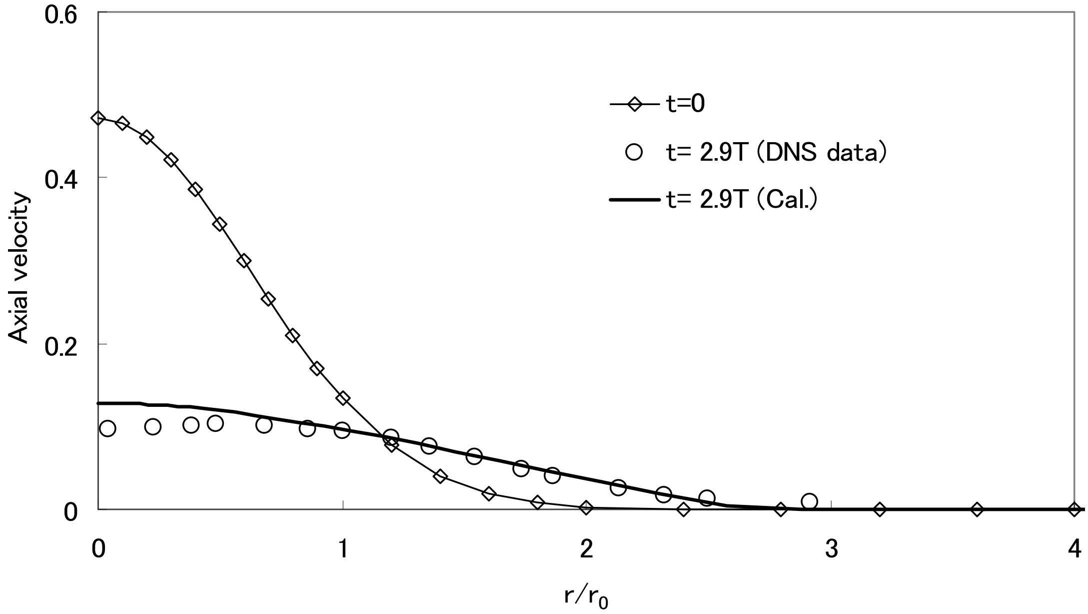

Fig. 6.23 Non-linear *k*–*ε* model prediction of axial velocity profile compared with DNS results of Duraisamy and Lele (2006) for q = 0.5

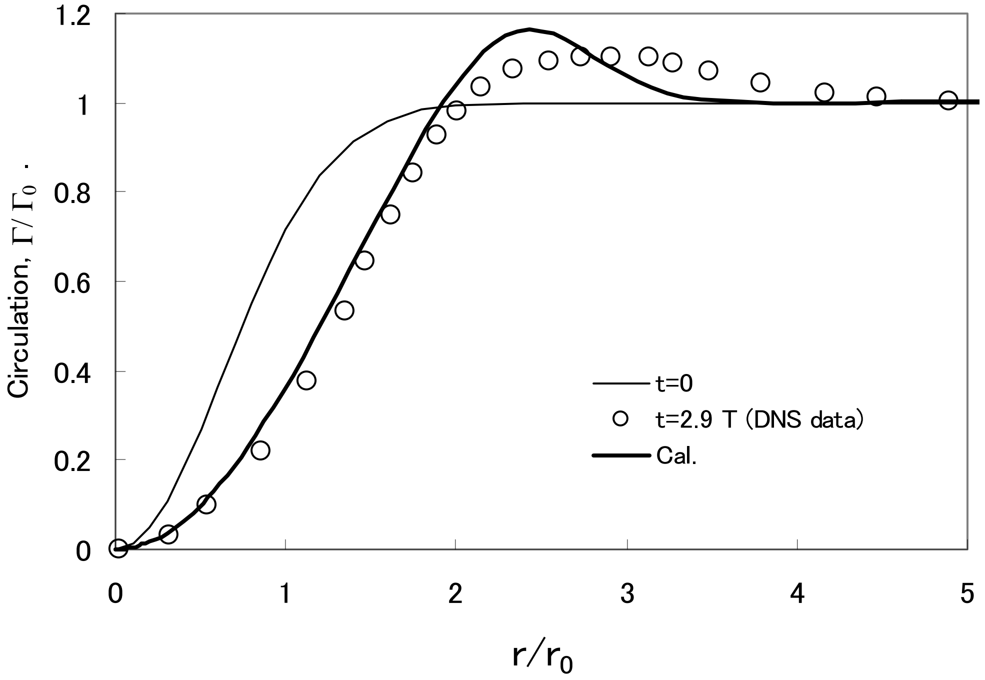

Fig. 6.24 Non-linear k–ε model prediction of normalized circulation compared with DNS results of Duraisamy and Lele (2006) for q = 0.5

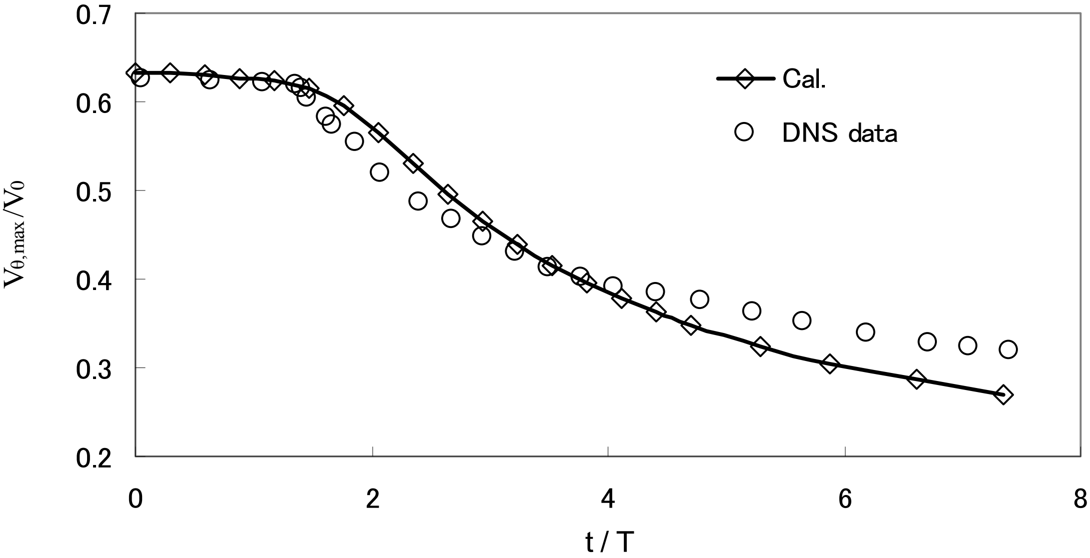

Fig. 6.25 Time decay of maximum tangential velocity (at r = $r_0(t)$) compared with DNS results of Duraisamy and Lele (2006) for q = 0.5

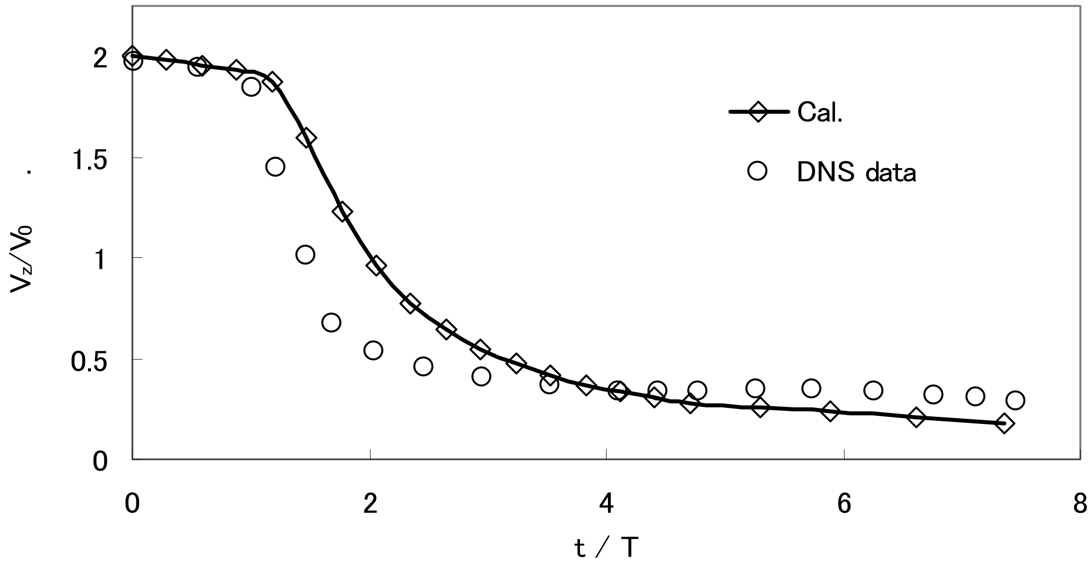

Fig. 6.26 Time decay of maximum axial velocity (at r = 0) compared with DNS results of Duraisamy and Lele (2006) for q = 0.5

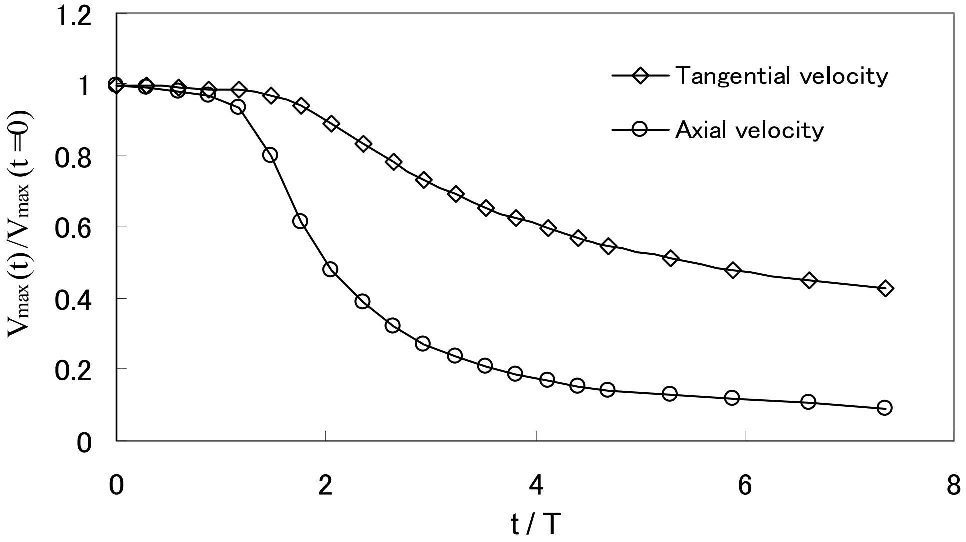

Fig. 6.27 Comparison of time decay in maximum axial and maximum tangential velocities (the velocities are normalized by their initial maximum values)

Figure 6.25 shows the calculated time decay of maximum tangential velocity (velocity at r = $r_0(t)$) for q = 0.5 along with DNS results of Duraisamy and Lele (2006). Such comparison for maximum axial velocity (velocity at r = 0) is shown in Fig. 6.26. The simulations show good agreement with DNS results. To study the comparative temporal decay between tangential and axial velocities, their maximum radial values are normalized by the initial maximum, and plotted in Fig. 6.27. In the initial period as well as the period after vortex stabilization (i.e. in the decay phase of turbulent kinetic energy, explained in Fig. 6.16), the decay rate is about same. However, in the turbulence growth periods, the decay of axial velocity is much higher compared to that of tangential velocity. The phenomena is same as the results for q_0 =1.0 as explained in Fig 6.12.

6.7 Simulation of Turbulent Trailing Vortex with no Axial Velocity

Figure 6.28 shows the comparison of time decay in tangential velocity for different swirl numbers; The DNS results of Duraisamy and Lele (2006) for no axial flow case is also shown to compare with calculated decay profile. The figure reveals that, the rate of temporal decay in tangential velocity increases with decreasing the swirl number q. Therefore, if no axial velocity is present in the flow field, which is the situation for q = ∝ , the temporal decay of tangential velocity should be smaller compared to the vortex filed with axial velocity.

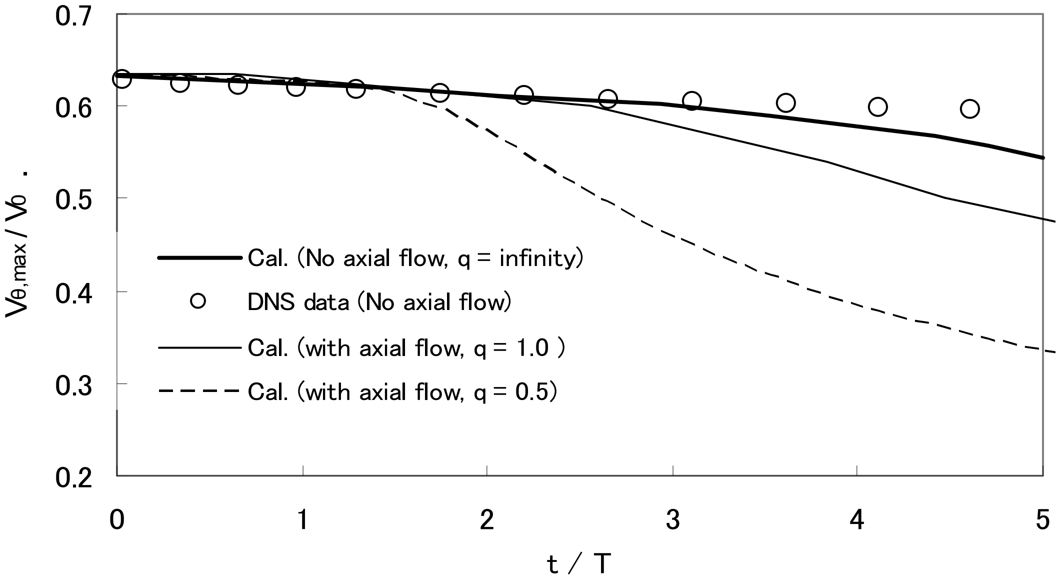

Fig. 6.28 Comparison of time decay of tangential velocity for different swirl numbers; the DNS

results of Duraisamy and Lele (2006) for no axial flow case is also shown to compare with calculated decay profile.

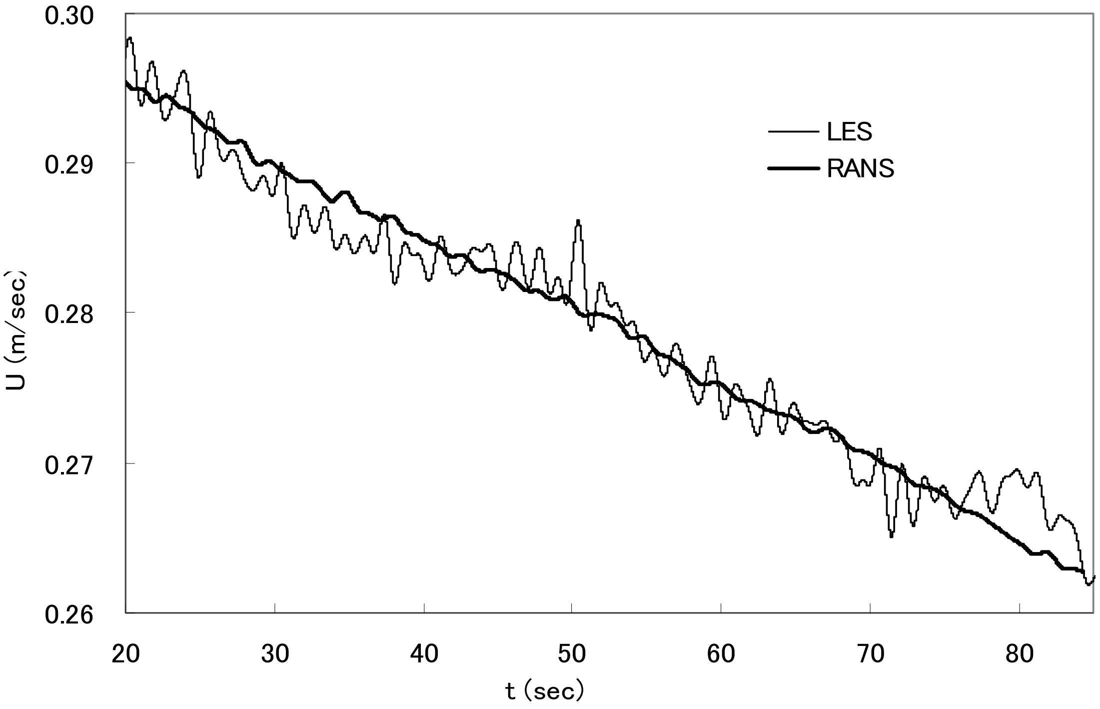

Fig. 6.29 Comparison of temporal fluctuations of velocity at a point by RANS and LES simulations.

6.8 3D Simulation of Rankine Vortex with no Axial Velocity using LES and RANS

For the case of trailing vortices, the axis of rotation is horizontal as shown in Fig. 6.4 as an example of a wing-tip vortex. However, in the present 3D simulation, the vortex flow field is given to rotate with the vertical axis in a free surface rectangular domain. Therefore, although the tangential flow equation for the present case is similar to previous cases, it differs from q-vortex from the view point of flow orientation, and thus, from boundary conditions. In natural flow such vortices can be found in whirlpools in tidal currents, dust whirls on the street or the coherent vortices in shear layer.

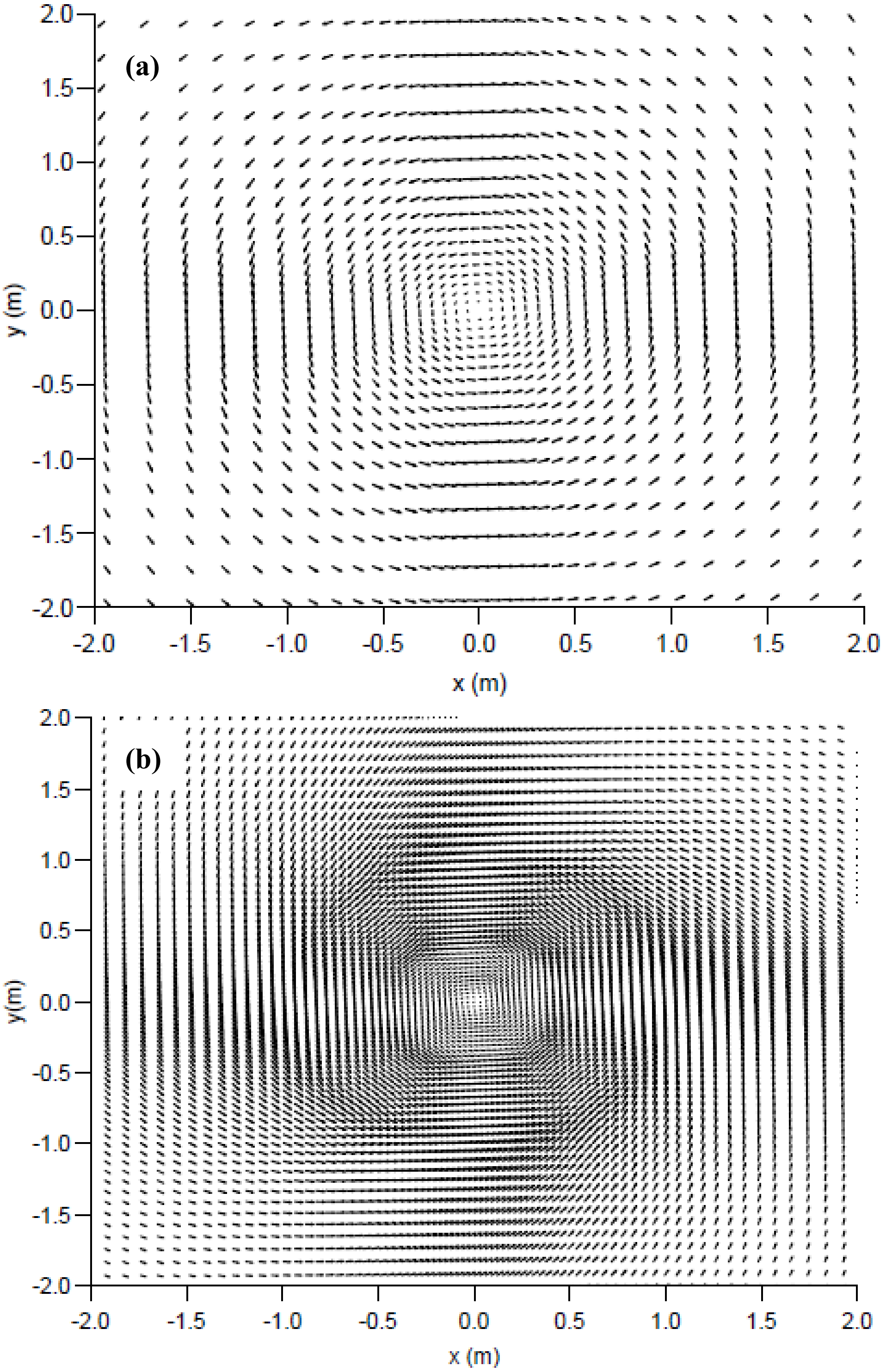

Fig. 6.30 Plan view of flow vectors at t = 40 sec by (a) RANS and (b) LES simulations.

The temporal change of velocity at a point is shown in Fig. 6.29 both for LES and RANS simulations. In addition to temporal decay of velocity, the typical velocity fluctuations are observed in LES results; on the other hand, RANS simulation shows a mean decay profile. In Fig. 6.30, plan view of velocity vector also shows some spatial fluctuations of velocity in LES simulations, which are absent in RANS results.

Figure 6.31 shows the radial distribution of tangential velocity at t = 3.06 T both by LES and RANS. They showed a good comparison. The comparison of circulation profile predicted by both the models for t = 3.06T and 4.84T is shown in Fig. 6.32. At t= 3.06T no circulation overshoot is visible. However, a very small overshoot (compare to previous cases of q-vortex) is observed at t = 4.84T both in LES and RANS results.

The variation of water surface for different times predicted by RANS and LES is shown in Fig. 6.33. The water surface found to be depressed near the central area with minimum water depth at the center of vortex. Since the strength of vortex decreases due to the decay of tangential velocity, the amount of depression in water surface is also decreased with time.

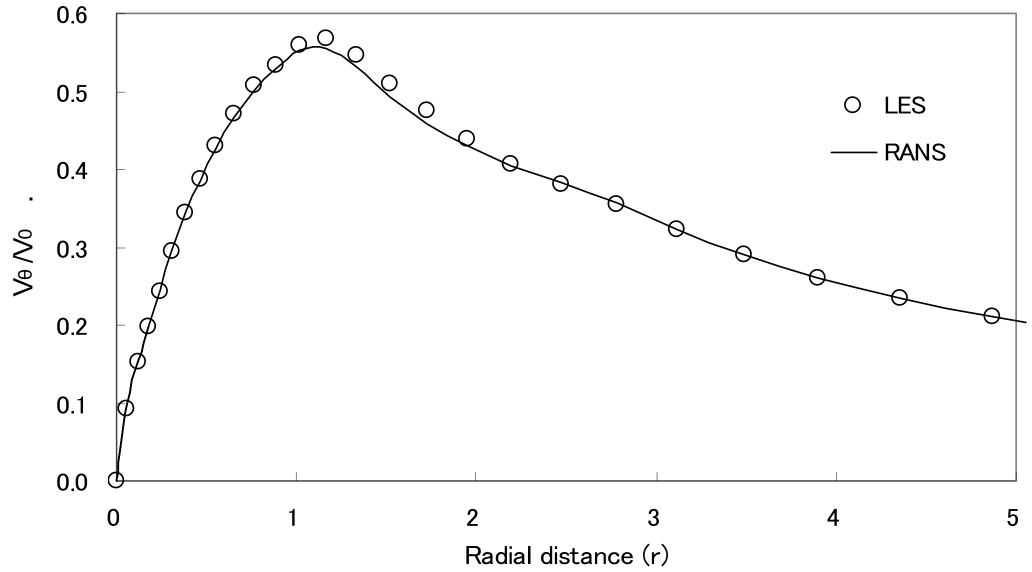

Fig. 6.31 Radial distribution of tangential velocity calculated by RANS and LES (t = 3.06T)

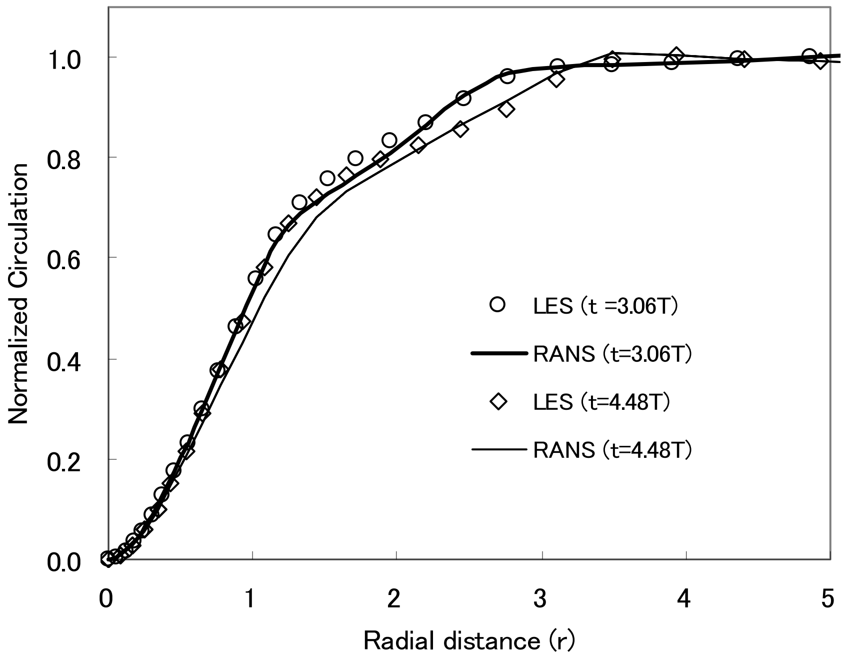

Fig. 6.32 Radial distribution of tangential velocity calculated by RANS and LES (t = 3.06T and 4.48 T)

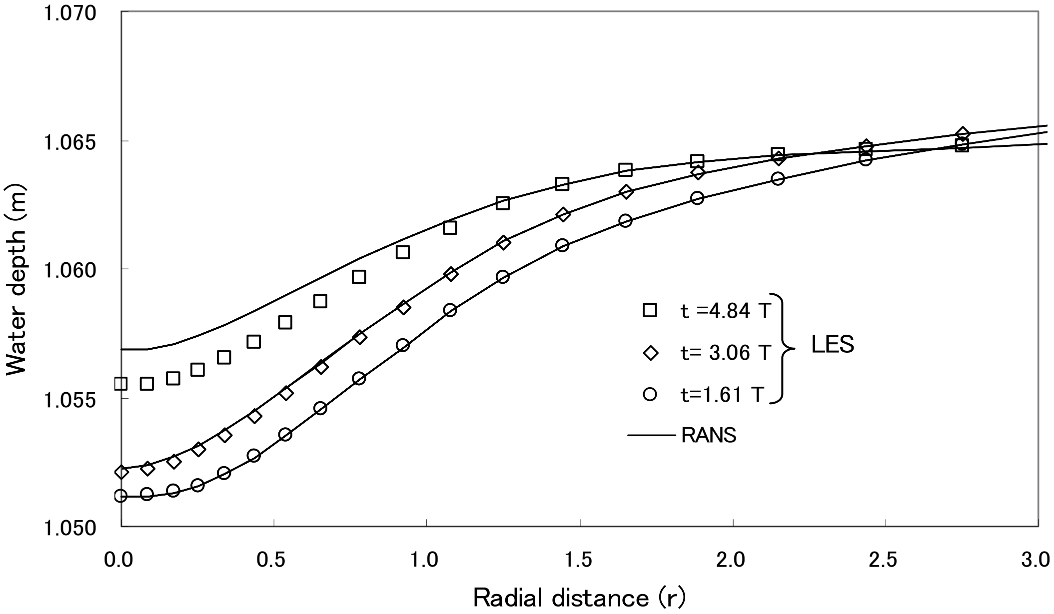

Fig. 6.33 Radial distribution of depth calculated by RANS and LES (symbols show LES prediction, and lines show corresponding RANS prediction)

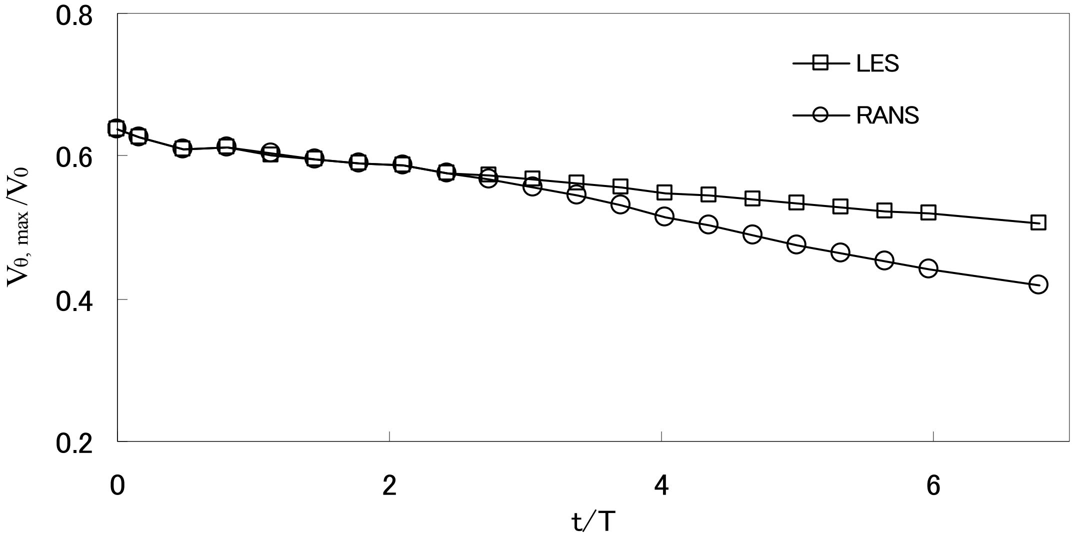

Fig. 6.34 Time decay of maximum tangential velocity calculated by RANS and LES

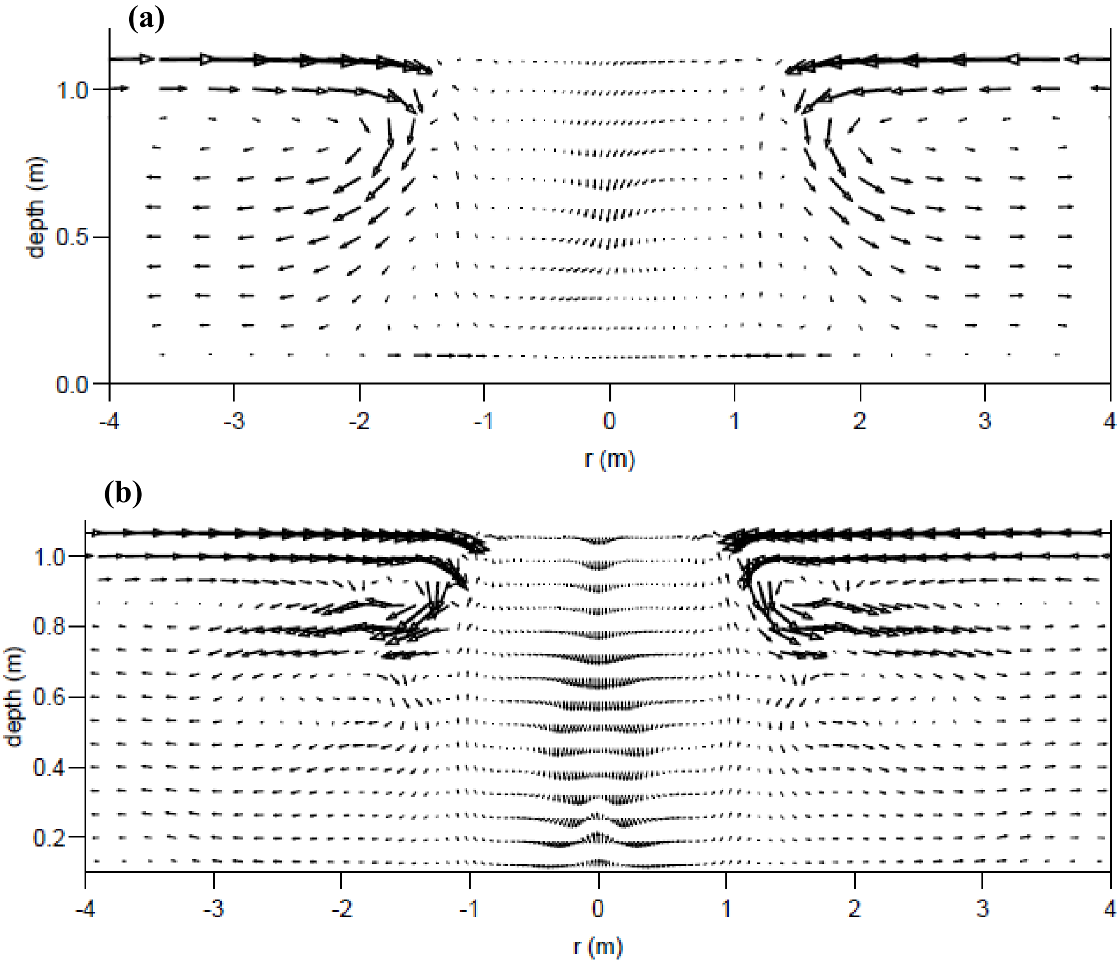

Fig. 6.35 Pattern of secondary current at t = 40 sec by (a) RANS and (b) LES simulations.

Figure 6.34 shows the calculated time decay of maximum tangential velocity both for LES and non-linear *k–ε* model. It is found that although the prediction of RANS model shows good agreement with LES in initial times, some deviation is observed at t> 3.0T. Such discrepancy in the decay phase of turbulence is also observed in previous cases (in Fig. 6.27). From these comparisons, it is observed that in the growth phase as well as in stabilized phase of turbulence, the decay rate of tangential velocity by RANS model is well comparable with LES and DNS. However, in the decay phase of turbulence, RANS model shows slight faster decay of tangential velocity due to its slower decay of turbulence compared to LES and DNS.

The secondary currents calculated by both the models are shown in Fig. 6.35. The flow vectors of secondary current shows three circulation cell in both side of centerline. Secondary current inside the vortex core is found relatively weaker than the out side of core. It is explained that (Fig. 6.1) the Rankine vortex is a combination of nearly solid body rotation and potential vortex. For both type of vortices, the patterns of secondary currents are reported by Lugt (1983). The LES as well as RANS predictions are found well agreed to that. In the vortex core, the secondary current shows the pattern similar to that of solid body rotation; and out side the core, the pattern is similar to that of potential vortex. The patterns as well as magnitudes of secondary currents predicted by two models are well comparable to each other.

6.9 Summary

The unsteady numerical simulations are performed for an isolated turbulent axial vortex using standard and non-linear *k–ε* models. Since the rotational effects of vortex are not captured by a standard k-ε model, it predicts extremely rapid and strong turbulence growth and causes a rapid decay of tangential and axial velocity. However, the non-linear model shows good agreement with DNS data. For the tangential velocity, the self similarity solution embraces regions I and II (defined by Phillips) for all the time periods, however region- III collapses in a single curve only for fully developed flow. Phillips' model equations for similarity solution of velocity and circulation profiles are perfectly fitted with the simulated results. Circulation overshoot is found in the well grown vortex field. Due to this overshoot, the self similarity solution seems hardly possible in region III.

It is observed that the decay rate of axial velocity is much higher than the tangential velocity. Since the vortex takes some time for initial adjustments, it is seen that the decay rate is small at initial times. For both the velocities, the high decay rate is seen in intermediate time period. After that the decay slows down, and the slope of decay proceeds towards minimum.

Five different time periods are observed in the growth/decay profile of turbulent kinetic energy. Initially the vortex changes very slowly to adjust with initial conditions, then an exponential growth is found that slows down before gaining its peak value. The peak value of turbulent kinetic energy remains about constant for a short period that finally follows the period of turbulence decay.

After the maturity of vortex, the turbulent normal stresses show two types of anisotropic behavior depending on the radial distance. Although the radial component is always greater than other two, the tangential component is greater near the center and smaller around the region of maximum tangential velocity in comparison to axial component. The decay rate of energy after the period of stabilization is much slower than the growth rate in the time zones before the stabilization. The decay of velocity field slows down as the turbulence decay period starts.

In the initial period as well as the period after vortex stabilization (i.e. in the decay phase of turbulent kinetic energy), the decay rate of axial and tangential velocity is about same. However, in the turbulence growth periods, the decay of axial velocity is much higher compared to that of tangential velocity.

The result reveals that the rate of temporal decay in tangential velocity increases with decreasing the swirl number q. Therefore, if no axial velocity is present in the flow field, which is the situation for $q = \propto$, the decay of tangential velocity with time should be smaller compared to the vortex filed with axial velocity.

3D numerical simulation is carried out for an ideal Rankine vortex using both RANS and LES. For the case of trailing vortices, the axis of rotation is horizontal. However, in this 3D simulation, the vortex flow field is given to rotate with the vertical axis in a free surface rectangular domain. The prediction of vortex decay by RANS model shows good agreement with LES. The water surface found to be depressed near the central area of the vortex with a minimum water depth at center of it. Since the strength of vortex decreases due to the decay of tangential velocity, the depression in water surface is also decreased with time.

6.10 References

1) Ali, M. S., Hosoda, T., Kimura, I. and Onda, S., Approximate solution of an axisymmetric Swirling jet using non-linear k- ε model with consideration of realizability, *Journal of Applied Mechanics, JSCE,* Vol. 9, pp. 821-832, 2006.
2) Bachelor, G. K., Axial flow in trailing line vortices, *J. Fluid Mech.,* 20(4), pp.645-658, 1964.
3) Devenport, W. J., Rife, M.C., Liapis, S.I., and Follin, G.J., The structure and development of a wing-tip vortex, *J. Fluid. Mech.,* 312, pp. 67-106, 1996.
4) Duraisamy, K. and Lele, S.K., DNS of temporal evolution of isolated turbulent vortices, *Proceedings of the 11th Biennial Summer Program, Center for Turbulence Research, Stanford,* pp. 35-47, 2006.
5) Ferziger, J.H. and Peric, M., *Computational Methods for Fluid Dynamics*, 2nd edition, Springer publications, 1999
6) Hoffmann, E.R. and Joubart, P.N., Turbulent line Vortices, *J. Fluid. Mech.,* 16, pp. 423-439, 1963.
7) Lessen, M., Singh, P.J. and Paillet, F., The stability of a trailing line vortex. Part I: Inviscid theory, *J. Fluid. Mech.,* 63, pp. 753-763, 1974.

8) Lugt, H. J., *Vortex Flow in Nature and Technology*, John-wiley & Sons, USA (ISBN 0-471-86925-2), 1983.
9) Phillips, W.R.C, The turbulent trailing vortex during roll-up, *J. Fluid. Mech.,* 105, pp. 451-467, 1981.
10) Phillips, W.R.C. and Graham, J.A.H, Reynolds stress measurement in a turbulent trailing vortex, *J. Fluid. Mech.,* 147, pp. 353-371, 1984.
11) Qin, J. H., *Numerical Simulation of a Turbulent Axial Vortex*, Phd thesis, Purdue University, USA, 1998.
12) Saffman, P.G., The structure and decay of turbulent trailing vortices, *Arch. Mechanics*, 26(3), pp. 423-439, 1974.
13) Smagorisky, J., General circulation experiments with primitive equations-I: the basic experiment, *Mon. Weather Rev.,* 91, 99-165, 1963
14) Uberoi, M.S., Mechanisms of decay of laminar and turbulent vortices, *J. Fluid. Mech.,* 90(2), pp. 241-255, 1979.
15) Wygnanski, I. and Fielder, H., Some measurements in the self-preserving jet, *J. Fluid Mech.,* 38, pp.577-612, 1969.

Chapter 7

3D UNSTEADY SIMULATION OF OPEN CHANNEL FLOWS WITH A RECTANGULAR SIDE CAVITY

7.1 Introduction

The floodplain encroachment in a river, such as embayment, spur-dykes, lateral intake etc., are constructed along the river for various hydraulic reasons such as flood protection, navigation, land reclamation, approach roads, bridges or other hydraulic structures. Besides the hydraulic reasons, such structures play an important role to increase the biodiversity of aquatic species by creating habitat and providing shelter for them. The main stream of a river, where the velocity is high, is not suitable for all kinds of aquatic species to live, especially for weak, small and young fishes. Such arrangement of shelter with the placement of embayment along the banks of the river is shown in Fig.7.1. In Japan, these inlets are called “Wando” and generally used to create a good habitat for natural lives there.

Since the flow velocity inside a dead zone is lower than that of main channel, a shear layer is formed at the interface due to velocity gradient. In a turbulent flow, this shear layer causes the generation of coherent vortices. In river engineering, turbulent flows with coherent vortices are observed in compound channel flow, in a flow with vegetation zone, in open channel flow with abrupt expansion, etc. The turbulent characteristics of coherent vortices and their spatial distributions with singular points are studied in previous chapters. The characteristics of such large scale vortices in a compound channel, and its contribution to the channel roughness as well as to the flow properties are also studied in chapter 5. However, in an open channel with a dead zone, the interaction of coherent vortices with other dominating flow structures makes the flow field complicated.

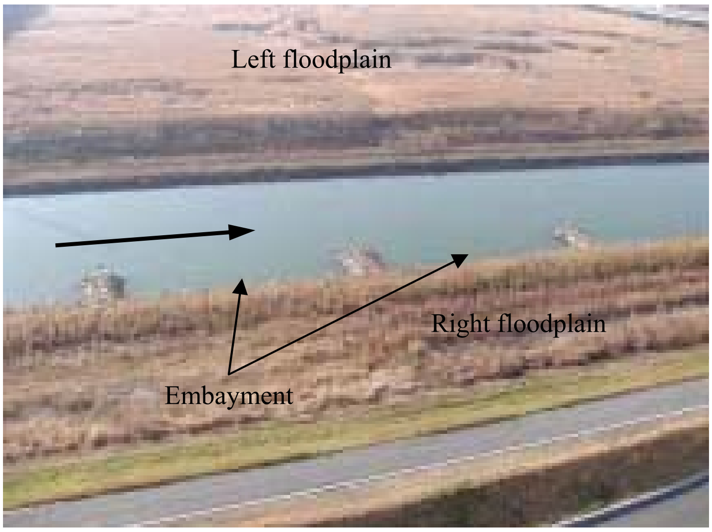

Fig. 7.1 Embayment with rock dykes in Yodo river, Japan (Muto et al., 2002)

Previous studies show that the interactive flow fields in and around the embayment largely depends on main stream Froude number. Kimura and Hosoda (1997) studied the fundamental properties of flows in a compound channel with dead zone both experimentally and numerically with 2D open channel flow equations. They reported that a circulation and free surface oscillation is observed inside the dead zone; and along the interface of mainstream and dead zone, the flow is characterized by formation of coherent vortices. They reproduce the flow features numerically by plane two-dimensional open channel flow equations. Mizumura and Yamasaka (2002) studied the 2D steady flow in an open channel embayment and concentrated only on mean circulation flow inside the cavity. They reported that a 2D flow model cannot express the 3D flow structure at the interface of embayment.

In this chapter, the three–dimensional numerical simulation is carried out to study the fundamental properties of an open channel flow with a rectangular side cavity. A curvilinear coordinate with a variable grid system is used in this study. The formation of coherent vortices at the interface of mainstream and dead zone, as well as its interaction with the circulation and water surface oscillation in the cavity will be studied. The flow pattern and velocity profiles will be compared with the experiments of Kimura & Hosoda (1997).

7.2 Non-linear *k–ε* Model in 3D Curvilinear Coordinate

The 3D flow equations in a *k–ε* model for an unsteady incompressible flow with contravariant components of velocity vectors on a curvilinear coordinate system can be written as follows.

Continuity Equations:

$$\frac{1}{\sqrt{g}}\frac{\partial V^{\alpha}\sqrt{g}}{\partial \xi^{\alpha}} = 0 \tag{7.1}$$

Momentum equation:

$$\frac{\partial V^i}{\partial t} + \nabla_j\left[V^i(V^j - W^j)\right] + V^i\nabla_j W^j + V^j\nabla_j W^i = F^i - \frac{1}{\rho}g^{ij}\nabla_j p + \nabla_j\left[-\overline{v^i v^j}\right] + 2\nu\nabla_j e^{ij} \tag{7.2}$$

k-equation:

$$\frac{\partial k}{\partial t} + \nabla_j\left[k(V^j - W^j)\right] + k\nabla_j W^j = -g_{il}\overline{v^l v^j}\nabla_j V^i - \varepsilon + \nabla_j\left\{\left(\frac{D_t}{\sigma_k} + \nu\right)g^{ij}\nabla_i k\right\} \tag{7.3}$$

ε-equation:

$$\frac{\partial \varepsilon}{\partial t} + \nabla_j\left[\varepsilon(V^j - W^j)\right] + \varepsilon\nabla_j W^j = -C_{\varepsilon 1}\frac{\varepsilon}{k}g_{il}\overline{v^l v^j}\nabla_j V^i - C_{\varepsilon 2}\frac{\varepsilon^2}{k} + \nabla_j\left\{\left(\frac{D_t}{\sigma_k} + \nu\right)g^{ij}\nabla_i \varepsilon\right\} \tag{7.4}$$

2nd-order non-linear turbulence model:

$$-\overline{v'^i v'^j} = D_t S^{ij} - \frac{2}{3} k \delta^i_s g^{sj} - \frac{k}{\varepsilon} D_t \left[\alpha_1 Q_1 + \alpha_2 Q_2 + \alpha_3 Q_3 \right] \ , \ D_t = C_\mu \frac{k^2}{\varepsilon} \tag{7.5}$$

Here,

$$Q_1 = S^{i\alpha} g_{\alpha l} \Omega^{lj} + S^{j\beta} g_{\beta l} \Omega^{li}, \ Q_2 = S^{i\alpha} g_{\alpha l} S^{lj} - \frac{1}{3} S^{k\alpha} g_{\alpha m} S^{m\beta} g_{\beta k} \delta^i_l g^{lj}, Q_3 = \Omega^{i\alpha} g_{\alpha l} \Omega^{lj} - \frac{1}{3} \Omega^{k\alpha} g_{\alpha m} \Omega^{m\beta} g_{\beta k} \delta^i_l g^{lj} \tag{7.6}$$

$$S^{ij} = g^{j\alpha} \nabla_\alpha V^i + g^{i\alpha} \nabla_\alpha V^j, \ \Omega^{ij} = g^{j\alpha} \nabla_\alpha V^i - g^{i\alpha} \nabla_\alpha V^j, S = \frac{k}{\varepsilon} \sqrt{\frac{1}{2} S^{i\alpha} g_{\alpha j} S^{j\beta} g_{\beta i}} \ , \ \Omega = \frac{k}{\varepsilon} \sqrt{\frac{1}{2} \Omega^{i\alpha} g_{\alpha j} \Omega^{j\beta} g_{\beta i}} \tag{7.7}$$

$$\alpha_1 = -0.1325 f_M \ , \ \alpha_2 = 0.0675 f_M \ , \ \alpha_3 = -0.0675 f_M \ , \ f_M = \frac{1}{1 + m_{ds} S^2 + m_{d\Omega} \Omega^2} \tag{7.8}$$

$$c_\mu = \frac{c_{\mu o} \left(1 + c_{ns} S^2 + c_{n\Omega} \Omega^2\right)}{1 + c_{ds} S^2 + c_{d\Omega} \Omega^2 + c_{ds\Omega} S \Omega + c_{ds1} S^4 + c_{d\Omega 1} \Omega^4 + c_{ds\Omega 1} S^2 \Omega^2} \tag{7.9}$$

The values of model constants are given in Table.2.1.

7.3 Computational Scheme and Flow Domain

The governing equations for mean velocities and turbulent flows are discretized with the finite volume method based on full staggered boundary fitted coordinate system. The arrangement of hydraulic variables on staggered grid in a 3D field is shown in Fig. 7.2. For the momentum equation, convective and diffusive fluxes are approximated with Quick and central difference schemes respectively. The hybrid central upwind scheme is used for the k and ε equations. Time advancement is achieved by Adam-Bashforth scheme of second-order accuracy, in each equation. The basic equations are discretized as fully explicit forms and solved successively with the time increment in step by step. The pressure field is solved using iterative procedure at each time step. The free surface elevation is solved by continuity equation integrated over the control volume of the surface layer.

The wall functions are employed as the wall boundary conditions for k and ε. The frictions near the bed and side walls are estimated by log-law. An inflow velocity is prescribed in upstream end, and fixed depth with zero velocity gradient is used as boundary condition at downstream end of the flow domain.

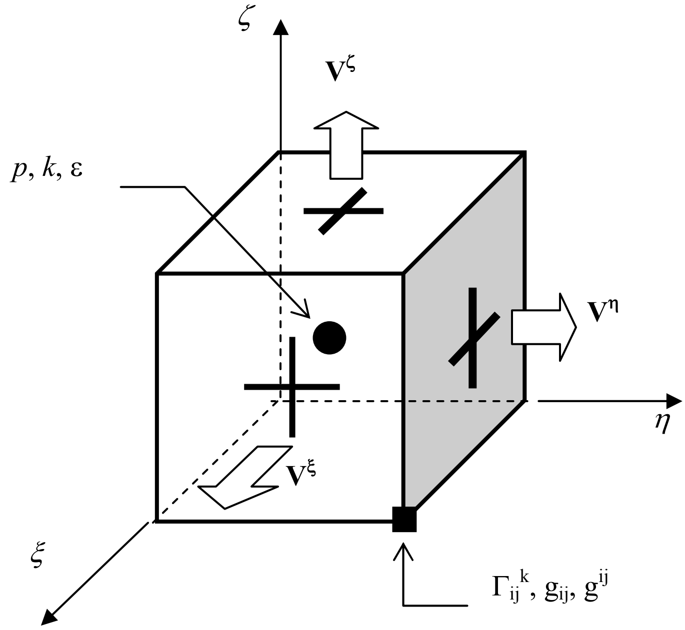

Fig. 7.2 Arrangements of variables in a staggered grid in the 3D computations (Curvilinear coordinate system)

Table. 7.1 Hydraulic parameters for the simulation of open channel with dead zone

Run	*Q_0 (cm^3/s)*	*h_e (cm)*	*ν (cm^2/s)*	*Froude no.*	*Bottom slope*	*Δt (sec)*
1	747.0	2.02	0.917×10^{-2}	0.83	1/500	0.0001

The numerical simulations for 3-D unsteady flows are performed under the same conditions of laboratory experiments conducted by Kimura and Hosoda (1997). The plan view of the computational domain is shown in Fig. 7.3. It consists of 76 grids in longitudinal (stream-wise, x), 42 in transverse (width-wise, y) and 10 in perpendicular to bed (depth-wise, z) directions. The hydraulic conditions are shown in Table 7.1.

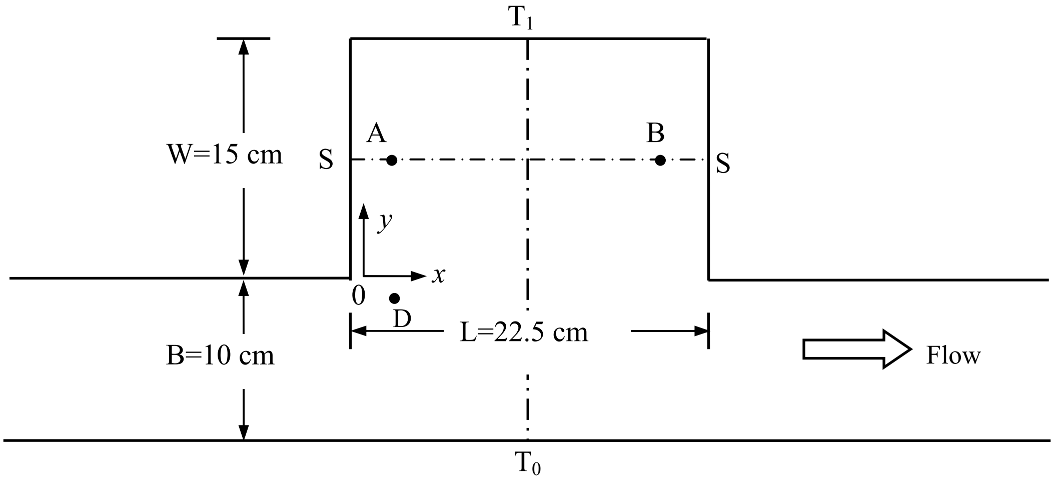

Fig. 7.3. Diagram of flow domain

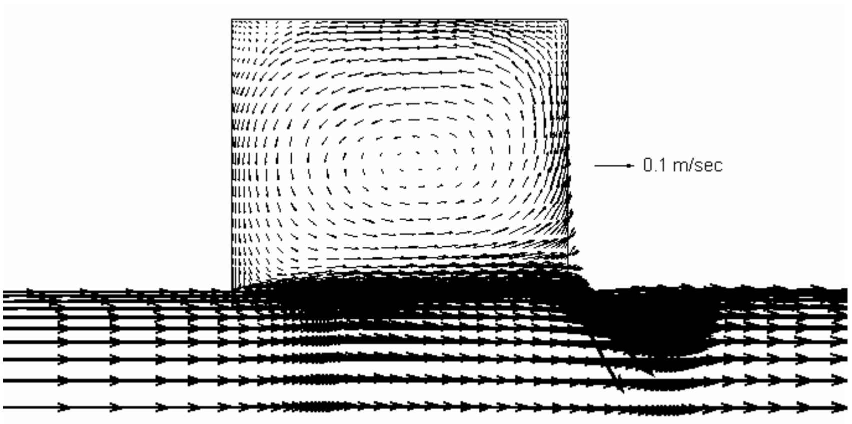

Fig. 7.4. Time averaged velocity vectors

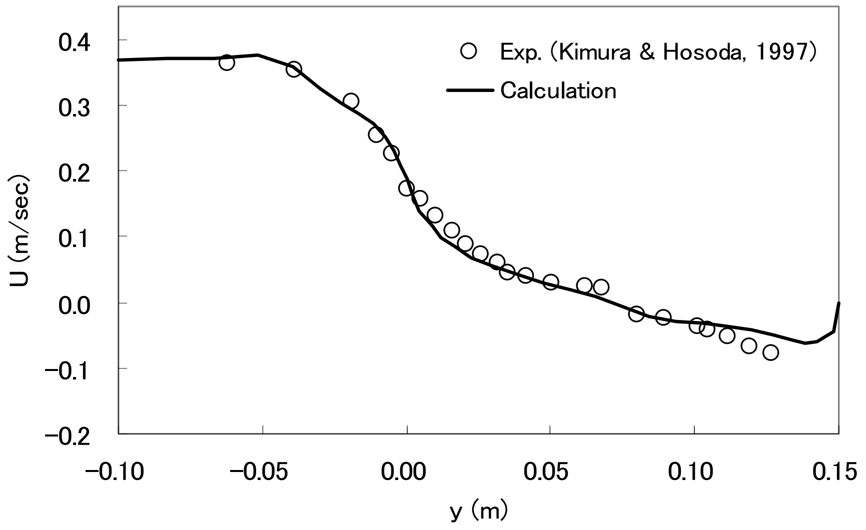

Fig. 7.5. Comparison of time averaged velocity profile along T$_0$-T$_1$

7.4 Numerical Results and Discussions

7.4.1 Time averaged flow properties

The unsteady flow in a dead zone is characterized by three important flow criteria: the circulation and oscillation inside the dead zone, and the coherent vortices at the interface of main stream and dead zone. However, the time averaged flow does not show instability characteristics. Fig. 7.4 shows the time averaged (averaging for 10 secs) velocity vector, which mainly characterized by the circulation inside the dead zone. The simulated vector field and the circulation pattern are very similar to the previous experimental and 2D numerical studies (Kimura and Hosoda, 1997; Takemoto et al.,1984).

Fig. 7.5 shows the time averaged profile of stream-wise velocity (u) along the transverse cross-section at centerline of dead zone (the section is shown in Fig. 7.3 as T_0-T_1). The comparison of simulated result with experiment shows good agreement.

7.4.2 Temporal variation of flows

The formation of instability vortices at the interface of main channel and dead-zone and its interaction with the dead zone circulation can be described by considering the temporal change of velocity vectors as shown in Fig. 7.6. In the figure, the flow vectors are presented at a periodic interval of 0.2 sec. It indicates that the vortices formed at the upstream end of the interface (just after x =0) moves downwards with increasing time. The deviation of velocity vectors from the main circulation near the interface shows the position of instability vortices. The center point of dead zone circulation (i.e. the location of minimum tangential velocity) is also found to be changed slightly depending on the location and maturity of instability vortices. Fig.7.7 shows close-up view of vector plot near the upstream corner of shear layer. The vortex formation and its temporal changes at an interval of 0.2 sec are illustrated in this figure. It is found that the instability vortex observed at upstream corner of interface moves downstream with gradual amplification with time, and the process continues repeatedly with a constant periodic interval. The velocity vectors at t = 57.2 sec and t = 58.0 sec show the instability vortices of about same maturity, it gives an estimation about the vortex period as about 0.8 sec.

The temporal variations of water surface distribution are demonstrated in Fig. 7.8, for the same time periods as discussed for vector plots. Two important phenomena can be explained from these figures. One is seiche inside the dead-zone, and another is hollow water surface at the center of instability vortices. The hollow of the free surface moves downward with time along the interface, as observed in the movement of large vortices in vector plots (in Fig. 7.6). In the present flow domain two to three hollows in water surface can be seen in an instantaneous flow field. Since, the vortices at the upstream corner are premature and those near the downstream corner are decayed due to merging with main circulation, the large vortices at the middle part of the interface are most matured and show highest depression in the surface. The feature can be further explained using a water depth profile along the interface. Fig. 7.9 describes the spatial distribution of water surface near the interface regions. The effect of instability vortices on the water surface as discussed above is clearly depicted in this figure. The depressions in the profile, that indicate the position of instability vortices, is gradually increasing with down stream distances and show maximum depression in the middle half of the interface.

The second important phenomenon described in Fig. 7.8 is the oscillation inside the dead zone. If we look beyond the interface it can be seen that, Figs. (a) and (b) show minimum depth at downstream end and maximum depth in upstream end of dead zone; on the other hand, Figs. (c) and (d) show reverse phenomena. Finally, in Fig.(e) the depth distribution returns to its nearly starting phase (as Fig.(a)) after 0.8 sec. A periodic change in the depth difference between upstream and down stream end of dead zone indicates the existence of oscillation in the cavity.

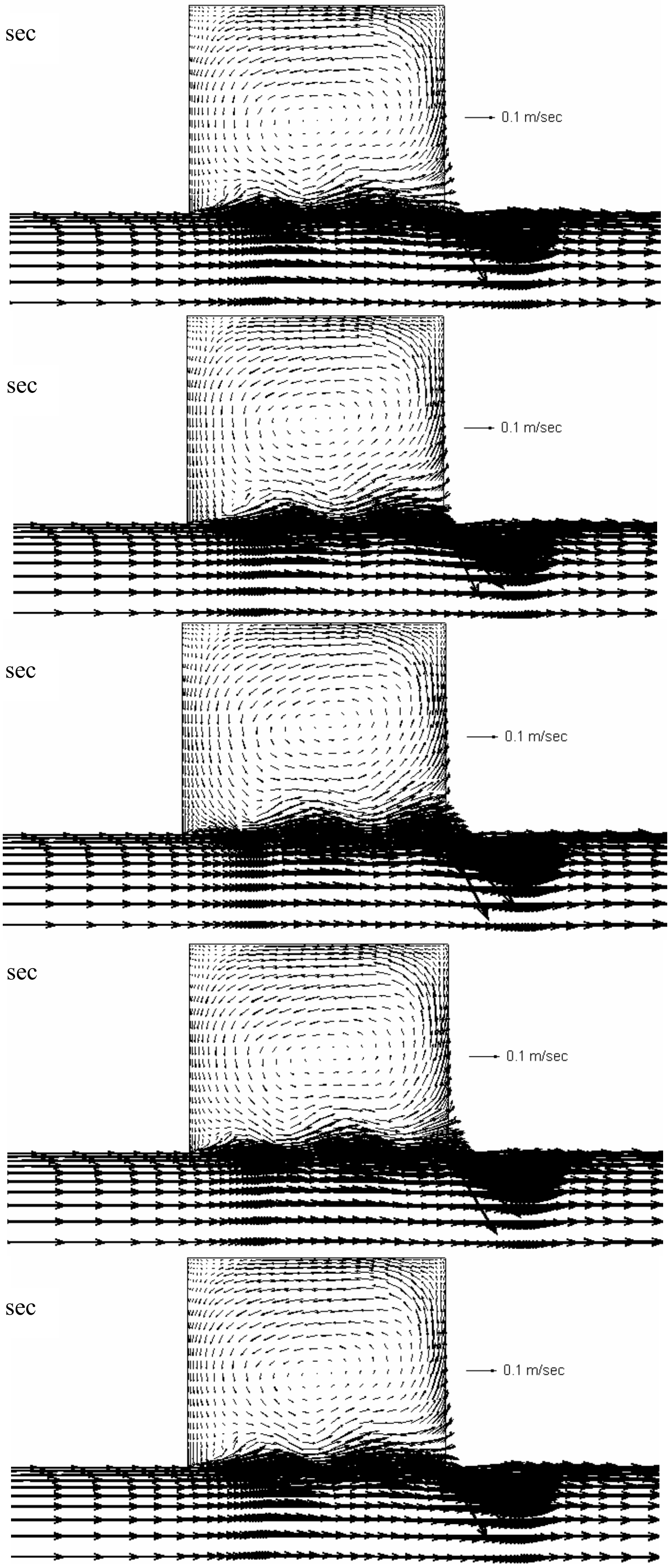

(a) t =57.2 sec

(b) t =57.4 sec

(c) t =57.6 sec

(d) t =57.8 sec

(e) t =58.0 sec

Fig. 7.6. Temporal change of velocity vectors at 0.2 sec intervals

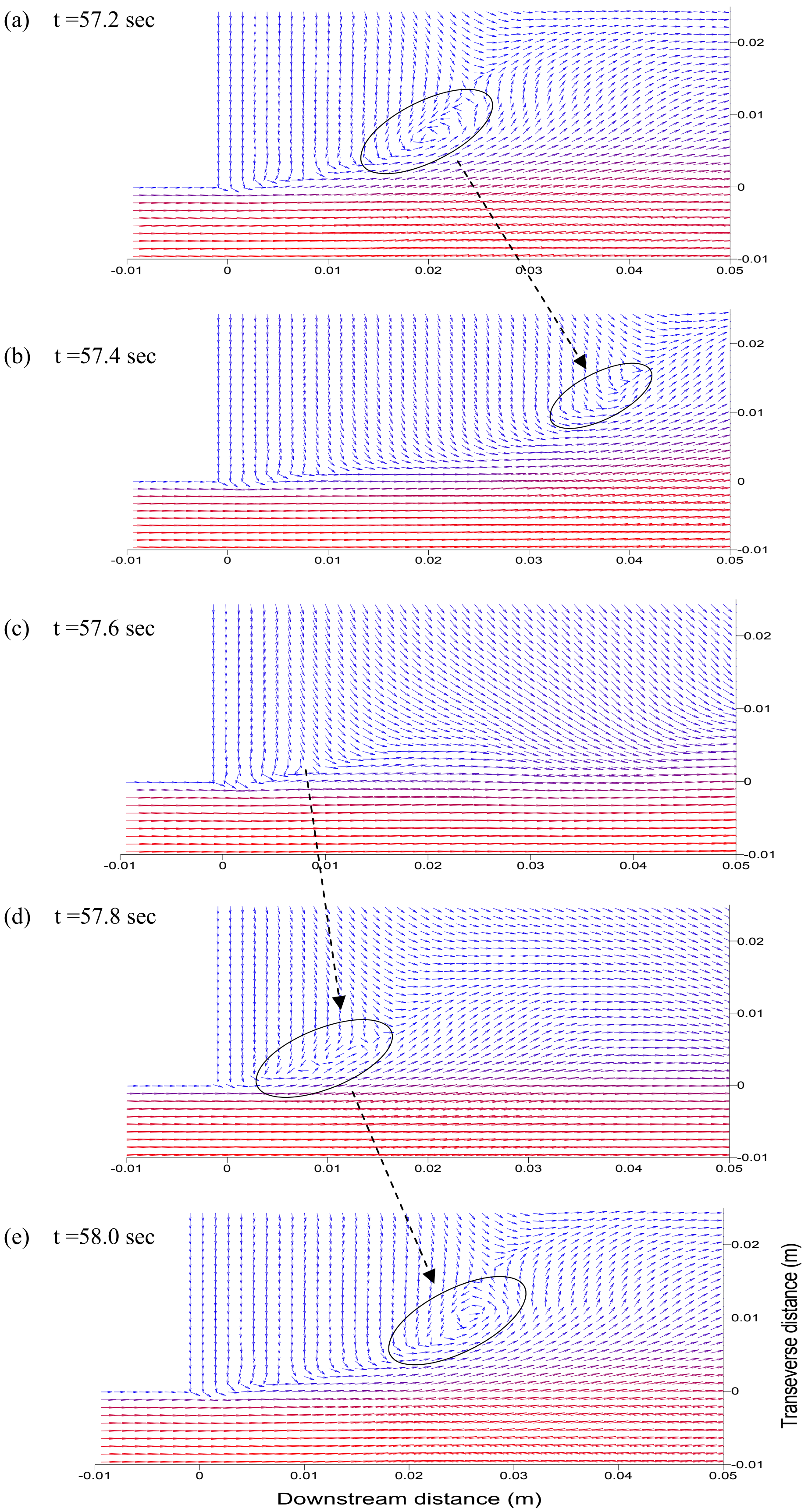

Fig. 7.7. Temporal change of instability vortices at 0.2 sec intervals

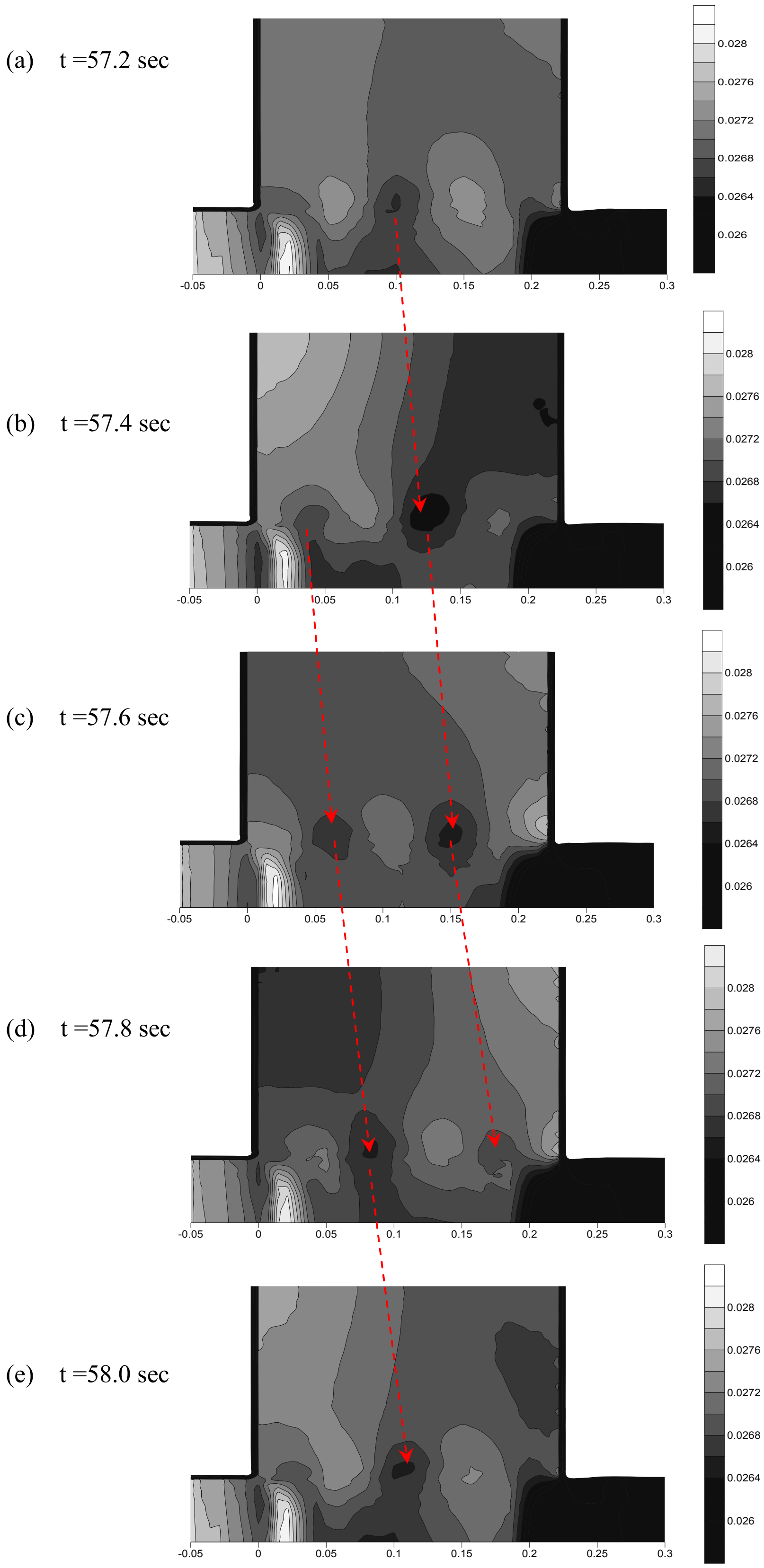

(a) t =57.2 sec

(b) t =57.4 sec

(c) t =57.6 sec

(d) t =57.8 sec

(e) t =58.0 sec

Fig. 7.8. Temporal change of water depth distribution at 0.2 sec intervals (the arrow indicates the stream-wise movement of depression in water surface)

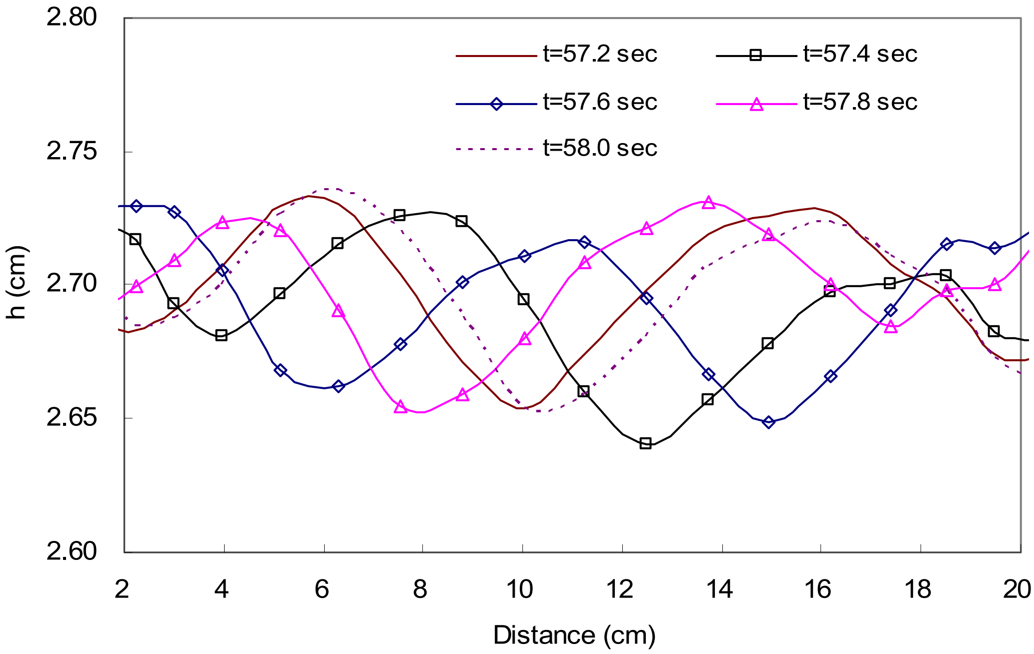

Fig. 7.9. Temporal change of water depth distribution along the interface

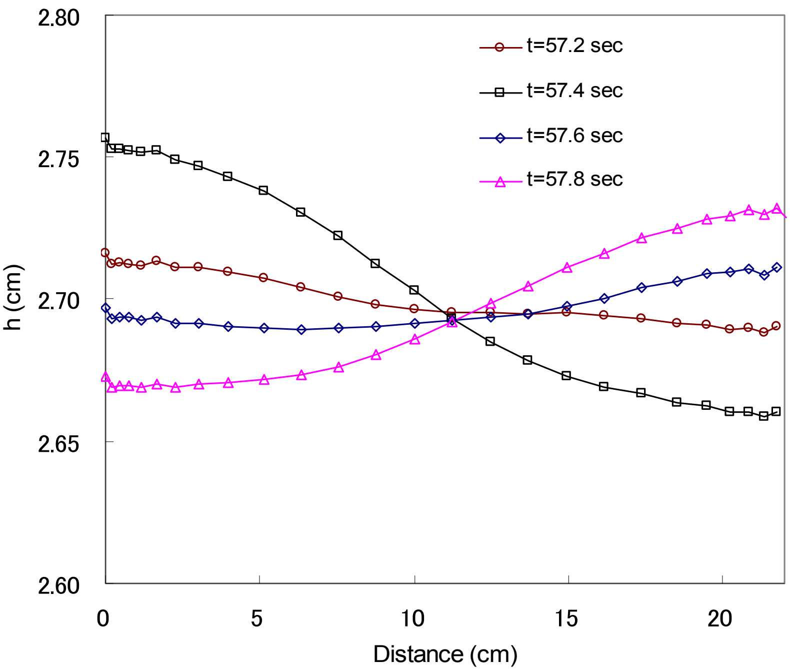

Fig. 7.10. Temporal change of water depth distribution along S-S section

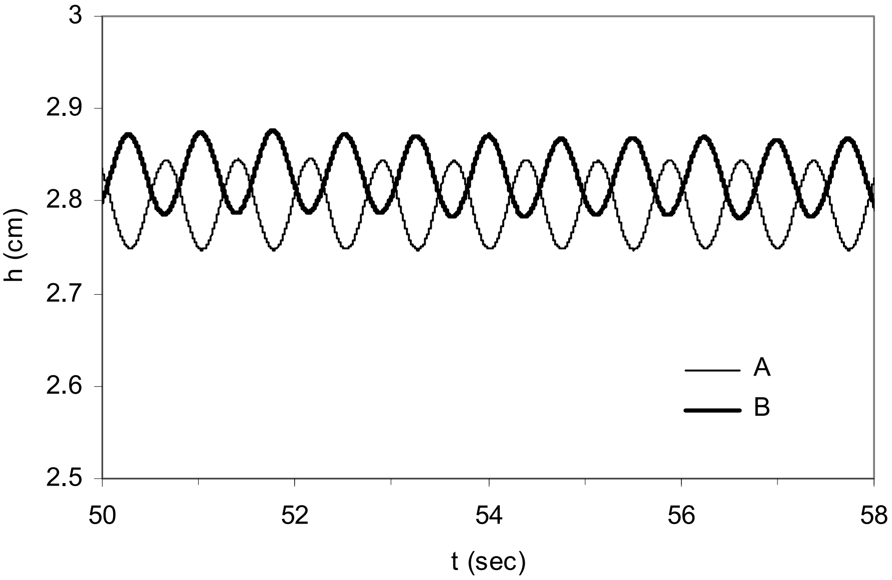

Fig. 7.11. Temporal variations of water surface at A and B

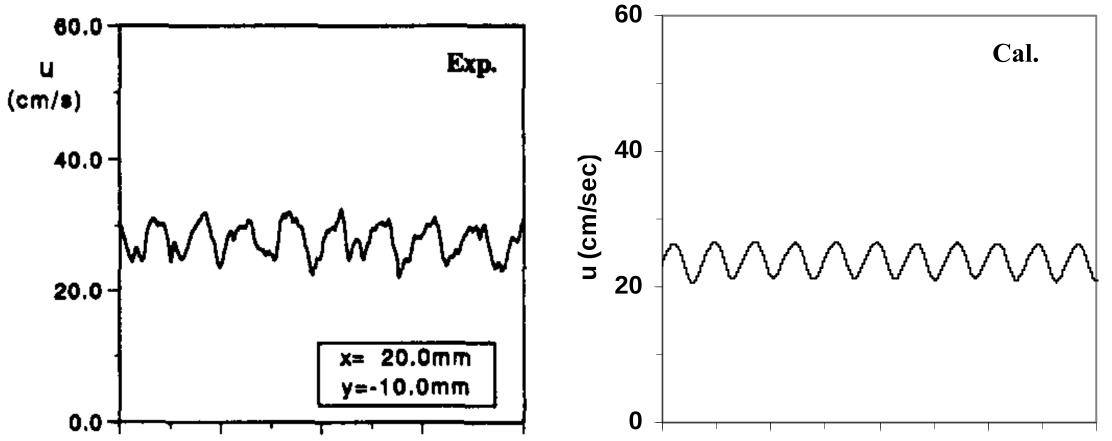

Fig. 7.12. Temporal variations in stream-wise velocity (*u*) at point D

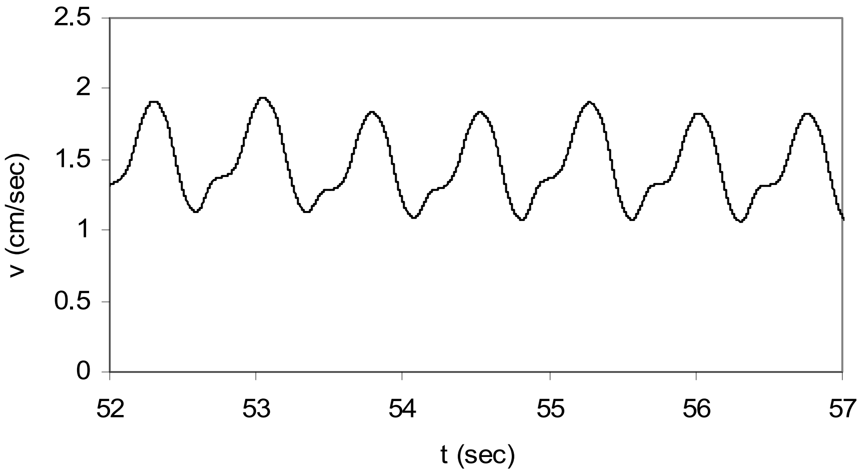

Fig. 7.13. Temporal variation of transverse-velocity component (v) at the interface (*x* =5 cm)

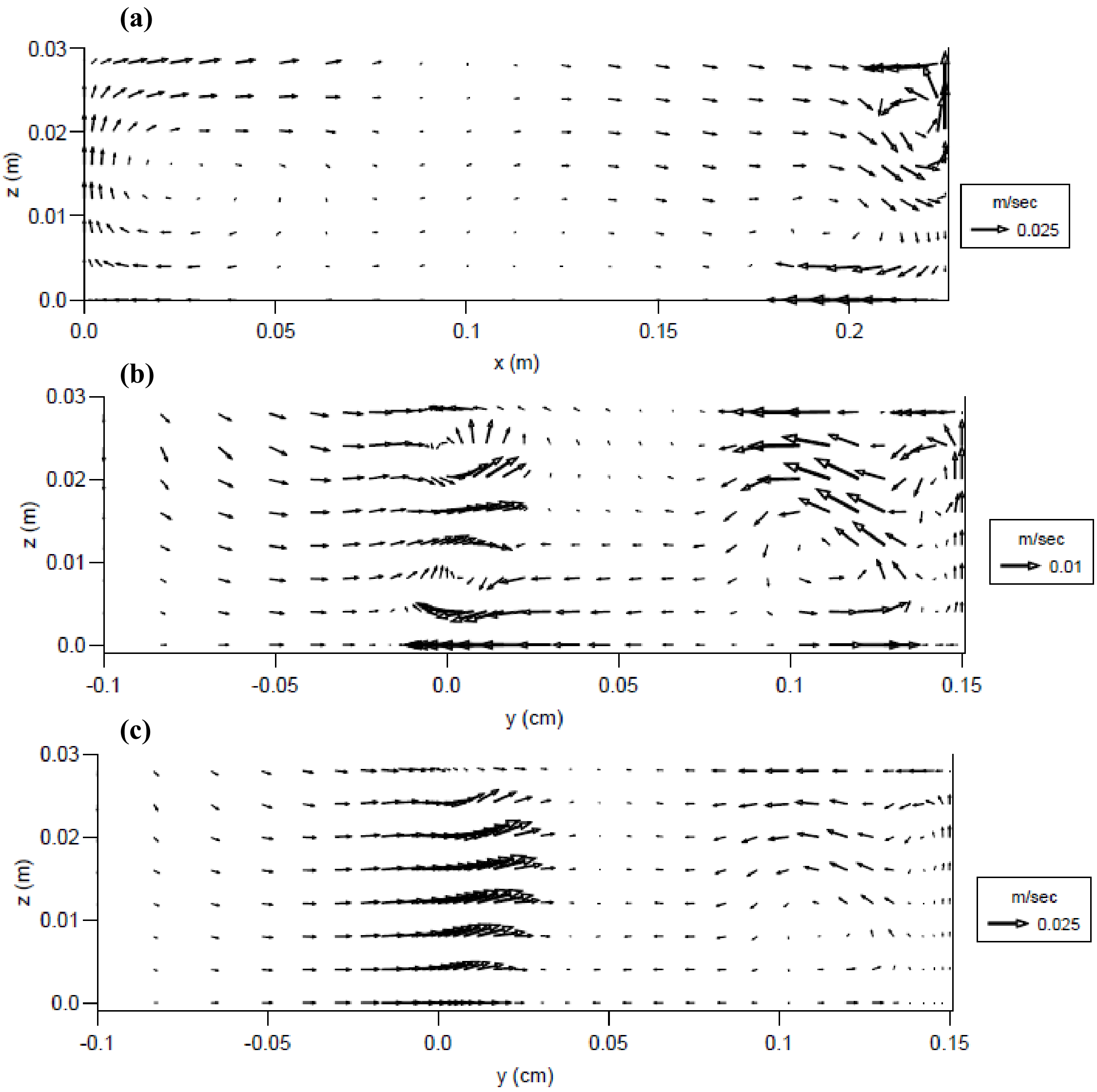

(d)

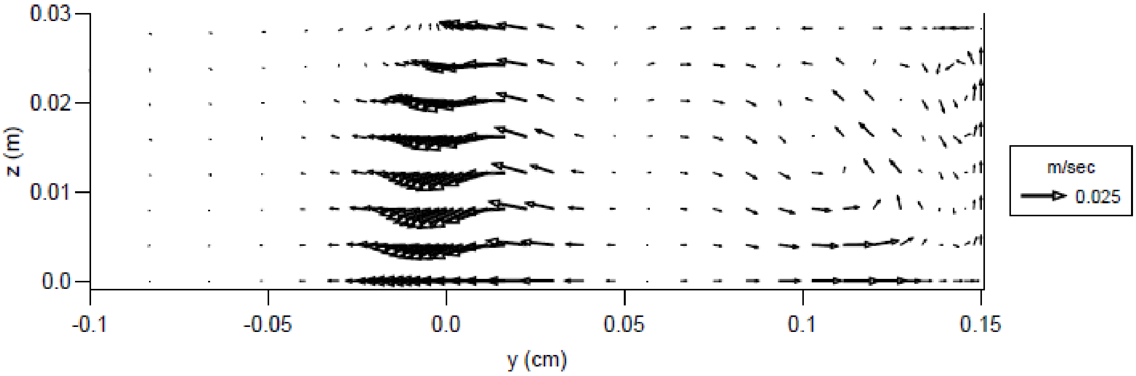

Fig. 7.14. Instantaneous pattern of secondary current at (a) S-S section (b) T_0-T_1 section (c) adjacent grid just upstream of T_0-T_1 section (d) adjacent grid just downstream of T_0-T_1 section (t = 57.2 sec)

This oscillation of water surface is clearly demonstrated in Fig. 7.9. In this figure, the spatial water depth distribution in the dead zone along the section S-S (as shown in Fig. 7.3) is shown for different time intervals. It explains that the node of oscillation, that contains the lowest seiche mode with a direction parallel to the main flow, is located near the center of the circulation. The wavelength of the oscillation is about twice the dead-zone length. Fig. 7.8 depicts that the water depth distribution at t = 57.2 sec and t = 58.0 sec show about same orientation of instability vortices as well as same seiche mode. It gives an estimation of the period of instability vortex , which is about the same as the oscillation (approximately 0.8 sec).

Comparing with Fig. 7.9, it is observed that the depth variation inside the dead zone is mainly due to the seiche, and near the interface it is governed by the instability vortices.

Figure 7.11 shows the calculated results for temporal free surface oscillation at point A and B. The period of oscillation is found as 0.75 sec, which is slightly smaller than the experimentally observed value of 0.87 sec. The temporal variation of stream-wise velocity (u) is compared with experiment in Fig. 7.12. The calculated magnitude of velocity variation is well agreed with experiment. The period of oscillation in the temporal changes of u-velocity is found same with the periodic oscillation of water surface.

The temporal change of transverse velocity component (v) at a point on the interface (x =5 cm, y =0) is shown in Fig. 7.13. It is observed that, each cycles of temporal velocity variations consists two components of oscillations. The long one is due to seiche and has a time period of 0.75 sec. The period of short oscillation component is about 0.15-0.25 sec, which is caused by the instability vortices. This phenomenon is also reported in previous experimental observations.

7.4.3 Secondary currents

Although the depth of the flow is small, strong secondary currents are found to be generated at inside the dead zone as well as near the interface area. Figure 7.14 shows the pattern of instantaneous secondary current at S-S section, T_0-T_1 section as well as the sections just upstream and downstream of T_0-T_1 for t = 57.2 sec. Some flow exchange between main-channel and dead zone is observed in Figs. 7.14(c) and (d).

The secondary currents in time-averaged flow filed are presented in Fig. 7.15 (for the sections perpendicular to main stream flow direction and across the dead-zone, T-T) and in Fig. 7.16 (for the longitudinal sections of the dead-zone, S-S). The sectional locations are shown in Fig. 7.15(a) for T-T sections and in Fig. 7.16 (a) for S-S sections. In the figure, Surface and corner circulation cells near the boundaries of dead-zone are clearly depicted. Although, several circulation cells are observed at the middle of dead-zone in T_2-T_2 section with the size equal to the depth, the circulation cell/cells near the interface region are found to be much stronger and seems to be a general feature of the dead zone flow (as it is seen in all the T-T sections).

Flow field with higher water depth and smaller grid size may give a better and improved presentation of secondary flow in such a complicated flow field.

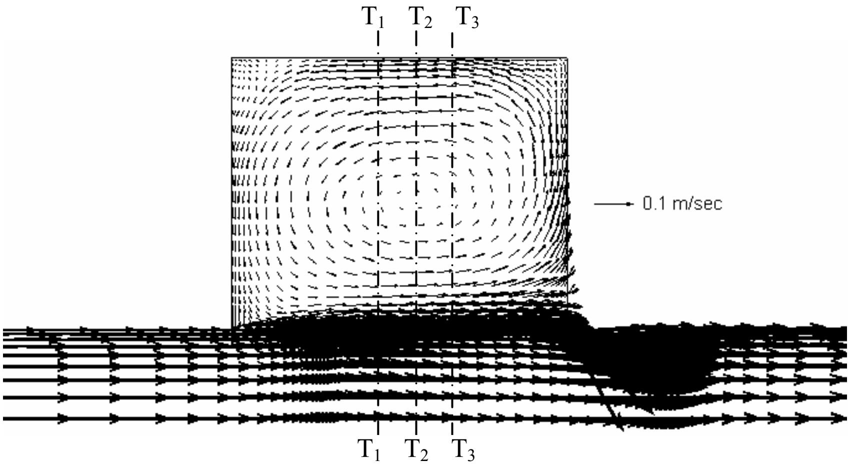

(a) Location of sections in the plan view of Time averaged velocity field

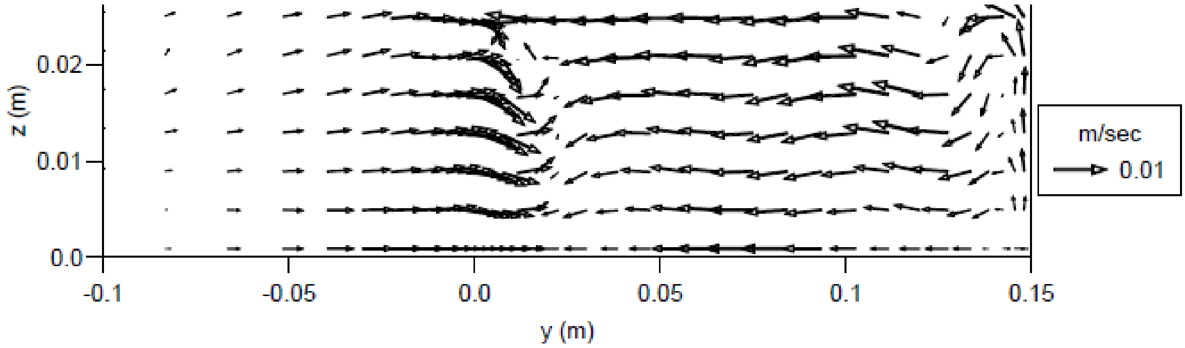

(b) Time averaged secondary current at Section T$_1$ – T$_1$

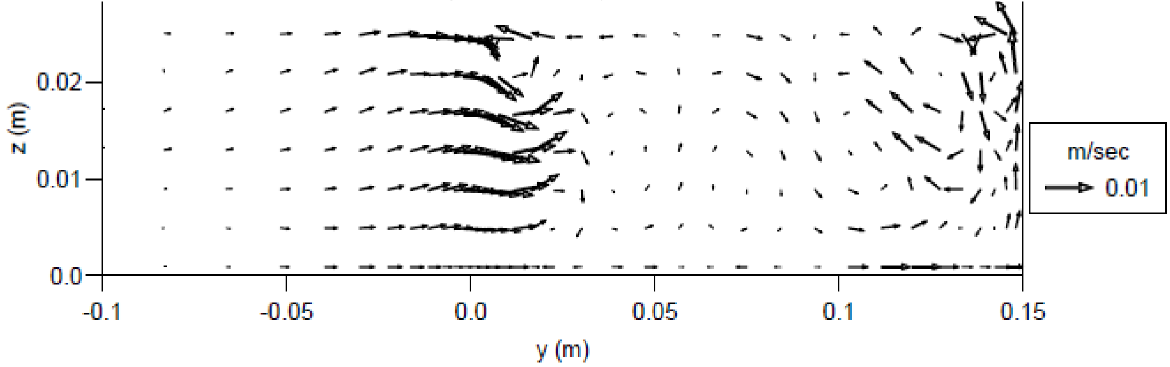

(c) Time averaged secondary current at Section T$_2$ – T$_2$

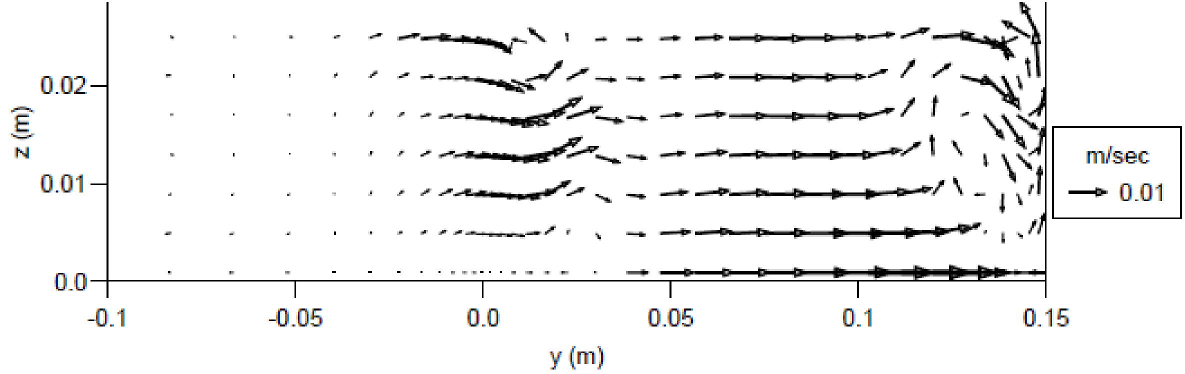

(d) Time averaged secondary current at Section T$_3$– T$_3$

Fig. 7.15. Pattern of time-averaged secondary current in transverse section (T-T)

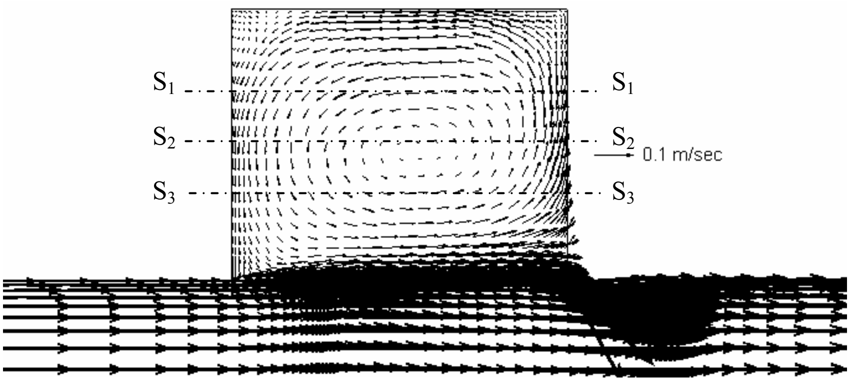

(a) Location of sections in the plan view of time averaged velocity field

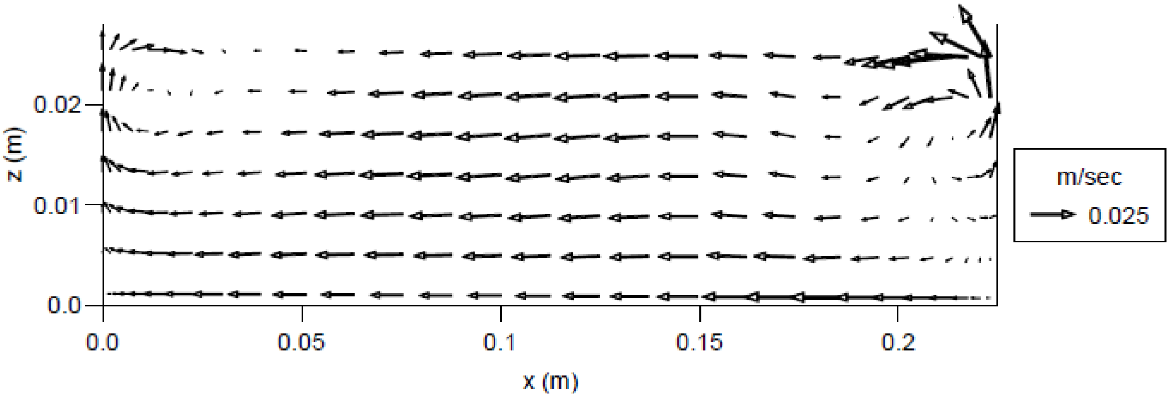

(b) Time averaged secondary current at Section $S_1 - S_1$

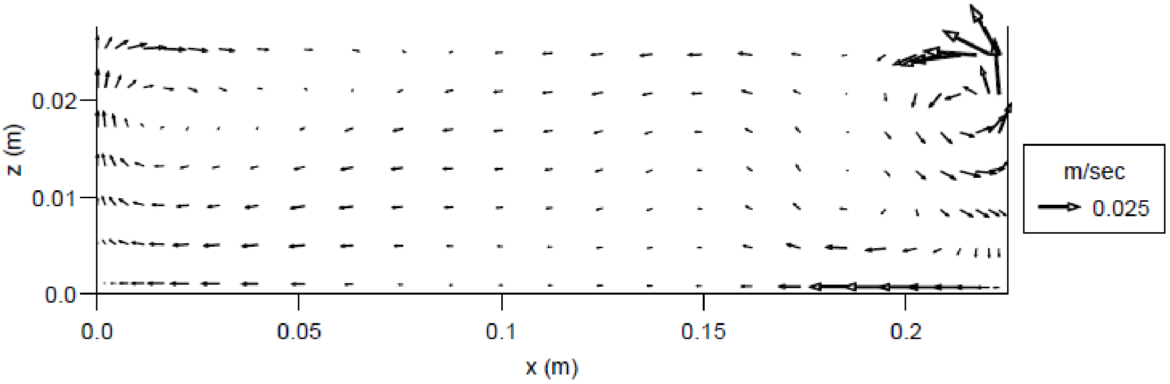

(c) Time averaged secondary current at Section $S_2 - S_2$

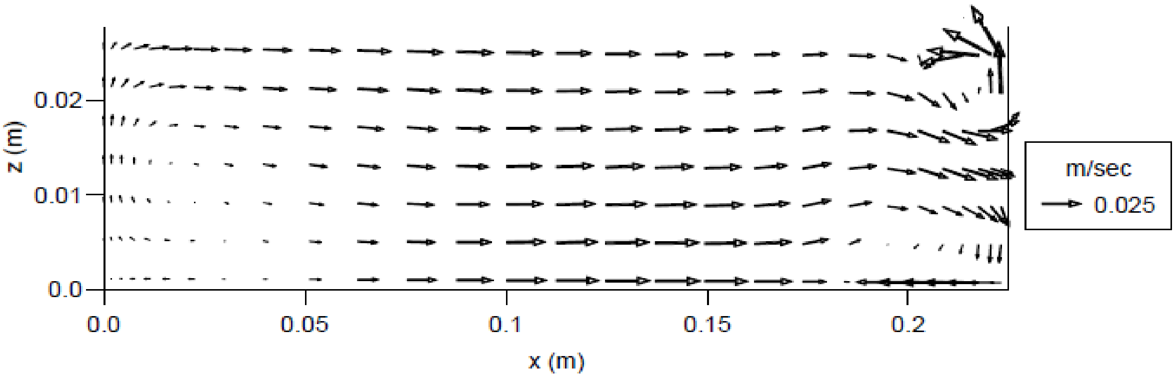

(d) Time averaged secondary current at Section $S_3 - S_3$

Fig. 7.16. Pattern of time-averaged secondary current in dead-zone (S-S section)

7.5 Summary

The flow field in an open channel with a rectangular side cavity is investigated by three-dimensional unsteady RANS computations. The time averaged flow properties and temporal change of velocity profiles are well compared with previous experimental results. It is found that the flow in a dead zone is characterized by three types of flow phenomena: the circulation inside the dead-zone, periodic coherent vortices at the interface of main stream and dead zone, and the water surface oscillation inside the dead zone. In this study all these characteristics are successfully reproduced by numerical simulation.

It is denoted that the instability vortex generated at upstream corner of interface moves downstream with gradual amplification with time that finally merges with the dead-zone circulation at the downstream corner. The process continues repeatedly with a constant periodic interval.

The temporal variation of water surface shows a depressed water depth at the center of coherent vortices. This hollow of the free surface moves downward with time along the interface, as observed in the movement of large vortices in vector plots.

In the calculated result, a periodic change in depth difference between upstream and down stream end of dead zone indicates the existence of oscillation in the cavity. The period of oscillation is found same as that of instability vortex.

It is observed that, each cycles of velocity variations consists two components of oscillations. The long one is due to seiche and has a time period of 0.75 sec. The period of short oscillation component is about 0.15-0.25 sec and caused due to instability vortices. This phenomenon is also reported in previous experimental observations.

Although the depth of the calculated flow field is small, strong secondary currents are found to be generated at inside the dead zone as well as near the interface area.

7.6 References

1) Kimura, I. and Hosoda, T., Fundamental properties of flows in open channels with dead zone, *J. Hydr. Engg., ASCE,* Vol. 123, pp. 98-107, 1997.

2) Mizumura, S.Y. and Yamasaka, C. J., Flow in open channel embayment, *J. Hydr. Engg., ASCE*, Vol. 128, pp. 1098-1101, 2002.

3) Muto, Y., Baba, Y., Aya, S.,Velocity measurements in open channel flow with rectangular embayments formed by spar dykes, *Annuals of Disas. Prev. Res. Inst., Kyoto Univ.,* No. 45B-2, 2002.

4) Takemoto, Y., Yamabe, H., Abe, Y. and Naitou, H., On the third upwind finite difference scheme in numerical analysis for initial value problem, *Res. Rep., Inst. Plasma Phys., Nagoya University, IPPJ-693, Nagoya, Japan*, 1984.

Chapter 8
CONCLUSIONS

8.1 Summary of the findings

The standard $k–\varepsilon$ model has the deficiency of predicting the flow field with high rate of strain and rotation due to its isotropic assumption of eddy viscosity. Therefore, a second order non-linear k-ε model is proposed incorporating some new functions for the model coefficients to explore the model applicability to complex turbulent flows. Firstly, the refinements are proposed, and model constants are turned considering some basic turbulent flows. Considering theoretical approach, the analytical solutions are derived for predicting the turbulent properties of these flows. After that, numerical simulations are carried out for several complex turbulent flows governed by coherent vortices, secondary circulation as well as water surface oscillations. The findings of this research are summarized below headed with sub-topics.

I. Refinement of the model

Considering the realizability principle and anisotropy of turbulence for some baseline turbulent flows, the coefficient of eddy viscosity (c_μ) and the coefficients of non-linear quadratic terms (c_β) are derived as a function of strain and rotation parameters. The simple shear layer, plane strain, axisymmetric contraction and axisymmetric expansion are considered as baseline flows to tune the model constants. It is observed that, both for shear straining and normal straining, the predicted normal stress separation is realistic, and the realizability is maintained even at high strain rates.

II. Round jet with and without swirl

Approximate solutions for the fundamental properties of swirl and non-swirl jets are derived based on the non-linear k–ε model. The approximate solutions are compared with the previous experimental results and further tuning of model constants are performed for best fitted comparison. The solutions of standard k–ε model is also presented. Reasonably, the non-linear model showed better comparison than standard one.

III. Turbulent structures in a coherent vortex

Based on the proposed non-linear k–ε model, approximate solutions are derived for the turbulent properties of an idealized vortex street to explore the predictability of the model for large scale vortices. The spatial changes of turbulent structures with the singular points in a coherent vortex are investigated. The qualitative results are compared to previous experiments to assess the models applicability.

The Stuart vortex, which contains both vortex and saddle patterns in its vorticity contour, is considered as an ideal simple vortex street. The turbulent structures at vortex center and saddle point obtained by approximate solution are found consistent with the previous experimental results of large scale coherent vortices in free shear flows. The turbulent structures of the vortex street are found sensitive to the functional form of the coefficient of eddy viscosity, c_μ.

The turbulent structures are found to be changed with the spatial distance depending on the structures of singular points. It is observed that the turbulent normal stresses show elliptical structure near vortex center, which changed to hyperbolic profile near saddle point at a stream-wise periodic distance of π. However, the shear stresses show hyperbolic structures at vortex center, and the structure changes to elliptical at saddle point.

The topological change of turbulent kinetic energy and dissipation rates with stream-wise spatial distance are found to be similar to turbulent normal stresses.

IV. Compound open channel flows

The flow field in a compound channel is generated using standard as well as non-linear k- ε models both including and omitting the horizontal vortices. The numerical results are assessed from the view point of coherent structures, such as horizontal vortices at the interface of subsections and secondary current of second kind. The predicted discharges by different models are compared and the contribution of eddy viscosity and quadratic term in non-linear model is evaluated. Comparing the predicted roughness coefficients with previous experimental results as well as with other methods, the contribution of vortices and secondary currents to the prediction of roughness coefficients are quantified.

The velocity and shear-stress profiles are found to be distorted significantly due to the generation of coherent vortices at the interface of main channel and flood plain. It is observed that the velocity and shear stress values are under-predicted near the interface region, if the momentum transfer due to horizontal vortices is not considered. The well agreed profiles are obtained when the effects of vortices are taken into account.

In the prediction of secondary current, although the pairs of surface vortices as well as the corner vortices in main channel are clearly depicted by both the non-linear models, the 3rd order model shows superior comparison with experiments than 2nd order model. It is seen that the magnitude of upwelling secondary currents at the interface are suppressed by the influence of flows caused by the coherent vortices. The secondary currents for higher depth ratios (H/h) are found higher in magnitude compared to lower depth ratios. It is observed that with increasing the flood plain depth, the scales of surface vortices are increased. The magnitude of secondary currents also increases significantly with the flood plain depth.

The resistance of compound channel is found to be increased due to the generation of coherent structures. The numerical result improves the prediction of compound resistance coefficient by about 21% over the separate channel method, where the vortices contribute about half of that and the rest is due to secondary currents and associated three-dimensional turbulent structures.

The turbulent structures in coherent vortices at interface are found to be changed with the stream-wise distance depending on the structures of singular points. The structures of turbulent stresses at vortex center and saddle point are found consistent with that of an idealized vortex street (Stuart vortex) as well as previous experiments of free shear flows.

V. The structure and decay of a turbulent Trailing vortex

The unsteady numerical simulations are performed for an isolated turbulent axial vortex using standard and non-linear k–ε models. Since the rotational effects of vortex are not captured by a standard k–ε model, it predicted extremely rapid and strong turbulence growth and caused a rapid decay of tangential and axial velocity. However, the non-linear model shows good agreement with DNS results. For the tangential velocity, the self similarity solution embraces regions I and II (defined by Phillips) for all the time periods, however region-III collapses in a single curve only for fully developed flow. Phillips' model equations for similarity solution of velocity and circulation profiles are perfectly fitted with the simulated results. Circulation overshoot is observed in the well grown vortex field. Due to this overshoot, the self similarity solution seems to be not possible in region III.

It is observed that the decay rate of axial velocity is much higher than tangential velocity. Since the vortex takes some time for initial adjustments, the decay rate is small at initial times. For both the velocities, the high decay rate is seen in intermediate time period. After that the decay slows down, and the slope of decay proceeds towards minimum.

Five different time periods are observed in the growth/decay profile of turbulence kinetic energy. Initially the vortex changes very slowly, then an exponential growth is seen that slows down before gaining its peak value. The peak value of turbulent kinetic energy remains about constant for a short period that finally follows the period of turbulence decay.

After the maturity of vortex, the turbulent normal stresses show two types of anisotropic behavior depending on the radial distance. Although the radial component is always greater than other two, the tangential component is greater near the center and smaller around the region of maximum tangential velocity in comparison to axial component. The decay rate of energy after the period of stabilization is much slower than the growth rate in the time zones before the stabilization. The decay of velocity field slows down as the turbulence decay period starts.

The result reveals that the rate of temporal decay in tangential velocity increases with decreasing the swirl number q. Therefore, if no axial velocity is present in the flow field, which is the situation for $q = \propto$, the decay of tangential velocity with time should be smaller compared to the vortex field with axial velocity.

3D numerical simulation is carried out for an ideal Rankine vortex using both RANS and LES. For the case of trailing vortices, the axis of rotation is horizontal. However, in this 3D simulation, the vortex flow field is given to rotate with the vertical axis in a free surface rectangular domain. The prediction of vortex decay by RANS model shows good agreement with LES. The water surface found to be depressed near the central area of the vortex with a minimum water depth at center of it. Since the strength of vortex decreases due to the decay of tangential velocity, the depth of depression in water surface is also decreased with time.

VI. Open channel flow with a rectangular side cavity

The flow in a dead zone is characterized by three types of flow phenomena: the circulation inside the dead-zone, periodic coherent vortices at the interface of main stream and dead zone, and the water surface oscillation inside the dead zone. In this study all these characteristics are successfully reproduced by numerical simulation.

It is found that the instability vortex generated at upstream corner of interface moves downstream with gradual amplification with time that finally merges with the dead-zone circulation at the downstream corner. The process continues repeatedly with a constant periodic interval.

The temporal variation of water surface displays a depressed water depth at the center of coherent vortices. This hollow of the free surface moves downward with time along the interface, as observed in the movement of large vortices in vector plots. A periodic change in depth difference between upstream and down stream end of dead zone indicates the existence of oscillation in the cavity. It is observed that the period of oscillation is same as that of instability vortex.

It is found that, each cycles of velocity variations consists two components of oscillations. The long one is due to seiche and has a time period of 0.75 sec. The period of short oscillation component is about 0.15-0.25 sec and caused due to instability vortices. This phenomenon is also pointed out in previous experimental observations.

8.2 Recommendation for Further Studies

Based on the analysis and results of the worked out problems as well as comparison of results with previous investigations, the following works are recommended for future studies concerning the further knowledge about the investigated problems.

In this study, all the analytical and numerical investigations are mainly based on a 2nd order non-linear k–ε model. A 3rd order model is also used in Chapter 5 as a trial case. It is observed that the secondary current predicted by 3rd order model is slightly better than the 2nd order. Detail investigations are necessary to estimate the coefficients of third order terms for further improvement of the model.

For the simulation of Rankine vortex, a Cartesian coordinate system is used in this study. A Cylindrical coordinate instead of Cartesian may give a better presentation of the flow field.

Flows in an open channel with a rectangular dead zone is studied for only one case. However, the change of hydraulic parameters such as Froude number, aspect ratio of the dead zone is necessary for better understanding of such a complicate flow field. The water surface oscillations found in the present 3D modeling is slightly smaller than the prediction of 2D model (Kimura & Hosoda, 1997). Although, such problem of 3D simulation is reported in previous researches (Kimura et. al., 2006), further study is required to identify the reasons behind this problem.

8.3 References

1) Kimura, I. and Hosoda, T., Fundamental properties of flows in open channels with dead zone, *J. Hydr. Engg., ASCE,* Vol. 123, pp. 98-107, 1997.

2) Kimura, I. and Hosoda, T., Computation of 2D and 3D computational models on 2D shallow mixing layer, *Proc. 61th Annual Conference, JSCE,*CD-ROM Proc, 2006.